Stony Brook University

Development of Carbon Sequestration Options by Studying Carbon Dioxide-Methane Exchange in Hydrates

A Dissertation Presented

by

Kristine Nicole Horvat

to

The Graduate School

in Partial Fulfillment of the

Requirements

for the Degree of

Doctor of Philosophy

in

Materials Science and Engineering

Stony Brook University

August 2015

Stony Brook University

The Graduate School

Kristine Nicole Horvat

We, the dissertation committee for the above candidate for the

Doctor of Philosophy degree, hereby recommend

acceptance of this dissertation.

Dr. Devinder Mahajan – Dissertation Advisor

Professor, Department of Materials Science and Engineering

Dr. Keith Jones - Chairperson of Defense

Adjunct Faculty, Department of Materials Science and Engineering & Senior Scientist Emeritus, Brookhaven National Laboratory

Dr. Tadanori Koga

Associate Professor, Department of Materials Science and Engineering

Dr. Stephen Masutani

Researcher, Hawaii Natural Energy Institute, University of Hawaii at Manoa

This dissertation is accepted by the Graduate School

Charles Taber

Dean of the Graduate School

Abstract of the Dissertation

Development of Carbon Sequestration Options by Studying Carbon Dioxide-Methane Exchange in Hydrates

by

Kristine Nicole Horvat

Doctor of Philosophy

in

Materials Science and Engineering

Stony Brook University

2015

Gas hydrates form naturally at high pressures (>4 MPa) and low temperatures (<4 ^{o}C) when a set number of water molecules form a cage in which small gas molecules can be entrapped as guests. It is estimated that about 700,000 trillion cubic feet (tcf) of methane (CH_4) exist naturally as hydrates in marine and permafrost environments, which is more than any other natural sources combined as CH_4 hydrates contain about 14 wt% CH_4. However, a vast amount of gas hydrates exist in marine environments, which makes gas extraction an environmental challenge, both for potential gas losses during extraction and the potential impact of CH_4 extraction on seafloor stability. From the climate change point of view, a 100 ppm increase in atmospheric carbon dioxide (CO_2) levels over the past century is of urgent concern. A potential solution to both of these issues is to simultaneously exchange CH_4 with CO_2 in natural hydrate reserves by forming more stable CO_2 hydrates. This approach would minimize disturbances to the host sediment matrix of the seafloor while sequestering CO_2. Understanding hydrate growth over time is imperative to prepare for large scale CH_4 extraction coupled with CO_2 sequestration.

In this study, we performed macroscale experiments in a 200 mL high-pressure Jerguson cell that mimicked the pressure-temperature conditions of the seafloor. A total of 13 runs were performed under varying conditions. These included the formation of CH_4 hydrates, followed by a CO_2 gas injection and CO_2 hydrate formation followed by a CH_4 gas injection. Results demonstrated that once gas hydrates formed, they show "memory effect" in subsequent charges, irrespective of the two gases injected. This was borne out by the induction time data for hydrate formation that reduced from 96 hours for CH_4 and 24 hours for CO_2 to instant hydrate formation in both cases upon injection of a secondary gas. During the study of CH_4-CO_2 exchange where CH_4 hydrates were first formed and CO_2 gas was injected into the system, gas chromatographic (GC) analysis of the cell indicated a pure CH_4 gas phase, i.e., all injected CO_2 gas entered the hydrate phase and remained trapped in hydrate cages for several hours, though over time some CO_2 did enter the gas phase. Alternatively, during the CH_4-CO_2 exchange study where CO_2 hydrates were first formed, the injected CH_4 initially entered the hydrate phase, but quickly gaseous CO_2 exchanged with CH_4 in hydrates to form more stable CO_2 hydrates. These results are consistent with the better thermodynamic stability of CO_2 hydrates, and this appears to be a promising method to sequester CO_2 in natural CH_4 hydrate matrices.

The macroscale study described above was complemented by a microscale study to visualize hydrate growth. This first-of-its-kind *in-situ* study utilized the x-ray computed microtomography (CMT) technique to visualize microscale CO_2, CH_4, and mixed CH_4-CO_2 hydrate growth phenomenon in salt solutions in the presence or absence of porous media. The data showed that under the experimental conditions used, pure CH_4 formed CH_4 hydrates as mostly spheres, while pure CO_2 hydrates were more dendritic branches. Additionally, varying ratios of mixed CH_4-CO_2 hydrates were also formed that had needle-like growth. In porous media, CO_2 hydrates grew, consistent with known growth models in which the solution was the sediment wetting phase. When glass beads and Ottawa sand were used as a host, the system exhibited pore-filling hydrate growth, while the presence of liquid CO_2 and possible CO_2 hydrates in Ottawa sand initially were pore-filling that over time transformed into a grain-displacing morphology. The data appears promising to develop a method that would supplant our energy supply by extracting CH_4 from naturally occurring hydrates while CO_2 is sequestered in the same formations.

Table of Contents

List of Figures

List of Tables

List of Abbreviations

2D - Two-Dimensional

3D - Three-Dimensional

$BaCl_2$ - Barium Chloride

BNL - Brookhaven National Laboratory

CCD - Charged-Coupled Device

CCS - Carbon Capture and Storage

CH_4 - Methane

CMT - X-ray Computed Microtomography

CO_2 - Carbon Dioxide

EIA - Energy Information Administration

GC - Gas Chromatography

H_2O - Water

H_3CO_3 - Carbonic Acid

HFZ - Hydrate Formation Zone

IDL - Interactive Data Language

NOAA - National Oceanic and Atmospheric Administration

NSLS - National Synchrotron Light Source

ppm - Parts per Million

SDS - Sodium Dodecyl Sulfate

sH - Structure H

sI - Structure I

sII - Structure II

tcf - Trillion Cubic Feet

List of Equation Nomenclature

D(gas)	Diffusion coefficient for the gas
D_0	Diffusion coefficient
T	Temperature
T_S	Singularity Temperature
m	constant
μ_w	chemical potential of water
μ_g	chemical potential of gas
μ_h	chemical potential of hydrate building blocks
n_w	number of water molecules in one hydrate building block
$\Delta\mu$	change in potential energy
$(dn_i/dt)_p$	number of moles of gas/second consumed by the hydrate
K*	hydrate growth rate
A_p	particle surface area
f_i^b	fugacity of component i in the liquid
f_i^{eq}	equilibrium fugacity of i in the liquid at the hydrate interface
k_r	reaction rate constant
k_d	mass transfer coefficient
dn/dt	moles of gas consumed/second
k_L	mass transfer coefficient
$A_{(g\text{-}l)}$	area of the gas-liquid interface
c_{wo}	initial water concentration
x_{int}	interfacial liquid mole fraction of the hydrate former component
x_b	component's bulk liquid mole fraction
δ	hydrate film thickness
$\partial T/\partial x \big\vert_{x=xh-}$	temperature gradient on the hydrate side
$\partial T/\partial x \big\vert_{x=xh+}$	temperature gradient on the water side

x_h	position
λ_h	thermal conductivity of hydrates
λ_w	thermal conductivity of water
Δh_H	heat of hydrate formation per hydrate mass
ρ_h	density of the hydrate film
v_f	linear growth rate of the hydrate film along the interface
P_h	pressure in the hydrate phase
P_w	pressure in the water phase
σ'	effective stress
γ_{hw}	hydrate-water interfacial tension
d_{th}	pore throat diameter
d_{10}	finest 10th percentile grain diameter
ψ	ratio of the hydrate-water capillary pressure to the effective stress
V_{cell}	volume of the reactor
$V_{solution}$	volume of the solution
V_{gas}	volume of the gas
$P_{cooling}$	pressure the system should drop to due to cooling
$P_{initial}$	initial system pressure
T_{bath}	temperature of the bath
$T_{initial}$	initial system temperature
ΔP	pressure drop due to hydrate formation
P_{final}	final system pressure
$n_{gas\ 100}$	number of moles of gas needed to convert 100% of the solution into hydrates
$V_{gas\ 100}$	volume that ngas 100 would occupy
$n_{gas\ initial}$	number of moles of gas initially added to the system
R	universal gas constant
$n_{gas\ final}$	number of moles of gas left in the system after hydrate formation

$n_{gas\ consumed}$	number of moles of gas consumed due to hydrate formation
V_{liquid}	volume of the solution in the system

Acknowledgments

I have truly enjoyed my time at Stony Brook University, and I am grateful for all of the experiences that I have had. If I had the opportunity to start all over again, I would not change a thing. I first need to thank my advisor, Devinder Mahajan, for all of his advice, encouragement, and help moving reactors in the lab. I am truly grateful for the freedom that he gave me to be involved in science outreach and teaching activities throughout my studies.

I am also indebted to Keith Jones; it would have been impossible to get such great data at X2B without his help. His encouragement and advice pushed me to do my very best, while providing a good laugh. We will publish our x-ray data soon!

I would also like to thank my committee, Devinder Mahajan, Keith Jones, Tadanori Koga, and Stephen Masutani for all of their time and feedback.

I would also like to thank Steve Bennet and Larry Fareria for all of their help troubleshooting X2B. Their speedy fixing of beamline equipment and willingness to answer weekend phone calls helped us collect all of the data that we needed.

I am grateful to Al Tobin for giving me responsibility as a teaching assistant for CME 304 and 314 and Tadanori Koga for giving me the opportunity to teach CME 304. It was a fantastic experience, and I am grateful to have had the chance to explore running a class at this stage of my career.

I owe a great deal of thanks to the Women in Science and Engineering (WISE) Program, Carrie-Ann Miller, and Doreen Aveni. I truly value their support throughout my entire college career and the opportunity that they gave me to coordinate the WSE 187 class. The leadership and organizational skills that I gained from this experience will be invaluable. I am also grateful to WISE for introducing me to Brookhaven Women in Science (BWIS) at Brookhaven National Lab. I have learned so much from working on the Career Advancement in Research Environments (CARE) Workshop series and from talking to the wonderful women of BWIS about careers and work-life balance.

I appreciate working with my labmates, Prasad Kerkar, Saurabh Patel, Wei Nan, Mason Yeh, Julia Hasty, and Celest Okoli. Thank you for all of the laughs and for making conferences extra enjoyable. I am also grateful to my friends, especially Olivia Donaldson, Alina Nazir, Katherine Flynn, and Annmarie Tedesco for providing a necessary outlet for grad school stresses and for getting me out of the lab from time to time.

Finally, I would like to thank my parents, Robert and Mariann Horvat, and my sister Kimberly for all of their support over the years. Their encouragement was the catalyst for making it this far, and I know I would not be where I am today without them.

I appreciate all of the experiences that I have had during my grad school career, and I look forward to the next many adventures that I will explore and create in my life and career.

Chapter 1

1.0 Introduction

During the late 19th century and through the 20th century, the average temperature of the planet has increased by 0.6ºC[1], and the amount of carbon dioxide (CO_2) in the atmosphere has increased from 280[2] to 403.3[3] ppm. The vast volume of CO_2 released from the burning of fossil fuels causes CO_2 to be the most significant contributor to global warming[1]. In 2010 alone, 34 billion tons[4] of CO_2 were released globally into the atmosphere, and it is expected that by 2025 over 39 billion tons will be released.[2] One of the goals of the Copenhagen Accord was to prevent global warming from increasing the average temperature of the planet by more than 2ºC above pre-industrial revolution conditions. To maintain this average temperature, the amount of CO_2 in the atmosphere must not exceed 450 ppm[5]. The National Oceanic and Atmospheric Administration (NOAA) indicates that, especially in recent years, the temperature of the planet and amount of CO_2 in the atmosphere has been increasing, and as of April 2015, the concentration of CO_2 in the atmosphere was 403.3 ppm[3]. Figure 1.1, created using a model developed by NOAA's Geophysical Fluid Dynamics Laboratory, indicates that prior to 2050, it is likely that this value will increase to 450 ppm CO_2. To prevent reaching CO_2 concentrations of this magnitude and to avoid raising the temperature of the planet further, renewable energy sources, improving energy efficiency, and carbon capture and storage (CCS) methods need to be considered. [4,5]

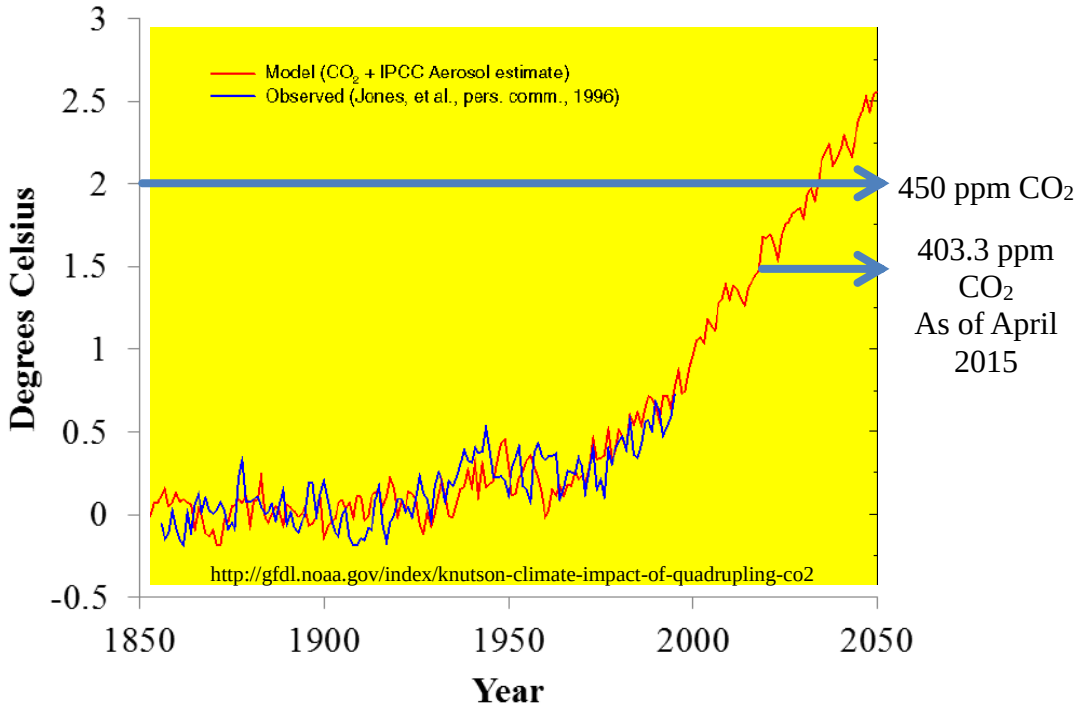

Figure 1.1: *Current trends in temperature changes on Earth (NOAA)*[6]

CCS is a carbon mitigation strategy that has garnered much interest, though this method involves multiple steps and a significant investment to build infrastructure. First, CO_2 must be collected and separated from stack gases released from power plants or other industrial facilities. The separation and compression of this CO_2 gas is the most expensive step of the process. Chemical absorption commonly uses monoethanolamine to capture CO_2 from flue gas. In absorption, flue gas is bubbled through a solvent in a packed absorber column where the solvent absorbs CO_2. In a distillation tower, the solvent is heated to collect the absorbed CO_2. Microporous membranes are currently being researched as a more cost effective CO_2 separation method, and methods to remove CO_2 prior to combustion, for example, through coal gasification, where carbon monoxide produced is reacted with water to form CO_2 and H_2 fuel, are also being investigated[1]. Once necessary pretreatment processes (pressurization and liquefaction) are performed, the collected CO_2 can be transported to geological sequestration locations, and CO_2

can be injected into a desired storage media[7]. The ocean, already a natural CO_2 sink, is one storage option, but the direct absorption of CO_2 in the ocean could have negative repercussions on marine life. Many CO_2 sequestration storage options have been proposed including reacting CO_2 with minerals to create carbonates[8], absorbing CO_2 in rock pores or coal beds[9], using it for advanced oil recovery[1], and storing it in exhausted oil and gas reserves[10] or in brines and deep saline aquifers[11]. While these sequestration locations are easy to reach, they have limited storage capabilities.[12]

At the same time, a need for energy sources, particularly natural gas, is increasing. Natural gas is used for almost one quarter of the energy supply in the United States,[13] and it is predicted to overtake coal to become the United States' prime fuel source for electricity production by 2035[14]. The number of plans to retire coal and nuclear power plants have risen, and while renewable energy sources will be increasingly utilized to help fill this void, additional natural gas plants will be needed to make enough energy available[14]. Energy demands in the United States, as well as in the rest of the world, are anticipated to continue to intensify over the next decades. It has been predicted by the Energy Information Administration (EIA) that the United States would need to produce 10% more methane (CH_4) for the next quarter of a century to keep up with our energy needs[13]. While the United States currently has access to enough natural gas to meet this demand, concerns for the future have led scientists to investigate alternative sources.[13]

Since natural gas is a fairly clean fuel when burned, the United States is looking for new sources of it for the future. CH_4 hydrates could be a valid new source of natural gas.[13] Around the world, it is believed that there are between 100,000 to 300,000,000 trillion cubic feet of natural gas hydrate reserves. The Department of Energy has estimated that if 1% of the CH_4 gas currently in place in natural hydrate reservoirs around the United States is collected, it could supply the United States with energy for the next eight decades.[15] If a cost effective way to extract these hydrates could be implemented, CH_4 hydrates could help the United States rely less on foreign energy suppliers.[13]

CH_4 hydrates found in arctic permafrost reserves have the most potential for extraction, since parts of these reserves could be accessed with already existing natural gas drilling equipment. Still, only about 100 trillion cubic feet of CH_4 exists in this form. Marine sediments

hold higher volumes of CH_4, as the most abundant amounts of CH_4 hydrates are located in deep, under the seafloor reservoirs, but many difficulties to their extraction, including the expense of obtaining them and maintaining seafloor stability, have prevented production.[13] To overcome these obstacles, the simultaneous extraction of CH_4 with the sequestration of CO_2 in natural gas hydrates reserves has been proposed[16].

1.1 Gas Hydrates and the Benefits of CH_4 Hydrate Extraction with CO_2 Sequestration

Gas hydrates are crystalline inclusion compounds that are produced when water molecules form hydrogen bonds to create a cage surrounding a guest gas molecule[17]. Hydrate cages are held together by weak van der Waals forces, and the water and gas do not chemically react[18]. Usually a hydrate is composed of 80% water and 20% gas by volume[19]. Various chemicals form gas hydrates, including CH_4, CO_2, argon, hydrogen, and hydrogen sulfide[17]. These gas hydrates have an ice or snow-like appearance, as shown in Figure 1.2 (a). CH_4 hydrates will burn when ignited as CH_4 gas escapes the hydrate cage, illustrated in Figure 1.2 (b). Each CH_4 hydrate molecule can hold ~160 volumes of CH_4 for every volume of water[15]. Usually between 70 to 90% of hydrate cages are occupied by CH_4 gas, and if a hydrate has 90% occupancy, a CH_4 hydrate with a 1:5.75 CH_4 to water ratio can contain 170 m^3 of CH_4[20]. Gas hydrates can be found naturally under conditions of high pressure and low temperature in permafrost or seafloor environments, though most gas hydrates are located hundreds of meters beneath the seafloor. CH_4 hydrates exist in natural environments in many shapes and sizes, ranging from small nodules 1-5 cm large to thick layers that are multiple meters in width.[19]

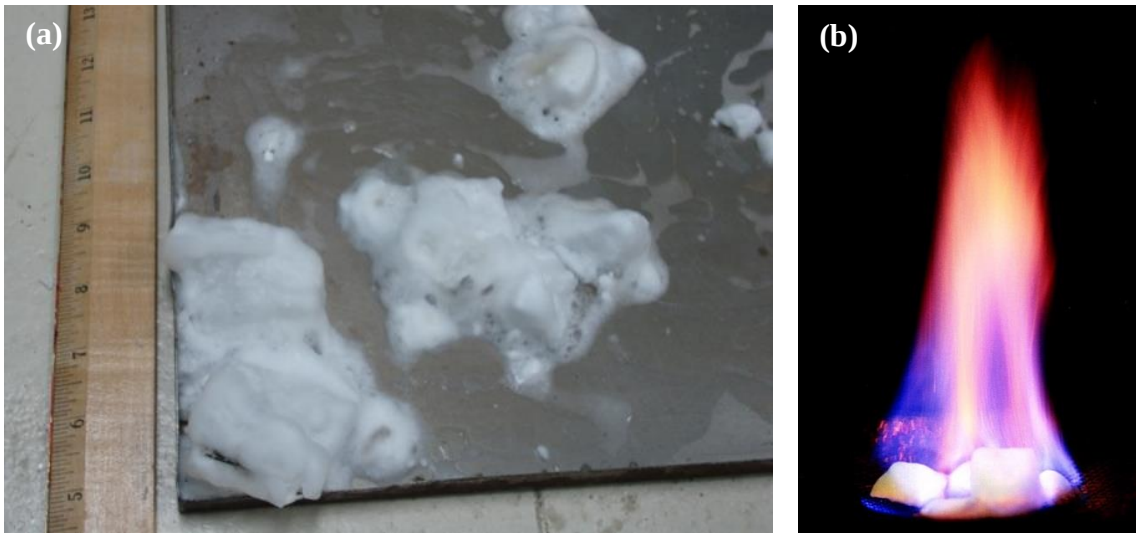

Figure 1.2: *(a) CH_4 hydrates formed during experiments in a Parr reactor (taken by Kristine Horvat) (b) A CH_4 hydrate burning (United States Geological Survey)*[21]

Gas hydrates were first witnessed by Joseph Priestly in the late 1700s when he bubbled gas in water at 0ºC. Still, many consider Sir Humphrey Davy to be the first to discover gas hydrates in the early 1800s when he called them hydrates of gas. Even though they were discovered centuries ago, gas hydrates were not extensively studied until the 1930s when E.G. Hammerschmidt found them to clog United States underwater gas pipelines.[19] It was not until the late 1960s and early 1970s that researchers realized the energy potential of these natural reserves. Throughout the 1980s and 1990s, deep sea exploration and laboratory experiments to better understand gas hydrates began to take place.[15] Recent studies of gas hydrates focus on their energy and CO_2 sequestration potential.

The idea of CO_2 storage in the form of gas hydrates was suggested by Sun and Duan (2005)[22]. Due to their stability in typical seabed conditions, CO_2 hydrates are a safe form in which CO_2 can be stored in saline aquifers and depleted reservoirs at the high pressure-low temperature conditions favorable for CO_2 hydrate formation[16]. Though some work has been done, the long-term stability of CO_2 hydrates is not well known. Theoretically, at depths in the ocean of 500-900 m, CO_2 can be injected and CO_2 hydrates will form. Since CO_2 hydrates have a density greater than that of water, once formed they will descend to the ocean floor and could remain stable there for long terms,[23] possibly for thousands of years[24]. Overall, there is much potential in this form of CO_2 storage as it is believed that the sequestration of CO_2 in gas hydrates could last for millennia due to hydrate stability and insulation[12], though temperature, pressure, and gas/water saturation must be within the hydrate stability zone to ensure hydrate stability over these large time scales. Still, this process is under development and not yet ready for large scale sequestration.

The obvious advantage of CO_2 sequestration in gas hydrates is a thermodynamically stable storage of CO_2 gas, but this process alone can be expensive. This was why Ohgaki et al. (1994)[16] devised the idea to sequester CO_2 in naturally found CH_4 hydrate reserves to make the CH_4 extraction process more cost efficient. The exchange process of CO_2 replacing CH_4 in gas hydrates is favorable as CO_2 hydrates are stable at lower pressures than CH_4 hydrates at temperatures below 10ºC[25], as seen in the phase diagram created using CSMHYD[26] in Figure 1.3. In addition, the heat released to form CO_2 hydrates is large enough to supply all of the energy needed to dissociate CH_4 hydrates found naturally as CO_2 hydrate formation is exothermic, as seen in Equations 1.1 and 1.2[2].

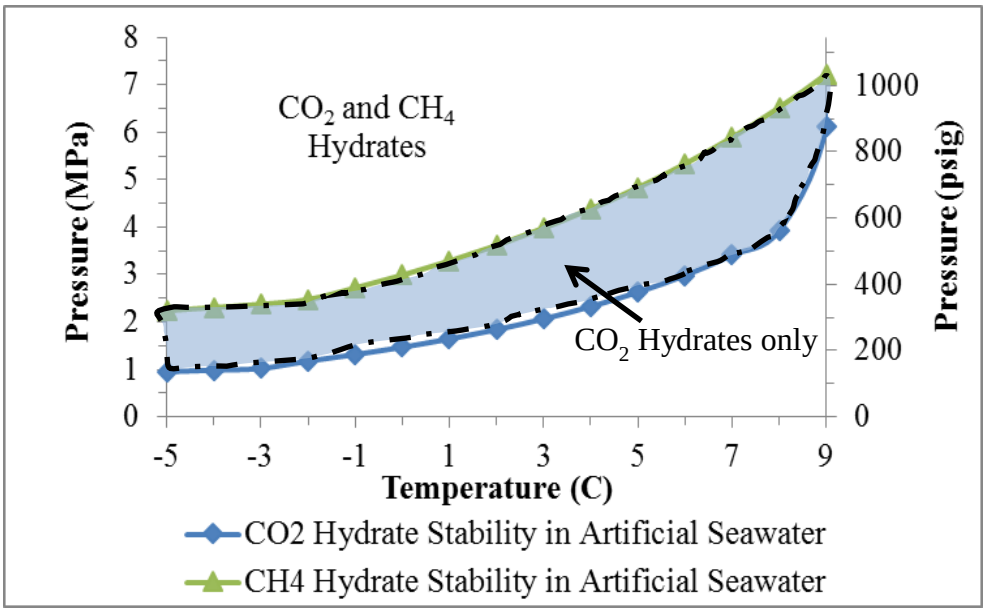

Figure 1.3: *CO_2 and CH_4 hydrate stability curves with and without salt created using CSMHYD*[26]

$$CO_2\ (g) + nH_2O \rightarrow CO_2\ (H_2O)_n\ \Delta H_f = -57.98\ kJ/mol \quad (1.1)$$

$$CH_4\ (H_2O)_n \rightarrow CH_4\ (g) + nH_2O\ \Delta H_f = 54.49\ kJ/mol \quad (1.2)$$

Another beneficial aspect to this exchange is that CO_2 and CH_4 form hydrates of the same structure. The most widespread gas hydrate structures are structure I (sI), structure II (sII) and structure H (sH). The differences between these three structures are described in Table 1.1. Both CO_2 and CH_4 form the sI hydrate, which is shown in Figure 1.4. Moreover, CO_2 molecules prefer larger $5^{12}6^2$ cages while CH_4 molecules easily fit in smaller 5^{12} cages[27]. This way, when CO_2 is introduced into a CH_4 hydrate reserve, not all of the CH_4 will be dissociated from the hydrates. Lee et al. (2003)[27] found that nearly 64% of CH_4 gas could be extracted from CH_4 hydrates with a composition of $CH_4 \cdot 6.05\ H_2O$. Kvamme et al.[28] used phase field theory models to determine that theoretically, up to 75% of CH_4 can be replaced with CO_2 if CO_2 only enters the larger hydrate cages, and almost all CH_4 in these larger cages could be exchanged with CO_2. In addition, the reverse reaction of CH_4 gas replacing CO_2 in hydrates is very slow, so it is not likely that CH_4 hydrates will reform.

Table 1.1: *Characteristics of Gas Hydrate Structures*[17]

	Structure I	Structure II	Structure H
Unit Cell Formula	$6(5^{12}6^2) \cdot 2(5^{12}) \cdot 46H_2O$	$8(5^{12}6^4) \cdot 16(5^{12}) \cdot 136H_2O$	$1(5^{12}6^8) \cdot 3(5^{12}) \cdot 2(4^35^66^3) \cdot 34H_2O$
Crystal Structure	Cubic	Cubic	Hexagonal
Lattice Arrangement	Primitive	Face Centered	Hexagonal
Chemicals that form this hydrate type	CH_4, CO_2, Ethane, Hydrogen Sulfide	Nitrogen, Hydrogen, Propane, Iso-butane	Iso-pentane*, Neohexane*

*These form sH in the presence of smaller molecules, for example CH_4, hydrogen sulfide, or nitrogen.

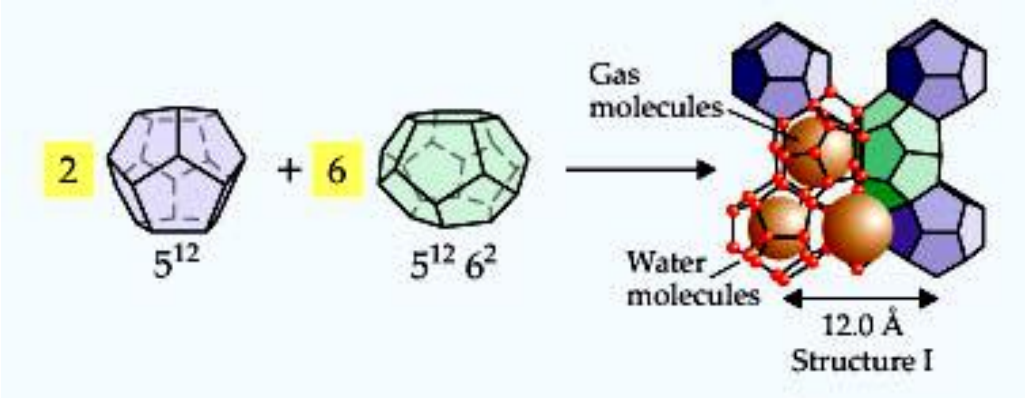

Figure 1.4: *Structure I CO_2 or CH_4 hydrate*[29]

Other advantages to CO_2 sequestration in gas hydrates include the immense storage potential of this application. Existing saline aquifers and depleted oil and gas reservoirs on the planet will not be large enough to hold the amount of CO_2 produced over the course of thousands of years.[30] Alternatively, there are many high volume areas around the world within the CO_2 hydrate stability zone.

1.1.1 CH_4 and CO_2 Properties in Water

CH_4 and CO_2 have different properties when interacting with water, as indicated in Table 1.2. Nonpolar gases have a lower solubility in water than polar gases,[17] therefore CO_2 is quite soluble in water while CH_4 is not. When CO_2 is solubilized in water, low concentrations of carbonic acid (H_2CO_3) are formed that can then convert into carbonate ions. The ocean is composed of 64 – 107 ppm CO_2. Though CO_2 only makes up 15% of the gas solubilized at the surface of the ocean, roughly one thousand times more CO_2 can be dissolved in water than nitrogen and oxygen, and the ocean contains 60 times more CO_2 than the atmosphere. This low concentration of CO_2 on the ocean's surface is due to plants' need for CO_2 during photosynthesis. Since photosynthesis requires sunlight, much CO_2 collects deep in the ocean. In addition, the solubility of CO_2 in water increases as pressure increases or temperature decreases. As there are high pressure, low temperature conditions on the ocean floor, there is a larger concentration of CO_2 at great ocean depths.[31]

Table 1.2: *CH_4 and CO_2 Gas Properties*[32]

	CH_4	CO_2
Molecular Weight (g/mol) [32]	16.043	44.01
Density at 1.013 bar and 15°C (kg/m^3) [32]	0.6797	1.8714
Solubility in water at 1.013 bar (vol/vol) [32]	0.054 (at 2°C)	1.7163 (at 0°C)
Diffusion Coefficient Prefactor (m^2/s)[33,34]	1.595×10^{-8}	1.3942×10^{-8}

CH_4 also diffuses through water at slower rates than CO_2. The diffusion of CO_2 and CH_4 in water is dependent on the temperature of the system. Guo et al.[33] and Lu et al.[34] derived Equation 1.3 to determine the diffusion coefficient for CH_4 and CO_2 respectively in water:

$$D(gas) = D_0[\frac{T}{T_s} - 1]^m \quad (1.3)$$

Where for CH_4, D_0 is 1.595 x 10^{-8} m^2/s, T_s is 229.8 K, and m is 1.8769,[33] while for CO_2, D_0 is 1.3942 x 10^{-8} m^2/s, T_s is 227 K, and m is 1.7094[34]. Both studies found that pressure did not have a large effect on the diffusion coefficients for these gases: for CO_2, as pressure increased, the diffusion coefficient decreased within a few percent (3%) for temperatures from 268-473 K and pressures from 10 to 45 MPa.[34] For CH_4, the pressure effect was smaller (1-2% difference) for temperatures from 273-473 K and pressures from 5 to 40 MPa.[33]

1.2. Gas Hydrate Environmental Effects

1.2.1 Seafloor Stability

While hydrate potential for energy is immense, there are many safety trepidations involved with their presence on the ocean floor[35]. Seafloor instability is a major concern to the extraction of CH_4 from natural hydrates. All currently proposed methods for CH_4 extraction involve the dissociation of CH_4 hydrates, and this dissociation of the hydrate structure may cause slope failures on the ocean floor.[36] Many current scars in the ocean terrain from ancient times are due to landslides, and it is possible that these landslides were a result of CH_4 hydrate dissociation.[35] Figure 1.5 depicts several hazards associated with CH_4 hydrates in the ocean. Historically, since most natural CH_4 hydrate regions are located in ocean floor sediments above sediments containing free CH_4 gas, it is believed that many ocean floor landslides have been a result of hydrate dissociation[35]. If the sediments in which hydrates form are unconsolidated, the presence of gas hydrates prevents a normal compaction increase as lithostatic pressure increases. If these regions' pressure-temperature conditions exit the hydrate stability zone, the hydrates will dissociate, degrading the compaction of the seafloor and potentially resulting in slope failure[37].

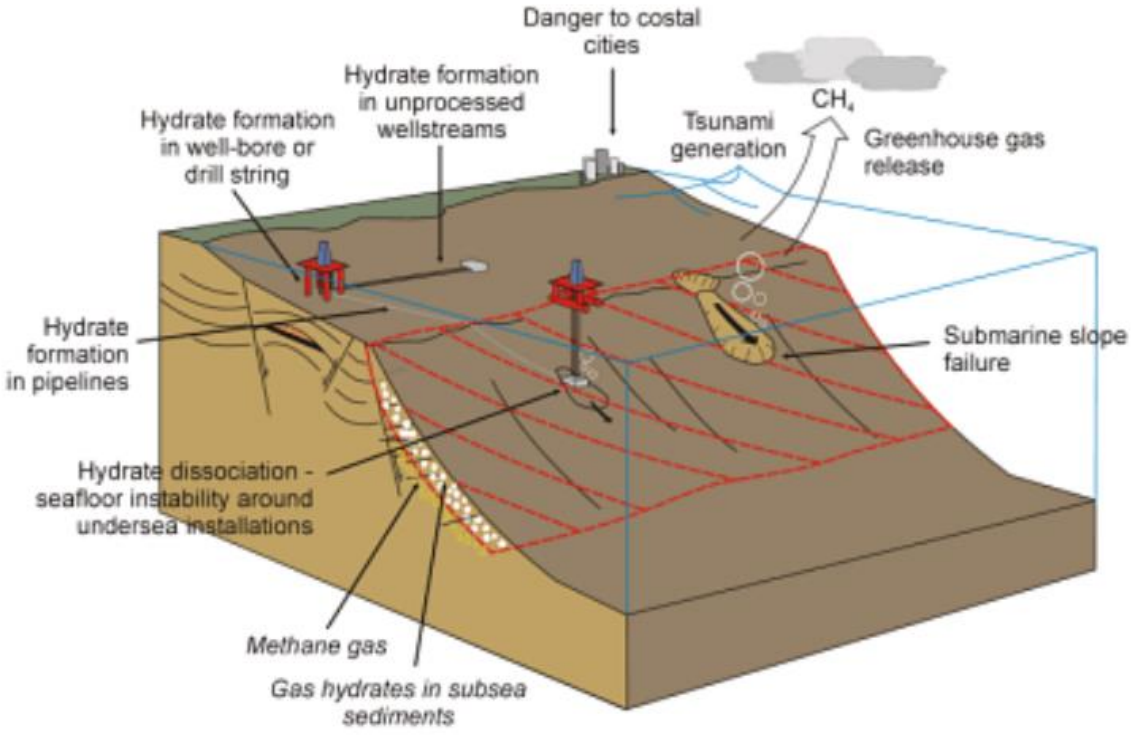

Figure 1.5: *Possible concerns associated with CH_4 hydrate dissociation from ocean floor reserves. (Heriot Watt Institute of Petroleum Engineering)*[38]

In addition, when oil and gas are drilled for in CH_4 hydrate regions on the ocean floor or in permafrost regions, hydrate dissociation can cause casing failure and an inability to control the well. Finally, the distribution of CH_4 hydrates on or beneath the ocean floor can vary over time, which can affect the stability of oil or gas drilling platforms, pipelines, and wellheads. CH_4 hydrate growth can also have negative effects on drilling platforms. Over time after drilling platforms are installed, CH_4 hydrates can grow on or around equipment[35]. Hydrate dissociation in under water locations can occur with large changes in the strength of the gas hydrate holding sediments[19]. As a result, changes can occur in the seafloor landscape and destabilize the platform, causing equipment damage or collapse[35]. The exact effect that producing CH_4 from hydrates would have on the ocean floor is not fully understood[35]. To prevent an unstable seafloor or permafrost terrain, the sequestering of CO_2 in place of CH_4 gas could cement sediments in place[30].

1.2.2 Global Warming

The geological history of the planet has shown that past large releases of CH_4 into the atmosphere were a result of CH_4 hydrate dissociation. The release of large volumes of CH_4 into the atmosphere could have disastrous effects on global warming. CH_4 is twenty-three times more potent as a greenhouse gas than CO_2 over a century, and in the short term, CH_4 is even more dangerous, as it is sixty-two times more powerful over a 20 year period.[35] If temperatures increase or pressures decrease in natural CH_4 hydrate reserves, hydrates could destabilize, releasing this potent gas. If this CH_4 hydrate dissociation is not properly controlled, the release of large amounts of CH_4 in shallow ocean regions could also create negative buoyancy that has the potential to sink ships[37]. If seafloor temperatures continue to increase as a consequence of climate change, CO_2 hydrates are more stable at higher temperatures than CH_4 hydrates, and it is more likely that CO_2 gas will not escape,[30] so by collecting CH_4 from hydrates now, any future changes in seafloor temperature will not result in the release of this major contributor to global warming.

1.3 Gas Hydrate Formation

Hydrate formation depends on the chemical potentials of water (μ_w), gas (μ_g), and hydrate building blocks (μ_h) of the system, as a change in the chemical potential in the system is what brings about hydrate formation. Equation 1.4 shows a balance of chemical potentials in the hydrate forming system, where n_w is the number of water molecules needed in one hydrate building block. If $\Delta\mu > 0$, gas hydrates can form, as the chemical potential for the hydrate building blocks will be lower than the chemical potential for the separate gas and water components of the system.[39] As the temperature of water is lowered, water molecules tend to cluster together, which helps to bring about this hydrate formation[40].

$$\Delta\mu = \mu_g + n_w\mu_w - \mu_h \qquad (1.4)$$

1.3.1 Hydrate Nucleation

Bulk hydrate nucleation can be either homogeneous or heterogeneous. Homogeneous nucleation has been widely used in hydrate formation calculations, but this method is highly unlikely to occur in real life[41]. Heterogeneous nucleation of hydrates is thermodynamically more favorable and tends to take place when hydrate nucleation occurs on an impurity or container surface.[17] Overall, bulk hydrate nucleation does not occur often, though highly mixed systems may appear to have nucleated in the bulk. Usually nucleation occurs at an interface (gas-liquid, liquid-solid, or liquid-liquid), where the Gibbs free energy for nucleation is the lowest and there is a high concentration of guest and water molecules. Many past studies have shown that both CH_4 and CO_2 hydrates tend to form at the gas-liquid interface[42-44]. Molecular dynamics simulations have yielded similar results[41,45,46]. When hydrates grow as a film at a gas-liquid interface or as a shell around a gas or water droplet, morphology is dependent on supersaturation. Induction times are dependent on driving forces, the reactor for hydrate formation, gas used, solution composition, surface area, and cell agitation. Once hydrates have nucleated, they begin to grow dependent on kinetics, mass transfer, and heat transfer.[17]

There are three proposed mechanisms for hydrate nucleation: labile cluster, nucleation at the interface, and local structuring. In labile cluster growth, visualized in Figure 1.6, the system starts out in the hydrate pressure-temperature stability zone, but the gas has not dissolved in the solution yet. Once the gas dissolves, labile clusters form that create the 5^{12} and $5^{12}6^2$ water cages needed to grow sI hydrates. As both cages are necessary for sI hydrates, if a mixture of these two types of cages does not form, hydrate nucleation is hindered pending the breaking and formation of new hydrogen bonds in the clusters to materialize the needed cage. These cage clusters begin to group together, and once these clusters have grown to a critical size, hydrate growth takes place. There is an activation energy barrier that must be overcome to allow the guest gas molecules to stabilize the cage cluster to bring about hydrate growth.[17]

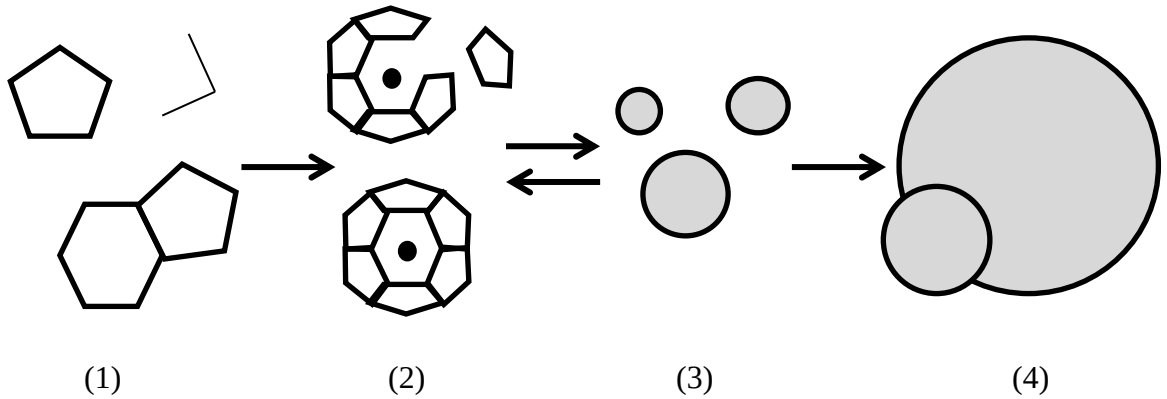

Figure 1.6: *Depiction of labile cluster growth. (1) The system has achieved pressure and temperature conditions within the hydrate stability region, but gas has not dissolved in the hydrate forming solution. (2) Once gas dissolves, labile clusters form. (3) Labile clusters agglomerate. (4) Hydrates begin to grow once the clusters reach a critical size. (recreated based on Figure 3.9 of Sloan et al.[17])*

The nucleation at the interface theory hypothesizes that hydrates nucleate on the gas portion of the interface. Gas molecules bombard the interface and find a location through surface diffusion to be adsorbed on the solution surface. At this point, partial water cages begin to form into full cages surrounding the gas molecules. Labile clusters then grow in the gas section of the interface until a critical size has formed.[17]

Radhakrishnan and Trout[47] calculated the free energy for the labile clustering method of hydrate growth for CO_2 and found that it was not thermodynamically stable. On the other hand, the local structuring theory was more likely for CO_2 hydrate growth. Due to temperature variation, guest gas molecules can organize into configurations, though they are not exactly hydrate cavities. Over time, the number of these structures increases and a critical nucleus is established.[17]

Overall, hydrate nucleation and growth was found to be stochastic, or more random, rather than deterministic, or having more established results. However, if there were higher driving forces for nucleation, the process can become more deterministic. Also, under high driving forces, gas hydrates can grow in several different places with rougher, more dendritic

growth while under lower driving forces hydrates form more regularly, with fewer nucleation locations and slower formation[48].

1.3.2 Hydrate Growth

Once hydrates have nucleated, they begin to grow dependent on kinetics, mass transfer, and heat transfer. Mass transfer is likely to govern hydrate growth, though as hydrate formation is exothermic, heat transfer will affect growth as well. It is believed that kinetics affect hydrate growth the least. Still, it is difficult to model hydrate growth as it can be dependent on the reactor used to form the gas hydrates, so these models have limitations. These models assume sI hydrate formation, and they do not account for metastable hydrate states.[17]

The kinetic model for sI gas hydrate growth, as determined by Englezos and Bishnoi[49-51], is given in Equation 1.5:

$$\left(dn_i/dt\right)_p = K^* A_p\left(f_i^b - f_i^{eq}\right) \tag{1.5}$$

Where

$$1/K^* = 1/k_r + 1/k_d \tag{1.6}$$

Where $(dn_i/dt)_p$ is the number of moles of species i consumed per second by the hydrate, A_p is the particle surface area, f_i^b is the fugacity of component i dissolved in the bulk liquid, f_i^{eq} is the equilibrium fugacity of i in the liquid at the hydrate interface, K^* is the hydrate growth rate, k_r is the reaction rate constant, k_d is the mass transfer coefficient, and $(f_i^b - f_i^{eq})$ is the driving force.

Skovborg and Rasmussen[52] created the mass transfer model for the guest gas species by modifying the Englezos-Bishnoi Equation 1.5 to Equation 1.7:

$$\left(dn/dt\right) = k_L A_{(g-l)} c_{wo}(x_{int} - x_b) \tag{1.7}$$

Where k_L is the mass transfer coefficient, $A_{(g\text{-}l)}$ is the area of the gas-liquid interface, c_{wo} is the initial water concentration, x_{int} is the interfacial liquid mole fraction of the hydrate former

component, and x_b is the component's bulk liquid mole fraction. Skovborg[52] found the mass transfer coefficient of CH_4 to be 4.076 x 10^{-5}.

Several system-specific models have also been created taking heat transfer into account. A more recent model created by Mochizuki and Mori[53] is shown in Equation 1.8:

$$\rho_h \Delta h_H v_f = \int_0^{\delta} \left(\lambda_h \frac{\partial T}{\partial x}\Big|_{x=x_{h-}} - \lambda_w \frac{\partial T}{\partial x}\Big|_{x=x_{h+}} \right) \quad (1.8)$$

Where δ is the hydrate film thickness, $\partial T/\partial x \,|_{x=xh-}$ and $\partial T/\partial x \,|_{x=xh+}$ are temperature gradients on the hydrate and water sides respectively at position x_h, Δh_H is the heat of hydrate formation per hydrate mass, and λ_h and λ_w are the thermal conductivities for hydrate and water respectively.

Hydrate crystals can grow by four different methods: single crystal growth, hydrate film growth at the gas-liquid interface, several crystal growths when a system is agitated, and metastable phase growth. When driving forces are low, hydrates are likely to grow as single crystals. The slowest growing crystal planes, which are the (110) plane for sI hydrates and the (111) plane for sII hydrates, form under this hydrate growth method. Hydrates can also grow as a film at the gas-liquid interface or as a shell around a gas or water droplet. In this case, morphology is dependent on supersaturation as a driving force. When hydrates grow this way, a thin film is first formed at the gas-liquid interface. This film develops to encase the droplet, and the hydrate is solidified. During hydrate growth, metastable phases (those that are less thermodynamically stable) can be seen. Both NMR and Raman spectroscopy analysis have found peaks for metastable phases during the hydrate growth period.[17]

1.3.3 Hydrate Memory Effect

Studies have shown that hydrate forming solutions can maintain a "memory" of their hydrate structure when warmed up slightly above the hydrate stability region. There are two theories as to why this occurs: (1) a hydrate frame assembly is intact in the solution, either as a partial or ordered configuration and (2) gas has been left dissolved in the solution after dissociation. On the other hand, if the solution is warmed up too much (above 25[54] or 28°C[17]) or for too long a time period (several hours), this retention effect will not occur.[17]

1.3.4 Microstructural Growth Models for Gas Hydrates

The mechanical strength and elastic properties of hydrate-sediment systems are governed by hydrate growth models. Hydrates in sediments are characterized as cementing at grain contacts, grain coating, supporting the grain, pore filling, or massive. Naturally occurring CH_4 hydrate structures in sediments play an important role in seafloor stability and climate change.

Dvorkin and Nur (1996)[55] theorized that there are six possible microstructures, described in Figure 1.7, for gas hydrates. Gas hydrates can grow heterogeneously at the contact point between individual grains, as in Model 1, or they can grow around each grain, forming a gas hydrate coat over the grain as in Model 2. When few hydrates have formed, elastic properties of hydrate growth systems following Models 1 and 2 will increase, but as larger quantities of hydrates form, elastic properties remain constant. Model 3 depicts gas hydrates as acting like a part of the supporting matrix of the system, and in Model 4, gas hydrates fill in the pore spaces between grains. These models portray hydrates as cementing in the system. Model 5 is an inclusion model where gas hydrates and grains both serve as the matrix that holds the system together. Models 1-5 theorize that hydrates grow throughout a sand pack evenly, but hydrates that form according to Model 6 form in larger fractures in sediments.[56] It was found that most naturally formed hydrates on the ocean floor follow a pore filling growth model[57].

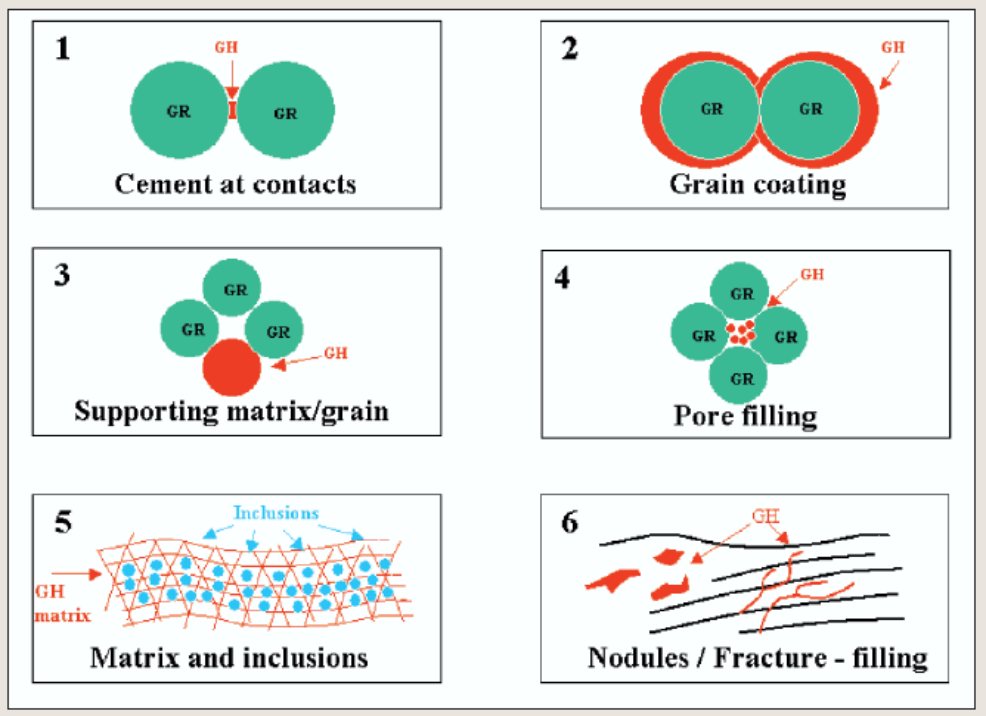

Figure 1.7: *Microstructural models of gas hydrate bearing sediments*[56]

In the hydrate stability zone, molecules in a system constantly move between the water-hydrate or gas-hydrate phases. When a hydrate crystal has grown to a minimum size for a stable hydrate, the hydrate will begin to grow among sediment grains. As these hydrates grow larger, they will become limited by the grains of the sediment, and they will further form around the grains according to one of the microstructural models described in Figure 1.7. The model through which hydrates will grow is governed by the ratio of the local effective stress and the capillary pressure of the hydrates formed. According to Dai et al. (2012), under equilibrium conditions, the pressure in the hydrate phase (P_h) will equal the pressure of the water phase (P_w) plus the effective stress (σ') felt in the grains, as shown in Equation 1.9[58]:

$$P_h = P_w + \sigma' \tag{1.9}$$

And P_h is related to P_w by:

$$P_h - P_w = \frac{4\gamma_{hw}\cos\theta}{d_{th}} \tag{1.10}$$

Where γ_{hw} is the hydrate-water interfacial tension (0.032 – 0.039 N/m), the contact angle $\theta = 0°$, and d_{th} is the pore throat diameter. This pore throat diameter is equivalent to $(\sqrt{2}-1)d_{10}$, where d_{10} is the finest 10^{th} percentile grain diameter in the grain distribution. To compare the ratio (ψ) of the hydrate-water capillary pressure ($P_h - P_w$) to the effective stress, Dai et al. (2012) determined Equation 1.11:

$$\psi = \frac{\frac{4\gamma_{hw}}{d_{th}}}{\sigma'} \approx \frac{10\gamma_{hw}}{d_{10}\sigma'} \tag{1.11}$$

When $\psi > 1$, capillary pressure is large enough for hydrates to displace grains instead of filling in sediment pores. Finer grained sediments are likely to be displaced by this method, and under low effective stresses, they will form nodules and massive hydrates. At moderate effective stresses, vein-like hydrates tend to form in fine-grained sediments. When $\psi < 1$, a large effective stress will avoid grain displacement and hydrates will fill existing pores. This would be the case for larger grained sediments to form patchy hydrates.[58]

The sediments in which hydrates form and how gases travel through those sediments have a significant effect on hydrate growth. Two gas movement methods are shown in Figure 1.8. Gases will enter the pore space between sediment grains when capillary pressure, which in this case is the pressure difference between the gas phase and the water phase, is larger than the capillary entry pressure. On the other hand, if this capillary pressure is large enough to overcome the compressional and frictional forces between sediment grains, it can displace sediment grains to form fractures.[59]

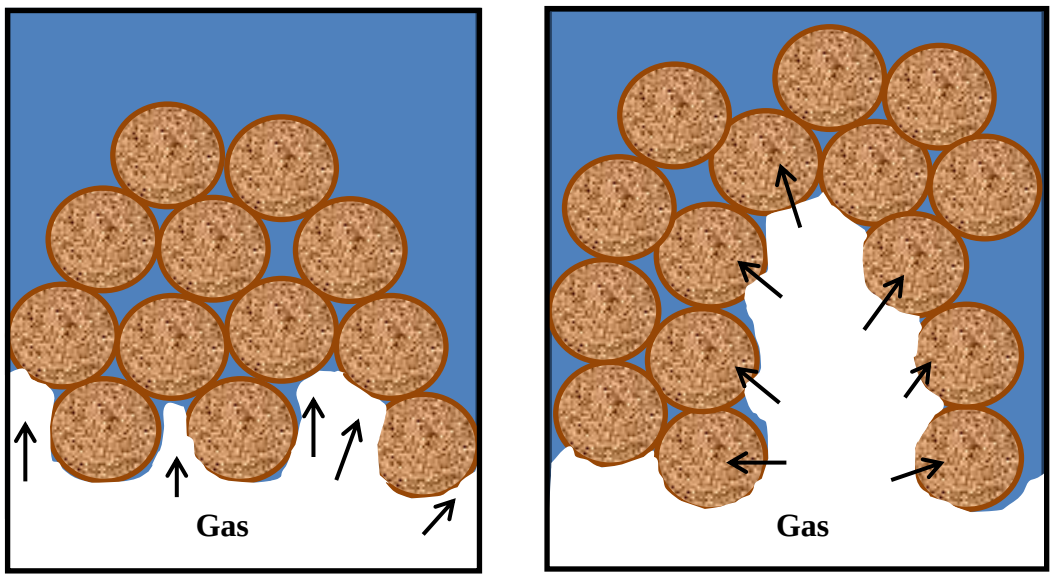

Figure 1.8: *Ways by which gas penetrates sediments. (a) Gas enters sediment pores when capillary pressure is higher than capillary entry pressure. (b) Gas forces apart sediment particles when capillary pressure is larger than compression forces and friction between sediment grains. (Recreation of Figure 5 in Juanes et al.[59])*

When formed within the ocean floor, gas hydrates have lower volumes than their components. The formation of hydrates results in a localized pressure drop, which could create instability that would break the hydrate cage. This breakage would create a new gas-water interface that could help move gas through ocean sediments. In addition, when hydrates are formed in a salt solution, the salt is not included in the hydrate phase, resulting in water with a higher salinity. Salt is a hydrate growth inhibitor, so this increasing salinity further destabilizes hydrates.[59]

1.3.5 Hydrate Structural Stability

Originally, it was believed that a guest molecule remained trapped in a water cage because the molecules were too big to escape, but now it is understood that the molecules rotate in their cages, and their interaction with the water cage makes the structure more stable. Guest molecules are not bound to one cage, and they can diffuse between different cages.[29] Changes in pressure in a hydrate environment can affect the shape of the hydrate's water cage. Instead of falling apart at high pressures, the structure of the water cage can change to denser phases of ice. Pressure can also force more than one guest molecule into one cage or increase the number of bonding arrangements, which has led to the creation of many new molecular solids[29]. For example, sI CH_4 hydrates under extremely high pressures (0.3-2.1 GPa) can reconfigure to form sH' hydrates. These hydrates have a structure that is different from sH hydrates created at standard pressures.[17]

1.3.6 Hydrate Dissociation

The process of hydrate dissociation is endothermic, thereby heat is used to break the hydrogen bonds and van der Waals forces holding the hydrate together. Dissociation can be brought about through thermal stimulation, depressurization, or thermodynamic inhibitor injection[17]. Dissociation has been found to occur radially along the diameter of a core/reactor, rather than axially along the length. In addition, heat transfer plays a dominant role in hydrate dissociation. It was also found that CO_2 hydrates dissociate faster than CH_4 hydrates due to the

higher solubility of CO_2 in water. Both large and small CH_4 hydrate cages were found to dissociate without preference[17,60]

Gas hydrates can exhibit self-preservation where they remain stable for prolonged periods of time outside of hydrate stability conditions, though not much is understood about this phenomenon[17]. Anomalous self-preservation has been seen for CH_4 hydrates between -31 to -2°C where hydrate dissociation has been found to be much slower than expected, possibly due to ice shielding[61]. Circone et al.[62] formed CH_4 hydrates and then kept the system at higher pressures but still outside of the hydrate stability region, and it was found that at higher pressures, dissociation rates were the slowest. Similarly, Falenty et al.[63] found that CO_2 hydrates also exhibit self-preservation at temperatures (-73 to -3°C) and pressures (0.6 kPa) outside of the CO_2 hydrate stability zone, likely due to the presence of an ice coating.

1.4 Hydrate Energy Potential

1.4.1 Natural CH_4 Hydrate Formation

Throughout time, these natural CH_4 hydrate reserves have existed, and they continue to form in the presence of biogenic or thermogenic gases and water[17]. Biogenic CH_4 is released when bacteria consume organic materials. This process occurs often and can create massive amounts of CH_4. Thermogenic CH_4 is created when buried organic matter is placed under conditions of heat and high pressure.[13] Figure 1.9 depicts how both marine and permafrost hydrates form. In natural hydrate reserves, the composition of gas hydrates can change over time as free gas is absorbed. Some of these hydrates contain heavy gases, which usually indicates that oil is located underneath hydrate deposits.[19]

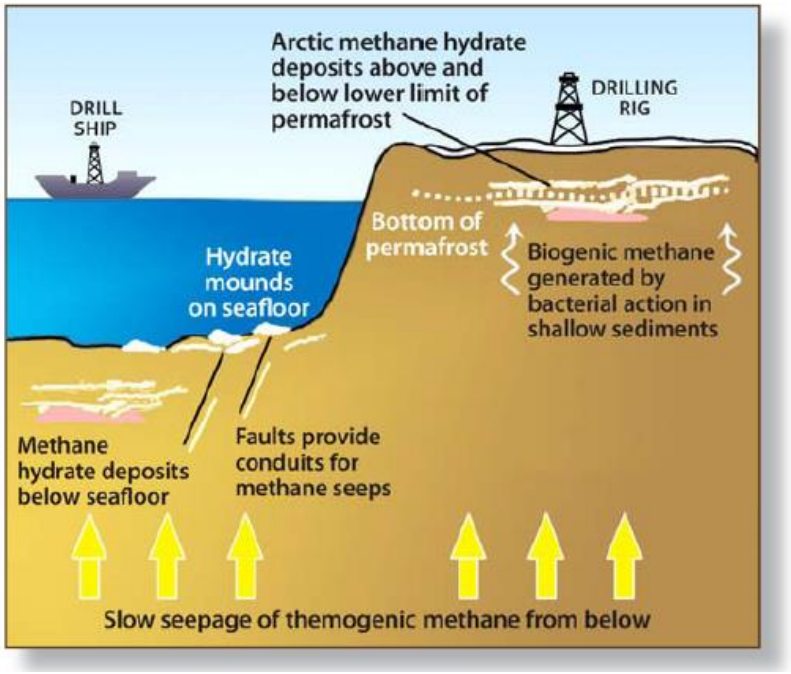

Figure 1.9: *CH_4 hydrates form naturally in marine and permafrost environments*[13]

Natural gas hydrate accumulations are found in either primary form, where hydrates have formed and never melted, or secondary form, where hydrates will form and dissociate over time with cycles in temperature. Primary deposits occur in deep water where temperature is constant, and they are formed from dissolved gases in seafloor sediments with high porosity and low strength[19]. Primary accumulations can be quite large in size, and many times, free gas or oil is present below these deposits.[19]

Secondary accumulations are generally found in permafrost regions. These hydrates are created from free gas reservoirs under impassible formation layers at very low temperatures. Over time, these hydrates will form and un-form following the temperature pattern of the region, and many times, there is also free oil or gas located beneath hydrate accumulations.[19]

1.4.2 Natural CH_4 Hydrate Locations and Structure

Around the United States, there are many known CH_4 hydrate regions, including permafrost areas in the north slope of Alaska, and marine locations in Blake Ridge off the coast of the Carolinas, Cascadia off the coast of Oregon, and the Gulf of Mexico[64]. Table 1.3 lists conditions for these marine CH_4 hydrate reserves. Areas containing CH_4 hydrates around the world are indicated in Figure 1.10.

Table 1.3: *Physical Properties of Marine CH_4 Hydrates at 3 U.S. Sites*

Location	Site	Water Depth (m)	Beneath Seafloor depth (m)	Average thickness of hydrate bank (m)	Water saturation	CH_4 hydrate saturation	Reference
Gulf of Mexico	*Green Canyon 184/185*	500-650	0-390	370	80-100%	5-20 %	Milkov and Sassen, 2003[65] Francisca et al., 2005[66]
Northern Cascadia	*U1326*	1820-1830	50-250	271	20%	40%	Expedition 311 Scientists, 2005[67]
Blake Ridge	*994, 995, 997*	250-300	450	250	80-100%	0-20%	Paull, 2000[68] Collett, 2000[69]

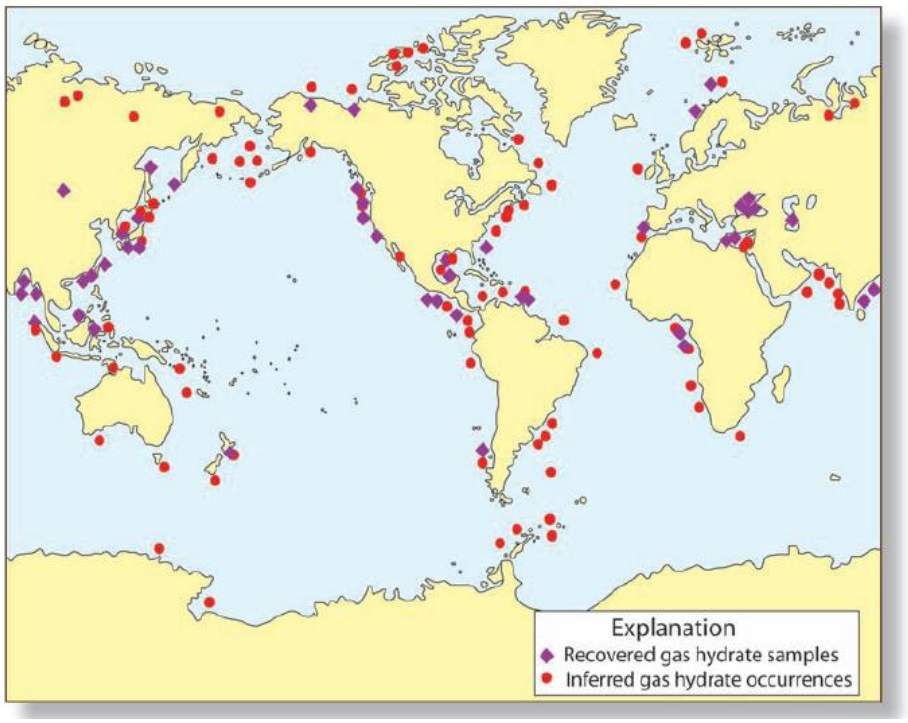

Figure 1.10: *Gas hydrate locations around the world (United States Geological Survey)*[21]

How and where gas hydrates form are greatly influenced by the thermodynamic properties of the region, generation and location of hydrocarbons, gas composition, salinity of the water, gas saturation, sediment structure, geothermal gradients, and the phase of the hydrate formers. The area where natural hydrate formation is thermodynamically possible is known as the hydrate formation zone (HFZ). These zones exist in cooler, wetter regions of the Earth. Higher water salinities and warmer temperatures cause the thickness of the HFZ to decrease. In permafrost regions, the HFZ can range from 400 to 800 m thick.[19]

Gas hydrates are known to increase the strength and stability of sediments[70]. When hydrates are located in reservoir rock, they can be spread throughout pore spaces without destroying the pores, though sometimes the rock can be changed. These accumulations also do not have good seals; once hydrates form in pore spaces, they continue to grow in a nodule or dispersed form until all gas pathways are blocked. In this way, hydrates act as cement connecting the sediments where they have formed. When gas hydrates dissociate, these sediments are likely to become destabilized.[19]

The ocean floor mostly consists of fine-grained sand[71]. When hydrates form in fine-grained sediments, they usually form in large pores or fractures. Once all pores larger than the critical size are filled, hydrates will grow to displace sediments, rather than filling very small pores.[72] In addition, fine-grained sediments may inhibit hydrate formation such that lower temperatures are necessary to nucleate them. Overall, fine-grained sands tend to result in hydrate growth as nodules or sheets while coarse-grained sands result in interstitial or cementing hydrate growth.[71]

Field measurements show that varying formation conditions exist at different naturally occurring hydrate reservoirs[58,73]. Natural gas hydrates found around the U.S. grow according to most of the proposed structural models. In Cascadia at Leg 146 in sites 889 and 892, hydrates were found to grow in sediment pore spaces and as macroscopic pellets[74]. In Blake Ridge at Leg 164 in sites 994, 996, and 997, hydrates seen were massive, vein filling, as well as pore filling[75]. In the Gulf of Mexico at site GC 184, hydrates were found to be massive and vein filling[76]. Gas hydrate growth is highly dependent on pressure-temperature conditions and the type of sediments in which they have grown.

Abegg et. al.[77] took fifty-seven sediment-hydrate samples from the Cascadia margin and analyzed them with x-ray computed tomography. According to their findings, there are six proposed models for *in situ* gas hydrate formation, some of which are depicted in Figure 1.11: disseminated, veinlet, vein, layered, nodular, and massive. Disseminated hydrates are the smallest formed, with grain sizes less than 3 mm. They are spread throughout the sediment in which they are formed, and as a result of their small size, they quickly dissociate when outside of the hydrate stability zone. Veinlet hydrates are very thin hydrates (1 mm thick) that look disc-shaped in three dimensions. Much like veinlets, vein hydrates are thin hydrates that are 1 mm to 10 cm thick and form non-parallel to the sediment layer. Layered hydrates are veins that form in the same direction as the sediment; hydrate layers are mixed between layers of fine sediment grains. Nodular hydrates are 1 to 5 cm in diameter and have a sphere-like shape. Finally, massive hydrates are thick hydrates that are greater than 10 cm in diameter. [77]

Figure 1.11: *Nature of gas hydrates within sediments: nodules, laminae, or veins (United States Geological Survey)*[21]

1.5 Status of CH_4 Extraction/CO_2 Sequestration Technologies in Gas Hydrates

In addition to sequestering CO_2 to extract CH_4 gas, other methods being studied include depressurization, thermal stimulation, and the injection of hydrate inhibitors[78]. Already existing oil and gas technologies can be used to extract CH_4 hydrates in conjunction with these new extraction methods[79]. Most current enhanced oil recovery technologies can be utilized for CO_2 sequestration[12].

Depressurization is a dissociation method that involves decreasing the pressure in a well to below the hydrate stability limit, and this method is depicted in Figure 1.12. This can be achieved by extracting gas from the free gas zone, which decreases the pressure in the hydrate zone and causes the hydrates at the edge of the hydrate zone to fall apart. This newly freed gas will move into the wellbore and can be extracted[78]. Comparably, natural gas is collected from gas reserves across the country by drilling a well into rock and planting a pipe down into the well. When the pipe is opened up, gas will fill the well, and gas can be collected up through the pipe. Sometimes gas will flow on its own into the pipe system and other times a pumping system is required to collect the gas.[13] A similar method could be used to obtain CH_4 from gas hydrates that are located in sandstone or sandy reserves. Since hydrate dissociation is an endothermic process that uses heat, there is a chance that hydrates could reform following depressurization if enough heat is removed to lower the system temperature into the hydrate stability zone once again. To prevent this, a method to ensure that the system is depressurized low enough to inhibit hydrate reformation must be used.[13] This depressurization method is the most economically feasible[80] and the best to be used on a large scale[70]. While this method has mostly been utilized to produce CH_4 gas from permafrost CH_4 hydrate reserves[78], Japan Oil, Gas, and Metals National Corporation (JOGMEC) successfully used a well depressurization method to extract 120,000 m^3 of CH_4 gas from deep-water regions off the coast of Honshu Island in Japan in 2013[81].

Thermal stimulation can be used to increase the temperature of a hydrate region above the hydrate stability limit to bring about hydrate dissociation as seen in Figure 1.12. To increase the temperature, usually steam or hot water is introduced into the system through electric or sonic processes. Disadvantages to this method include that much energy is needed to heat the water or steam used to dissociate the hydrates and the hydrate bearing sediments must have a good porosity (>15%) for effectual heating.[78] In addition, this method is costly[80].

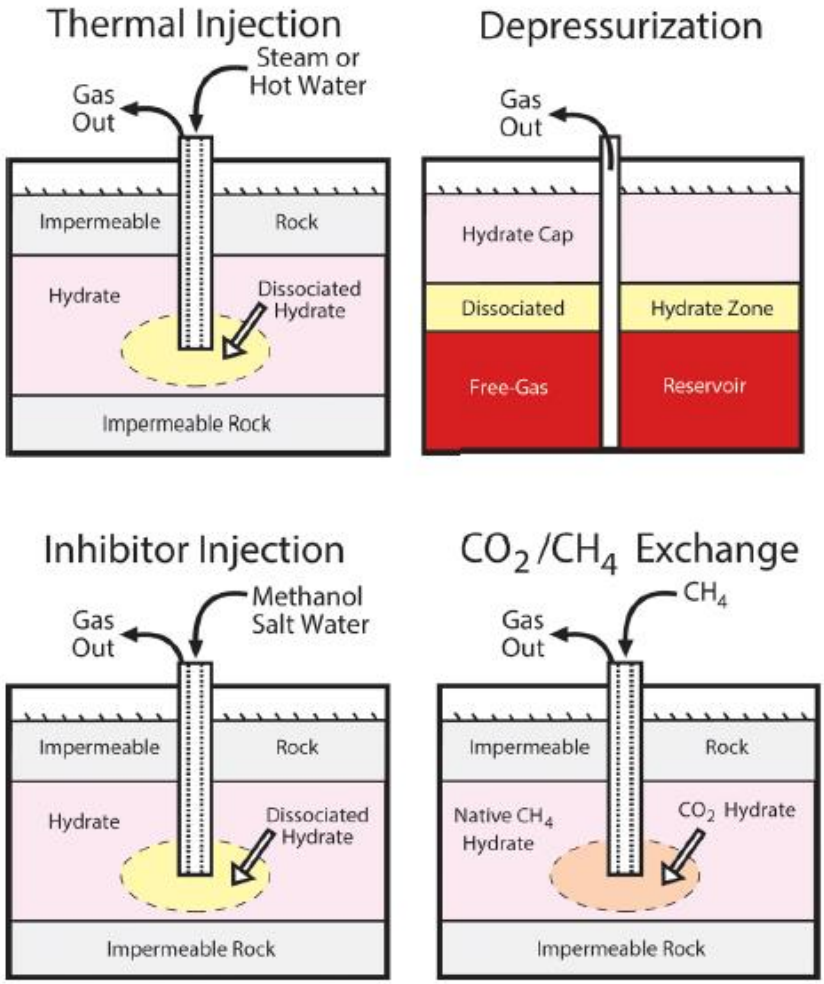

Figure 1.12: *Schematics of gas hydrate dissociation methods*[82]

Injecting hydrate inhibitors, such as methanol, changes the stability curve for CH_4 hydrates, which can bring about hydrate dissociation. This method is currently used in underwater natural gas pipelines to avoid forming ice and natural gas hydrates. A chemical inhibitor is injected into the hydrate zone which will shift the pressure-temperature stability region for gas hydrates above the conditions of the hydrate zone.[78] While this technique takes longer to dissociate hydrates than thermal stimulation, less energy is used to break apart hydrates with this method[70]. Still, there is a high cost for these chemicals and a potential negative impact of these chemicals on the environment[80].

Since both the thermal stimulation and chemical inhibitor methods are costly, to achieve the most reasonable financial expenditure and good extraction percentages, a method that combines depressurization and thermal stimulation seems ideal. Japan is currently working to extract hydrates using a depressurization method with heated well walls to get better dissociation results with a lower cost. Still, the process of simultaneously extracting CH_4 with CO_2 sequestration shows a lot of potential.[78]

Other obstacles to overcome with CH_4 hydrate extraction will include keeping commercial gas flow rates while large amounts of water are produced, keeping temperatures and pressures low in the well, avoiding sand from collecting in the well, and maintaining the stability of the well structure. There are methods that exist to work around these issues, but there are high expenses to installing all of the equipment necessary for CH_4 production. Dealing with environmental and safety trepidations related to this production will also need to be addressed. In the Arctic, for example, groundwater, animal, and plant impacts need to be considered in an extraction plan.[13] The largest obstacle to CH_4 hydrate extraction is how spread out and deep natural gas hydrate deposits can be[80]. One major issue with dissociating hydrates is that the changes in mechanical stress caused by such an extraction method are unknown[78], and the release of CH_4 gas into the atmosphere must be prevented[13]. In addition, new roads, power lines, and structural foundations might need to be built depending on the location of hydrate reserves. Gas storage and transportation systems must also be created to hold and deliver the gas obtained[13], though current enhanced oil recovery transportation, gas flow, and gas delivery systems could be utilized[12].

1.6 CH_4-CO_2 Hydrate Experimental Studies

Several phase field simulation studies have been performed to model CH_4-CO_2 exchange in hydrates. While pure CO_2 hydrates are more stable than pure CH_4 hydrates, mixed gas hydrates wherein CO_2 fills a majority of the larger cages and CH_4 fills a majority of the smaller cages are the most stable in mixed gas systems at all pressures and temperatures[28]. The process of exchanging CH_4 and CO_2 in hydrates is slow due to mass transportation hindrances, but the formation of new CO_2 hydrates from free water upon CO_2 injection is a fast exothermic process. Quick transfer of the heat released during CO_2 hydrate formation helps speed up CH_4 hydrate dissociation.[28] Baig et al.[83] used phase field theory to determine that the rate of conversion of CH_4 hydrates into CO_2 hydrates directly correlates to the amount of free water near the hydrate. Initially, new CO_2 hydrates will form, which is a fast process. When there is no available free water in the system (due to CO_2 or mixed CH_4-CO_2 hydrate formation), this gas exchange process is governed by a slower solid-state mass transport mechanism.[83]

In addition, much research is currently being conducted to test the feasibility of CH_4 and CO_2 exchange in gas hydrates on a laboratory scale for sequestration purposes. One study[84] to form CH_4 hydrates, followed by CO_2 gas injection found that systems with excess gas and larger interfaces between CH_4 hydrates and CO_2 gas are more likely to result in a CH_4-CO_2 exchange. In addition, in sediment containing systems with excess water, the effective stress and strength of the system decreased after the gas exchange. Deusner et al. (2012)[85] formed CH_4 hydrates in quartz sand and then injected hot supercritical CO_2 into the system to find that CH_4 gas could be produced. Experiments to inject both hot and cold CO_2 were performed, and hot CO_2 overcame mass transportation issues. The temperature of the hydrate reserve was found to affect the exchange process as well; cooler temperatures led to CO_2 hydrate formation under excess water conditions, which clogged pore space and limited CH_4 production.

Laboratory studies to test the feasibility of CH_4 release from hydrates by CO_2 gas injection are mostly limited to analytical investigation tools, such as nuclear magnetic resonance (NMR), Raman, and magnetic resonance imaging (MRI), to provide a basic understanding of the exchange process[86]. Raman spectroscopy established that upon liquid CO_2 injection into preformed CH_4 hydrates, there was essentially a mol to mol correlation with the liberated CH_4 and the CO_2 lost due to CO_2 hydrate formation. In one experiment, 70 mmol CH_4 was recovered

from hydrate decomposition while 71 mmol CO_2 was consumed to form hydrates, indicating that the CH_4 guest molecule was indeed replaced by CO_2 in the hydrate structure during the gas exchange[25]. Similarly, another study[87] grew CH_4 hydrates and then charged the system with CO_2 gas and measured CH_4 recovery to be 8.3 mol% in 206 hours using gas chromatography (GC). An *in-situ* MRI measurement of CO_2 injection into CH_4 hydrates contained in a Bentheim sandstone core sample yielded 50-85% CH_4 gas recovery after flushing three times with CO_2 using GC[88]. Another MRI study of brine solutions in Bentheim sandstone showed that CH_4 hydrates spontaneously converted to CO_2 hydrates when exposed to liquid CO_2, and the hydrates were not found to dissociate to liquid water during the exchange[89].

Since CH_4 hydrates located in permafrost regions are easier to access than those in marine environments, the technology for carbon sequestration has reached larger-scale field testing in permafrost regions. Studies have shown that there is an estimated 2.4 trillion m^3 of recoverable gas from accessible hydrate accumulations in the North Slope of Alaska alone [90]. In 2012, a ConocoPhilips led test showed success when a 23 mol% CO_2 in nitrogen mixture was injected to release over 24,210 m^3 of CH_4 from a hydrate reservoir in Alaska. CO_2 was preferred over nitrogen in the hydrate phase, as about 70% of the nitrogen gas injected was recovered, while only 40% of the 1376 m^3 of CO_2 injected was retrieved[91].

In terms of actual sequestration experiments in the ocean, Oak Ridge National Laboratory created a continuous jet hydrate reactor to make CO_2 hydrates for ocean sequestration. Field tests took place in the Pacific Ocean off the coast of Monterey, California at depths of 1200-2000 m, and flow rates ranging from 1.5 to 3.0 L/min for liquid CO_2 were used. It was found that initially, the ocean pH dropped from 7.76 to 6.57 as liquid CO_2 was injected into the ocean, but over a short time (6 minutes) as hydrates formed and moved in the ocean, the pH returned to its initial value. In the laboratory, researchers were able to convert about 30% of CO_2 gas into hydrates, while when they performed field tests, a 45% conversion was seen.[92] Recently, a marine field test was performed off the coast of California to exchange CO_2 in CH_4 hydrates. In the experiment, a pure CH_4 hydrate was brought to the seafloor at a depth of 690 m and then enclosed in a cylinder filled with a 25% CO_2 - 75% nitrogen gas mixture. The CH_4 hydrate was found to dissociate to form a mixed gas phase, though no CO_2 hydrates were found to form under these simulated conditions.[93]

1.7 Feasibility of Carbon Storage in Gas Hydrates

Economic analyses performed by Walsh et al.[94] found that generally, natural gas produced from a large ocean reservoir of hydrates would cost $3.50-4/Mscf (2008 value) more than conventional gas deposits. For several specific hydrate reserves, preliminary economic analyses have been calculated to determine if it is cost effective to consider CH_4 extraction. Geography of the hydrate reserve, technology needed to obtain the gas, and profit potential were all considered. Gas hydrate extractions from the north western part of the Gulf of Mexico were found to be cost effective to extract. There, gas hydrates are located in shallow, porous sediments, which will result in a larger percentage of gas recoveries. It is believed that a thermal stimulation and chemical inhibitor method could be used to dissociate the hydrates and petroleum infrastructure could transport the gas obtained. On the other hand, gas hydrates located in mini-basins in the Gulf of Mexico have very little economic feasibility. These deposits have low permeability, small gas concentration, and are located deep under the ocean floor, so the costs to develop equipment to mine this gas would be tremendous. Similarly, some hydrate deposits in the Blake Ridge region were found to be uneconomical due to their low concentrations, high depths, and disseminated structure. The only dissociation method that would work in this region is thermal stimulation, and large quantities of hot water or steam would be necessary.[95]

In addition, feasibility studies have taken place to determine if CO_2 sequestration in gas hydrates is a viable storage method. When determining if a geological storage site is good for sequestration, many factors must be considered, including pressure-temperature conditions, porosity of the storage media, permeability, size of the geological site, geochemistry and the chemicals present that could react with CO_2, making sure that water at the geological site could not come into contact with drinking water, location to CO_2 production sites, and accessibility.[12] Wright et al.[12] studied the potential for CO_2 sequestration in the Great Lakes, and found that Lake Ontario and Lake Erie would not be able to safely store CO_2 as gas hydrates due to large thermal gradients. On the other hand, Lake Huron was found to have some potential for storage while Lake Michigan had a very high storage capacity. Overall, Lake Superior holds the most CO_2 sequestration potential based on its depth, thermal gradient, and thermal conductivity. A majority of Lake Superior is more than 100 m deep and has a temperature around 4°C. It was

estimated that realistically a volume of 8.5 x 10^{12} m^3 could be used to sequester CO_2 hydrates or up to 256 Gt of CO_2.[12]

1.8 Thesis Goal

The goal of this study was to better understand CO_2 hydrate formation with and without porous media, as well as to understand CH_4-CO_2 interactions under hydrate forming conditions. In particular, this thesis has investigated pure CO_2 hydrate and pure CH_4 hydrate growth, as well as mixed CH_4-CO_2 hydrate growth under seafloor conditions. The formation of CH_4 hydrates, followed by a CO_2 injection and the formation of CO_2 hydrates, followed by a CH_4 injection were studied to better understand the sequestration process and to test the theory that CO_2 hydrates are more stable than CH_4 hydrates. This hypothesis was based on the known thermodynamic stability of hydrates of CO_2 over CH_4. We sought to demonstrate that CO_2 gas can substitute for CH_4 in performed CH_4 hydrates. In addition, the microstructural growth of CO_2, CH_4, and mixed CH_4-CO_2 hydrates was explored with and without porous media to monitor hydrate growth and sediment stability using x-ray computed microtomography (CMT).

Chapter 2

2.0 Experimental Equipment

Custom experimental reactors and equipment were utilized to study the formation of CH_4 and CO_2 hydrates.

2.1 FISH Unit

The Flexible Integrated Study of Hydrates (FISH) Unit at Brookhaven National Laboratory (BNL), shown in Figures 2.1 and 2.2, consists of a gas supply system, high pressure cells, and a gas discharge system. FISH is called flexible because there are a variety of pressure reactors that can be interchanged into the system depending on the needed study.

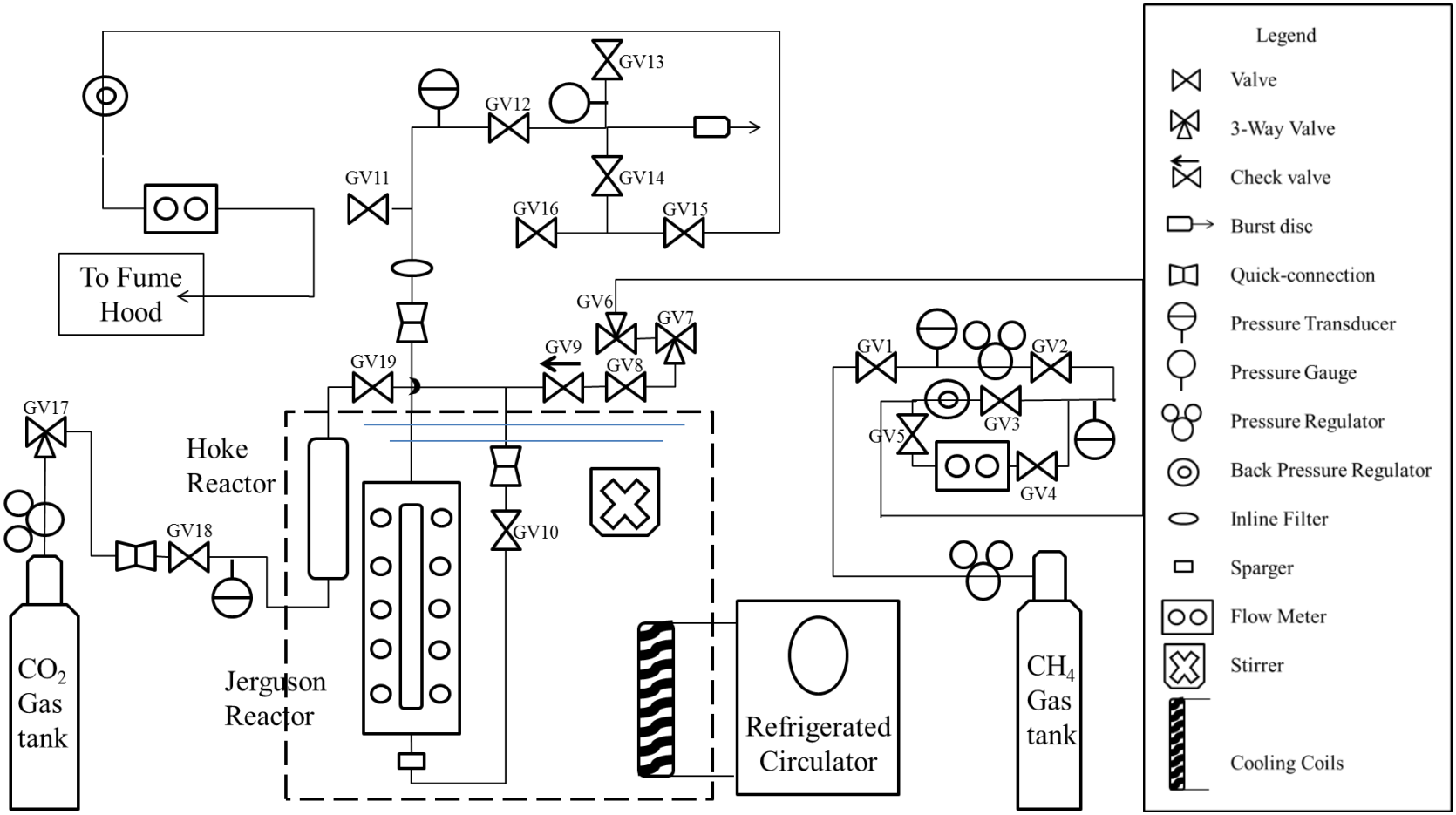

Figure 2.1: *Process flow diagram of the FISH Unit*

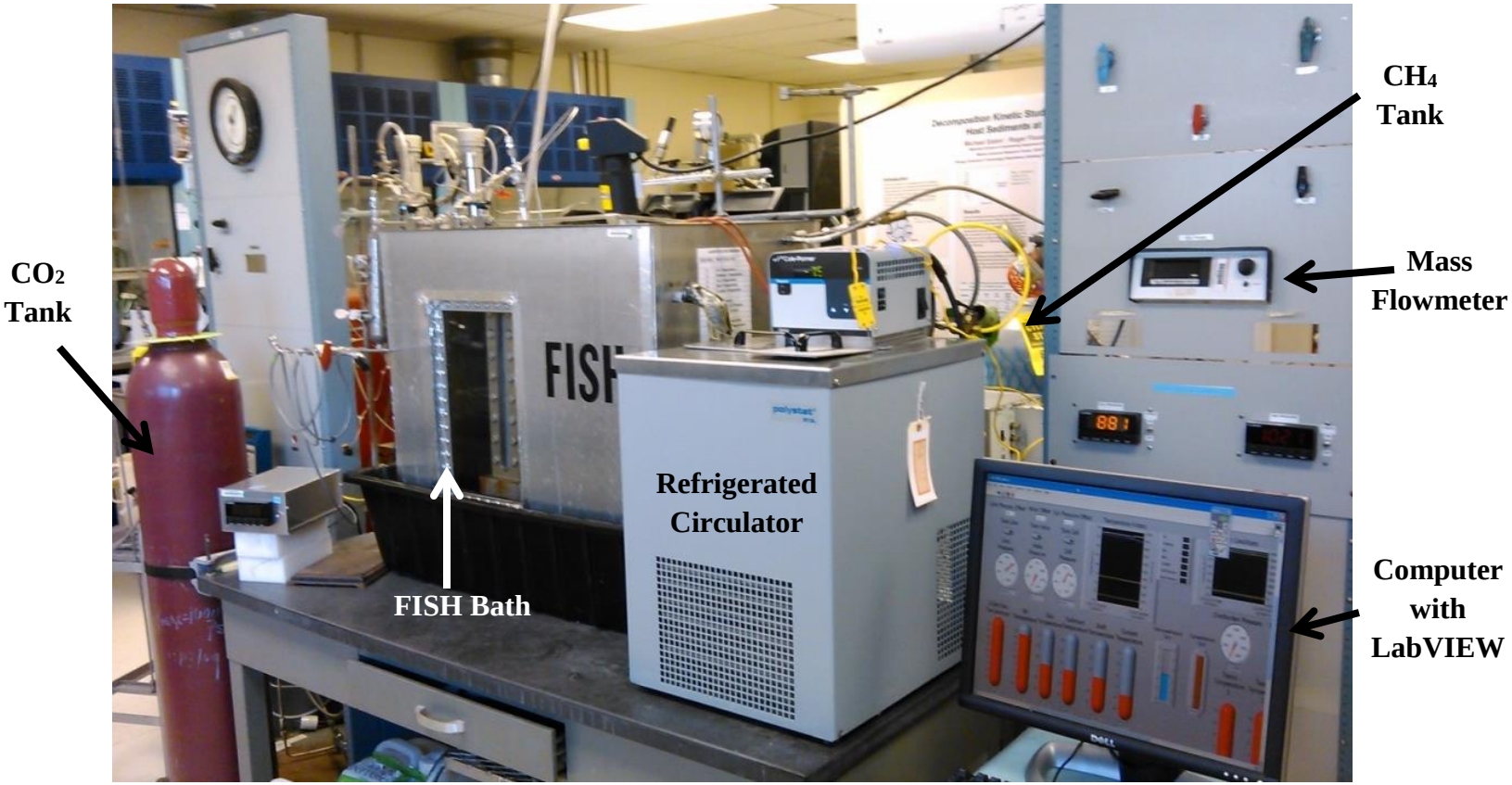

Figure 2.2: *FISH Unit at BNL- actual set-up*

The gas input system comprises of CH_4 and CO_2 gas sources connected to a series of stainless steel tubing, valves, pressure regulators, thermocouples, and a flow meter/controller. Gas delivery line pressure, cell pressure, and Hoke reactor pressure are measured and displayed with Omega strain gauge pressure transducers (Omega PX4100-1.5KGV) and display units (DP-25B-S-A) respectively. Several Type J or K stainless steel Omega thermocouples are utilized to measure the temperature of the air, bath water, ethylene glycol coolant, and inside various reactors. A Brook's model 5850TR flow meter is located on the CH_4 gas delivery line to monitor the volume of CH_4 flowing into the system.

Reactors can be immersed in a water bath maintained at isothermal temperatures with an ethylene glycol-water cooled refrigerated circulator (Cole-Parmer Polystat R13L or Neslab 111) to form gas hydrates. Ethylene glycol-water flows through a series of coils within the water bath to cool the system. A stainless steel 18" x 26" x 21.5" container of 17.4 gallons volume with two plexiglass windows serves as the water bath to hold and cool the larger reactor. Smaller reactors are normally cooled directly in the ethylene glycol-water bath of the refrigerated circulator.

A Hoke reactor is used to mix CH_4 and CO_2 gases during mixed gas experiments in the Jerguson reactor. The Hoke reactor is a 9" long cylinder with an outer diameter (OD) of 1.5", and a total volume of about 150 mL. Located in the CO_2 gas delivery side of the FISH Unit, the reactor can be pressurized with CO_2 or CH_4 gas, and once this reactor is sealed off from the gas cylinder, the valves between the Hoke reactor and Jerguson reactor can be opened to allow for gas mixing. A one-way check valve (Omega SS-53S4) is located on the CH_4 inlet lines to allow for the direct injection of CH_4 gas into the Jerguson reactor in an experiment where CO_2 hydrates have already been pre-formed to prevent any CO_2 gas from seeping into the CH_4 inlet lines.

A high pressure relief valve is installed in the system for use with the Jerguson reactor to vent gas if the pressure in the system exceeds safe values. When experiments are over, gas from the reactors is vented into a fume hood via gas discharge lines.

A LabVIEW data acquisition system was used to record pressure, temperature, and flow values throughout the experiments. A National Instrument (NI) SCXI-1000 (Signal Conditioning Extension for Instrumentation) frame with NI SCXI-1303 module is utilized to collect data from the pressure transducers, thermocouples, and flow meters for LabVIEW. Signals from each device are acquired in specified time increments and are transferred to the computer (Dell Optiplex 6X620) as filename.lvm files, and the pressure-temperature values are

displayed as a function of time on a waveform graph through the DAQ assistant in the LabVIEW program. Figure 2.3 shows the LabVIEW program screen: pressures from the CH_4 entry lines, CO_2 entry lines in the Hoke reactor, and Jerguson reactor, and temperatures from the room/air, gas portion of the Jerguson cell, sediment/solution portion of the Jerguson cell, water bath, and ethylene glycol-water coolant were all recorded and displayed throughout experiments.

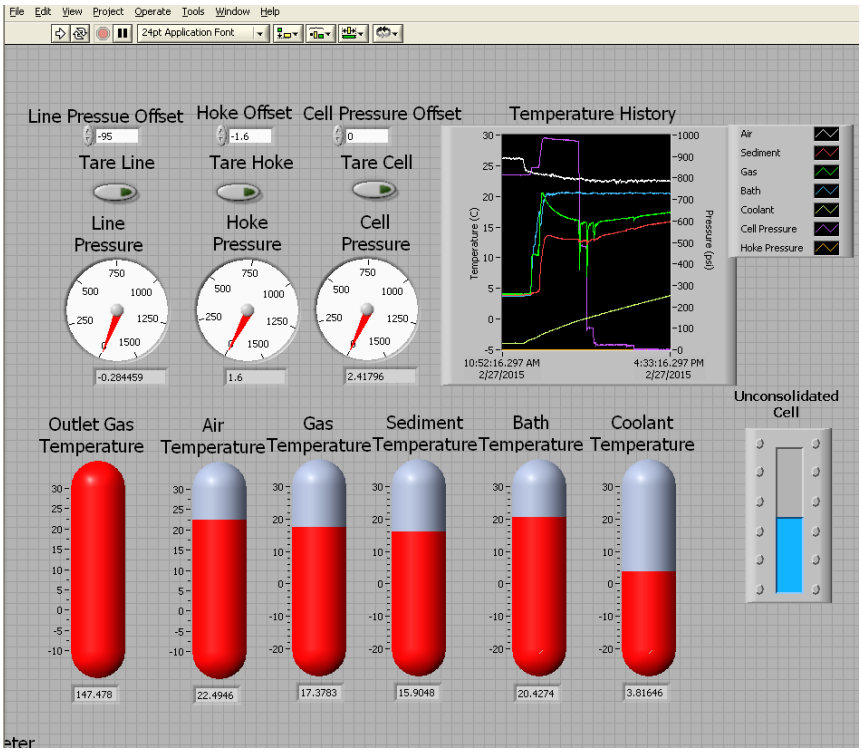

Figure 2.3: *LabVIEW data acquisition screen for hydrate systems in the FISH Unit*

The three types of reactors that are described herein are: 1) see-through Jerguson cell, 2) small volume test cells, and 3) computed microtomography (CMT) cell. All reactors can be connected to the FISH Unit for cell pressurization and to a LabVIEW program for pressure and/or temperature monitoring. Since the equipment used in these experiments measures pressure values in psi units, the values throughout this thesis are left in these units for precision. The units can be converted to SI units using the formula: 1 psi = 0.00689 MPa.

Gas samples (~0.5 mL) from the cell after the formation of CH_4-CO_2 hydrates and during dissociation were analyzed using GC with a Gow Mac series 580 gas chromatograph containing a Supelco Carbonex 1000 45/60 (1.5 m × 0.32 mm) packed column. Helium was used as a carrier gas during GC. Gas compositions were calculated using pure CH_4 and CO_2 as reference gases. GC uncertainties were low, and most times when gas sampling was repeated, GC readings were identical or within $\pm$1%.

2.1.1 Jerguson Cell

The see-through Jerguson cell (~198 mL) can hold a sediment-water slurry and allows for gas pressures up to 2000 psi [14 MPa] as a representation of seafloor conditions. The 14” x 4” x 3” reactor, shown in Figure 2.4, is made of stainless steel. The see-through, 1” thick borosilicate windows on the Jerguson cell allow for a visual observation of hydrate formation. There is a pressure transducer at the top of the cell and thermocouples located at the top and bottom of the cell measuring the temperature of the gas and liquid/sediment phases respectively.

Figure 2.4: *Jerguson reactor (Clark-Reliance, Jerguson Gauge and Valve)*

CH_4 or CO_2 gas can be bubbled in from the bottom of the reactor through a hydrate forming solution and, in some experiments, seafloor simulating sand. A sparger was created using steel wool and mesh to create a stream of small gas bubbles, rather than one large gas bubble when gas is input into the cell. This sparger also prevents sand from collecting in the gas inlet lines. The gas outlet lines at the top of the cell contain a valve used for GC sample taking and an inline filter, to prevent any sand from getting into the outlet gas lines. The Jerguson cell is held inside the water bath tank of the FISH Unit on two stainless steel blocks.

2.1.2 Small Volume Cells

The small volume test cells, shown in Figure 2.5, consist of three pressure reactors made of stainless steel with 1", ½", and ¼" [2.54, 1.27, and 0.635 cm] OD and volumes of 72 mL, 17.6-24.9 mL, and 7.4 mL respectively. These cells were created as test cells to see if gas hydrates would form in small diameter, small volume reactors. The cells are made up of two parts: a cell where hydrate forming solution is loaded and hydrates form, and a top assembly with a three-way safety valve and pressure transducer (Omega PX4100). The cell and top assembly can be connected by a quick connect fitting. Gas is added to the top of the cell through the top assembly, which can be connected to the inlet lines of the FISH Unit. A safety three-way relief valve has been employed to purge pressure from the system at any time during the experiment if necessary. All stainless steel fittings, quick-connects, and ball valves are rated up to a maximum pressure of 3000 psig [20.8 MPa], which is much higher than the experimental pressure maximum of about 1000 psig [7.0 MPa]. These cells are cooled to experimental temperatures inside the ethylene glycol-water bath of the refrigerated circulator or in a secondary small water bath.

Figure 2.5: *Small volume test cells*

2.1.3 CMT Cell

The CMT cell was designed for CMT imaging at the National Synchrotron Light Source (NSLS) at BNL. The main component of the experimental set-up is a high pressure ¼" [0.635 cm] OD seamless 6061 aluminum tubing as shown in Figure 2.6. Aluminum is chosen over a series of materials considered suitable for high pressure cells since it has the lowest mass attenuation coefficient, aside from Beryllium and diamond. A 8.5" [21.5 cm] long ¼" OD aluminum tubing provides about 3.5 mL volume for the sample. This part of the cell is composed of a valve and stainless steel quick-connect for easy loading of the sample. Two bore-through tees have been placed on the outside of the aluminum tubing with polypropylene ferrules and a polypropylene fitting on the tee at the top of the reactor and a stainless steel fitting at the bottom tee. When CMT imaging takes place, the cell is installed in a goniometer on the sample stage at this stainless steel fitting to allow for cell rotation. The 5/8" [1.59 cm] OD and 3/8" [0.952 cm] inner diameter (ID) vinyl tubing clamped onto the tees serves as a cooling jacket when ethylene glycol-water is passed through it with the refrigerated circulator. The sample cell is attached to the same top assembly described for the small volume cells. As with the small volume cells, all the stainless steel fittings are rated up to a maximum pressure of 3000 psig. When CMT imaging is about to take place, the valve on the sample section of the cell is closed, and the top assembly is purged of gas via the three way valve. The top assembly can then be removed and the sample cell is placed in the goniometer with a self-centering chuck on the sample stage.

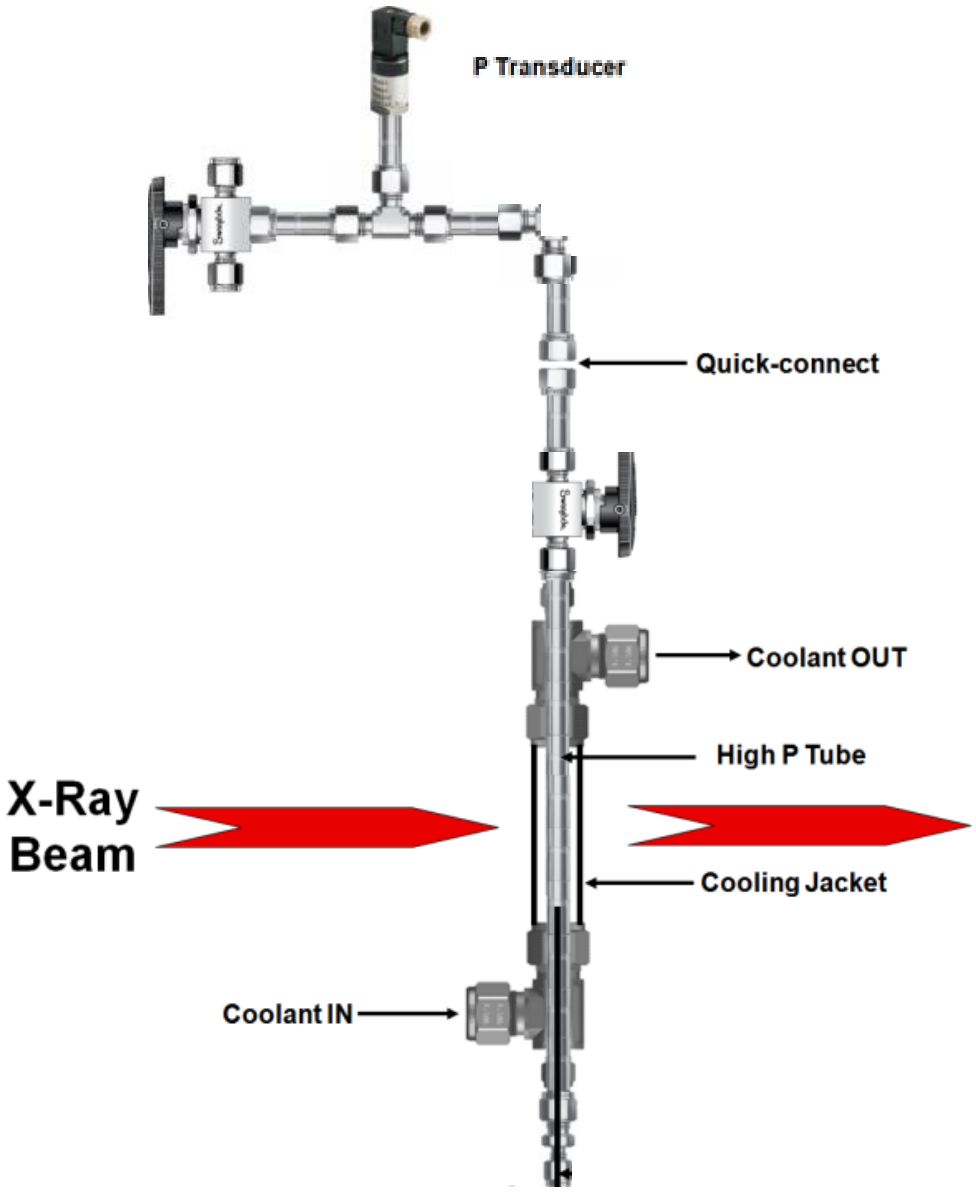

Figure 2.6: *CMT cell built to form and x-ray image gas hydrates*

2.2 X-ray CMT

The X2B beamline at the NSLS consists of a beamline (Figure 2.7) that leads into an experimental hutch (Figure 2.8). This hutch contains a filter, stage with sample holder, scintillator, mirror, and charged-coupled device (CCD) camera as shown in Figure 2.8. At the NSLS, synchrotron radiation is created when high speed electrons change directions in an x-ray ring. A synchrotron light source uses an electron gun to create electrons and accelerates these electrons to high energies around a ring. When electrons pass through bending magnets located inside this ring, they are deflected to change their path and x-rays are given off at a tangent. These x-rays are guided into one of many beamlines that use varying techniques to utilize the x-rays produced.[96] At X2B, the x-ray beam is created from a bending magnet as a filtered white beam with energies ranging from 6.5 – 35 keV, and a flat single crystal Si<111> Bragg spectrometer is sealed in a helium purged area in the hutch.[97,98] This x-ray beam of 5 mm width and 1 mm height passes through a specimen and collides against a thin, high resolution CsI scintillator. An image is created based on the amount of x-rays that are absorbed by a specimen. There are two magnification lenses: the 2.5X magnification lens allows for 7.5 micron resolution and keeps the entire sample horizontally in the field of view, whereas 5X lens provides 4 micron resolution, which can be used to observe the wall of the sample. A flat mirror, angled at 45^{o} to the beam, bends the picture produced by scintillator into the CCD camera. A Kodak CCD with 0.0067 mm pixel size and an area of 1340 x 1300 pixels was utilized to collect data. The sample to be imaged is held in a goniometer on a stage that can rotate the sample 360° for CMT imaging. A stepping motor under the stage can move the sample horizontally through the beam, and there is a vertical translator for changing the section of the sample to be imaged.

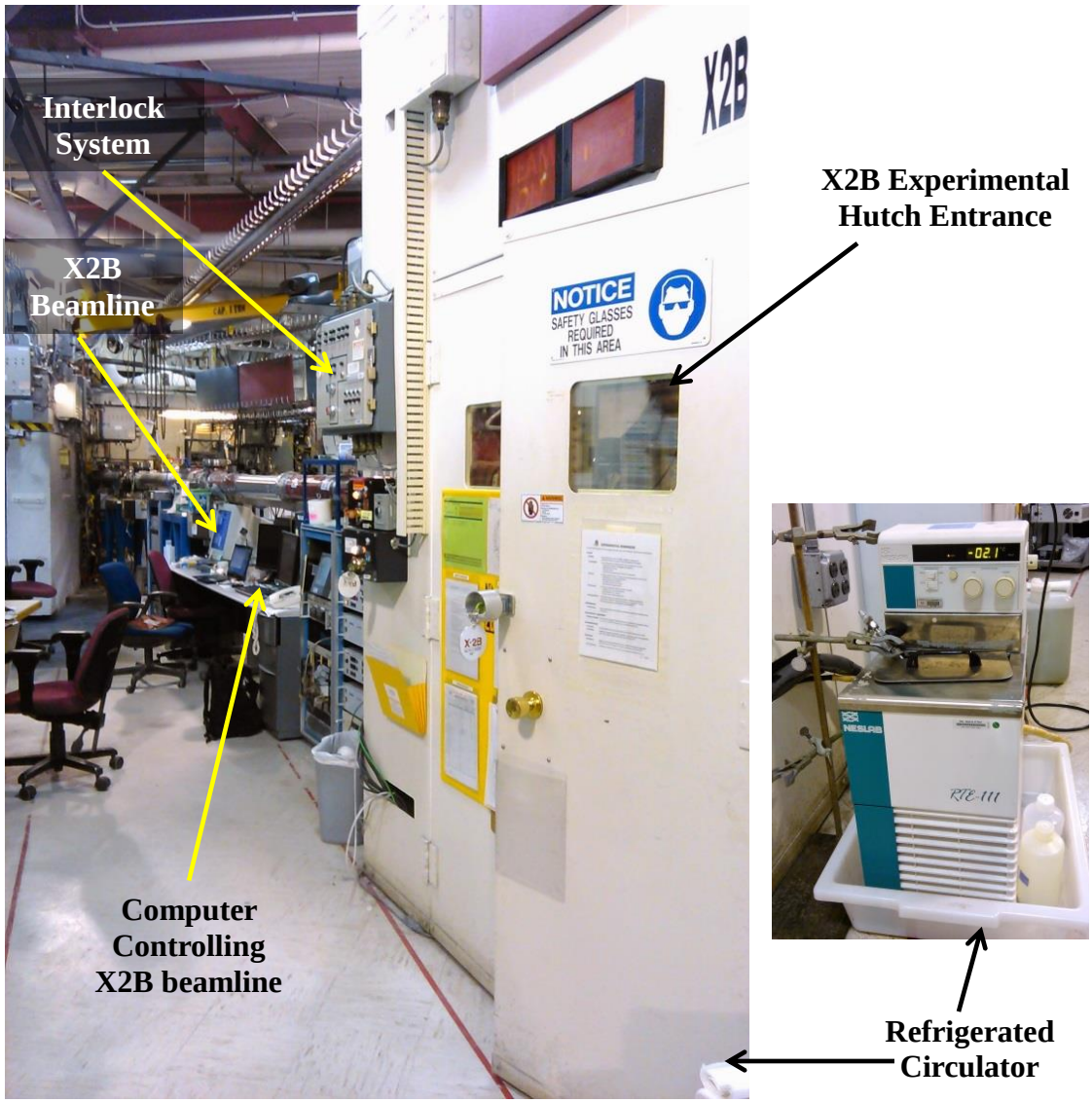

Figure 2.7: *X2B beamline, BNL*

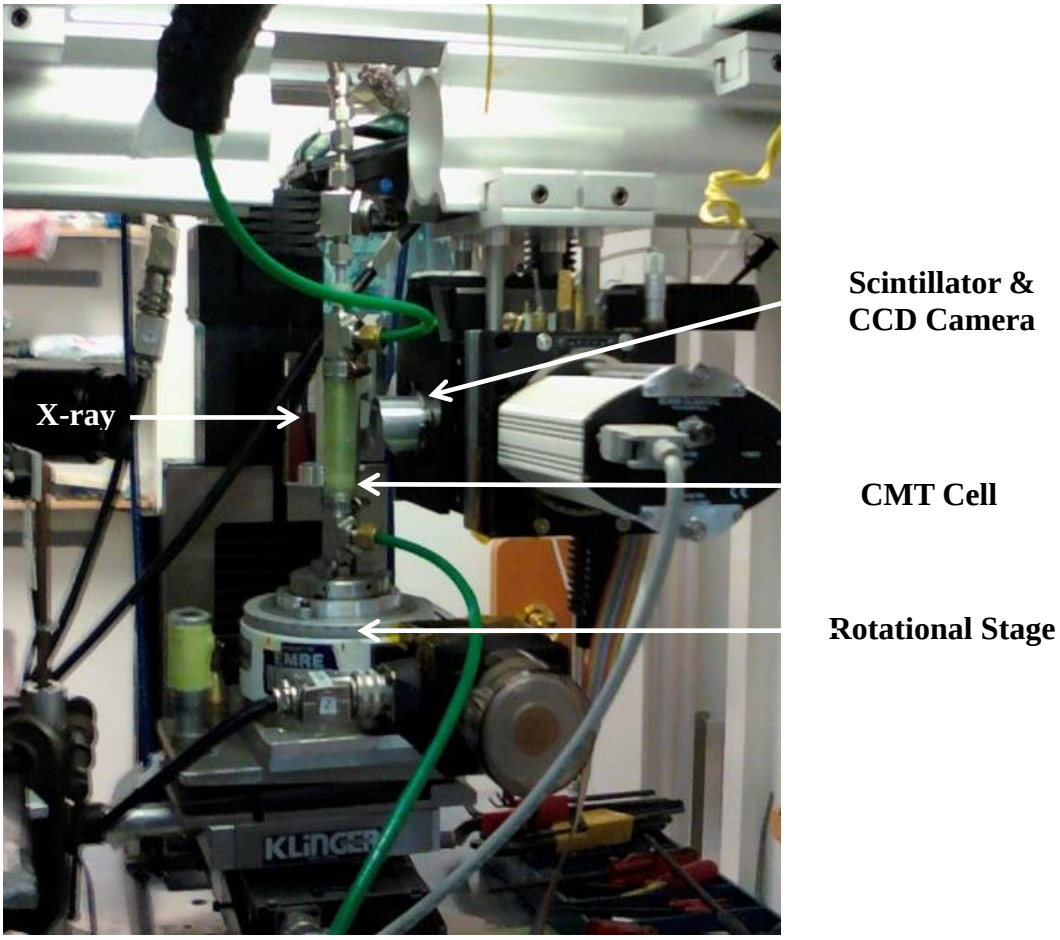

Figure 2.8: *X2B experimental hutch, BNL, with the CMT cell in place*

IPLab software, created by ExxonMobil Research & Engineering, was used to configure the beam and for data acquisition[97,98]. Typical data acquisition involved around 1200 images with 2000 msec exposure time for each image at every 0.15^{o} increment from 0 to 180^{o}, and the entire scan would take about 2.6 h. The number of images collected (and thereby the rotational increment for each image), as well as the exposure time was varied to improve the quality of the images produced (more images with longer exposure time) or to decrease the scan time needed (fewer images with shorter exposure time). An output .prj file made up of the data from 1200 tomographic image slices would require about 1 GB of memory, and after all image processing had taken place, roughly 10 GB of memory was required for each scan performed. This .prj file could be converted into a .volume file and then processed into a recon.volume file using Interactive Data Language (IDL) Virtual Machine. The recon.volume file can be converted into individual slice images that depict horizontal slices of the cell. All of these individual images can be then stacked into three-dimensional (3D) volumes with ImageJ or volume rendering software Drishti[99].

2.3 Reagents

2.3.1 Gases

For the experiments described, 99.0% CH_4 gas from Scott Specialty Gases and 99.9% CO_2 gas from Praxair were used, where possible impurities included nitrogen, water, and oxygen. Leak tests were performed using nitrogen gas from Praxair and helium gas used as a carrier gas for GC samples was from CGI Gas Technologies.

2.3.2 Hydrate Forming Solutions

2.3.2.1 300 ppm Sodium Dodecyl Sulfate (SDS)

A 300 ppm SDS solution was used to form hydrates in several Jerguson and small volume experiments. SDS is a hydrate promotor which was utilized in experiments to shorten the induction time for hydrate formation. SDS was used with distilled water to create the solution.

2.3.2.2 Artificial Seawater

To simulate ocean floor hydrate formation, an artificial seawater solution was used in many Jerguson cell experiments. The solution was created following the guidelines published in Kester et. al[100] and listed in Table 2.1. The presence of salt inhibits hydrate formation[17]. While lower molecular weight gases are encaged in a hydrate, salts are not included in the hydrate structure. Dissolved ions (Na+ Cl-) remain in the hydrate forming solution,[101] therefore they do not affect the structure of the gas hydrate.

Table 2.1: *Artificial Seawater Composition*[100]

1	kg Distilled H_2O
23.926	g NaCl
4.008	g Na_2SO_4
0.677	g KCl
0.196	g $NaHCO_3$
0.098	g KBr
0.026	g H_3BO_3
0.003	g NaF
5.0719	g $MgCl_2$ 6 H_2O
1.146	g $CaCl_2$ 2 H_2O
0.0143	g $SrCl_2$ 6 H_2O

2.3.2.3 Barium Chloride ($BaCl_2$) Solution

Solutions of $BaCl_2$ with various weight percentages (5 wt%, 10 wt%, 15 wt% and 20 wt%) in distilled water were used to form hydrates in Jerguson, small volume, and CMT experiments. As with artificial seawater, salt inhibits hydrate formation, but $BaCl_2$ was necessary for CMT experiments to provide a contrast difference between gas hydrates and unused hydrate forming solution. Phases in CMT imaging can be determined based on x-ray attenuation coefficients. The attenuation coefficients for CH_4 and CO_2 hydrates are 0.3270 cm^{-1} and 0.4033 cm^{-1} respectively, while the coefficient for water is 0.3580 cm^{-1}. This difference is difficult to detect on CMT images, so the addition of $BaCl_2$ salt to the water increases the attenuation coefficient for the hydrate forming solution enough to be more distinguishable from the hydrates. More details about distinguishing between phases present in CMT imaging can be found in Chapter 6.

2.3.3 Porous Media

2.3.3.1 Sand

Ottawa sand obtained from the United States Geological Survey was used for these experiments. This F-110 foundry sand is used commonly in gas hydrate formation experiments because of its grain size and rounded shape. This sand is a white, tan powder with an average grain size of 110 µm. It is composed of 99.0-99.9% SiO_2, less than 1.0% AlO_2, less than 0.1% FeO, and less than 0.1% TiO_2.[102]

2.3.3.2 Glass beads

Lead free soda lime (SiO_2 - Na_2O) glass beads with a 500 µm diameter were obtained from Biospec for these experiments. These glass beads have a density of 2.5 g/cm^3.[103]

2.4 FISH Experimental Procedures

Several experiments were conducted to form CH_4, CO_2, and mixed gas hydrates. Prior to an experiment, the cell to be utilized was cleaned and aired out with either pressurized air or nitrogen gas. Leak tests were performed every time after a fitting was loosened in one of the systems. To perform a leak test, the system was pressurized with ~900-1050 psig of nitrogen gas. Nitrogen was chosen for leak tests due to its inert nature and small molecular size relative to CH_4 and CO_2. Most leak tests were performed for at least twenty-four hours to ensure long term pressure stability. Results of all leak tests were recorded and archived.

2.4.1 Jerguson CO_2 / CH_4 / CO_2-CH_4 Hydrate Experiments

2.4.1.1 Gas Hydrate Formation Procedure

i. First, a LabVIEW program was begun to record pressure, temperature, and flow rate values several times every minute. A stirrer and water filter were turned on to better mix and circulate water in the bath to avoid thermal gradients.

ii. There were two possible methods for loading the cell prior to pressurization with CH_4, CO_2, or both CH_4 and CO_2 gas. If an experiment was to be performed without porous

media, 75 mL of hydrate forming solution was added to the cell. If hydrates were to be formed in porous media, first 103.73 g (29.2 mL volume) of Ottawa sand was added, and then 38 mL of hydrate forming solution was syringed into the cell. Various hydrate forming solutions were used, including 300 ppm SDS, artificial seawater, and 5 wt% $BaCl_2$.

iii. For some experiments, the water bath was pre-cooled to between 2-5°C, and then gas was slowly bubbled into the system, while in other experiments, the cell was pressurized up to a desired pressure at room temperature, and then cooling to 2-5°C commenced. To pressurize the cell, either CH_4 or CO_2 from gas cylinders was passed through a series of valves, pressure transducers, and for CH_4, a gas flow meter. Valves in the FISH Unit were opened slowly, one by one, to gently bubble gas into the Jerguson cell.

iv. Several visual observations were recorded and photographs were taken throughout hydrate formation.

v. In some of the runs performed, the cell was pressurized a second time with the initial gas added to the system to encourage further hydrate formation. Sometimes the cell was pressurized with a new gas (CH_4 or CO_2) to monitor the exchange of gases in hydrates. For an experiment where CH_4 hydrates were initially formed and CO_2 was later injected, the cell was partially depressurized following CH_4 hydrate formation to allow for the addition of CO_2 in gaseous form. CO_2 is a liquid at high pressures, so care was taken to avoid the presence of liquid CO_2 in the Jerguson reactor. Once the cell was partially depressurized to a pressure below 600 psig, CO_2 gas of a higher pressure was added to the cooled Hoke reactor. Once the valve between the Hoke reactor and the CO_2 inlet lines was sealed, the valve between the Hoke reactor and Jerguson cell was opened and gases were allowed to mix as CO_2 bubbled into the Jerguson cell. If CO_2 hydrates were formed first followed by a CH_4 injection, no partial depressurization was necessary.

vi. If a system was pressurized with both CH_4 and CO_2 gas, GC samples were taken at regular intervals.

2.4.1.2 Gas Hydrate Dissociation Procedure

Dissociation was achieved by either thermal stimulation where the cell was warmed up to room temperature or by depressurization, where the cell was depressurized in steps.

To Dissociate Hydrates by Thermal Stimulation

i. System cooling was ended by turning off the refrigerated circulator, ending the stirring of the FISH bath, and ending filtration of the FISH water.

ii. If the system was allowed to warm up slowly over several days, water and packing peanuts would be left in the FISH bath. If it was desired to dissociate hydrates sooner, packing peanuts were removed from the water bath, and water was drained out of the FISH water bath. Room temperature water was then added to fill up the bath to warm the cell quickly.

iii. Hydrate dissociation was completed once hydrates could no longer be seen in the Jerguson cell. For experiments with mixed CH_4-CO_2 hydrates, during dissociation and/or once dissociation was completed, GC samples were taken to determine the composition of the gas phase eluted from the hydrates.

iv. For mixed gas hydrates, most times the cell was depressurized in several psi steps and further GC samples were taken once hydrates were no longer stable to determine the gas phase of the cell. As CO_2 is highly soluble in water, these GC samples allowed for monitoring the percentage of CO_2 that had been dissolved in the hydrate forming solution.

v. Once hydrates had dissociated, or once GC sampling was completed, the cell was completely depressurized into a fume hood and the LabVIEW program was stopped. For experiments with CO_2 gas, the system was left open to vent into the fume hood for several hours as CO_2 continued to evolve from the hydrate forming solution.

To Dissociate Hydrates by Stepwise Depressurization

i. The Jerguson cell outlet valve was opened slowly to allow for some of the gas in the reactor to be vented into a fume hood to achieve a desired system pressure decrease. Usually system pressure was reduced by 100-300 psig (0.8-2.2 MPa) before closing the outlet valve.

ii. The system was then given time to restabilize, as the venting of gas from the system and hydrate dissociation resulted in a temperature decrease. If the system being depressurized contained both CH_4 and CO_2 gas, a GC sample was taken upon this pressure decrease.

iii. Steps i and ii were repeated until all gas hydrates had dissociated from the system. For mixed CH_4-CO_2 systems, further gas purges were performed with GC sampling to determine the gases de-solubilizing from the hydrate forming solution.

iv. Once system pressure was too low for further depressurization steps, the cell was entirely vented of gas into a fume hood and the LabVIEW program was stopped. For systems with CO_2 gas, the system was left open to vent into the fume hood for several hours as CO_2 continued to evolve from the hydrate forming solution.

2.4.2 Small Volume Test Cell Experiments

i. In these experiments, 1", ½", and ¼" OD stainless steel cells or the CMT cell were used to form gas hydrates. Varying volumes of 5 wt% $BaCl_2$, 300 ppm SDS, or mixed 5 wt% $BaCl_2$-300 ppm SDS solution were syringed into the different cells. Sometimes, two stainless steel balls were added to the cell to provide extra system mixing.

ii. These cells were then evacuated with a vacuum pump for one minute to remove most of the air in the system.

iii. Next, the cells were pressurized to the experimental pressure; for CO_2 hydrates, a pressure of ~450-800 psig (3.2-5.6 MPa) was used and for CH_4 hydrates a pressure of ~950 psig (6.7 MPa) was used.

iv. The cell was then either placed horizontally into a water bath with an isothermal temperature above freezing that was controlled by an ethylene glycol-water cooled refrigerated circulator set at varying temperatures or it was cooled at a 45° angle directly in the refrigerated circulator's bath.

v. The cell was sporadically shaken to agitate the solution (and stainless steel balls in some experiments) in an attempt to trigger hydrate formation.

vi. In 24 hours to 1 week, a pressure drop occurred, indicating the formation of gas hydrates. Pressure and temperature values over time were recorded.

vii. Once a run was completed, the cell was depressurized slowly into a fume hood, and the cell was cleaned out with water. Pressure drop data were used to estimate the percentage of gas that was converted into gas hydrates. This analysis has shown that mass transfer area (tube diameter), temperature, gas/liquid ratio, and system agitation have a significant effect on the percent conversion of gas into gas hydrates.

2.4.3 Calculating the Conversion of Gas into Gas Hydrates

To provide a rough estimate of the conversion of gas into hydrates in a system, first the following values must be noted based on experimental conditions: volume of the system (V_{cell}), volume of solution added to the system ($V_{solution}$), initial temperature of the system immediately following system pressurization ($T_{initial}$), initial pressure of the system at $T_{initial}$ ($P_{initial}$), the bath temperature at which the system is cooled (T_{bath}), and the final pressure of the system at T_{bath} (P_{final}). The volume of the gas (V_{gas}) can be calculated by Equation 2.1:

$$V_{cell}\text{-}V_{solution} = V_{gas} \quad (2.1)$$

The ideal gas law (PV=nRT) can be used to determine the final pressure that the system should reduce to due to cell cooling. Gas compressibility (Z) was negligible for the conditions of these experiments. Since the volume, number of moles, and universal gas constant (R) have constant values, the equation can be reduced to Equation 2.2. With this new pressure value the pressure drop of the system due to hydrate formation (ΔP) can be calculated by Equation 2.3:

$$P_{cooling} = P_{initial}\, T_{bath}/T_{intial} \quad (2.2)$$

$$\Delta P = P_{cooling} - P_{final} \quad (2.3)$$

In order to calculate gas conversion, it is necessary to know the number of moles of gas needed for 100% conversion of all of the solution in the system to hydrates ($n_{gas\ 100}$). This can be calculated through Equation 2.4, where 6 refers to the average 6:1 molar ratio of water to gas composition for each gas hydrate structure and 18 g/mol is the molecular weight of water. We can use Vgas in this equation because 1 mL of hydrate forming solution is equivalent to 1 g of solution. The volume that $n_{gas\ 100}$ would occupy ($V_{gas\ 100}$) can be determined by Equation 2.5, where the volume of an ideal gas is 22.4 L/mol:

$$n_{gas\ 100} = V_{solution}/ (6 \times 18) \quad (2.4)$$

$$V_{gas\ 100} = 22.4 \times n_{gas\ 100} \quad (2.5)$$

To calculate the number of moles of gas initially in the system ($n_{gas\ initial}$) and the number of moles of gas in the system at the end of hydrate formation ($n_{gas\ final}$), Equations 2.6 and 2.7 can be used respectively:

$$n_{gas\ initial} = (P_{initial}\, V_{gas}) / (R\, T_{initial}) \quad (2.6)$$

$$n_{gas\ final} = (P_{final}\ V_{gas}) / (R\ T_{bath}) \quad (2.7)$$

Next, the number of moles of gas consumed due to hydrate formation ($n_{gas\ consumed}$) based on the pressure drop can be calculated by Equation 2.8:

$$n_{gas\ consumed} = (\Delta P\ V_{gas}) / (R\ T_{bath}) \quad (2.8)$$

An excess gas system is limited by the amount of water in the system, thereby, conversion of gas into hydrates can be determined by dividing the number of moles of gas consumed by the system by the number of moles of gas that could be converted into hydrates based on the ratio of 6 moles of water to 1 mole of gas to form hydrates. An excess solution system is limited by the amount of gas in the system, thereby, the conversion of gas into hydrates is dependent on the number of moles of gas consumed by hydrate formation. To determine if a system is composed of excess water or excess gas, the number of moles of gas in the system available to form hydrates can be computed by Equation 2.6, and the number of moles of solution available in the system to form hydrates can also be calculated by determining the number of moles of liquid input into the system by Equation 2.4. By this calculation, if there are more moles of solution available to make hydrates, the system is excess solution, whereas if there are more moles of gas available, the system is excess gas. Note that when using these equations, care must be taken to ensure that proper units are used in calculations.

If the system is composed of excess gas, conversion is given by Equation 2.9, while if the system contains excess water, conversion can be calculated by Equation 2.10:

$$\%\text{Conversion Excess Gas} = \Delta P\ V_{gas} / (R\ T_{bath}) / (V_{liquid} / 6 \times 18) \times 100 \quad (2.9)$$

$$\%\text{Conversion Excess Water} = n_{gas\ initial} - n_{gas\ final} / (n_{gas\ initial}) \times 100 \quad (2.10)$$

2.4.4 NSLS Experiments

2.4.4.1 Preparing for Hydrate Formation and CMT Imaging

i. To perform x-ray CMT runs, in Building 815 at BNL, the aluminum CMT cell was filled with a desired volume (2-2.5 mL) of 5, 10, 15, or 20 wt% $BaCl_2$ solution. If hydrates were to be formed in porous media, first the desired amount of sand or glass beads was added to the cell, then $BaCl_2$ solution (about 1 mL) was injected into the cell.

ii. The cell was evacuated for one minute using a vacuum pump to remove excess air.

iii. Gas was charged into the cell to the target pressure, which was 950 psig [6.7 MPa] for CH_4 and 650 psig [4.6 MPa] for CO_2. If mixed gas hydrates were to be formed, the cell was first pressurized with CO_2 gas up to a desired pressure, depending on the desired CH_4-CO_2 ratio, and then CH_4 was added to the cell.

iv. Once the cell was pressurized, it was transported to the NSLS (<1 mile). The cell was transported in a vertical orientation secured to a lab stand to ensure that the cell did not move too much during transit.

2.4.4.2 NSLS Beamline Preparation

i. Since X2B is a user beamline utilized by many scientists to image a variety of samples, prior to performing a hydrate imaging scan, all of the parameters of the beamline must be set up for this application. First, the energy of the beamline must be changed to 30 keV. High x-ray energy is necessary to see through the aluminum tubing in the cell. To do this, the energy of the beam must be changed on a computer by going to the EXT menu and selecting 'Camac Set Energy.' On the window that appears, the desired energy (30 keV) can be typed in, and upon submitting the energy change, the beamline energy will be modified.

ii. Next, inside the experimental hutch, the magnification lens for imaging can be changed. Most of the time, a 2.5X magnification lens was used to image the entire width of the cell. To change the magnification lens if another lens is in place, the scintillator can be unclasped, and the magnification lens in place can be screwed off, and a new one can be installed. Then the scintillator can be re-clasped in place.

iii. Finally, there are various sample holders that can be connected to the sample stage for rotating samples. A goniometer made from a modified 2.5" (6.4 cm) OD 3-jaw chuck is used to hold the CMT cell for imaging. This goniometer can be installed on the stage with 2 clips screwed onto the stage.

iv. The next steps taken depended on whether continuous visualization of hydrate formation was desired or if hydrate growth over time was to be monitored.

2.4.4.3 Continuous Visualization of Gas Hydrate Formation

i. To image the cell as hydrates formed and through hydrate induction, the two-way valve between the top assembly and cooled aluminum tubing portion of the cell was sealed, and gas was vented from the top assembly. The top assembly was then disconnected. Once the top assembly was removed, monitoring of cell pressure was no longer possible.

ii. Cooling lines for the refrigerated circulator were attached to the stainless steel tees of the cell's cooling jacket, but the refrigerated circulator was not turned on yet.

iii. The cell was placed into the beam's path by positioning the cell in the goniometer, and tightening the goniometer on the nut of the tee on the bottom of the cooling jacket.

iv. Rotation of the CMT cell in the X2B experimental hutch was then tested. The cell was slowly rotated 180° to ensure that the cooling lines would not get caught during CMT imaging. The coolant inlet line (bottom of the cell) was taped down to the table holding the CMT equipment while the coolant outlet line (top of the cell) was tied to the top of the CMT imaging equipment. Limiting the movement of the cooling lines guaranteed that these cooling lines would not move in a manner that could damage the CMT imaging equipment, cause the cell to be pulled out of the beam's path, cause the plastic cooling lines to break and leak coolant, or cause cooling lines to get in the path of the beam.

v. Once the cell was found to be stable and safely in place on the sample stage, the doors to the experimental hutch were interlocked. The NSLS at BNL has a strict interlock system to act as a safeguard against human exposure to x-ray radiation. To activate the interlock, a black button inside the experimental hutch was pressed, and the beamline door was shut and locked with a key. Once the door was locked, the key was removed and placed into a designated slot in the hutch interlock panel (Figure 2.9), which was to the left of the hutch doors. A black button slightly above this slot was pressed once the key was turned into its slot. A light above the hutch doors with the word 'interlocked' would light up (as shown in Figure 2.10) if the interlock was properly set. If the hutch doors were interlocked, the beam could be enabled. To enable the beam, a green button on the interlock panel could be pressed to open the safety shutters on the beamline. If the beam was successfully enabled, a light above the hutch door with the words 'beam on' would also light up (as shown in Figure 2.10). At this point, the x-ray beam would be flowing into the hutch and through the hydrate sample.

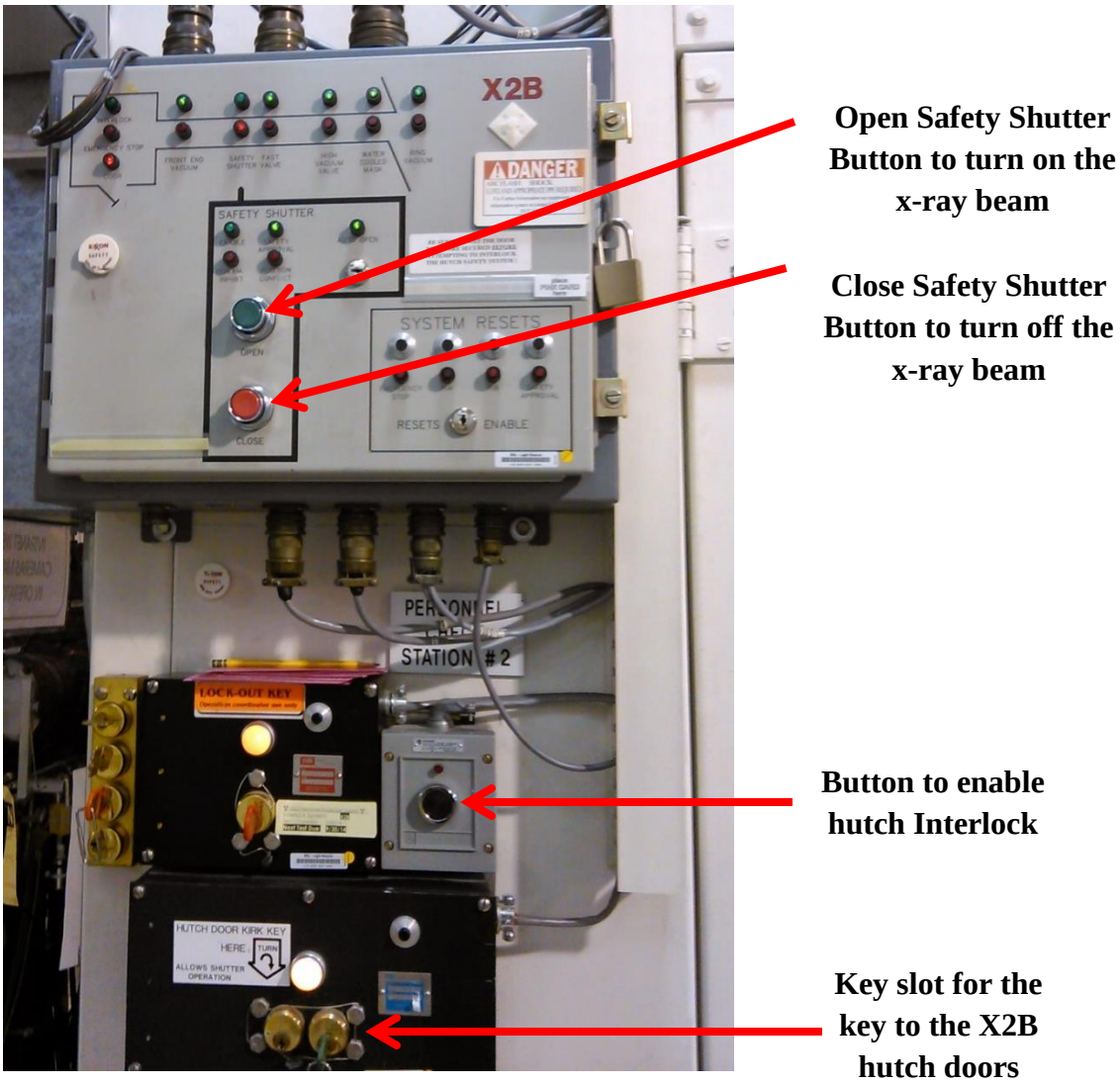

Figure 2.9: *Interlock panel to the left of the experimental hutch doors*

Figure 2.10: *Interlock and Beam On indictor lights above the experimental hutch doors*

vi. At this time, a continuously running scan of the cell can begin. First, an imaging region in the cell was located. For experiments without porous media, the gas-liquid interface was imaged while in experiments with a sand pack, a location within the sand pack was chosen. To find the interface or another good region to image, the stage height was changed via up/down buttons on a Klinger motor controlling the stage outside of the hutch. Every time the height of the stage was changed, an x-ray image of the cell was taken to view the interior of the cell by clicking EXT, Image.

vii. Once a region of interest was located, a tau map image was taken to ensure that the set point for the beamline's energy worked well for the sample. All x-ray images and tomographic scans were taken using a program created by ExxonMobil for IPLab.

viii. Next, an x-ray image of the cell was taken, and a region of interest was defined on that x-ray image by outlining a region with a box as shown in Figure 2.11. Once the region was defined, a scan could be initiated by clicking EXT, μCTScan, where a window would appear. On that window, the exposure and calibration times, number of views, views per calibration, and sample translation for calibration could be modified. A box for a 'continuous' run could be checked off. Once a file name was set, the scan would begin. The scan would image the sample through 180°, and then the sample would rotate back to its initial angle, and a new scan would be restarted. This cycle would keep repeating until the scan was cancelled by the user.

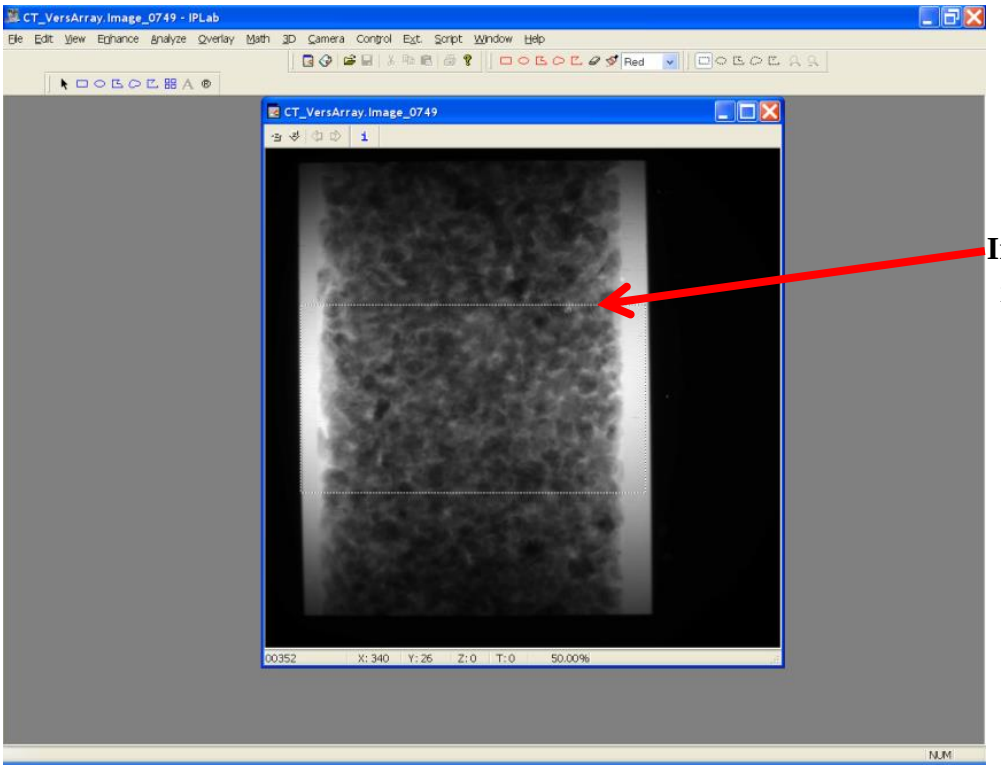

Figure 2.11: *X-ray image with a defined region of interest*

ix. Once a continuous scan had begun, the refrigerated circulator was turned on to begin cooling the sample to a temperature above the freezing point of the $BaCl_2$ solution used in the cell.

2.4.4.4 Monitoring Gas Hydrate Growth over Time

i. Alternatively, to monitor hydrate growth over time without continuous imaging, the cell was placed in the ethylene glycol-water bath of a refrigerated circulator in a 45° angled orientation at the NSLS. The cell was kept at this angle throughout formation when the cell was not being imaged to allow for a greater mass transfer area and a larger gas-liquid interface. The cooling jacket was filled with ethylene glycol-water from the refrigerated circulator. The refrigerated circulator was turned on, and the cell was cooled to a temperature slightly above the freezing point for the $BaCl_2$ solution used in the cell.

ii. Once cell pressure stabilized, the CMT cell was taken out of the refrigerated circulator bath, and as quickly as possible (within 2 minutes), cooling lines for the refrigerated circulator were attached to the stainless steel tees of the cell's cooling jacket. Coolant was allowed to flow through these lines to keep the portion of the cell to be imaged cold.

iii. The cell was positioned in the beam by placing the bottom of the cell in the goniometer, and tightening the goniometer on the nut on the tee connecting the bottom of the cooling jacket to the cell. The beam was enabled following step v from the Continuous Visualization of Gas Hydrate Formation procedure.

iv. A tau map image of the cell was taken to locate the gas-liquid interface in the cell (or in the presence of porous media, a tau map was taken to locate the sand pack) and to determine if hydrates had formed yet. After this image was taken, the cell was taken out of the goniometer.

v. If no hydrates were seen in the images, the cooling lines were disconnected from the cell, and the cell was placed back into the bath of the refrigerated circulator for further cooling. Steps ii – iv were repeated either until hydrates were seen or until it was decided to start a new experiment.

vi. If the presence of hydrates was seen in the image taken, the two-way valve between the top assembly and cooled aluminum tubing portion of the cell was sealed, and gas was

vented from the top assembly. The top assembly was then disconnected, and the CMT cell was placed back into the goniometer.

vii. As hydrates formed, several tomograms were taken with a 180º sample rotation. To do this, steps iii – vii from the Continuous Visualization of Gas Hydrate Formation procedure were performed, except in step vii, the 'continuous' box was not selected.

2.4.4.5 Ending a CMT scan

i. Once the CMT scan was completed, and no further CMT scans were going to be performed at that time, the cell was disconnected from the goniometer, and cooling lines were removed. If the cell was to be reimaged another day to study hydrate growth over time, the cell was placed back in the ethylene glycol-water bath of the refrigerated circulator in a 45° angled orientation to maintain the hydrates that had formed in the cell.

ii. Further scans could be repeated using one of the above procedures

2.4.4.6 Ending a CMT Experiment

i. When CMT imaging of an experiment in the CMT cell was completed, the cell was vented into a fume hood. The cell was then cleaned out with water and allowed to dry for several hours prior to beginning another hydrate formation experiment.

ii. CMT data can be copied from the X2B computer to convert the .prj output file into 3D images.

2.4.4.7 Reconstructing CMT Data

i. To reconstruct the data, the .prj output file was opened using IDL Virtual Machine created by Exelis. An IDL routine created by Mark Rivers of the University of Chicago, convert_x2b_netcdf_display.sav, was utilized to convert the .prj file into a .volume file. This was accomplished by choosing 'Convert to netcdf' on the Convert X2B to netcdf menu, selecting the .prj file to be converted, and typing in the new name of the .volume file, as shown in Figure 2.12.

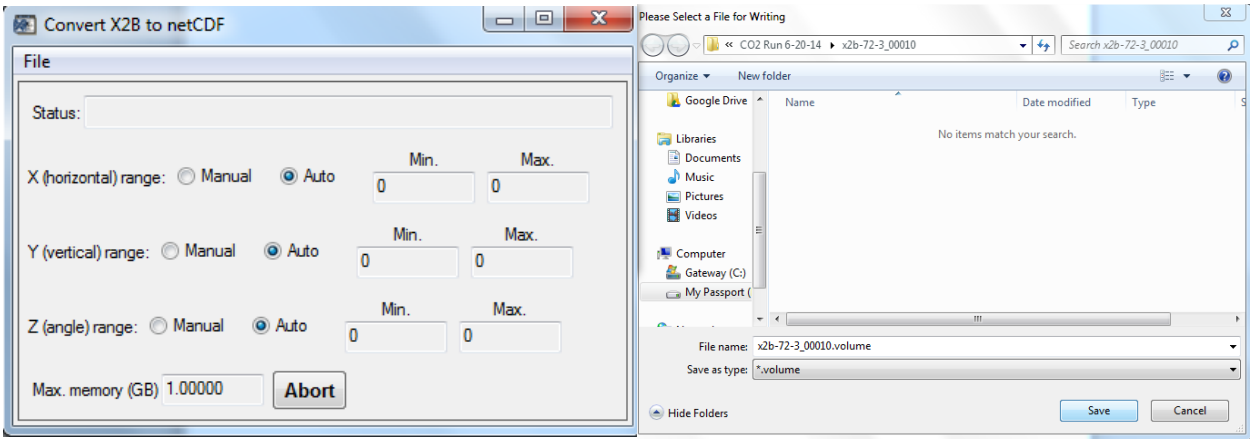

Figure 2.12: *IDL Virtual Machine convert_x2b_netcdf_display.sav routine to convert .prj files to .volume files*

ii. Once the program was complete and a .volume file was created, the .volume file was opened using a tomo_display.sav routine in IDL Virtual Machine. Once opened, the rotation center for the .volume file had to be determined. To do this, the value of the rotation center under the 'Reconstruct' heading was modified, and 'reconstruct slice' for slice 60 was attempted. Any value for the rotation center was initially chosen, and then based on how well aligned the slice reconstructed, the rotation center value was modified. When the rotation center chosen resulted in an image that looked well aligned, as in Figure 2.13(a), 'optimize center' with an optimize range of 10 and optimize step of 1 was performed. IDL extrapolates the best center for the data, which was the rotation center with the lowest 'image entropy' value, as shown in Figure 2.13(b).

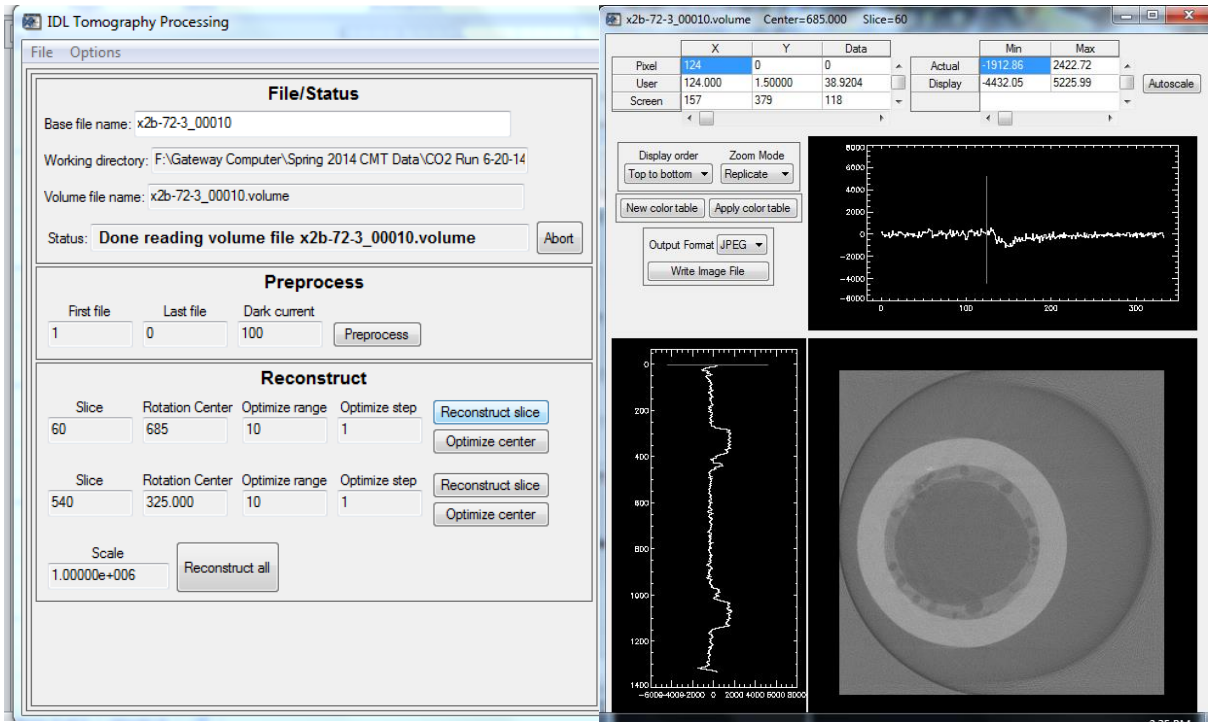

(a)

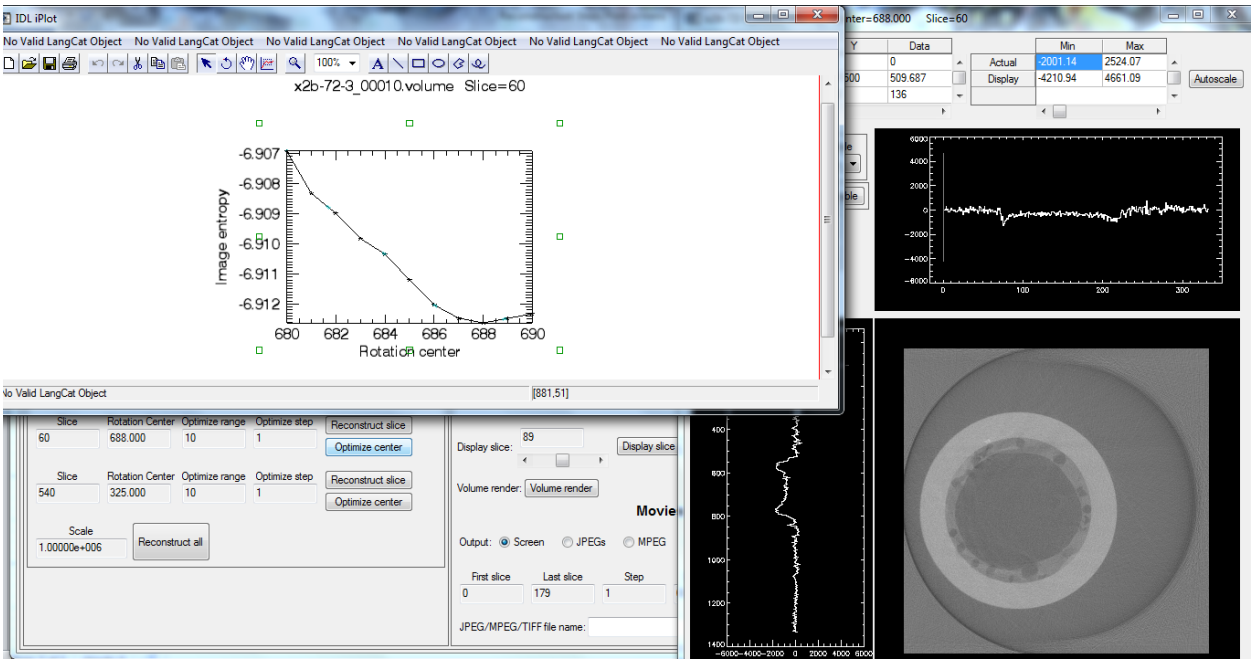

(b)

Figure 2.13: *IDL tomo_display.sav routine to (a) reconstruct an image slice to determine the rotation center and (b) to optimize the center to find the most ideal rotation center for the data.*

iii. To verify that the rotation center optimized for slice 60 also worked well for other slices, slice 540 was reconstructed at the rotation center value determined in step ii. Occasionally the best rotation center for these two slices was not the same; if that was the case, the average value of the best rotations centers for slices 60 and 540 was chosen.

iv. Once the same rotation center was input for both slices, 'Reconstruct all' was selected to reconstruct all of the image slices into a recon.volume file. This step usually took the most time (about 10-20 minutes).

v. Once the reconstruction was complete, the recon.volume file was opened on the same tomo_display routine screen. Under the 'Visualize' heading, the reconstructed slices were viewed by choosing 'display slice.'

vi. Under the 'Movies' heading, a movie showing all of the image slices, from the top image slice to the bottom image slice, could be viewed on screen. To be able to create 3D volume images, 'TIFF' and 'Make movie' were selected to save these image slices as individual tiff files.

vii. Next, the Drishti-Import program was opened. 'Files,' 'Load,' 'Files,' and 'Grayscale TIFF Image Files' were selected as shown in Figure 2.14(a). All image slices were highlighted and uploaded. This opened a screen displaying all of the image slices and a histogram of the gray values in all of the images (Figure 2.14(b)). Under 'Files,' the file was saved as a .pvl.nc file, and 'yes' was selected for all prompts asked.

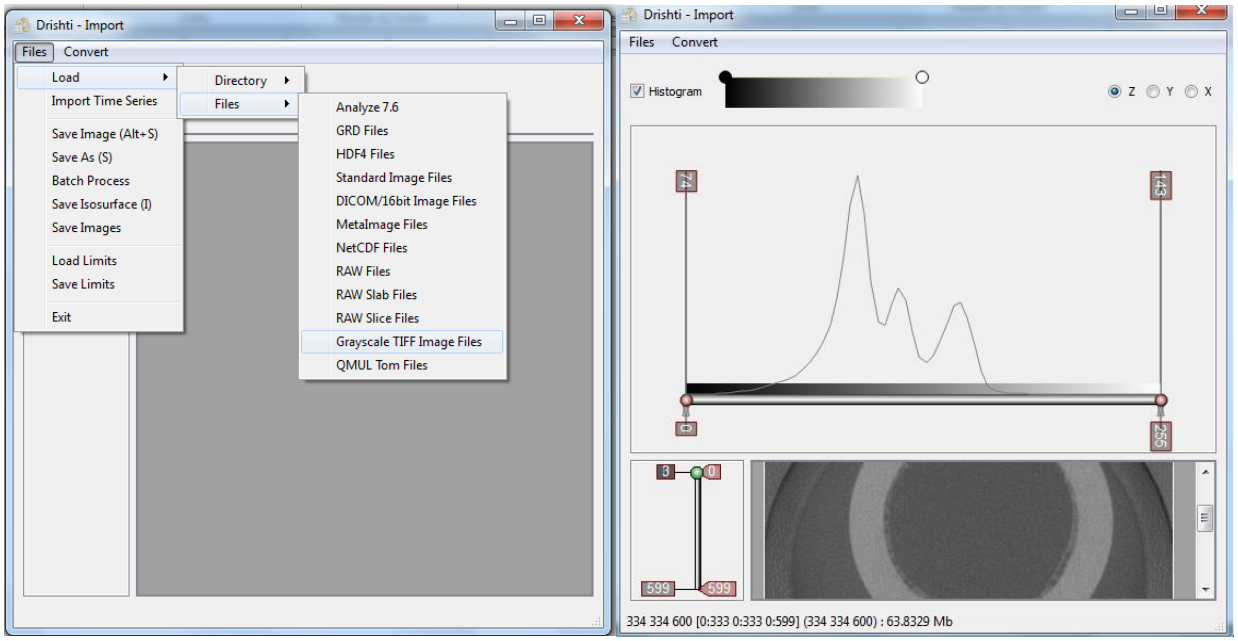

(a) (b)

Figure 2.14: *Drishti-Import program to (a) open all tiff files for a CMT scan and (b) display all image slices and the overall histogram for the data to create a pvl.nc file.*

viii. The Drishti program was next opened, and ‘File’ and ‘Load Volume,’ was selected to open the .pvl.nc file that was created in step vii. A 3D volume was opened as in Figure 2.15. The area of the 3D block was modified by moving the Xs on all six sides of the volume.

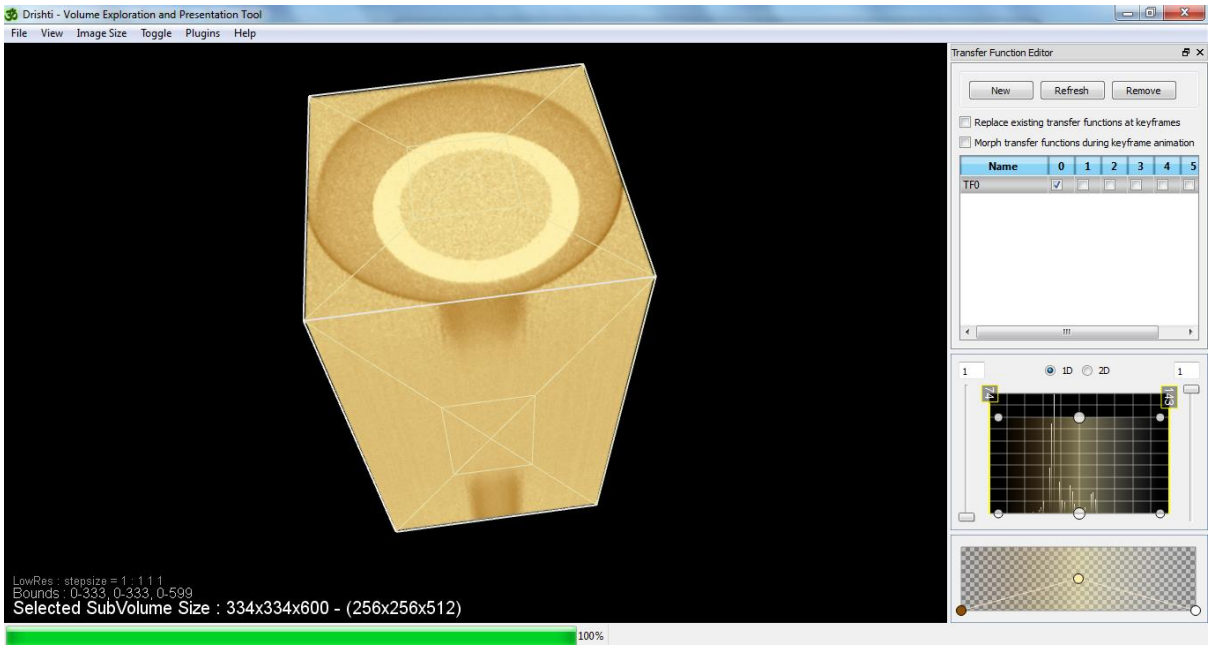

Figure 2.15: *Initial appearance of a 3D volume in Drishti*

ix. To better distinguish between the phases present in the cell, transfer functions were defined and edited using the ‘Transfer Function Editor.’ A ‘New’ transfer function was created for each phase present in the cell. To modify the colors of the transfer functions, the center dot in the checkered region underneath the 1D histogram peaks was double clicked to prompt a color palette. For each transfer function, the regions that the colored peaks of each transfer function highlighted in the 3D volume image were modified by moving the dots indicating the end points of the transfer function on the histogram peaks. This modification can be seen in Figure 2.16. Higher attenuating phases (aluminum) will be on the right side of the histogram, and lower attenuating phases (gases) will be on the left side. The peaks for gas and gas hydrates overlap, therefore the left side of the peak represents gas and the right side of the peak represents gas hydrates.

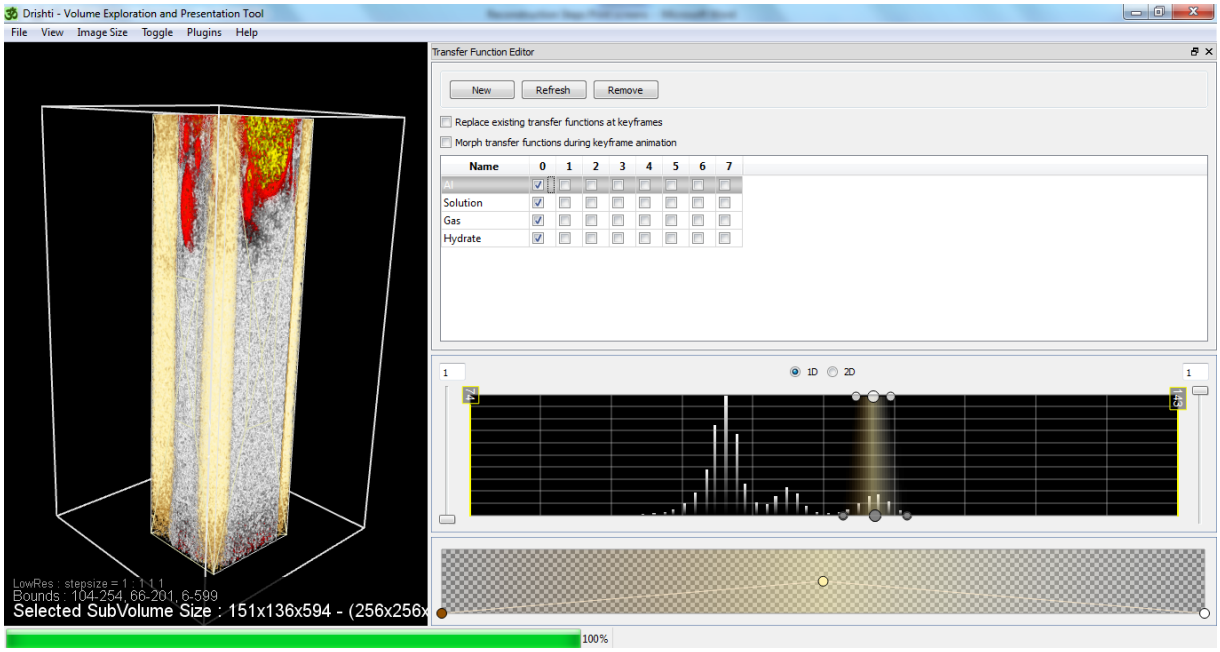

Figure 2.16: *Using transfer functions to define the phases present in the 3D volume*

x. Once each phase has been properly defined with a transfer function, the cursor was placed over the 3D volume image and F2 was pressed to view a higher quality version of the 3D volume, as shown in Figure 2.17(a). In Figure 2.17(a), sections colored beige are aluminum tubing, gray sections are solution, red sections are gas hydrates, and yellow sections are gas. To only show some of the phases present in the cell, the box next to transfer functions not to be shown was unchecked, as in Figure 2.17(b), where only the hydrate phase is shown in red. The red seen at the bottom of Figure 2.17(b) is an artifact of CMT imaging, so in this CMT scan, hydrates were found to coat the gas-liquid interface at the top of the cell.

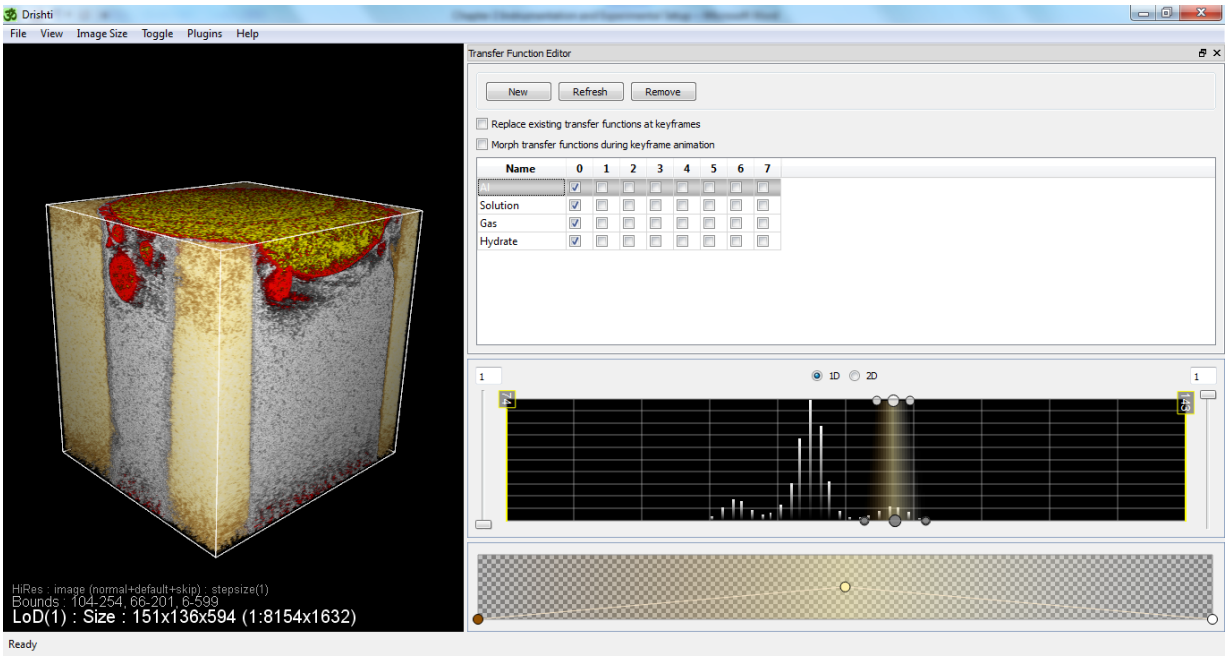

(a)

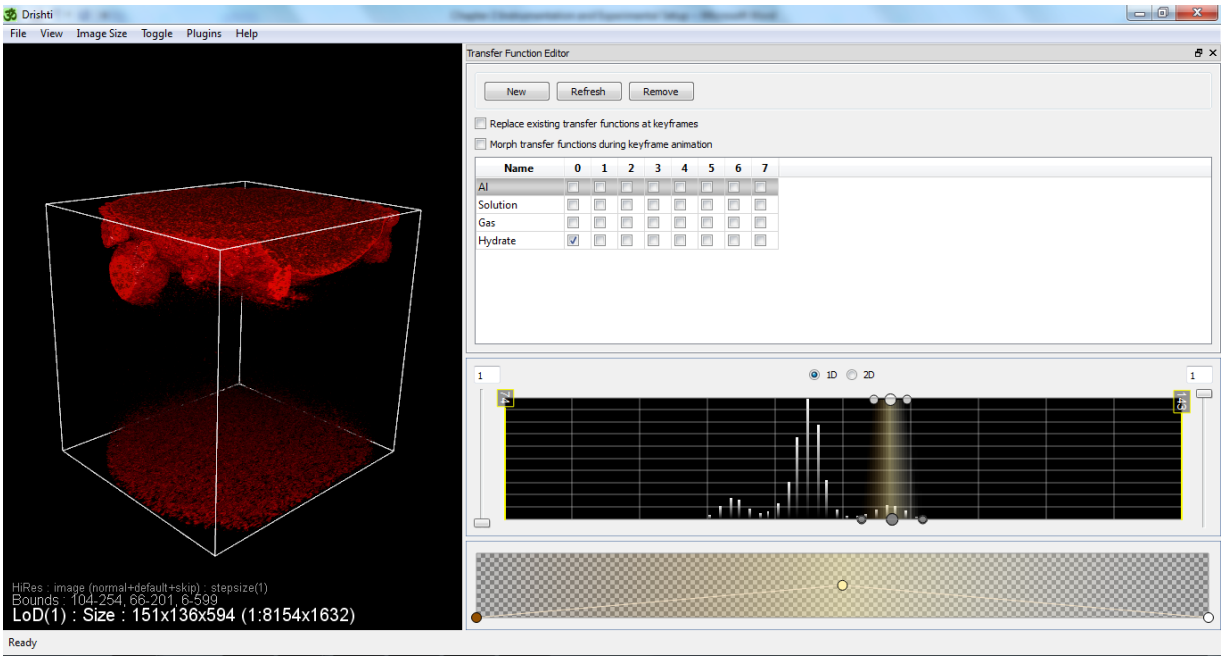

(b)

Figure 2.17: *(a) High quality version of a 3D volume (b) All phases except for gas hydrates (red) have been removed to better show hydrate structure*

xi. This project was saved in Drishti as an .xml file, and 3D volume images could be separately saved under various image file types. Movies of the cell rotating could be created in Drishti as well. An overview of the images produced during the steps to reconstruction CMT data is shown in Figure 2.18

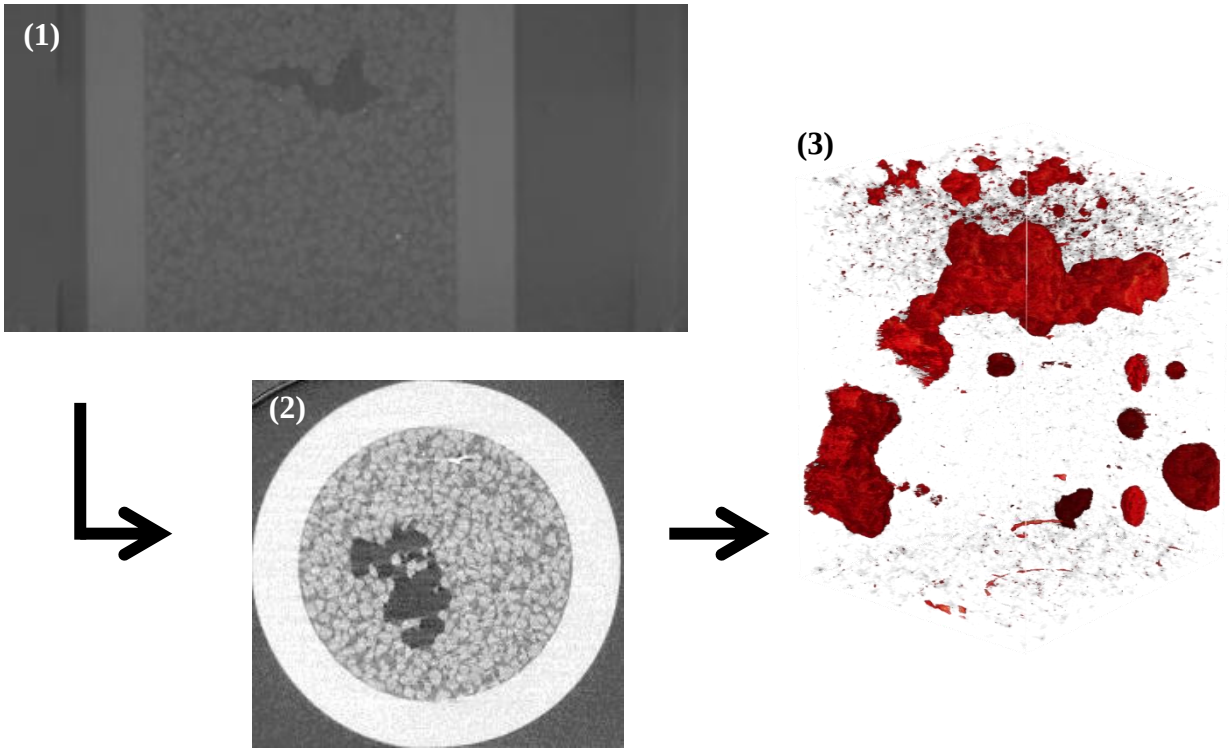

Figure 2.18: *The steps in CMT reconstructions. First, .prj files are converted into .volume files (1). Next, .volume files are converted into recon.volume files that can be converted into horizontal image slices (2). These image slices can be stacked to create 3D volume images (3).*

Chapter 3

3.0 Macro-Scale Baseline Experiments: Jerguson Cell[104]

A series of hydrate formation runs were performed to study the stability of CO_2 hydrates in a water-SDS solution at −1°C and to create a baseline for CO_2 and mixed CH_4-CO_2 hydrate formation. Table 3.1 lists experimental pressure-temperature conditions, theoretical yields, and actual percent conversions achieved. These high pressure, low temperature, and excess water conditions resulted in CO_2 hydrates that were observed from gas absorption and visual monitoring through the glass window on the cell. It is thermodynamically evident that gas hydrates formed as system pressure decreased below the pressure that the system should have remained at for the given temperature conditions.

Table 3.1: *Experimental Conditions and Results from Runs in the FISH Unit. (Liquid volume: 75 mL of 300 ppm SDS Solution)*

Run #	Gas	T_{exp}	Charge #	Initial Pressure	Pressure Drop (ΔP)	Measured Conversion	Maximum Possible Theoretical Conversion
		°C		Psig	Psi	%	%
1	CO_2	-1	1	425	132	30.0±0.5	63.6
			2	503	170	32.8±0.5	69.0
2	CO_2	-1	*	590	140	23.2±0.5	73.5
3	CO_2	-2	1	449	152	32.8±0.5	67.9
			2	512	44	8.4±0.6	71.7
4	CH_4-CO_2 (62%-38%)	-1	1	992	427	42.4±0.5	77.6
5	CH_4-CO_2 (62%-38%)	-1	1	1004	603	59.2±0.4	77.9

* Recharge after Run 1.

3.1 CO_2 Hydrate Formation (Runs 1-3)

To perform an experiment, CO_2 gas was bubbled through 75 mL of 300 ppm SDS solution up to a desired pressure, and then bath water cooling began to initiate CO_2 hydrate formation. In some runs, CO_2 gas was charged into the cell a second time to bring about further hydrate formation. A detailed experimental procedure can be found in Chapter 2.

The first gas charging in Run 1 led to a 30% conversion of CO_2 into hydrates after about 67 hours (Figure 3.1). After gas charging, the initial cell pressure drop from 425 psig to 390 psig was attributed to CO_2 solubilizing and gas cooling inside the cell. CO_2 is very soluble in water, and studies have found that CO_2 solubility is similar in 0.3 wt% SDS-water solutions, though CO_2 solubilizes in SDS-water solutions faster than in pure water solutions[105]. Any further pressure drop under isothermal conditions was attributed to hydrate formation. As it is possible that CO_2 hydrates were forming while CO_2 gas was still solubilizing in the hydrate forming solution, the conversions listed are likely to be under or overestimated, therefore all values reported provide an estimation of hydrate conversion. In this case, a total pressure drop of 132 psig was observed over a period of 55 hours at -1^{o}C. After cell pressure remained constant for 15 hours, the cell was repressurized to 503 psig. The pressure again dropped and resulted in a 33% conversion of CO_2 into hydrates. Figure 3.2 is an image taken after CO_2 hydrates were viewed at the bottom aqueous phase of the cell, about 96 hours into the experiment.

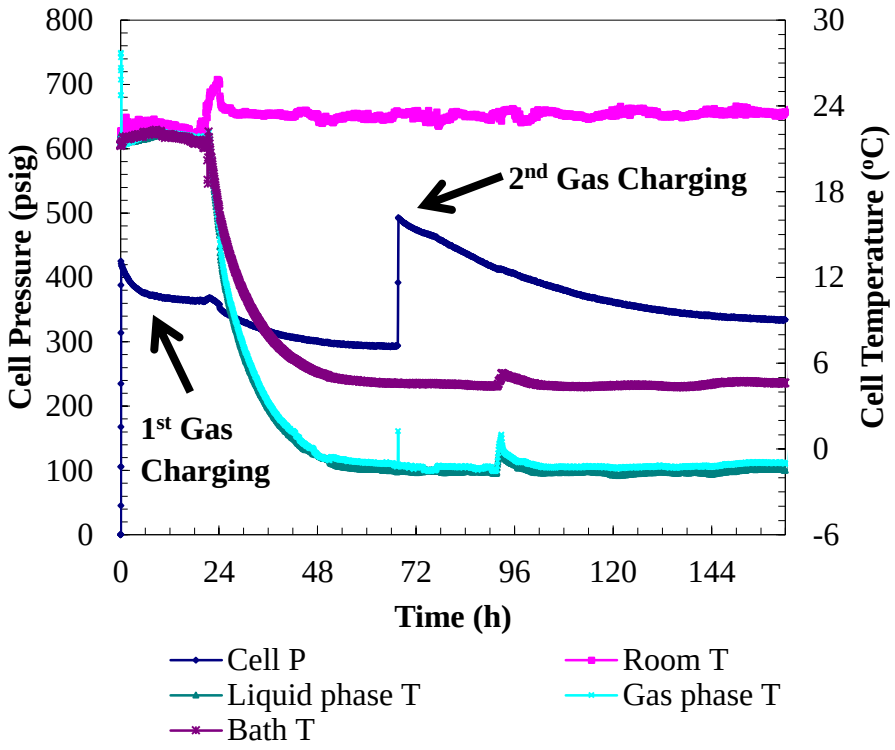

Figure 3.1: *Pressure and temperature versus time data plots during gas charging and hydrate formation in Run 1. Cell volume: 198 mL; Solution: 75 mL 300 ppm SDS; Bath T: 5°C; Actual cell T: −1°C; Initial charging P: 425 psig (charge #1); Charge #2: 503 psig.*

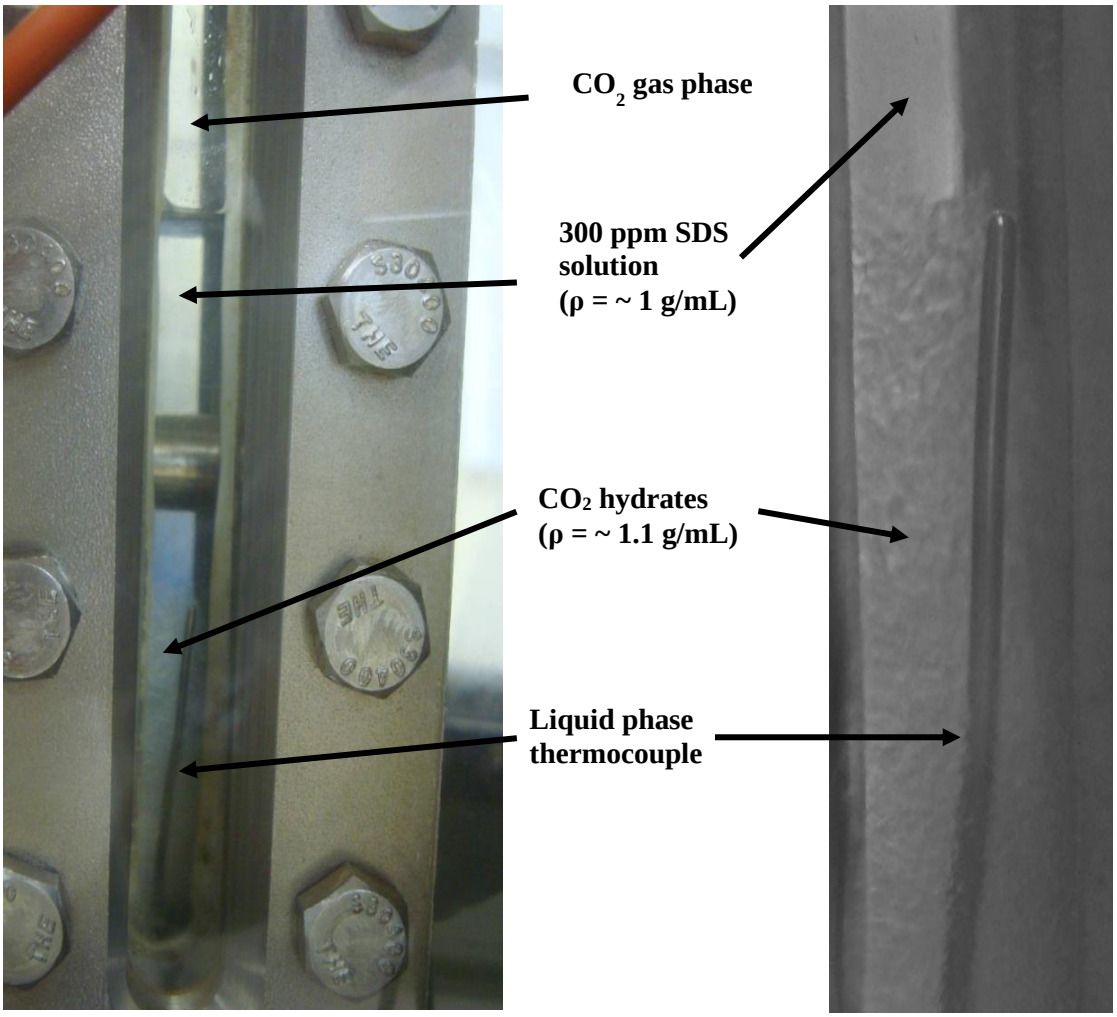

Figure 3.2: *CO_2 hydrates formed during Run 1. The image on the right is a close up of the hydrates shown in the reactor on the left.*

Figure 3.3 is a close up of dissociation cell pressure and temperature as functions of time for Run 1. The images shown in Figure 3.4 were taken during CO_2 hydrate formation and their thermally induced dissociation. The numbers shown in Figure 3.3 correspond to the lettered images in Figure 3.4 such that point 1 in Figure 3.3 represents pressure and temperature conditions for image (a) in Figure 3.4. During dissociation, gas bubbles were seen to form uniformly throughout the viewing area in ice pockets as hydrates reverted back to water and CO_2 was released, as shown in Figure 3.4(b), (c), and (d).

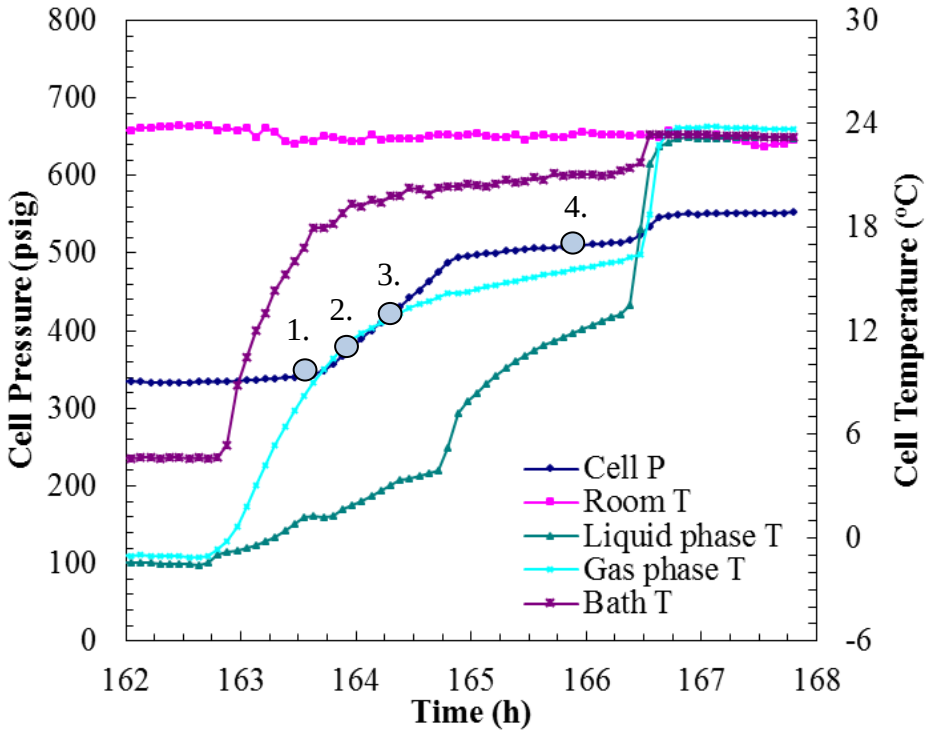

Figure 3.3: *Pressure and temperature versus time data plots during dissociation by thermal stimulation for Run 1.*

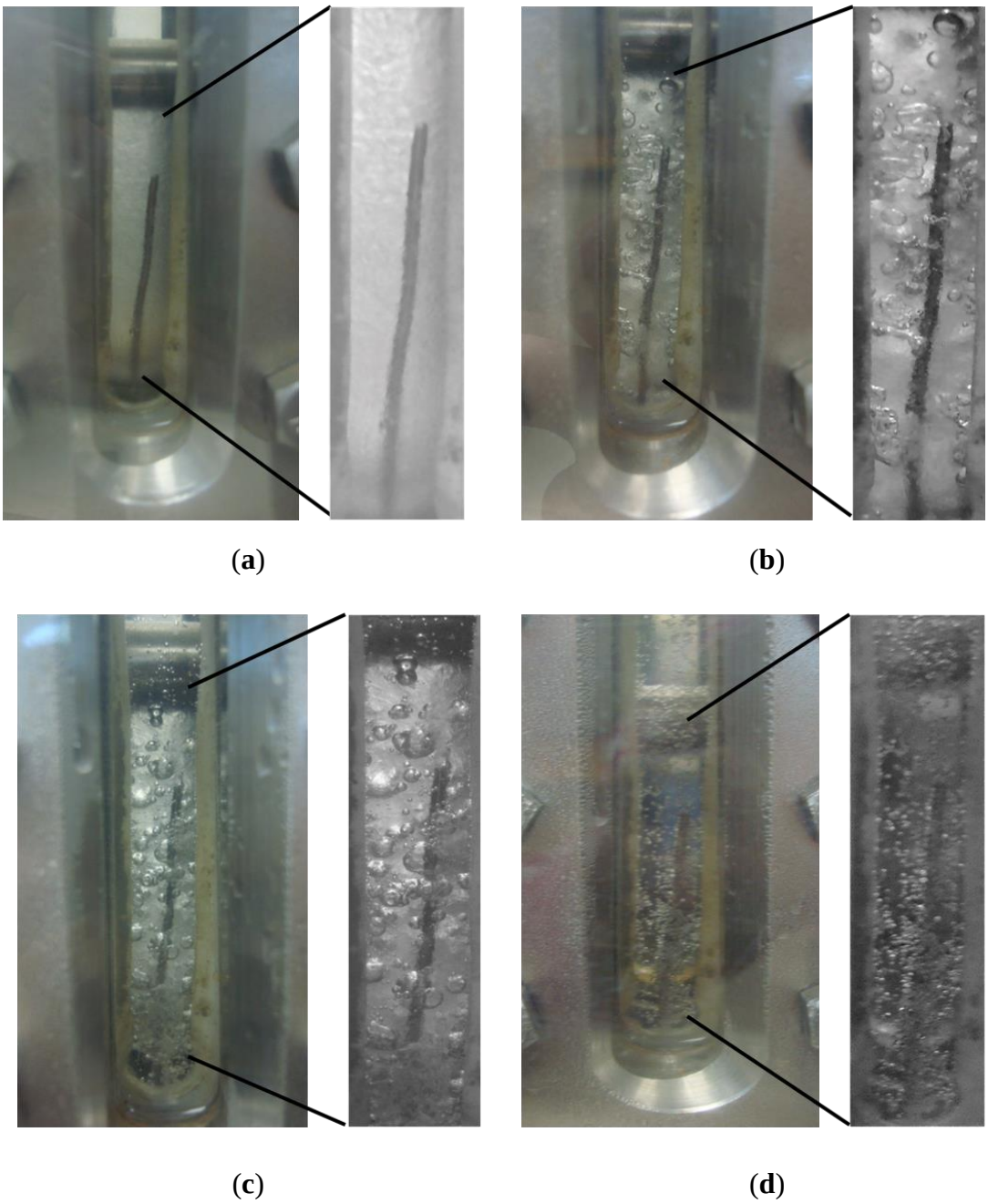

Figure 3.4: *Time resolved visual observations of the CO_2 hydrate phase during Run 1 at (**a**) 339 psig, 5.46°C; (**b**) 369 psig, 1.62°C; (**c**) 428 psig, 12.98°C; (**d**) 508 psig, 15.28°C. These letters correspond to the numbered pressure-temperature conditions shown in the dissociation plot of Figure 3.3 where point 1 in Figure 3.3 represents (a) shown above. CO_2 hydrates (density 1.1 g/mL) were observed to have an ice-like appearance in the aqueous phase at temperatures above the freezing point of the water-SDS solution.*

Run 2 was performed using the same CO_2 gas and 300 ppm SDS solution that was used in Run 1. Once the cell warmed up to room temperature and all CO_2 hydrates formed during Run 1 had dissociated (no more gas evolution was observed), 40 psi of additional CO_2 gas was added to the system to thoroughly mix the gas and liquid phases inside the cell. Over nine days, the initial cell pressure of 590 psig slowly dropped to 450 psig while the cell temperature was held at −1°C. At this time, the system was warmed to increase the temperature of the cell to 1°C to melt any ice that had formed and leave only CO_2 hydrates. A total pressure drop of 140 psig resulted in a hydrate conversion of 23%. Figure 3.5 shows pressure and temperature data for the entire Run 2, and Figure 3.6 details cell pressure and temperature during the thermally induced hydrate dissociation. Ice-like CO_2 hydrates, similar to those formed in Run 1, were seen, and images of hydrates before and during dissociation are shown in Figures 3.7(a) and (b). The numbers shown in Figures 3.5 and 3.6 correspond to the lettered images in Figure 3.7 such that point 1 in Figure 3.5 represents the pressure and temperature conditions for image (a) of Figure 3.7. CO_2 hydrates are still intact in Figure 3.7(c) as cell temperature has begun to rise, and most CO_2 hydrates have dissociated by Figure 3.7(d), where CO_2 gas is seen bubbling out of hydrate cages and the water-SDS solution.

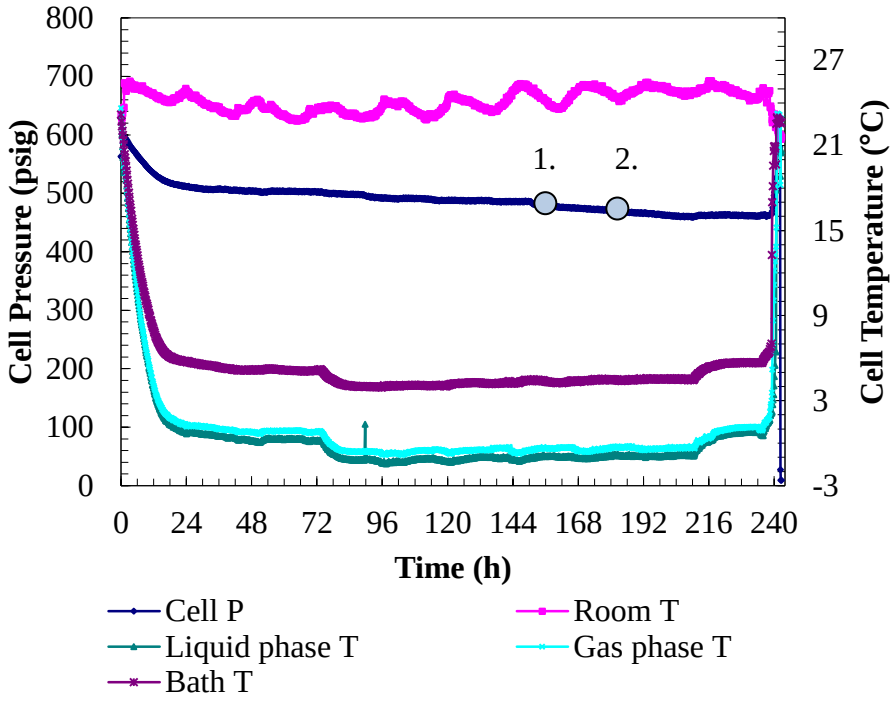

Figure 3.5: *Pressure and temperature versus time data plots during gas charging and hydrate formation in Run 2.*

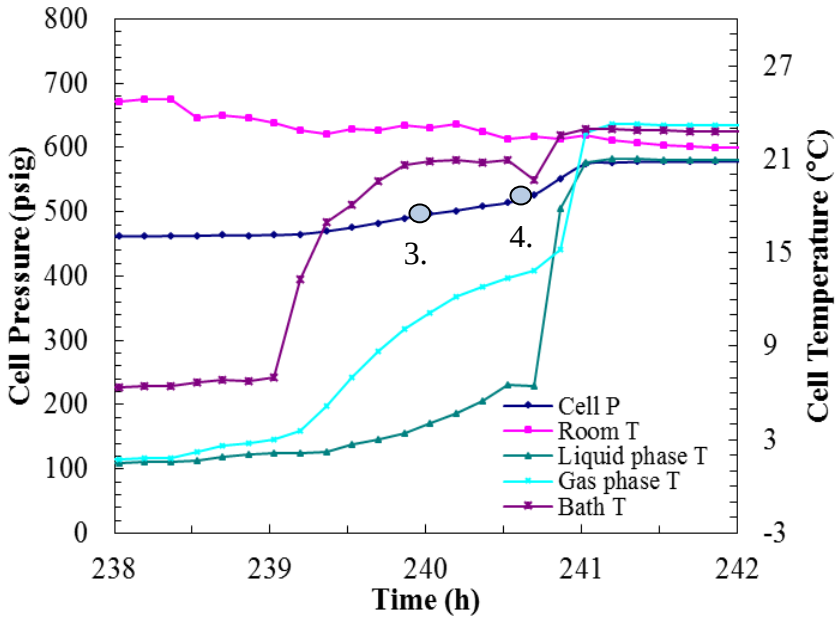

Figure 3.6: *Pressure and temperature versus time data plots during dissociation by thermal stimulation for Run 2.*

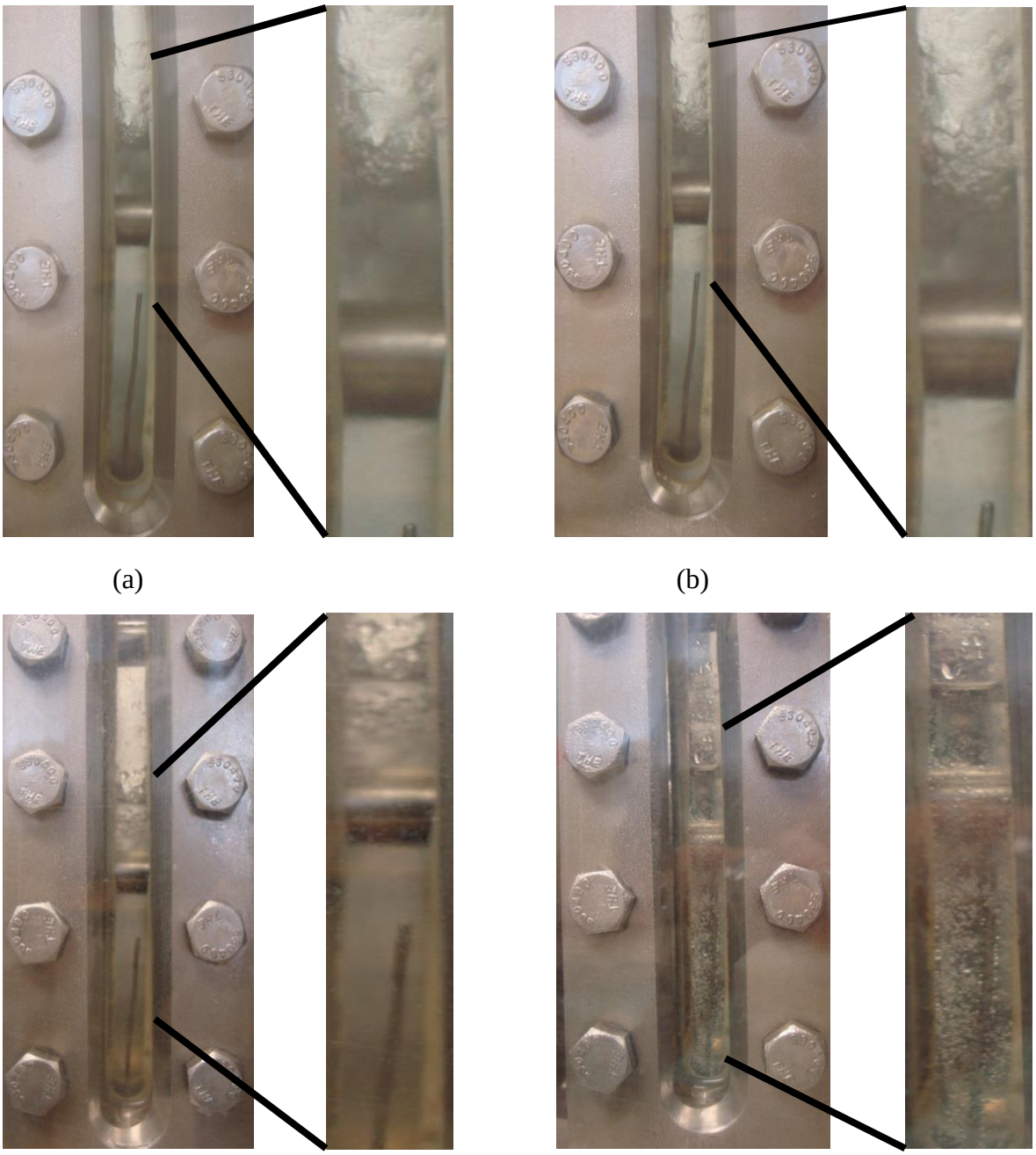

Figure 3.7: *Time resolved visual observations of the CO_2 hydrate phase during Run 2 at (**a**) 457 psig, -0.85°C; (**b**) 452 psig, 0.24°C; (**c**) 474 psig, 2.96°C; (**d**) 503 psig, 6.00°C. These letters correspond to the numbered pressure-temperature conditions shown in Figures 3.5 and 3.6 where point 1 in Figure 3.5 represents (a) shown above. CO_2 hydrates (density 1.1 g/mL) were observed to have an ice-like appearance in the aqueous phase at temperatures above the freezing point of the water-SDS solution.*

After the hydrate formation event in Run 2 was complete, the cell was depressurized. The SDS solution used in the previous run was left in the cell and used again in Run 3, and the cell was pressurized to 449 psig with fresh CO_2 at room temperature. After charging, the initial cell pressure dropped from 449 psig to 297 psig which was attributed to CO_2 solubility, gas cooling inside the cell, and hydrate formation. The first gas charging in Run 3 led to a 33% conversion of CO_2 into hydrates, and formation pressure and temperature are shown in Figure 3.8. A total pressure drop of 152 psig was observed over a period of 42 h at −2°C. After this time period, cell pressure remained constant over 30 h. The cell then was repressurized to 512 psig at −2°C. The initial pressure drop was due to CO_2 solubility and cell cooling but once isothermal conditions were attained, the pressure drop was attributed to hydrate formation. After a total of 144 h, the temperature of the cell was raised to 2°C to ensure hydrate rather than ice formation. When the temperature was raised above freezing, pressure continued to drop, indicating further hydrate formation until the cell was warmed to room temperature. This second charging event resulted in a hydrate conversion of 8%. Figure 3.9 details cell pressure and temperature during the thermally induced hydrate dissociation. Ice-like CO_2 hydrates, similar to the previous runs, were seen, and images of hydrates before and during dissociation are shown in Figure 3.10. The numbers shown in Figure 3.9 correspond to the lettered images in Figure 3.10 such that point 1 in Figure 3.9 indicates pressure and temperature conditions for image (a) in Figure 3.10. CO_2 hydrates are clearly seen in Figure 3.10(a) and (b), and as the cell temperature begins to rise, hydrates begin to dissociate in Figure 3.10(c), where the gas-liquid meniscus is no longer ice-like. In Figure 3.10(d), it is clear that there was a layer of water-SDS solution above some still intact CO_2 hydrates below the metal bar in the cell.

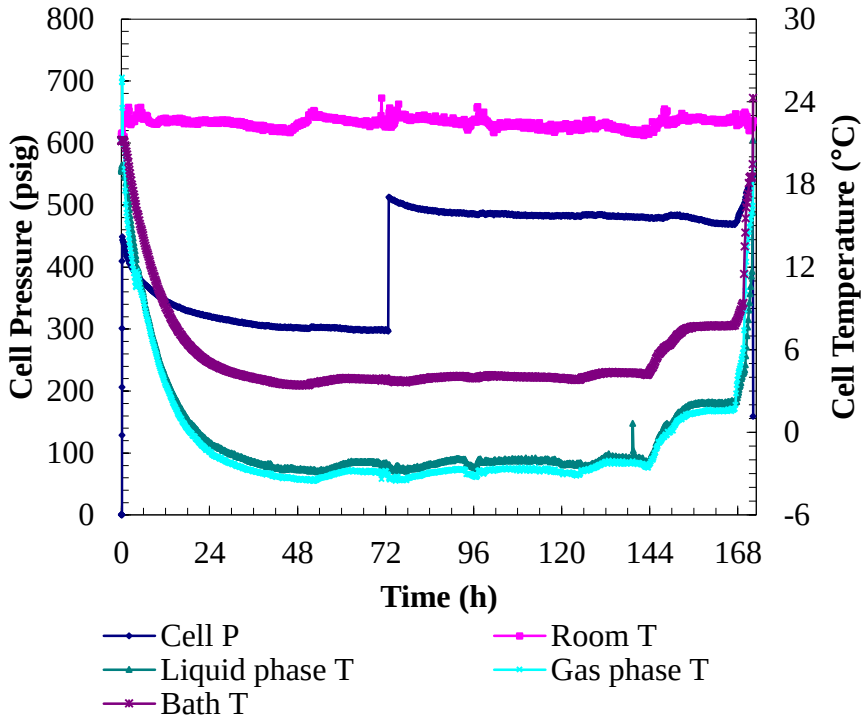

Figure 3.8: *Pressure and temperature versus time data plots during gas charging and hydrate formation in Run 3.*

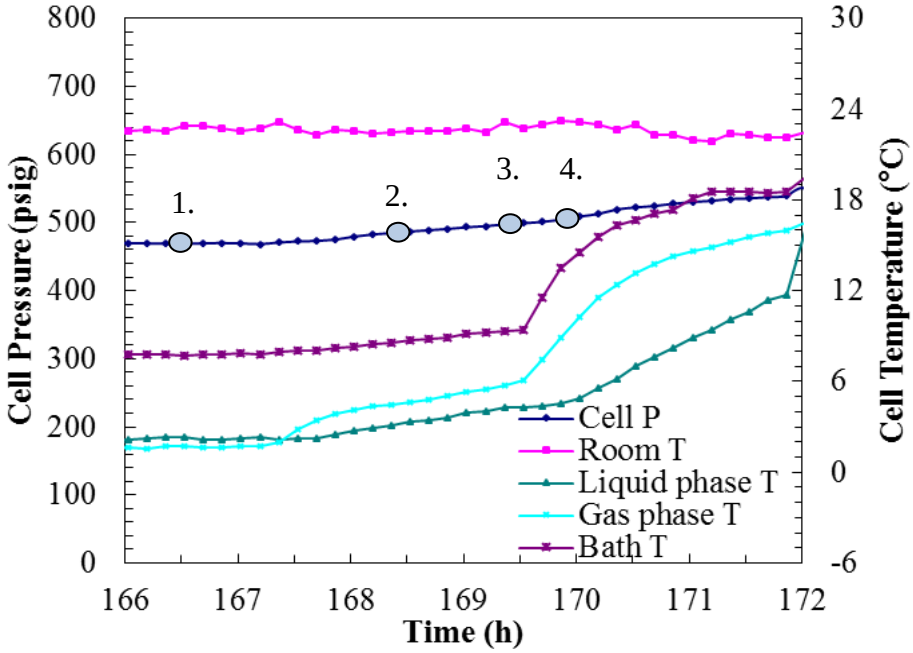

Figure 3.9: *Pressure and temperature versus time data plots during dissociation by thermal stimulation for Run 3.*

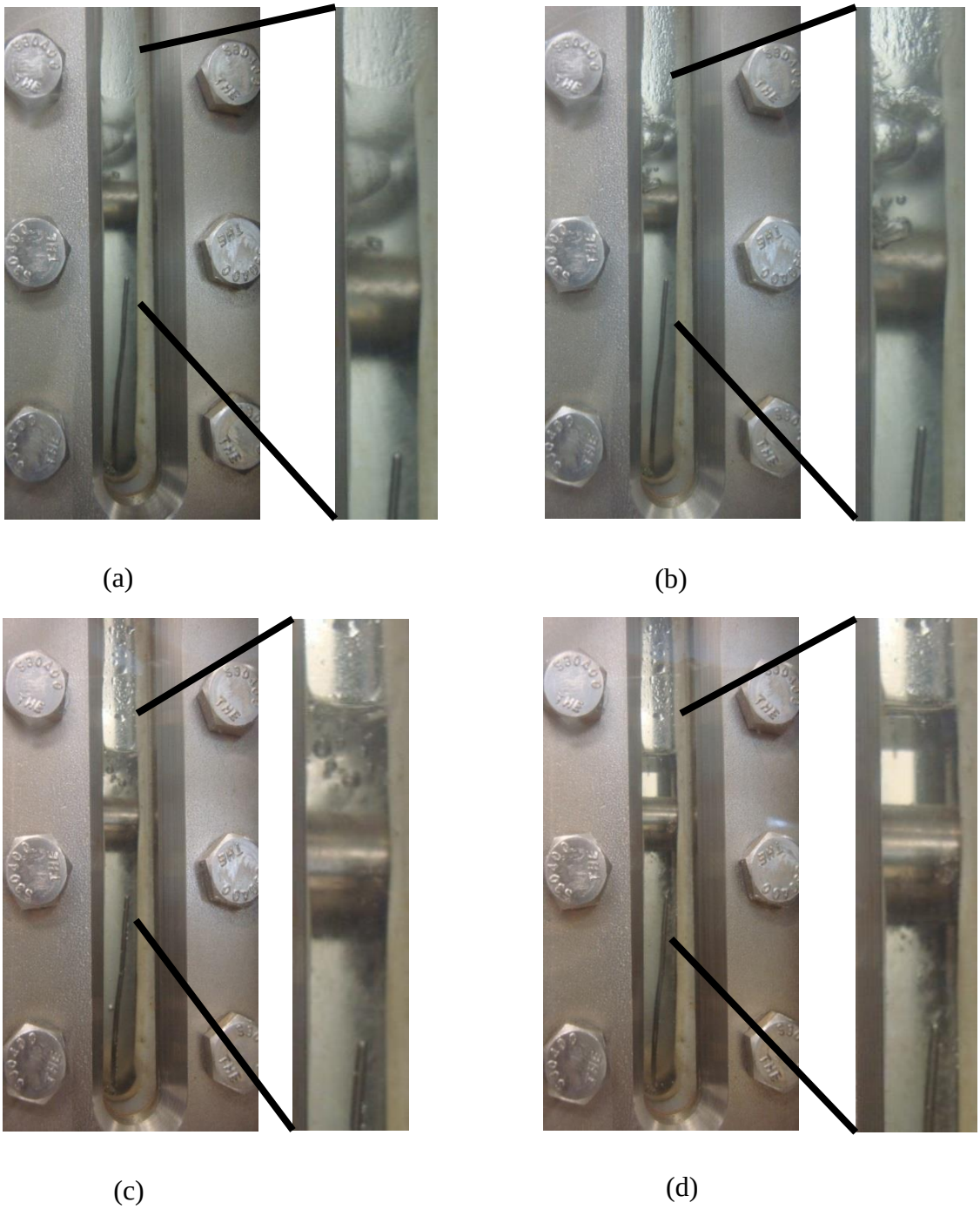

Figure 3.10: *Time resolved visual observations of the CO_2 hydrate phase during Run 3 at (**a**) 477 psig, 2.29°C; (**b**) 479 psig, 2.64°C; (**c**) 492 psig, 3.84°C; (**d**) 496 psig, 4.31°C. These letters correspond to the numbered pressure-temperature conditions shown in the dissociation plot of Figure 3.9 where point 1 in Figure 3.9 represents (a) shown above. CO_2 hydrates (density 1.1 g/mL) were observed to have an ice-like appearance in the aqueous phase at temperatures above the freezing point of the water-SDS solution.*

Recharging Runs 1 and 3 with CO_2 showed an additional 33% and 8% gas conversion into hydrates respectively. This is expected because these were water-excess systems where hydrate formation was limited by the amount of CO_2 gas in the cell. Initially, 0.16 to 0.23 moles of CO_2 were charged into the cell while 4.17 moles of solution were present. The ratio for this system of gas to solution is far below the 1:6 mole ratio of CO_2 to water needed for the full cage occupancy of CO_2 hydrates. The higher charging pressure was found to result in a higher percentage conversion during charge #2 in Run 1, though a low hydrate formation during charge #2 in Run 3 may be due to poor gas-liquid mass transfer. Hydrates are usually found to nucleate at the gas-liquid interface[106], but there is a potential for hydrates to nucleate at the gas-liquid interface and then accumulate in the aqueous phase due to density differences between the aqueous phase (1 g/mL) and the CO_2 hydrates (1.1 g/mL). Hydrates have also been hypothesized to nucleate in the aqueous phase by "local structuring" or "labile clustering"[107], as described in Chapter 1.

Of the runs with CO_2 (Runs 1–3), Run 2 achieved the least conversion (~23%) of CO_2 into hydrates as the solution and CO_2 gas previously used in Run 1 were reused to form hydrates. The SDS used as a promoter in these runs has a tendency to precipitate out of aqueous solutions. This was confirmed in a previous study by Lee *et al.*[108] in which a high concentration of SDS under higher pressures was found to precipitate out earlier than that at lower concentrations. The least conversion observed in Run 2 may be due to the precipitation of SDS after a cumulative 17 days for Runs 1 and 2. SDS precipitation seems to have inhibited the hydrate memory effect in Run 2. In addition, it has been shown that if the hydrate depleted solution reaches temperatures above 25[54] or 28°C[17], the memory effect will not occur. During dissociation, it is possible that the temperature of the cell reached 28°C.

3.2 CH_4-CO_2 Hydrate Formation (Runs 4-5)

After successfully forming CO_2 hydrates, runs were conducted to form hydrates from a CH_4-CO_2 mixed gas system. In Run 4, a fresh 300 ppm SDS solution was injected into the cell. Cell pressure was increased to 380 psig with CO_2 gas and then increased to 1000 psig with CH_4 gas, thus forming a mixed gas system. A more detailed experimental procedure can be found in Chapter 2. Hydrates were observed 2 days after cooling had begun, so the initial cell pressure drop from 992 psig to 810 psig was attributed to CO_2 solubility and gas cooling inside the cell at

−1°C. Any further pressure drop under isothermal conditions was attributed to hydrate formation. Upon initial formation, the cell temperature was increased to 2°C to thaw the ice phase to confirm hydrate stability and distinguish these hydrates from the ice phase. The cell was allowed to equilibrate and pressure remained constant around 750 psig for the following 4 days, after which a second drop in pressure was recorded, indicating further hydrate formation. This drop can be clearly seen at 228 h in the pressure and temperature versus time plot in Figure 3.11. After about 3 h of formation, the pressure remained constant for the next 24 h at 565 psig, after which the cell was warmed to room temperature. A simple recorded pressure difference and change in the number of moles of gas present in the cell at the end of formation were calculated to show that 42% of the gas in the system was converted into hydrates, though CO_2 and CH_4 hydrates were indistinguishable.

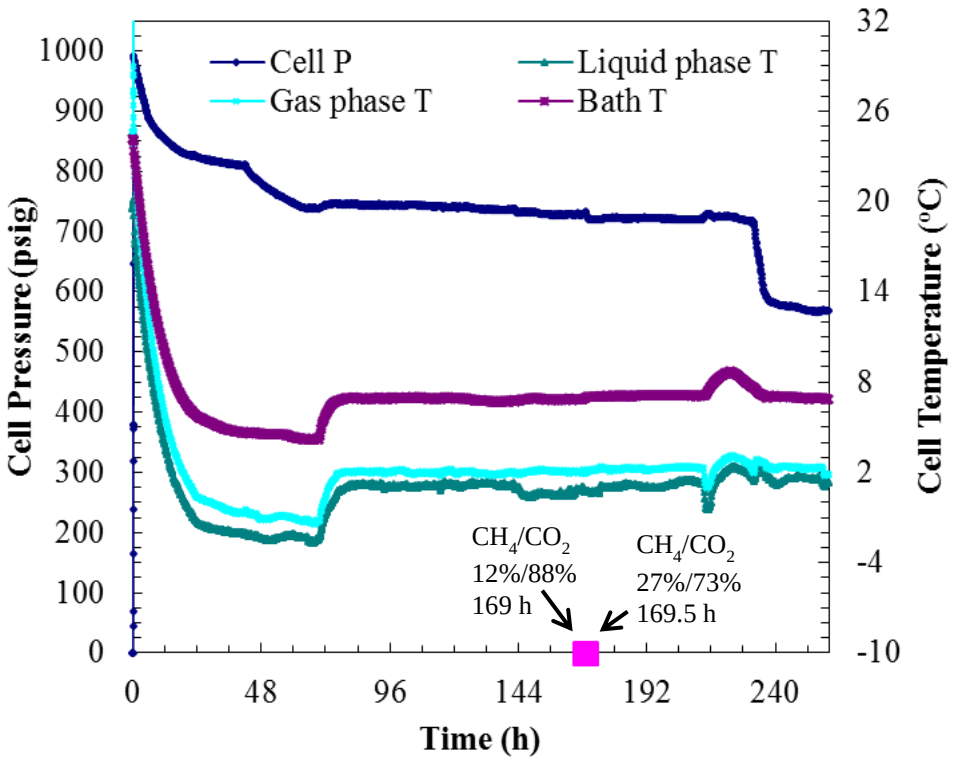

Figure 3.11: *A plot of pressure and temperature versus time during charging and hydrate formation in Run 4. Hydrate formation was achieved from a CH_4-CO_2 mixture. The embedded pink dots represent gas compositions measured by analyzing gas samples at corresponding times.*

To discern the identity of hydrates, several gas samples (0.5 mL) were taken from the vessel and analyzed during hydrate formation and dissociation. The GC data as % volume values for each gas are shown in Figures 3.11 and 3.12. In Figure 3.11, it was found that at 169 h when cell pressure was 748 psig and cell temperature was 1°C, the gas phase of the cell consisted of 12% CH_4 and 88% CO_2. Subsequently, 30 minutes later, under the same pressure and temperature conditions, another gas sample was taken and was found to be made up of 27% CH_4 and 73% CO_2. This indicates that initially, CH_4 hydrates formed, but as formation continued in the cell, more CO_2 gas replaced CH_4 in hydrates. Following the second pressure drop, three more GC gas samples were taken in Figure 3.12. The first gas sample, taken at 284.5 h under conditions of 568 psig and 1.4°C, showed the gas composition as 66% CH_4/34% CO_2. One hour later, a sample taken at 567 psig and 1.3°C showed the gas composition as 63% CH_4/37% CO_2. The last gas sample, taken 1.5 h after thermal stimulation had begun at 638 psig and 1°C, showed gas as 68% CH_4/32% CO_2. Similar concentrations of CH_4 and CO_2 before and after formation were measured with GC analysis, which confirmed similar relative percent conversions for both gases. Embedded in Figure 3.13 are images taken of the gas hydrates that formed in the cell over time. The numbered points in Figure 3.12 represent the conditions for the lettered images in Figure 3.13 where point 1 in Figure 3.12 corresponds to image (a) of Figure 3.13. Figure 3.13(a) and (b) show the CH_4-CO_2 hydrates that formed in the cell, and Figure 3.13(c) shows two hydrate chunks left in the cell in the middle of the thermally induced hydrate dissociation. In Figure 3.13(d), most gas hydrates have dissociated as gas bubbles can be seen.

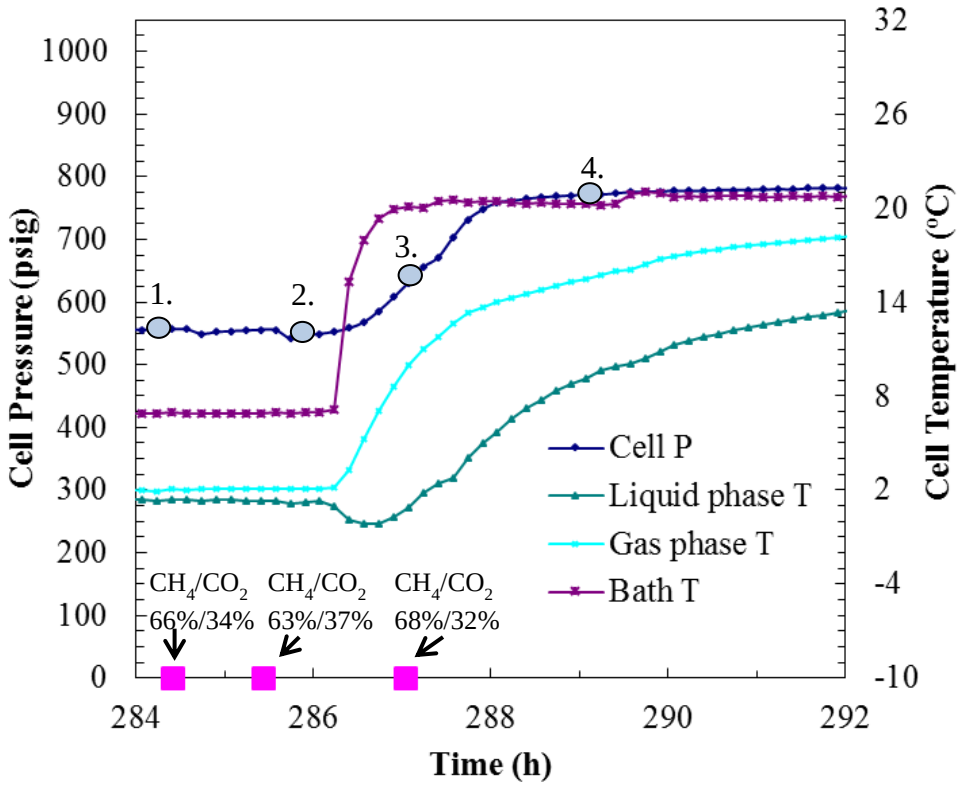

Figure 3.12: *Pressure and temperature against time during dissociation by thermal stimulation in Run 4. Hydrate formation was achieved from a CH_4-CO_2 mixture. The embedded pink dots represent gas compositions measured from gas samples analyzed in a Gow-Mac 580 series gas chromatograph.*

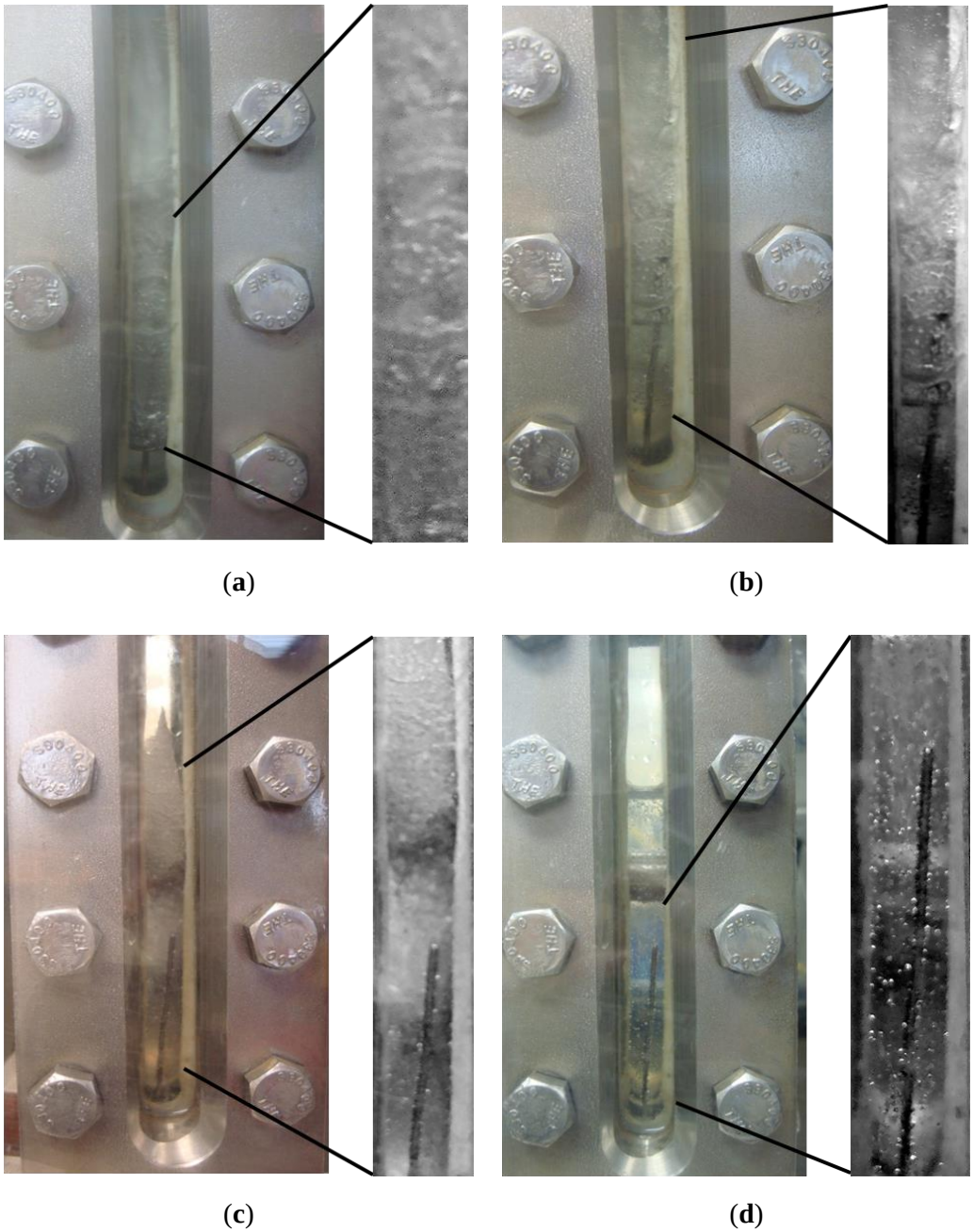

(**a**) (**b**)

(**c**) (**d**)

Figure 3.13: *Time-resolved observations of the CH_4-CO_2 hydrate formation at the end of formation and during dissociation in Run 4 at (**a**) 574 psig, 1.38°C; (**b**) 559 psig, 1.34°C; (**c**) 629 psig, 0.77°C; (**d**) 770 psig, 8.92°C. These pressure-temperature conditions correspond to the numbers shown in the dissociation plot of Figure 3.12 where point 1 in Figure 3.12 represents (a) shown above.*

Run 5 was performed using the same procedure as described for Run 4 where the cell was pressurized to 380 psig with CO_2 gas, followed by 1000 psig with CH_4 gas. Hydrates formed rapidly one day after cell cooling began. As shown in Figure 3.14, a pressure drop from 1004 psig to 880 psig due to CO_2 solubility and cooling to −1°C was observed over the first 24 h, followed by an abrupt pressure drop to 475 psig, which was attributed to hydrate formation. A pressure of 410 psig was maintained for two days, after which the cell temperature was increased to 2°C to confirm the presence of the hydrate phase. Once the cell was warmed above freezing, pressure remained stable at 565 psig for 24 h until the run ended. An overall conversion of 59% of gas into hydrates was achieved.

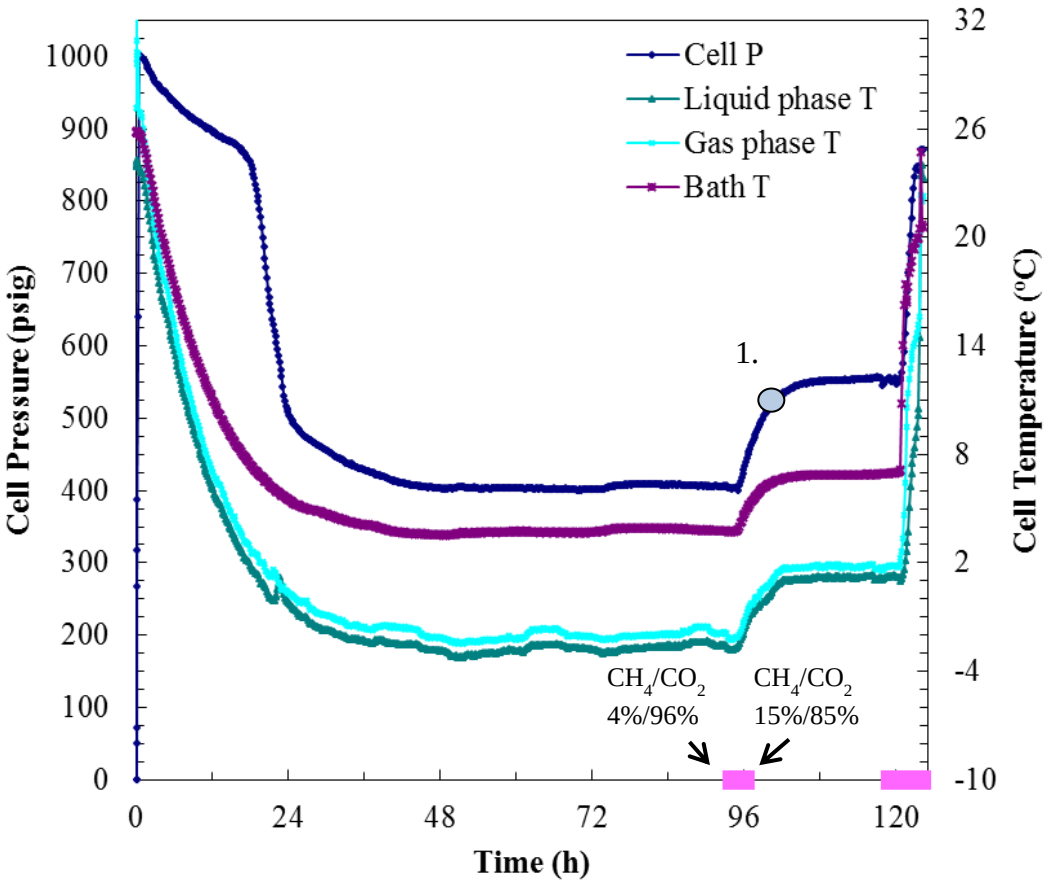

Figure 3.14: *A plot of pressure and temperature versus time during charging, formation, and dissociation from a CH_4-CO_2 mixture in Run 5. The embedded pink dots represent calculated gas compositions from GC data.*

As described for the previous run, several gas samples were analyzed during formation and dissociation to calculate individual % gas (CO_2 or CH_4) in the gas phase of the system. Figures 3.14 and 3.15 show pressure and temperature versus time plots and Figure 3.16 shows images of gas hydrate formation over time for Run 5. In Figure 3.14, a gas sample was taken 94 h after the experiment had begun at 417 psig and −2.5°C, and the gas composition was measured to be 4% CH_4/96% CO_2. Two hours later, at 406 psig and −2.7°C, the gas composition was 15% CH_4/85% CO_2. Similarly to Run 4, CH_4 hydrates were seen to form in the earlier stages of formation, and as time went by, more CO_2 hydrates formed. At this point, the cell temperature was raised above freezing to ensure that the ice phase was not present in the cell. Five GC samples were taken prior to and during dissociation as shown in Figure 3.15, which is a close up of day five of the experiment. The gas compositions under a pressure of 566 psig and temperature of 1.3°C, at various time intervals were as follows: (1) Sample #1, Time: 119 h: 59% CH_4/41% CO_2; (2) Sample #2: Time: 120 h: 66% CH_4/34% CO_2. At this point, thermal stimulation was begun to bring about the dissociation of formed hydrates. At 122 h under pressure and temperature conditions of 644 psig and 2.4°C, the gas phase was composed of 64% CH_4 and 36% CO_2. At 123 h, cell pressure was 811 psig at 7.7°C, and the corresponding gas analysis was 69% CH_4 and 31% CO_2. At 124 h, the pressure had increased to 860 psig as the temperature increased to 10.2°C but the gas phase composition was unchanged. The numbered points in Figures 3.14 and 3.15 represent pressure and temperature conditions in the cell when the lettered images in Figure 3.16 were taken, where point 1 in Figure 3.14 corresponds to image (a) of Figure 3.16. It is clear that icy cage shaped hydrate structures are seen in Figure 3.16(a) and (b). In the middle of thermally induced hydrate dissociation, hydrates shown in Figure 3.16(c) still retained some structure, but gas bubbles are seen to be evolving from the hydrates. Upon total hydrate dissociation in Figure 3.16(d), no hydrate structures can be seen as gas bubbles are being emitted from the water-SDS solution.

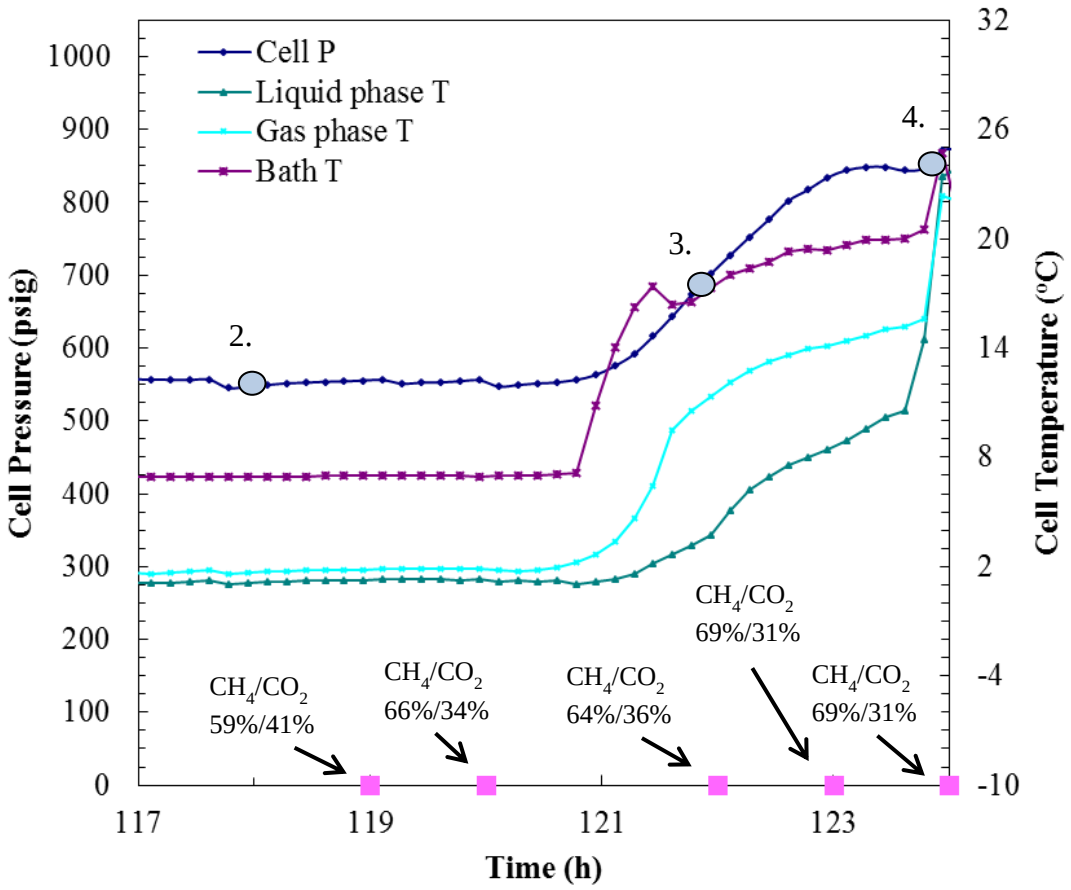

Figure 3.15: *A close-up view of hydrate dissociation by thermal stimulation during Run 5. The embedded pink dots represent calculated gas compositions from GC data.*

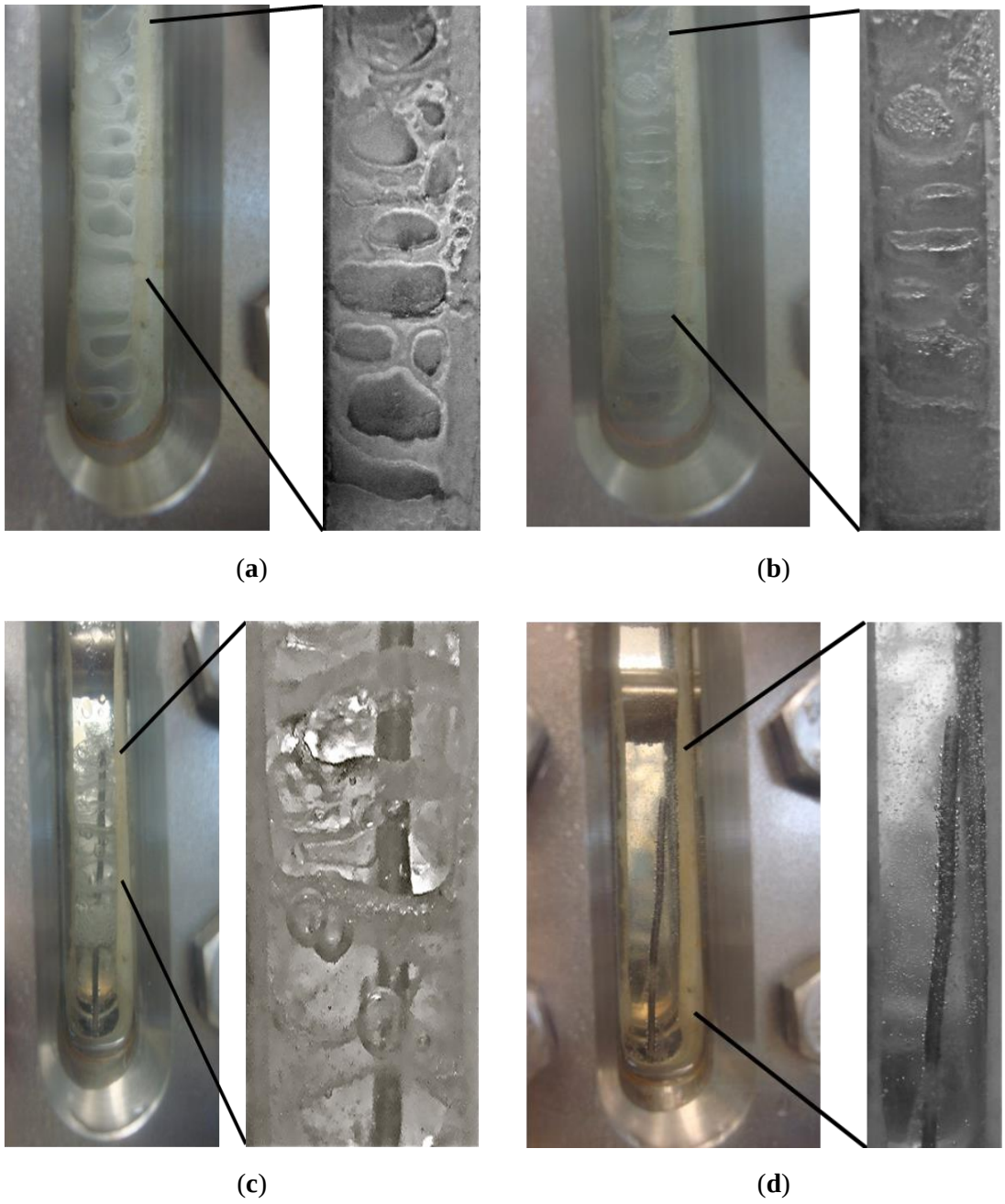

(**a**) (**b**)

(**c**) (**d**)

Figure 3.16: *Time resolved visual observations of the CH_4-CO_2 hydrate phase at the end of formation and during dissociation for Run 5 at: (**a**) 460 psig, −1.05°C; (**b**) 564 psig, 1.24°C; (**c**) 635 psig, 2.44°C; (**d**) 848 psig, 10.25°C. These pressure-temperature conditions correspond to the numbers shown in the formation and dissociation plots of Figures 3.14 and 3.15 where point 1 in Figure 3.14 represents (a) shown above.*

The hydrate formation runs with 62% CH_4/38% CO_2 gas mixtures resulted in gas conversions as high as 42% and 59%. Hydrates from the CH_4-CO_2 mixture were found to grow uniformly throughout the cell as a massive structure. A solid structure in the form of hydrates was visually observed on the entire the viewing glass (1/2" × 12"). Dissociation was also observed randomly throughout the hydrate phase. Both CO_2 hydrates and CH_4 hydrates were indistinguishable in terms of morphology to the naked eye, so it is unknown if CO_2 and CH_4 hydrates or mixed gas hydrates formed.

It is apparent from the completed runs in the FISH unit that facile formation of both CO_2 and CH_4 hydrates was observed under the pressure and temperature conditions used. It was also found that, especially in the early stages of hydrate formation, a majority of the gas that was stored in hydrates was CH_4. Seo *et al.* (2001)[109] observed that at lower pressures, CO_2 preferentially formed hydrates. Uchida *et al.* (2005)[110] formed CH_4-CO_2 hydrates and found that when the gas phase consisted predominantly of CO_2, CH_4 preferentially formed hydrates in the early stages of hydrate formation. The observed data are consistent with these observations.

3.3 Conclusions

A facile formation of CO_2 hydrates was observed at high pressures and temperatures above freezing in a system in which water was in excess. It is important to note that duplicate experiments were not performed to replicate hydrate formation results. Due to the stochastic nature of hydrate formation and dissociation, many of the experiments performed were focused on understanding the nature of hydrate growth under different experimental conditions. The hydrates formed in these experiments were found to accumulate in the aqueous phase at the bottom of the cell and not at the gas-liquid interface. The liquid interface was observed to be intact throughout the hydrate formation phenomenon, which indicates that hydrates may have nucleated in the bulk solution or at the gas-liquid interface and then accumulated in the aqueous phase due to density differences.

Hydrate formation time was found to vary from 17 h to seven days. A conversion up to 33% of CO_2 gas into hydrates was measured when SDS, a known hydrate former, was present. The overall CO_2 hydrate yield could be increased with multiple gas charges though subsequent hydrate yield was low. This may be explained by the decreased concentration of SDS in the solution as SDS tends to precipitate out after single use. A finding that CH_4-CO_2 gas mixtures

that are CH_4-rich yield a higher concentration of CH_4 hydrates is contradictory to many previous findings, though these studies did not have gas mixtures made of predominantly CH_4. It was also found that while initially the gas phase of the cell was predominantly CO_2, as time went on, the concentration of CH_4 in the gas phase increased, indicating that CH_4 and CO_2 exchanged in the hydrate form, which is in agreement with previous studies.

Chapter 4

4.0 Macro-Scale CH_4-CO_2 Exchange Experiments[111]

A series of experiments were performed to study the exchange of CH_4 and CO_2 in gas hydrates on a macro-scale. Five experiments, as detailed in Table 4.1, were performed in artificial seawater[100] in the Jerguson reactor to study CH_4 hydrate stability upon CO_2 gas injection and to study CO_2 hydrate stability upon CH_4 gas injection. The cell capabilities allowed us to: 1) measure the percentage of hydrates formed in the system, 2) visualize hydrate formation and observe their morphology, and 3) measure the composition of free gas above the liquid phase to quantify the mixed CH_4-CO_2 system. More details on the Jerguson reactor can be found in Chapter 2.

Table 4.1: *Operating Conditions for the CH_4-CO_2 Exchange Runs in the 200 mL Jerguson Cell*

Run #	Gas	Host Media	Water Source	$P_{initial}$ at T_{bath} psig	T_{bath} °C
6	CH_4, followed by CO_2	None	Artificial Seawater	918	4
7	CO_2, followed by CH_4	None	Artificial Seawater	398	4
8	CH_4, followed by CO_2	Ottawa Sand	Artificial Seawater	945	4
9	CO_2, followed by CH_4	Ottawa Sand	Artificial Seawater	451	6
10	CH_4, followed by CO_2	Ottawa Sand	Artificial Seawater	950	3

The first two experiments used only 75 mL of artificial seawater while the last three used 38 mL of artificial seawater and 104 g of 110 μm diameter Ottawa sand. The cell was pressurized with gas flowing through the bottom such that the entering gas bubbled through the artificial seawater. The cell was initially charged with either CO_2 or CH_4 gas, and after hydrates started to form, the second gas was injected into the cell. For example, by initially forming CH_4 hydrates, and then injecting CO_2 gas, CH_4-CO_2 exchange in hydrates could be monitored. In experiments with preformed CH_4 hydrates, the pressure in the cell was reduced by depressurizing the cell below 560 psig prior to CO_2 injection to ensure that CO_2 would be injected as a gas rather than a liquid. We also conducted two runs that involved the formation of CO_2 hydrates followed by a charge with CH_4 gas to allow for monitoring the stability of CO_2 hydrates if they were to come into contact with CH_4 gas, as could potentially occur in a free CH_4 gas zone or if CO_2 hydrates formed near a CH_4 plume in the ocean. Gas samples for GC analysis were taken periodically to monitor the composition of the gas phase of the system. During the depressurization cycle, the system pressure was lowered in multiple steps wherein during each step the pressure was reduced a few hundred psig, and then the system was allowed to stabilize for several minutes to an hour prior to subsequent pressure reduction. This process was repeated until the system was totally depressurized. A detailed experimental procedure is listed in Chapter 2.

The known mole stoichiometry of water/gas in CH_4 hydrate and CO_2 hydrate are 5.75/1 and 6/1 respectively. The unit was operated in either water-excess or gas-excess mode, depending on the mole ratio of water/gas added to the system. These data were used to calculate theoretical maximum gas to hydrate conversion values from which the extent of hydrate saturation was calculated by the gas consumed during a given run.

4.1 Baseline Runs: No host Ottawa Sand (Runs 6-7)

In Run 6, 75 mL of freshly prepared artificial seawater was syringed into the Jerguson cell, and the cell was pressurized to 1010 psig with CH_4 gas at room temperature and then cooled until the bath temperature was about 4°C. After several days, an observed pressure drop of 285 psig was attributed solely to hydrate formation. After repressurization to 872 psig with CH_4, the pressure dropped to 747 psig. Together, total gas consumed corresponded to 44%$\pm$0.7 of the gas

in this excess-water system after two gas charges. At this point, the cell was switched to CH_4-CO_2 exchange mode by depressurization to 401 psig CH_4 and was then pressurized with CO_2 gas three times until cell pressure increased to 660 psig, resulting in instant gas hydrate formation. This was necessitated by the fact that at partial pressures above about 560 psig, CO_2 is in the liquid phase. The data are consistent with instantaneous CO_2 hydrate formation upon CO_2 charges, indicating that the initial CH_4 hydrate formation facilitated CO_2 hydrate formation, possibly due to the memory effect[112]. The hydrate memory effect states that hydrate induction times are reduced when hydrates are formed using water in which gas hydrates have previously dissociated. While there is no discussion of the hydrate memory effect on gas hydrate formation from two different gases, it is likely that the presence of CH_4 hydrate cages facilitated fast CO_2 hydrate formation.

Figure 4.1 shows images of formed mixed gas hydrates over time. GC samples taken showed > 99% CH_4 (< 1% CO_2) in the gas phase, and these readings remained essentially unchanged over the next 16 hours. Over the following 2 hours, the formed gas hydrates were dissociated by multi-step depressurization. Figure 4.2 shows the gas composition in the cell and cell pressure over time. The amount of CO_2 in the gas phase increased sharply as hydrates dissociated, until it maximized at 95%. Over the next 1.5 hours, the percentage of CO_2 in the gas phase decreased to 56% while the percentage of CH_4 present increased. After this time, the percentage of CO_2 began to increase again.

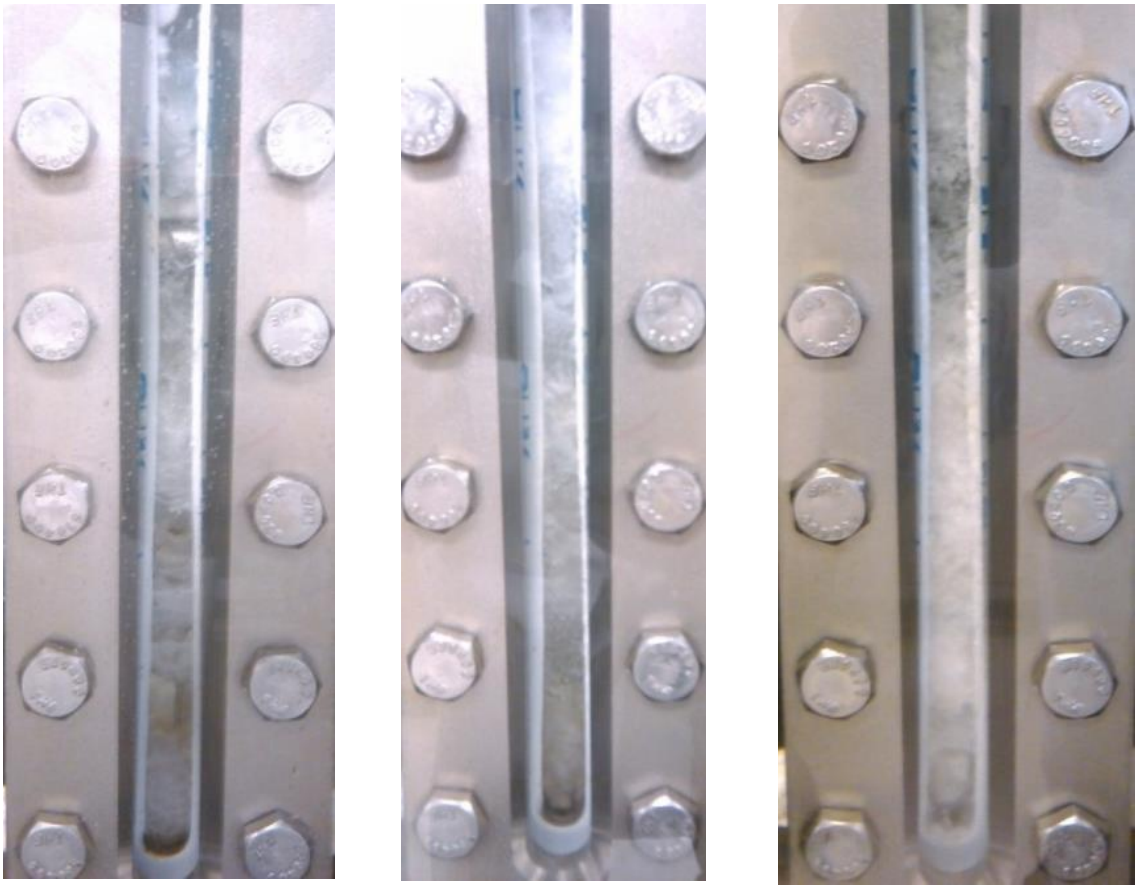

	1	2	3
Time Elapsed after Cooling (h)	288	295.7	312
Pressure (psig)	748	638	585
Temperature (°C)	4.5	4.5	3.2
Gas Composition (GC Analysis)	CH_4	CH_4 only, no gas-phase CO_2 was detected	99% CH_4 1% CO_2

Figure 4.1: *Time-resolved visualization of hydrates in the Jerguson cell during Run 6, where hydrates were found to fill the entire viewing area of the cell. The system was initially pressurized to 1010 psig with CH_4 at 25°C, and then cooled to 4°C. (1) Though hydrates began forming at 120 h, this image was taken at 288 h. Prior to this image, at 193 h the cell was repressurized with CH_4 and further hydrates were formed. (2) Taken at 295.7 h. Prior to (2), at 290.2 h, the cell was depressurized to 401 psig and then repressurized to 649 psig with CO_2. CO_2 was charged three times. (3) Taken at 312 h. After this image was taken, the cell was fully depressurized to dissociate remaining hydrates.*

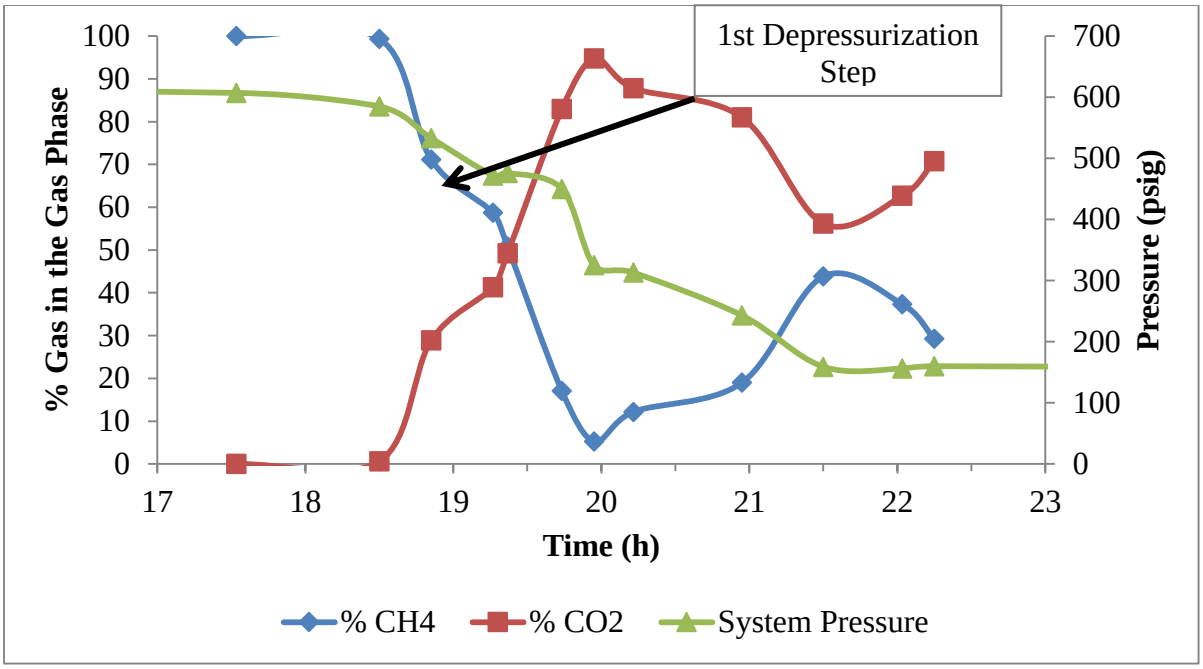

Figure 4.2: *Plot of the composition of CH_4 and CO_2 in the cell over time. Cell pressure versus time after CO_2 injection is also plotted, and the temperature of the cell was -1.7 to 6.4°C. As system pressure was decreased, the concentration of CO_2 in the gas phase increased drastically, until the gas composition evened out as system pressure decreased.*

Hydrates existed as cell pressure decreased, and at 243 psig, hydrates were seen to be dissociating. Table 4.2 lists the temperatures and partial pressures of the system for CH_4 and CO_2 as the system was depressurized in steps. Figure 4.3 plots the partial pressures of CH_4 and CO_2 from Table 4.2 versus temperature. CH_4 and CO_2 hydrate stability curves in artificial seawater are also plotted, where CH_4 hydrates are stable above the green CH_4 hydrate stability line and CO_2 hydrates are stable above the purple CO_2 hydrate stability line. The partial pressures of CH_4 and CO_2 gas in the system affect the composition of the mixed gas hydrates that form[113]. It is clear that based on partial pressures, neither CH_4 nor CO_2 hydrates should have been stable for many of the system's pressure and temperature conditions, yet gas hydrates were seen until the total system pressure was below 300 psig. This seems to indicate that the total system pressure might have a larger effect on the stability of mixed gas hydrates than the partial pressures of CH_4 and CO_2.

Table 4.2: *Partial Pressure Data during the Stepwise Depressurization of Run 6*

P_{total}	Partial P CH_4	Partial P CO_2	$T_{sediment}$
psig	**psig**	**psig**	**°C**
641	641.0	0.0	6.4
643	643.0	0.0	4.5
607	607.0	0.0	3.2
585	581.3	3.7	3.8
533	379.2	153.8	4.6
472	277.2	194.8	4.7
476	241.8	234.2	4.2
450	76.8	373.2	3.3
325	17.0	308.0	2.1
313	38.1	274.9	1.9
243*	46.2	196.8	1.2
159	69.7	89.3	-1.7
156	58.2	97.8	2.6
160	46.8	113.2	3.1
35	4.0	31.0	21.6

* Hydrates began dissociating at this point

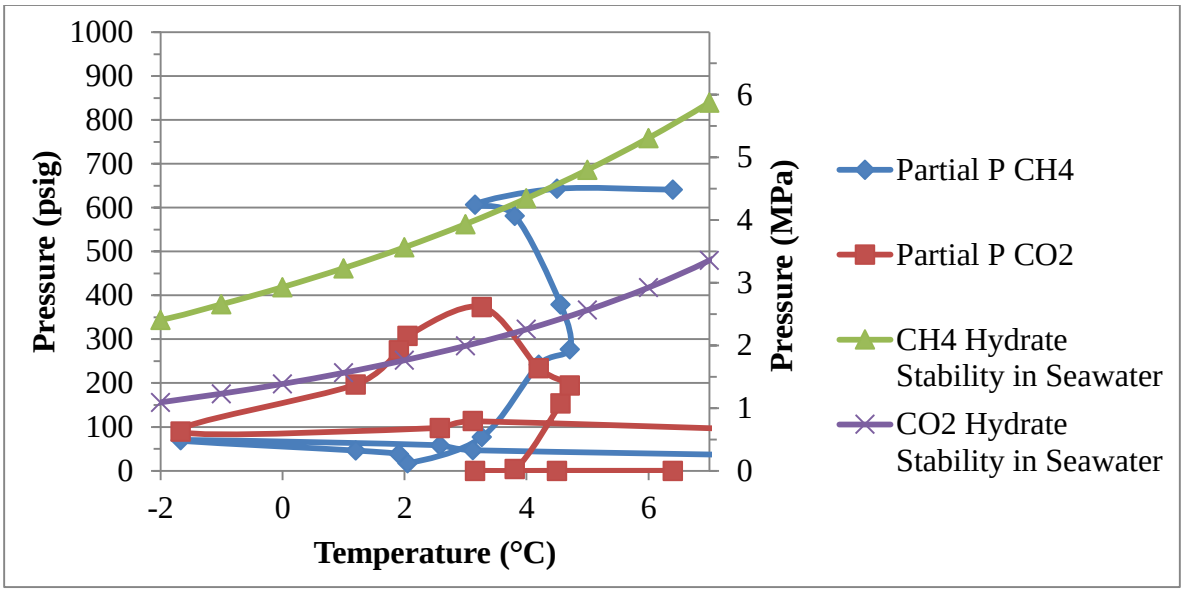

Figure 4.3: *Plot of CH_4 and CO_2 partial pressure data versus temperature from Table 4.2 for Run 6.*

Once CO_2 began to evolve from the cell, the volume of gas emitted from the cell was determined by depressurizing the Jerguson cell into an inverted graduated cylinder filled with water. About 11.7 L exited the cell in gas form, though CO_2 and some CH_4 gas was dissolved in water as it exited the Jerguson cell. An estimated volume of 15.1 L of CO_2 and CH_4 gas was discharged from the cell over 2.5 h as shown in Figure 4.4. During this time, cell pressure decreased from 333 psig to 5 psig at 4°C. The system was allowed to warm up and stabilize for five days, and a GC sample of the cell taken at 34 psig and 21.6°C resulted in 87% CO_2 and 13% CH_4 gas in the gas phase. As the system warmed up, much CO_2 evolved from the artificial seawater.

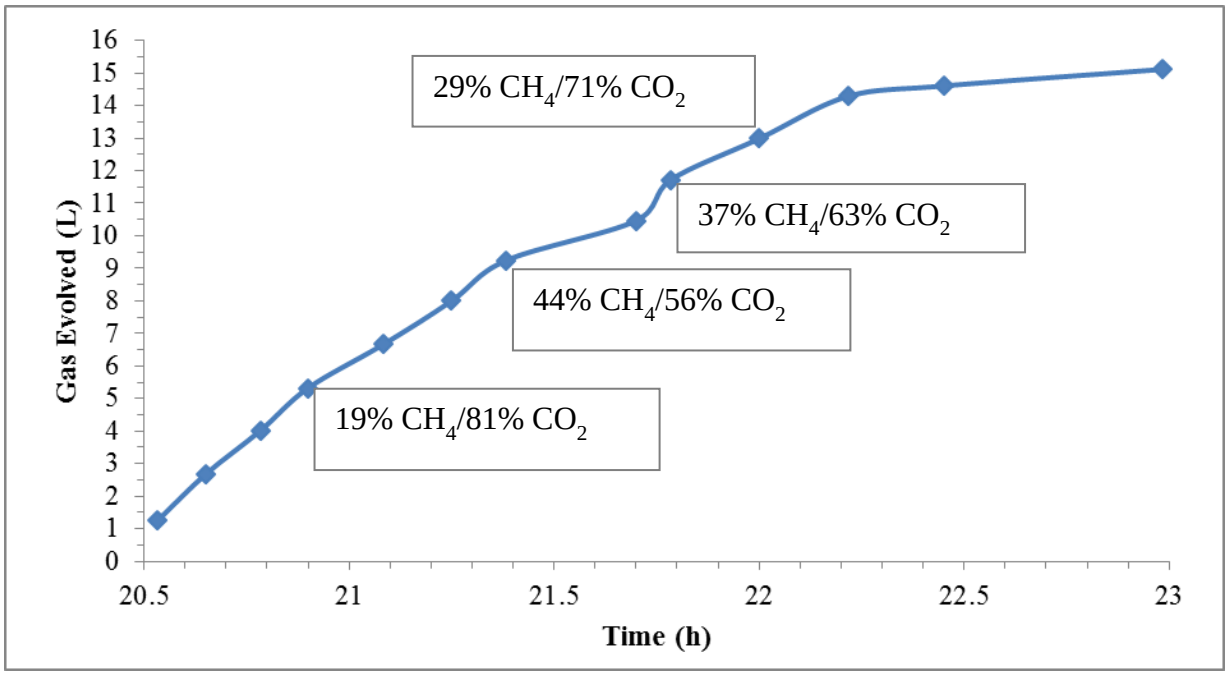

Figure 4.4: *Plot of total gas evolved during depressurization versus time after the CO_2 injection. Gas composition values from GC data are shown at various points.*

In Run 7, artificial seawater from the previous Run 6 was used again. The cell was flushed with nitrogen gas and pressurized to 398 psig with CO_2 after the bath had cooled the cell to 4.5°C. After 22 hours no hydrates were seen, so the cell was charged with additional CO_2 gas. Upon repressurization to 565 psig at 5.2°C, liquid CO_2 was observed above the artificial seawater in the cell. After two hours, transparent needle-like CO_2 hydrates were observed at bottom of the cell, and after an additional hour, CO_2 hydrates were seen at the aqueous-liquid CO_2 meniscus. These hydrates appeared more like solid ice, unlike the needle-like hydrates still at the bottom of the reactor. One hour later, the gas was discharged from the cell to reduce cell pressure to a point where liquid CO_2 was no longer stable, and many of the hydrates present dissociated. The cell was again repressurized to 460 psig with CO_2 gas that resulted in instant hydrate formation during charging. No further pressure drop was noted after the cell was sealed. Shortly thereafter, the cell was operated in the CO_2-CH_4 exchange mode by first depressurization to 174 psig and repressurized to 894 psig with CH_4 wherein instantaneous CH_4 hydrate formation was observed during CH_4 charging. Figure 4.5 shows recorded images of mixed CH_4-CO_2 hydrates, and the hydrates that formed instantly after the CH_4 injection are clearly seen as small spheres beneath the gas-liquid interface. Though the physical appearance of CH_4 and CO_2 hydrates is indistinguishable, the time resolved analysis of free gas above the aqueous phase by GC sampling was used to quantify the gas phase composition in the mixed gas system. Gas samples taken from the cell one hour after the CH_4 charge established the CH_4/CO_2 ratio to be 35%/65%, and this ratio changed to 50%/50% over the next 26 hours, as shown in Figure 4.6.

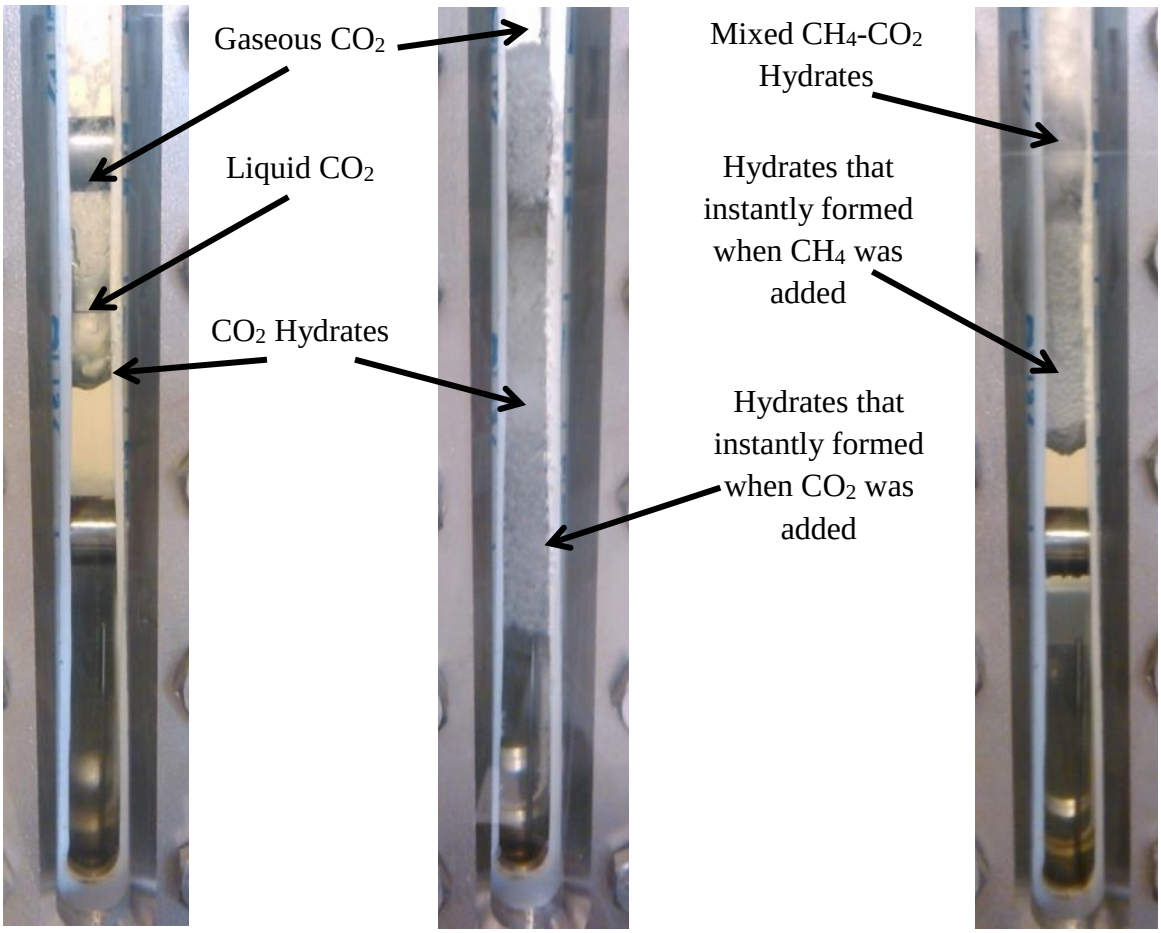

	1	2	3
Time Elapsed after Cooling (h)	26.5	47.2	52.8
Pressure (psig)	557	453	861
Temperature (°C)	3.9	4.4	4.0
Gas Phase Composition	Pure CO_2	Pure CO_2	Mix: 41% CH_4/ 59% CO_2

Figure 4.5: *Time-resolved images of hydrate formation in the Jerguson cell during Run 7. (1) Taken 26.5 h after the pre-cooled reactor was initially pressurized with CO_2. The reactor was pressurized twice with CO_2 gas, and CO_2 hydrates formed after charge #2 at 25 h. Liquid CO_2 was also observed above the water interface after CO_2 charge #2. (2) Taken at 47.2 h with only CO_2 present in the cell. Prior to (2), the reactor was depressurized to remove liquid CO_2. At 47.1 h, the cell was repressurized with CO_2 gas, during which CO_2 hydrates instantly formed. (3) Taken at 52.8 h when both CH_4 and CO_2 had been added to the cell. At 47.4 h, partial depressurization dissociated CO_2 hydrates. The cell was then repressurized to 894 psig with CH_4 when instant hydrate formation was observed.*

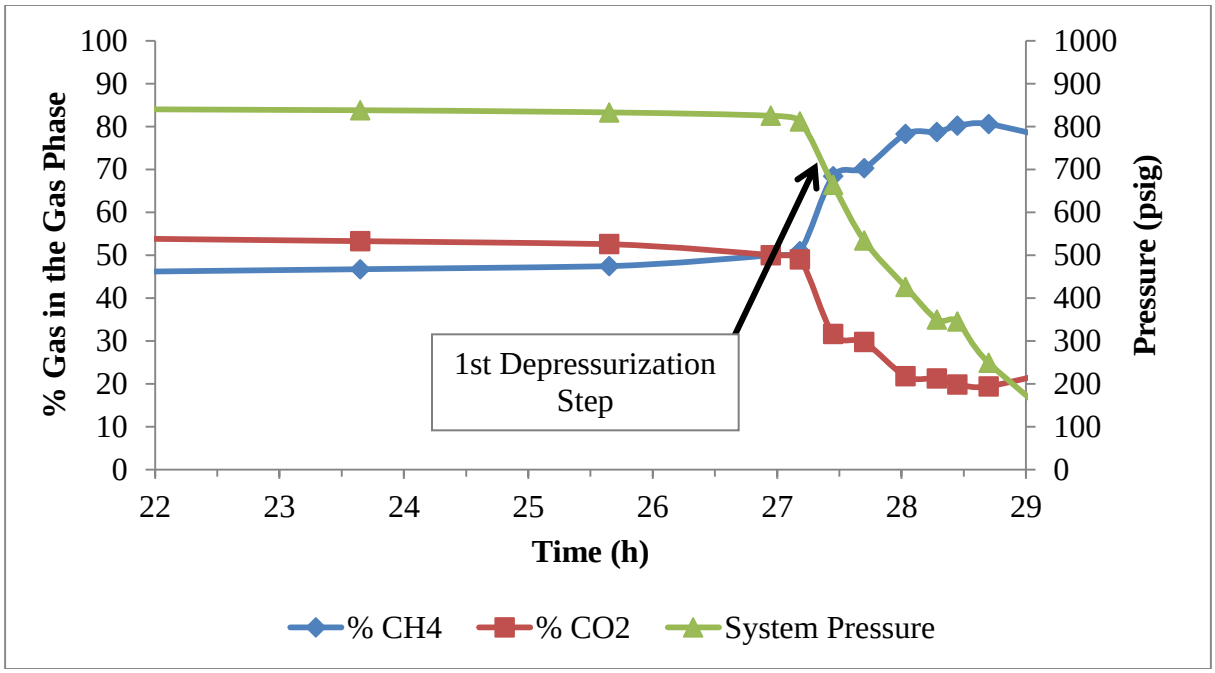

Figure 4.6: *Plot of the composition of CH_4 and CO_2 in the cell over time. Cell pressure versus time after CH_4 injection is also plotted, and the temperature of the cell was 3.4 to 4.0°C. As system pressure was decreased, the concentration of CH_4 in the gas phase increased.*

At this point, a stepwise depressurization of the system was initiated. Figure 4.6 shows the composition of the gas phase in the cell as system pressure was decreased. GC analysis indicated that initially CO_2 dominated the gas phase, but as the cell was slowly depressurized, the amount of CH_4 in the gas phase increased. The stability of CH_4 hydrates was noted, even when the partial pressure of CH_4 was below the hydrate equilibrium curve (Table 4.3 and Figure 4.7), indicating that complete CH_4 hydrate decomposition may be a slow phenomenon. A week after cell pressure was decreased to below hydrate stability, a GC sample taken at 23 psig and 22.0ºC indicated that the gas composition was 41.7% CH_4 and 58.3% CO_2.

Table 4.3: *Partial Pressure Data during the Stepwise Depressurization of Run 7*

P_{total}	Partial P CH_4	Partial P CO_2	$T_{sediment}$
psig	psig	psig	°C
882	296.5	554.5	4.0
867	330.8	527.9	3.9
861	336.6	493.0	4.0
838	356.1	405.9	3.4
833	398.5	441.7	3.4
825	410.9	411.2	3.4
812	409.6	394.2	3.4
664	455.3	210.4	3.3
534	375.3	158.7	3.4
426*	333.9	92.9	3.4
350	274.3	74.1	3.4
345	275.2	68.0	3.4
249	198.2	47.7	3.4
38	27.5	9.3	3.4
23	8.3	11.6	22.0

*Hydrates began dissociating at this point

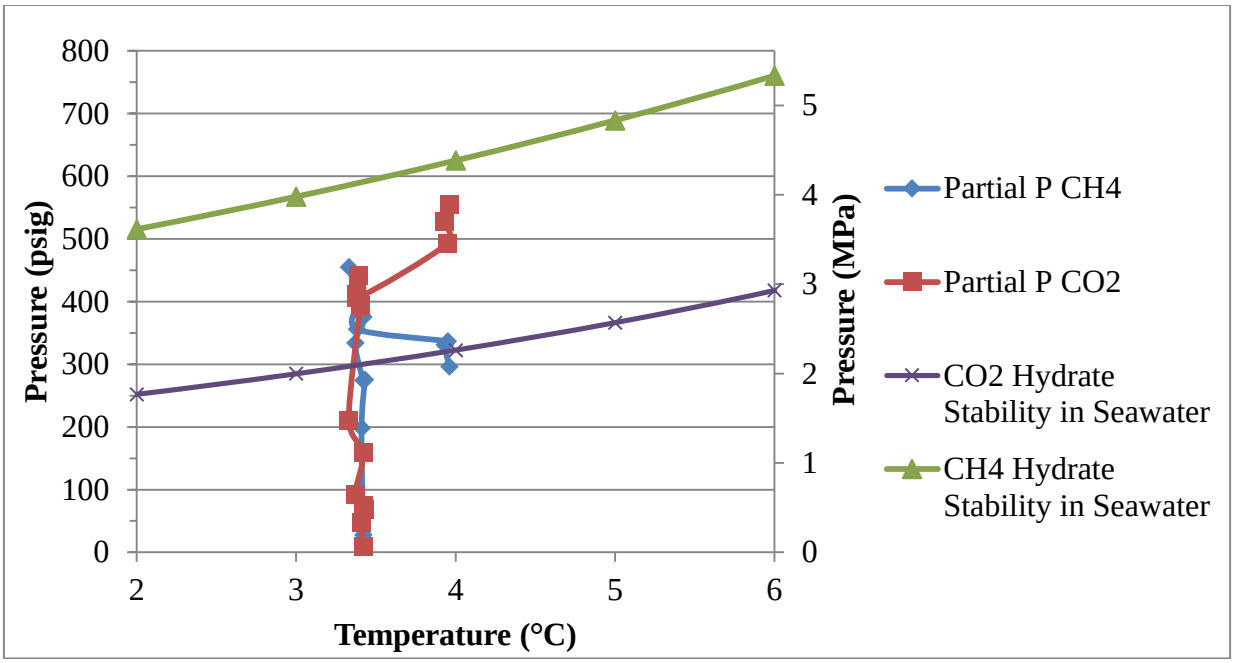

Figure 4.7: *Plot of CH_4 and CO_2 partial pressure data versus temperature from Table 4.3 for Run 7.*

4.2 Gas Exchange Experiments in Ottawa Sand (Runs 8-10)

Run 8 was conducted with 104 g of Ottawa sand as a host that was fully saturated and filled from above with 38 mL of artificial seawater. After cooling to 4°C, the cell was pressurized with 945 psig CH_4 gas, and hydrates were observed at the gas-liquid interface in about 24 hours. Over time, the hydrates grew downwards into the solution until they reached the top of the sand pack (Figure 4.8). The pressure drop corresponded to 11% conversion in 48 hours in this excess-gas system. At this point, the cell was depressurized below hydrate equilibrium conditions to allow complete hydrate dissociation. The cell was repressurized to 942 psig and within 10 minutes, hydrates were observed as a thin film on part of the glass window and at the gas-liquid interface. The pressure decreased continuously as hydrates grew from the gas-liquid interface downwards into the solution until the pressure stabilized at 828 psig, which corresponded to 12%$\pm$0.6 gas conversion into hydrates over two days. The observed relatively fast hydrate formation is attributed to the memory effect.[54]

A similar phenomenon of instantaneous hydrate formation was observed during subsequent CO_2 charges in the partial depressurization/repressurization cycle. It is notable that in these runs, hydrates formed above the sand pack; few if any hydrates formed on a macroscale within the sand pack most likely due to capillary inhibition[71]. The gas phase of the cell was pure CH_4 for five hours after the CO_2 injection. After this time, the concentration of CO_2 in the gas phase rose very slowly, until two days later when the gas phase CH_4/CO_2 ratio was 86.5%/13.5%, as shown in Figure 4.9.

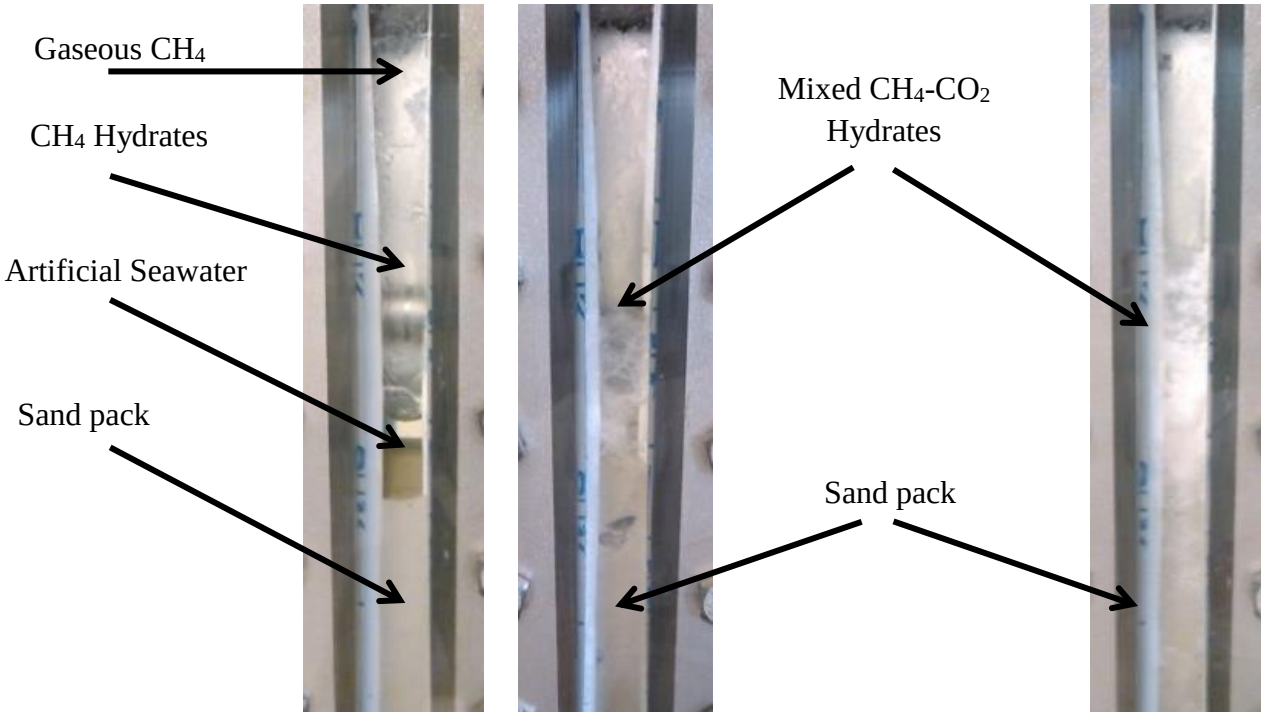

	1	2	3
Time Elapsed after Cooling (h)	20.1	194.8	235.9
Pressure (psig)	911	381	354
Temperature (°C)	3.5	3.6	3.6
Gas Phase Composition	Pure CH_4	> 99% CH_4 (though the cell was charged with both CO_2 and CH_4)	89% CH_4 11% CO_2

Figure 4.8: *Time resolved images of hydrate formation in the Jerguson cell during Run 8. (1) Taken 20.1 h at 911 psig CH_4 and 3.5°C. Prior to (1), the cell was charged with 945 psig of CH_4 gas. (2) At 194.8 h under 381 psig at 3.6°C. Prior to (2), after CO_2 hydrates formed for several days, the cell was partially depressurized, left cooling for 3 days and then partially depressurized and repressurized several times. (3) At 236 h under 354 psig at 3.6°C. Prior to (3), CO_2 gas was charged into the system twice. Shortly after (3), the cell was depressurized in steps to bring about the complete dissociation of hydrates.*

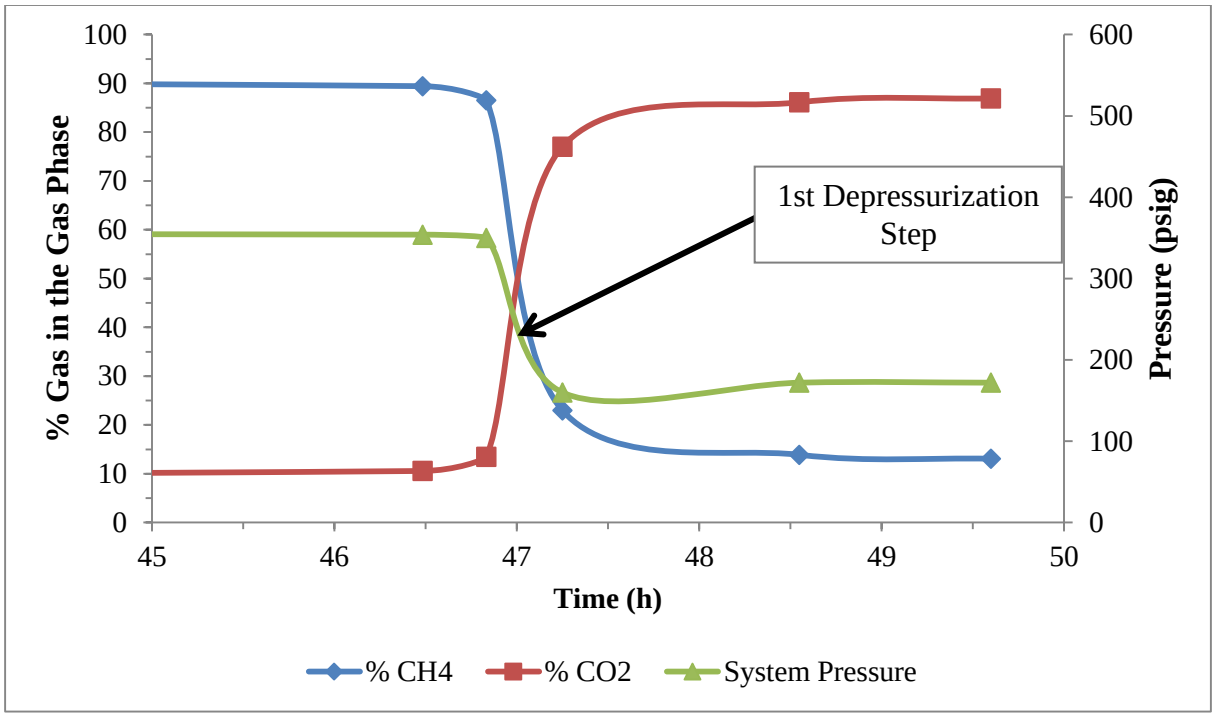

Figure 4.9: *Plot of the composition of CH_4 and CO_2 in the cell over time. Cell pressure versus time after CO_2 injection is also plotted, and the temperature of the cell was 2.7 to 4.1°C. As system pressure was decreased, the concentration of CO_2 in the gas phase increased considerably.*

Subsequently, hydrate dissociation was induced by depressurization. The concentration of CO_2 in the gas phase increased greatly upon depressurizing the system below 200 psig. A final GC sample taken at 172 psig and 3.7°C (below the hydrate stability zone) indicated a gas phase CH_4/CO_2 ratio of 15%/85%, suggesting that the cell mostly contained CO_2 hydrates prior to dissociation and that much CO_2 was solubilized in the solution. Interestingly, when GC data was used to calculate and plot the partial pressures of CH_4 and CO_2 throughout hydrate formation (Table 4.4 and Figure 4.10), the partial pressures of CH_4 were never within the CH_4 hydrate stability region, and similarly, the partial pressures of CO_2 were never in the CO_2 hydrate stability region. Gas hydrates were consistently viewed in the see-through window of the Jerguson reactor for most of the data points plotted in Figure 4.10. As found with previous runs, the total system pressure must have a greater effect on hydrate stability.

Table 4.4: *Partial Pressure Data during the Stepwise Depressurization of Run 8*

P_{total}	Partial P CH_4	Partial P CO_2	$T_{sediment}$
psig	psig	psig	°C
496	496.0	0.0	3.5
520	520.0	0.0	3.5
355	355.0	0.0	3.5
325	325.0	0.0	3.5
413	413.0	0.0	3.7
445	445.0	0.0	4.1
437	423.4	13.6	3.6
425	404.2	20.8	3.6
368	344.6	23.4	3.2
365	340.6	24.4	3.2
363	339.6	23.4	3.2
359	333.2	25.8	3.2
354	316.6	37.4	3.6
350	302.9	47.1	3.6
160*	36.8	123.2	2.7
172	23.9	148.1	3.7
172	22.5	149.5	3.6

*Hydrates began dissociating at this point

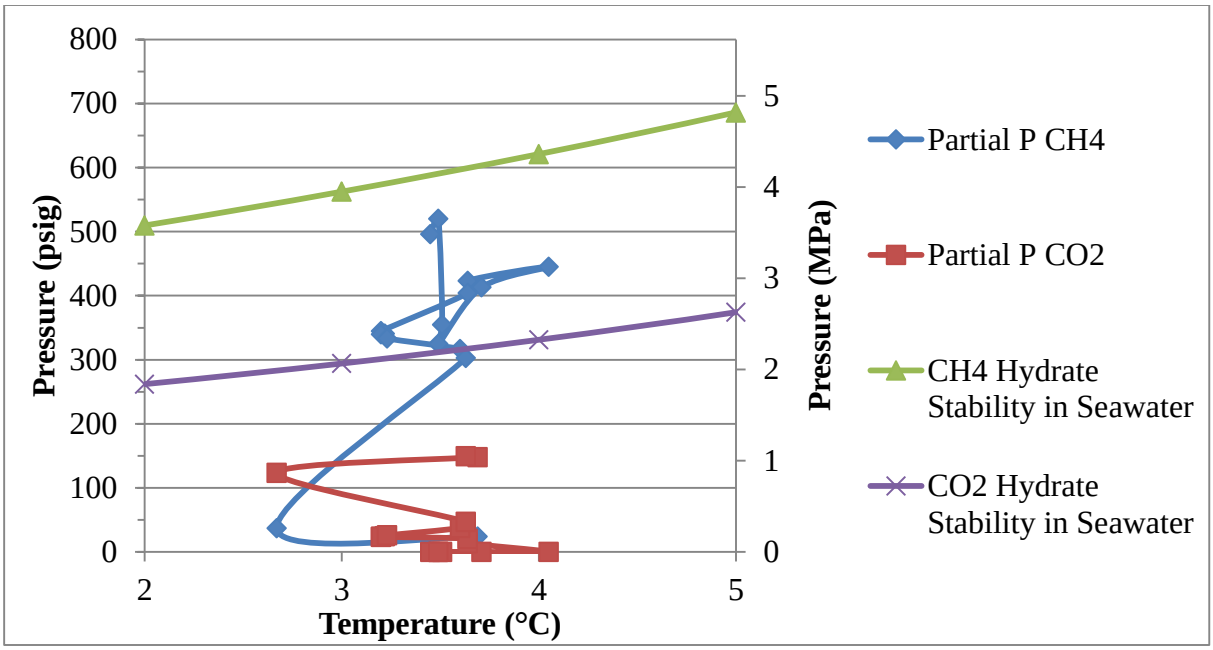

Figure 4.10: *Plot of CH_4 and CO_2 partial pressure data versus temperature from Table 4.4 for Run 8.*

In Run 9, the Ottawa sand/artificial seawater from the previous run were reused after flushing the system with nitrogen gas. In this run, the addition of two gases was reversed to establish the effect of added CH_4 gas on preformed CO_2 hydrates. After pre-cooling to 6°C, the cell was pressurized to 451 psig with CO_2 when transparent, needle-like CO_2 hydrates were observed on top of the sand pack within 7 hours. After 24 h, the hydrates had spread to the gas-liquid interface, and in the following 24 hours, hydrates were visible within the host sand. The cell pressure stabilized and corresponded to 11%$\pm$0.6 conversion of CO_2 into hydrates in this excess-water system. Another CO_2 charge resulted in instantaneous CO_2 hydrate formation. Shortly thereafter, CH_4 was injected to increase the cell pressure to 756 psig at 3.1°C to observe CO_2-CH_4 exchange. Figure 4.11 is an image of mixed gas hydrates seen above and in the sand pack. The GC analysis established the CH_4/CO_2 ratio as follows: 6.4%/93.6% 5 minutes after CH_4 injection, and 30.4%/69.6% 36 minutes after CH_4 injection. These data are consistent with the liberation of CH_4 from the hydrate phase shortly after CO_2 was introduced into the system and displaced CH_4 to form CO_2 hydrates. A second charge of CH_4 increased cell pressure to 875 psig, and the measured CH_4/CO_2 ratio was 34.9%/65.1% 5 minutes after the second CH_4 injection. After 3 hours, this ratio changed to 47.9%/52.1%, as shown in Figure 4.12. It is known that initially CH_4 molecules fill both the small and larger hydrate cages, but as time elapses, the majority of large hydrate cages are filled with CO_2 which results in increased CH_4 concentration in the gas phase[110].

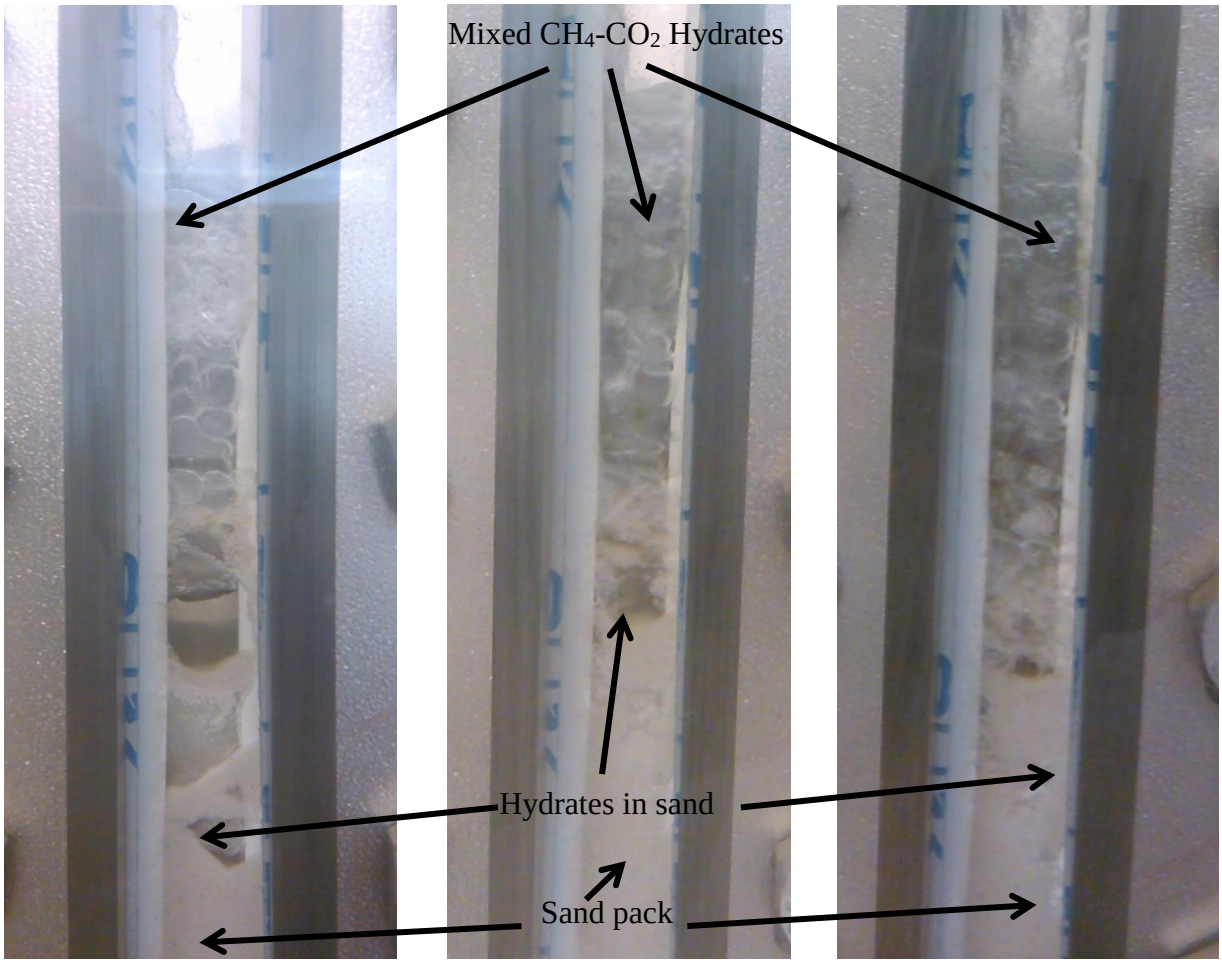

	1	2	3
Time after Cooling (h)	23.3	24.8	30.4
Pressure (psig)	483	756	857
Temperature (°C)	3.0	3.1	3.1
Gas Phase Composition	Pure CO_2 Taken after second CO_2 charging	6% CH_4 – 94% CO_2	48% CH_4 - 52% CO_2

Figure 4.11: *Time resolved images of hydrate formation in the Jerguson cell during Run 9. (1) Taken 23.3 h after the pre-cooled cell was initially pressurized under 483 psig CO_2 at 3.0°C. Prior to (1), the reactor was initially charged with 451 psig CO_2 gas, and then recharged to this pressure. (2) Taken at 24.8 h under 756 psig at 3.1°C. Prior to (2), after CO_2 hydrates formed in 24 h, the cell was repressurized to this new pressure with CH_4 gas. At 26.2 h, the cell was repressurized with CH_4 to 875 psig. The cell was then partially depressurized and repressurized one more time. (3) Taken at 30.4 h under 857 psig at 3.1°C. Mixed hydrates filled much of the reactor above the sand pack though few hydrates were seen in the sand pack. Shortly after this time, the cell was depressurized in steps to bring about hydrate dissociation.*

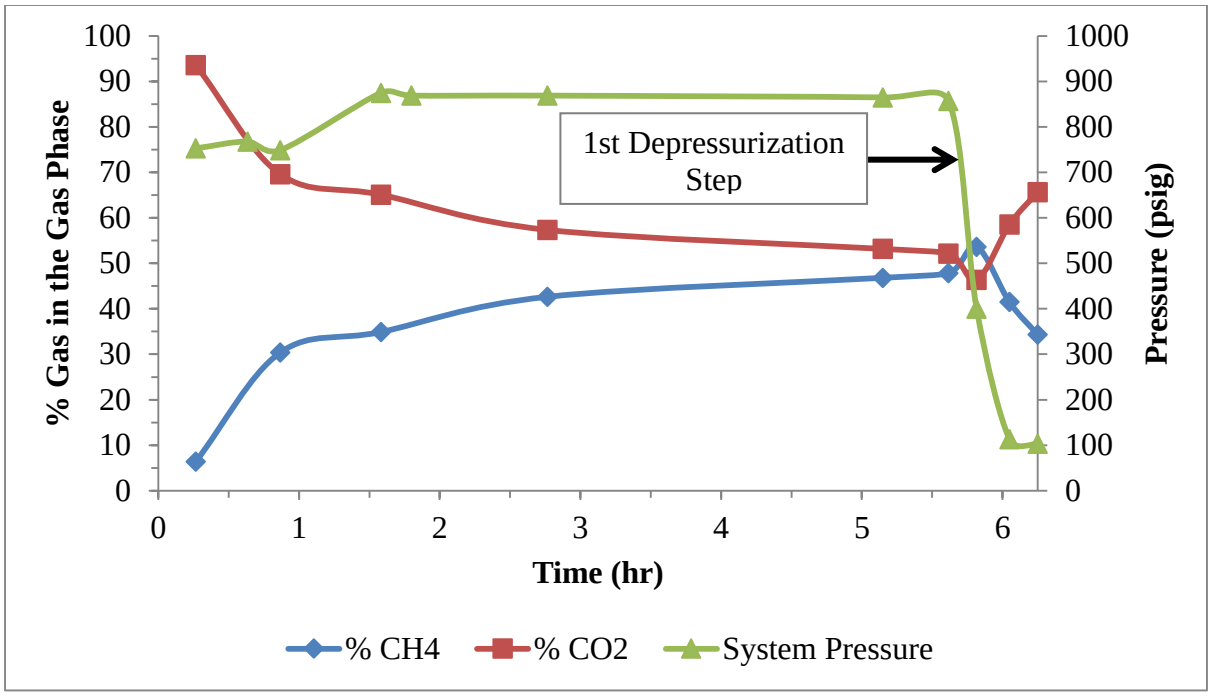

Figure 4.12: *Plot of the composition of CH_4 and CO_2 in the cell over time. Cell pressure versus time after CH_4 injection is also plotted, and the temperature of the cell was 2.8 to 3.1°C. As system pressure was decreased, the concentration of CO_2 in the gas phase briefly decreased and then increased considerably.*

A step-wise depressurization of the cell to bring about hydrate dissociation initially resulted in an increase of CH_4 in the gas phase, but as system pressure decreased, the gas phase quickly became richer in CO_2. When the pressure was reduced to 400 psig, the gas phase composition was 53.7% CH_4/46.3% CO_2. However, as pressure further decreased to 103 psig, the gas phase became richer in CO_2 (65.7%) as CO_2 hydrates dissociated. Contrary to the previous experiment, the partial pressure of CO_2 was within the CO_2 hydrate stability zone for nearly the entire time that gas hydrates were viewed in the cell, as shown in Tables 4.5 and Figure 4.13. The partial pressure of CH_4, on the other hand, was never in the CH_4 hydrate stability zone.

Table 4.5: *Partial Pressure Data during the Stepwise Depressurization of Run 9*

P_{total}	Partial P CH_4	Partial P CO_2	$T_{sediment}$
psig	psig	psig	°C
753	48.3	704.7	3.0
749	227.5	521.5	3.0
875	305.4	569.6	3.1
869	370.6	498.4	3.0
865	405.0	460.0	3.1
857	410.2	446.8	3.1
400	214.6	185.4	2.9
113*	46.9	66.1	3.0
103	35.3	67.7	2.8

*Hydrates began dissociating at this point

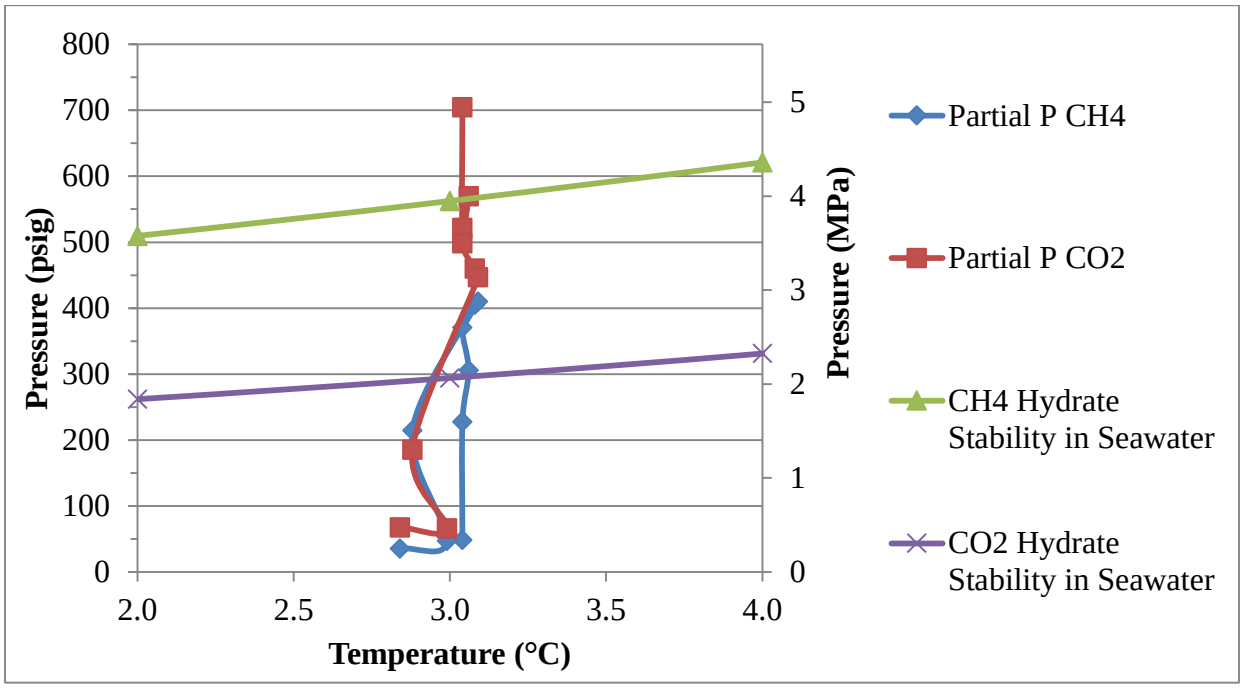

Figure 4.13: *Plot of CH_4 and CO_2 partial pressure data versus temperature from Table 4.5 for Run 9.*

In Run 10, the Ottawa sand and artificial seawater from Runs 8 and 9 were reused, and the experiment was performed similarly to Run 8 to establish the exchange of CO_2 gas with preformed hydrates of CH_4. The cell was flushed with nitrogen gas, pre-cooled to 3°C, and then pressurized to 950 psig with CH_4 gas. Within minutes, a thin coating of ice-like hydrates was seen on the cell glass windows above the gas-liquid interface that spread to the gas-liquid interface after one hour and then moved downwards into the solution. The noted pressure drop corresponded to $6\% \pm 0.1$ hydrate saturation in this excess-gas system. After 26 hours, the second charge with CH_4 corresponded to an additional $2\% \pm 0.1$ gas conversion of CH_4 into hydrates. The cell was partially depressurized, then repressurized with CO_2 up to 587 psig, and then one hour later, the cell was again partially depressurized and charged with CO_2. Figure 4.14 shows images of hydrate growth throughout Run 10. Multiple GC samples over three hours established the presence of a pure CH_4 gas phase, as shown in Figure 4.15.

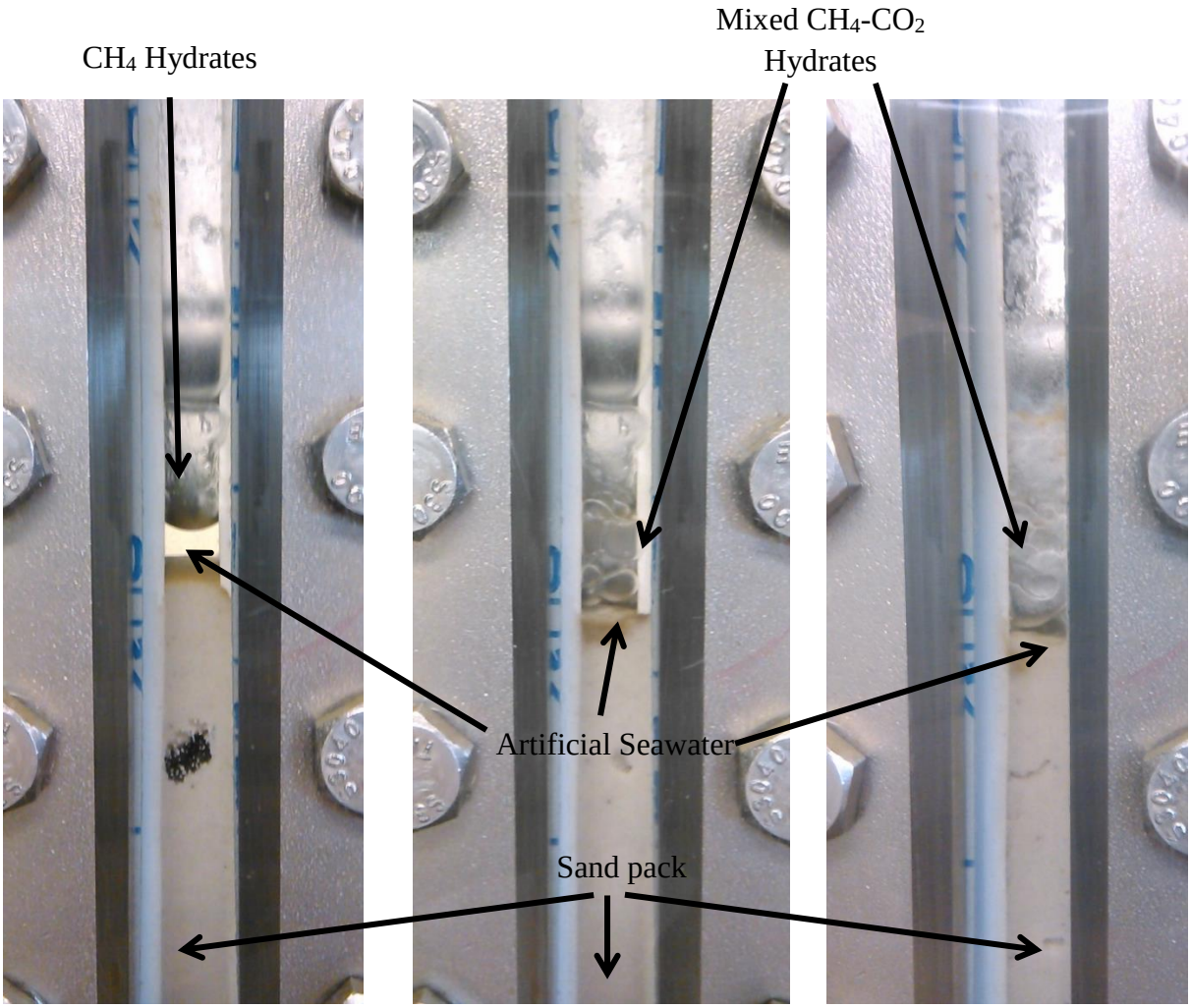

	1	2	3
Time after Cooling (h)	25.0	46.7	52.2
Pressure (psig)	887	935	536
Temperature (°C)	2.9	2.9	3.0
Gas Phase Composition	Pure CH_4	Pure CH_4	Pure CH_4 (though the cell was charged with both CO_2 and CH_4)

Figure 4.14: *Time resolved images of hydrate formation in Jerguson cell during Run 10. (1) Taken 25.0 h after the pre-cooled cell was initially pressurized with 887 psig CH_4 at 3.5°C. Prior to (1), the reactor was charged with 950 psig of CH_4 gas. After CH_4 hydrates formed in 26.0 h, the cell was repressurized with CH_4 gas to 955 psig. (2) At 46.7 h under 935 psig of CH_4 at 2.9°C. After this image was taken, the cell was partially depressurized and repressurized with CO_2 gas twice. (3) Taken at 52.2 h under 536 psig at 3.0°C. Shortly after (3), the cell was depressurized quickly to induce hydrate dissociation.*

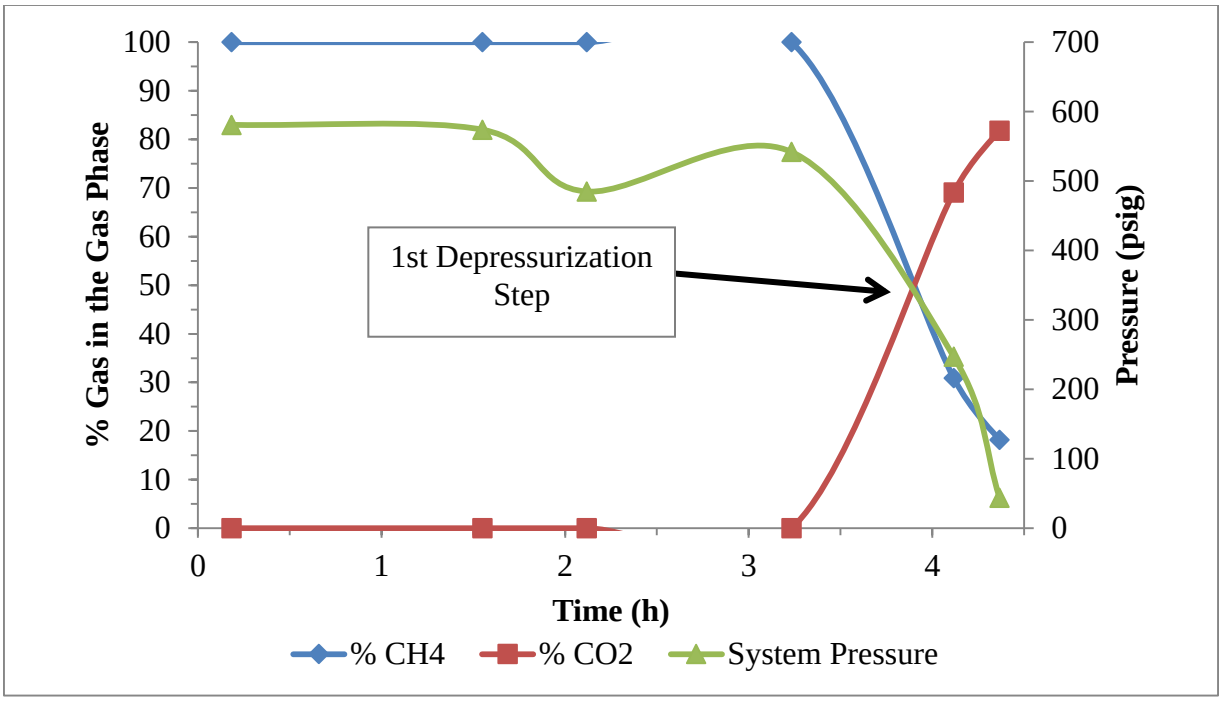

Figure 4.15: *Plot of the composition of CH_4 and CO_2 in the cell over time. Cell pressure versus time after CO_2 injection is also plotted, and the temperature of the cell was 2.9 to 3.0°C. As system pressure was decreased, the concentration of CO_2 in the gas phase greatly increased.*

Upon quick depressurization to 245 psig (below the hydrate stability zone), GC analysis established the gas phase to be rich in CO_2 (69.1%), indicating the presence of CO_2 trapped as hydrate that became unstable during depressurization. Further depressurization to 44 psig increased CO_2 (81.8%) and decreased CH_4 (18.2%) in the gas phase. This seems to show that CO_2 hydrates had formed in the system, but as with Run 8, the partial pressure of CO_2 in the system was never large enough to be within the CO_2 hydrate stability zone (Table 4.6 and Figure 4.16). This again shows that the overall pressure of the gas phase of the cell plays a large role in hydrate stability.

Table 4.6: *Partial Pressure Data during the Stepwise Depressurization of Run 10*

P_{total}	Partial P CH_4	Partial P CO_2	$T_{sediment}$
psig	psig	psig	°C
581	581.0	0.0	2.9
574	574.0	0.0	3.0
485	485.0	0.0	3.0
542	542.0	0.0	3.0
247*	76.3	170.7	3.0
44	8.0	36.0	2.9

*Hydrates began dissociating at this point

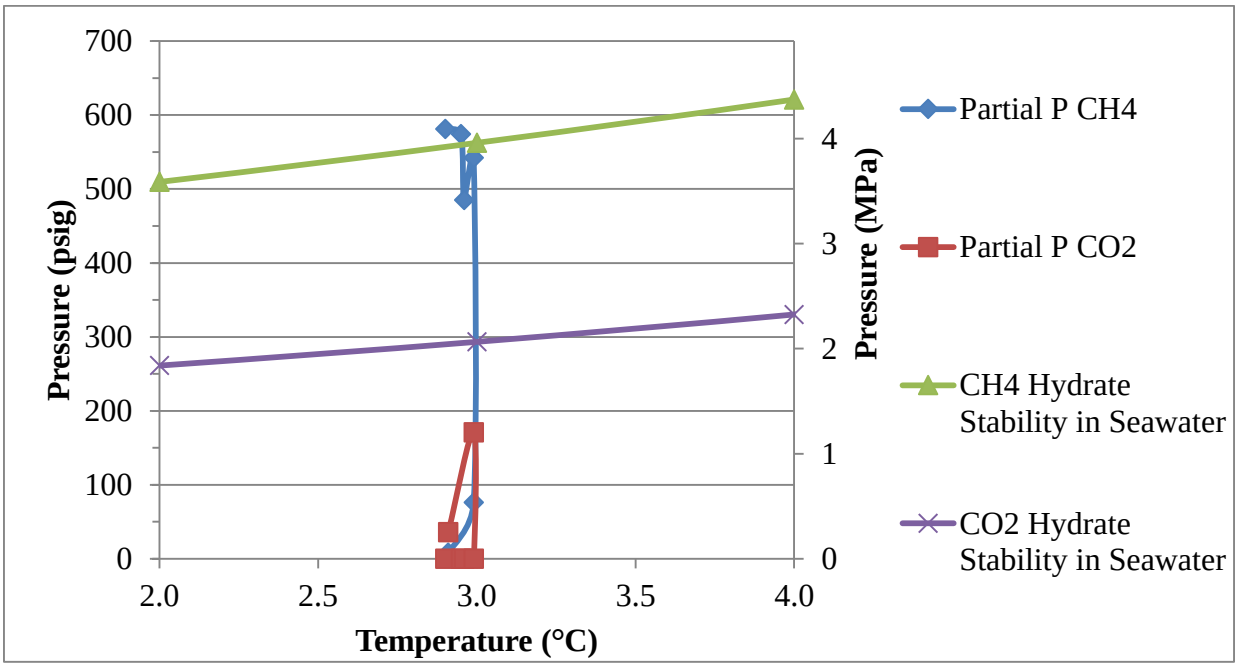

Figure 4.16: *Plot of CH_4 and CO_2 partial pressure data versus temperature from Table 4.6 for Run 10.*

4.3 Comparison and Discussion of Runs 6-10

This investigation comprised of experiments conducted to understand a CH_4-CO_2 system in which gas phase CO_2 is pumped into a natural CH_4 hydrate reservoir and results in sequestered CO_2 as hydrates with the concomitant liberation of CH_4. Specifically, the completed five runs focused on understanding the extent and rates of the CH_4-CO_2 exchange phenomenon. The conditions of all experiments are listed in Tables 4.1 and 4.7. Runs 6 and 7 were baseline (without host sediments), while Runs 8, 9, and 10 included Ottawa sand as a host. In Runs 6, 8, and 10, the cell was initially charged with CH_4, and once CH_4 hydrates formed, CO_2 was added to the cell. The opposite sequence was repeated in Runs 7 and 9, wherein CO_2 gas was initially added to the cell, and once CO_2 hydrates were observed, CH_4 was added to the system.

Table 4.7: *Induction Time Measured when Hydrates were First Sighted in the Jerguson Cell**

Run #	Host Sediments	Gas Addition Sequence	Induction Time (h)	
			Charge 1	Charge 2
6	No	CH_4 / CO_2	96	Instant
7	No	CO_2 / CH_4	22+	2
8	Ottawa Sand	CH_4 / CO_2	24	< 0.5
9	Ottawa Sand	CO_2 / CH_4	7	Instant
10	Ottawa Sand	CH_4 / CO_2	< 5 min	Instant

*The bath temperature was maintained at 3-6°C. +No hydrates were observed to have formed prior to injecting CO_2 gas a second time

Induction time data for hydrate formation (the time when hydrates could be seen by the naked eye) was extracted from completed runs to better understand its dependence on the nature of the hydrate forming gas (CH_4 and CO_2), host sediment, and memory effect. The data in Table 4.7 shows that, in systems without sand, the induction time for CH_4 hydrate appearance was the largest at 96 h (Run 6) while with CO_2 hydrate, the time shortened to 24 h (Run 7, though gas was added to the cell a second time). Runs 6, 8, and 10 followed the same sequence- initially CH_4 gas was added to the system, and once hydrates were visible in the reactor, CO_2 gas was added. CH_4 hydrates formed much more quickly (24 h) in the presence of Ottawa sand (Run 8) than without it (4 days for Run 6). Similarly in Run 9, in which CO_2 hydrates were formed and then CH_4 gas was injected within the host sand, had a shorter hydrate induction time (7 h) than Run 7 (24 h) in which no porous media was present. The presence of porous media is known to affect the stability of gas hydrates. Higher pressures and/or lower temperatures are needed to form hydrates in sand systems[71]. In one instance, Handa and Stupin[114] found that systems containing CH_4 or propane hydrates in silica gel required equilibrium pressures 20 - 100% higher than systems without sediments to form hydrates. The lack of hydrate formation within the Ottawa sand pack herein is in agreement with these studies. While hydrates did not form in large quantities within the sand pack where there was less gas available for hydrate formation, the runs containing sand within the cell did result in faster hydrate formation at the gas-liquid interface. The shortened induction time observed in runs with Ottawa sand may be due to sand particles acting as nucleation sites for hydrate formation. It is likely that sand particles became stuck to the walls near the gas-liquid interface in the cell while bubbling gas through the sand pack during charges, and these impurities affected hydrate nucleation and induction times[115].

A comparison of pure hydrates of CH_4 and CO_2 in studies found that CO_2 hydrates had shorter induction times than CH_4 hydrates[116,117]. A gas hydrate phase diagram (Figure 1.3) shows that in artificial seawater, CO_2 hydrates are stable at higher temperatures and lower pressures than CH_4 hydrates. In agreement with previous studies[116,117] and thermodynamics, the induction times in Runs 7 and 9 wherein CO_2 hydrates were initially formed were shorter than the induction times for CH_4 hydrates (Runs 6 and 8).

Interestingly, the shortest induction time was noted in Run 10 wherein CH_4 hydrates formed almost instantly after the cell was pressurized. This speedy formation is likely due to the

hydrate memory effect. Studies[54,118] have shown that hydrate forming solutions can maintain a "memory" of their hydrate structure when warmed up slightly above the hydrate stability region[17]. There are two theories as to why this occurs: (1) a hydrate frame assembly remains intact in the solution, either as a partial or ordered configuration once hydrates had formed and (2) some gas is left dissolved in the solution after dissociation[17]. For Runs 8-10 in which the same Ottawa sand and artificial seawater were utilized for hydrate formation, the induction time was significantly reduced even though different gases (CH_4 or CO_2) were initially used to form hydrates. In Run 8, CH_4 hydrates formed after about 24 h, while in Run 9, CO_2 hydrates formed in 7 h, and in Run 10, CH_4 hydrates formed within minutes. In between each of these runs, the cell was completely depressurized and flushed with nitrogen gas. Mazloum et al.[119] observed that the depressurization of a system of natural gas hydrates, followed by repressurization with fresh natural gas did not result in the hydrate memory effect for gas hydrate formation. It was found that the hydrate memory effect was destroyed by depressurization to atmospheric pressure, but reducing the pressure of the system slightly would still result in the hydrate memory effect[119]. In addition, if the solution is warmed above 25[54] or 28°C[17] or for too long a time period (several hours[17]), this retention effect will not occur. In between each of these experiments, the cell was left depressurized and uncooled for extended periods of time ranging from seven days to two months. All of these factors are contrary to the decreased hydrate formation time observed herein with systems composed of CH_4 and CO_2.

The sequence of gas addition to the cell also affected hydrate stability. In all experiments, once gas hydrates had formed, any additional gas charge, independent of the gas (CO_2 or CH_4), resulted in near instant hydrate formation. This fast formation indicates that, if CO_2 is to be sequestered in a CH_4 hydrate reservoir, it is likely that CO_2 hydrates will form instantly. The fast formation of new hydrates, upon adding fresh gas into the system, correlates well with phase field studies of CO_2 gas injections into CH_4 hydrate systems[83]. The liquid transport mechanism for forming new hydrates from free water is much faster than the solid-state mass transport mechanism for exchanging gases in already existing hydrates. Once new hydrates have formed utilizing free water to form new hydrates, the slower process of exchanging gases in hydrates will begin.[83]

In addition, whether CO_2 or CH_4 was the initial gas for hydrate formation, when a second gas was charged into the reactor, initially the gas phase of the cell was mostly if not entirely, composed of the initial system gas while the newly injected gas presumably entered the hydrate phase. For systems where the cell was initially filled with CH_4 and then charged with CO_2 gas, the gas phase of the cell consisted of pure CH_4 for several hours after the CO_2 injection. Whereas for systems originally pressurized with CO_2 and then injected with CH_4, the gas phase was initially mostly composed of CO_2, but over a much shorter time period, the percentage of CH_4 in the gas phase increased, indicating that CO_2 gas exchanged with CH_4 gas in the hydrate structure. System pressure either remained constant or decreased over time as these gas composition values were obtained, therefore this change in composition must be a result of gas exchange rather than solely the evolution of CH_4 from hydrates. Uchida et al.[110] reported similar results with the following explanation: during the initial stages of the hydrate formation, CH_4 molecules were able to occupy both small and large hydrate cages, but over time the larger cages mostly trap CO_2 gas, resulting in increased CH_4 in the gas phase[110]. Phase field simulation models have yielded similar results[120]. Overall, whether CH_4 or CO_2 gas is introduced into a system of gas hydrates via bubbling, an instant formation of hydrates of the injected gas is likely to occur.

While comparing the composition of the gas phase in each run, it is difficult to calculate hydrate composition directly from these GC data. Upon analyzing varying CH_4-CO_2 gas phase compositions using the CSMHYD program[26], the compositions of the hydrate phase for various gas phase compositions at hydrate equilibrium could be determined. Table 4.8 shows the hydrate phase composition when the gas phase of the system is 35%-65%, 50%-50%, 70%-30%, and 80%-20% CH_4-CO_2. It is clear that the concentration of CH_4 in the hydrate phase is 12-15% below the concentration of CH_4 in the gas phase, while the concentration of CO_2 in the hydrate phase is 12-15% above the concentration of CO_2 in the gas phase. This trend is consistent with the fact that CO_2 hydrates are more stable in the hydrate phase than CH_4 hydrates. While the values in Table 4.8 are all at hydrate equilibrium and all of the experiments performed herein were within the hydrate stability region but not at equilibrium, it can be inferred that when comparing GC gas composition data to the composition of hydrates present in the system, the amount of CO_2 in hydrates is likely to be higher than anticipated, while the amount of CH_4 in hydrates is likely to be lower.

Table 4.8: *Comparison of the Theoretical CH_4-CO_2 Gas Phase Composition to CH_4-CO_2 Hydrate Phase Composition at Hydrate Equilibrium Conditions (values obtained for CH_4-CO_2 systems in artificial seawater from the CSMHYD prediction program[26])*

Equilibrium Pressure	%CH_4 gas	%CO_2 gas	%CH_4 Hydrates	%CO_2 Hydrates
psig	%	%	%	%
376.3	35	65	23	77
409.3	50	50	35	65
468.3	70	30	54	46
507.3	80	20	66	34

Analysis of the partial pressures of CH_4 and CO_2 in the system based on GC sample data showed that in each run, only certain types of hydrates should have been stable as a system's gas phase make up affects the composition of mixed gas hydrates[113]. Based on partial pressures, both CH_4 and CO_2 hydrates could have been stable during Run 6, only CH_4 hydrates were stable for Run 10, only CO_2 hydrates were stable for Runs 7 and 9, and neither CH_4 nor CO_2 hydrates were stable for Run 8. As Runs 7 and 9 were the runs in which CO_2 hydrates formed first and then CH_4 was injected into the system, the order of gas addition can explain the lack of enough CH_4 gas in the gas phase to have a partial pressure within the hydrate stability zone. The instantly formed hydrates upon CH_4 gas injection, and the fact that initially, both Runs 7 and 9 resulted in an increase in CH_4 concentration in the gas phase of the cell during dissociation suggest that CH_4 had formed hydrates, even though they should not have been stable based on partial pressures. Similarly with Run 10, the instant formation of hydrates upon CO_2 gas injection and the lack of any CO_2 gas in the gas phase of the cell for three hours after CO_2 injection indicate that CO_2 hydrates had formed. While CO_2 solubility in seawater must also be considered as CO_2 is more soluble in water at lower temperatures and higher pressures[121] whereas CH_4 has low solubility in water[116], the initial lack of any CO_2 in the gas phase of the cell must be due to CO_2 solubility as well as hydrate formation. The most interesting experiment in terms of partial pressures was Run 8, where neither CH_4 nor CO_2 hydrates should have been stable based on partial pressures, yet hydrates were viewed filling nearly the entire glass window

in the Jerguson cell. The temperature in the cell (3.6°C) was well above the freezing point of the 35% salinity artificial seawater used (-1.921°C at atmospheric pressure[122]), so it is clear that gas hydrates did indeed form in the cell at partial pressures outside of the hydrate stability region.

Upon stepwise depressurization of the system, GC analysis clearly showed that for experiments where CH_4 hydrates were formed and CO_2 was injected (Runs 6, 8, 10), the amount of CO_2 in the gas phase greatly increased. For experiments where CO_2 hydrates were formed and CH_4 was injected (Runs 7 and 9), initially both runs exhibited a spike in the concentration of CH_4 in the gas phase during hydrate dissociation. This indicates that the secondary gas injected into the system did form gas hydrates that remained stable after the initial gas injection. However, for Run 9 as the cell was depressurized in steps, the amount of CO_2 increased in the gas phase considerably, most likely due to CO_2 evolving from the seawater and CO_2 hydrates dissociating. On the other hand, the gas phase composition of the cell remained as mostly CH_4 for all of the depressurization steps for Run 7. It was not until a GC sample was taken a week later that CO_2 was found to make up the majority of the gas phase of the system. This suggests that the hydrates formed during Run 7 were mostly composed of CH_4 gas, yet as discussed, the partial pressure of CH_4 in this run (and Run 9) was not within the CH_4 hydrate stability region. The results of all of these experiments show that partial pressure studies for mixed CH_4-CO_2 hydrate formation merit further investigation.

4.4 Conclusions

The experiments described in this chapter examined characteristics of the CH_4-CO_2 exchange phenomenon. Several noteworthy observations are as follows: 1) the induction times of hydrate formation were generally shorter for CO_2 than CH_4, by as much as a factor of four, with or without sediments; 2) the hydrate formation data showed that when a secondary gas was injected into a system containing preformed hydrates, the entering gas formed the hydrate phase instantly (within minutes); 3) CO_2 hydrates formed in a system that already contained CH_4 hydrates were found to be more stable, whereas CH_4 hydrates formed in a system consisting of CO_2 hydrates as hosts were initially stable, but CH_4 gas in hydrates quickly exchanged with free CO_2 gas to form more stable CO_2 hydrates; 4) gas hydrates were found to form in the cell, even when the partial pressures of CH_4 and CO_2 were outside of the hydrate stability region; and 5)

the hydrate memory effect was noted during the three runs performed to form sand-hosted gas hydrates. In all five runs, even though the system was depressurized, left over a week at room temperature, and flushed with nitrogen gas in between runs, the system still exhibited the memory effect. These results contradict those previously reported in the literature. As with Chapter 3, run repeatability was not investigated due to the stochastic nature of hydrate formation. In summary, the observed fast CO_2 hydrate formation from free CO_2 gas in the presence of preformed CH_4 hydrates indicates the feasibility of developing a CO_2 sequestration scheme using natural CH_4 hydrate reservoirs.

Chapter 5

5.0 Baseline Runs to Prepare for CMT Imaging

As pointed out by Goel[2], one of the challenges to gas hydrate research is the ability to directly visualize hydrate nucleation and growth on a microscale, rather than by indirect calculations. To overcome this limitation, CMT is a unique tool for viewing time-resolved hydrate formation. Tomography is an imaging process that takes two-dimensional (2D) cross section images of a sample over a range of angles. These 2D projections can then be stacked and reconstructed into 3D images.[97] CMT was established in the 1980s[123] and can be a great tool for viewing the microstructure of materials without damaging the specimen. CMT, like computed tomography (CT) imaging, works when x-rays are passed through a sample on to a scintillation detector that measures the amount of radiation that has passed through each section of the sample as the sample is rotated between 0 to 180 degrees. The scans collected can be used to generate a 3D image of the sample using the attenuation differential of the x-rays that passed through the sample. CMT is able to acquire data for various sized materials, making it well suited to study the interaction between hydrates and the mineral grains of rocks, soils, and sediments.

Several studies have made use of similar technologies when studying gas hydrates. Freifeld and Kneafsey[124] used a portable CT scanner to take 2D images of laboratory made hydrates. Their images indicated that hydrates dissociate from their reactor's exterior surface towards the interior. Additional 2D imaging by Kneafsey et al.[125] studied temperature and density gradients during CH_4 hydrate formation and dissociation in a partially saturated sand specimen made in an x-ray transparent aluminum reactor. Priest et al.[126] took CT images of gas hydrates recovered from the ocean floor in India and found that, at this location, gas hydrates grew as fracture filling veins. Choi et al.[127] studied how gas traveled through water-saturated sediments and found that gas moves in sand through pore capillary invasion and through silt by

creating channel openings. CT scans were used by Rees et al.[128] to investigate CH_4 hydrate formation in sediments from the Mount Elbert test well, and hydrates were found to form in varying shapes whereby CH_4 hydrates initially formed a dendritic structure that reconfigured to form more energy efficient morphologies over time. Kerkar et al.[129] and Kerkar et al.[130] performed time-resolved CMT of tetrahydrofuran and CH_4 hydrates respectively formed within 500 µm glass beads and measured the contact angle between hydrates and glass beads. Still, there has been little work on imaging the time-resolved growth of CO_2 or mixed CH_4-CO_2 hydrates. Several hydrate formation experiments were performed on a macroscale to compare bulk hydrate growth to microscale growth, and numerous CH_4 and CO_2 hydrate formation experiments in small volume test cells were performed prior to attempting CMT imaging of hydrates.

5.1 Jerguson CH_4-CO_2 Hydrate Experiments in 5 wt% $BaCl_2$ (Runs 11-13)

To establish macroscale CO_2, CH_4, and mixed CH_4-CO_2 hydrate growth in $BaCl_2$ – water solutions, three experiments were performed under excess water conditions to form (1) 50-50% CH_4-CO_2 hydrates, (2) CH_4 hydrates first, then inject in CO_2 gas, and (3) CO_2 hydrates first, then inject in CH_4 gas. These experiments were important to establish hydrate structure and formation kinetics on a macroscale in hydrate forming solutions containing $BaCl_2$ as a comparison to the hydrates that resulted in microscale formation during CMT imaging.

Prior to the first experiment, Run 11, the reactor was cleaned out and leak tested with nitrogen gas. Then 75 mL of 5 wt% $BaCl_2$ was injected into the reactor, and it was first pressurized to 525 psig with CO_2 gas. Immediately following CO_2 addition to the cell, 525 psig of CH_4 was added to reach a final cell pressure of 1050 psig. Although a 50% CH_4 - 50% CO_2 gas ratio was added to pressurize the cell, GC samples taken at this time at room temperature (22°C) indicated that 63.7% of the gas phase was made up of CO_2 gas and 36.3% was CH_4 gas. The difference in gas phase GC data versus the known composition of gas added to the cell is likely due to the order in which gas was added into the cell. Since CH_4 was the second gas bubbled through the solution in the bottom of the Jerguson reactor, it is likely that initially CH_4 was more solubilized in the solution, and quickly over time, CH_4 evolved while CO_2 was solubilized in the solution. Pressure was quite high in the system, so at this point, some pressure

was bled off to reduce system pressure to 976 psig. A GC sample taken at this time indicated a more even gas phase of 53.2% CH_4 and 46.8% CO_2. Figure 5.1 shows cell pressure and temperature over time throughout cell cooling and hydrate dissociation, and Figure 5.3 (a) plots initial gas composition values in the cell. The cell was left cooling, and 20.8 h after cooling was begun, another GC sample was taken at 873 psig and 6.1°C that indicated a gas phase of 54.6% CH_4 and 45.4% CO_2, and no hydrates were seen in the cell. The composition of the gas phase of the cell had not changed as cell pressure decreased due to the cooling of the reactor.

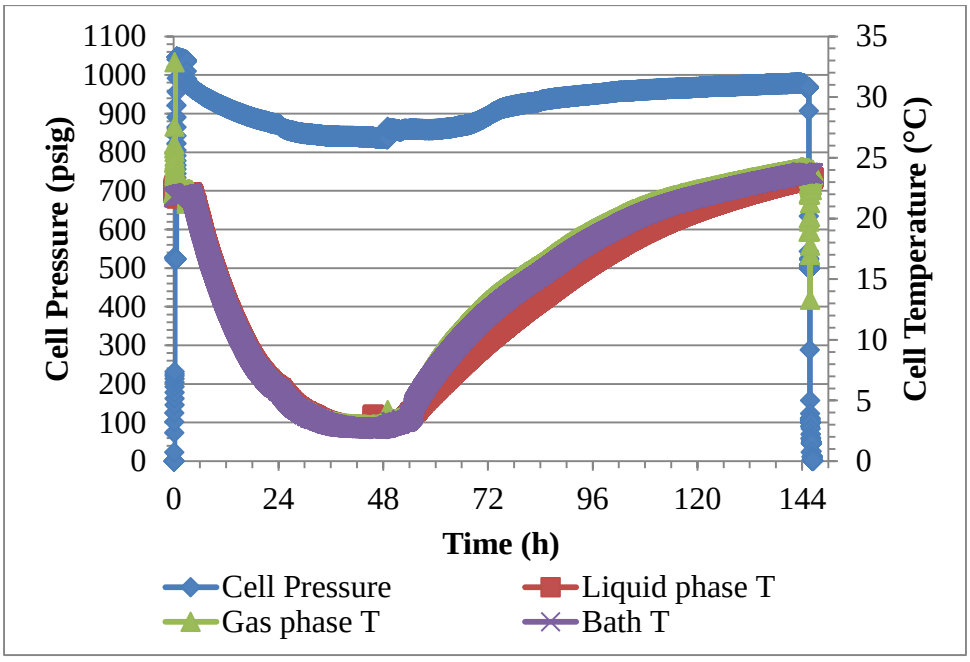

Figure 5.1: *Cell pressure and temperature data over time during Run 11*

After 47.9 h, hydrates were visible in the cell window, encasing the entire solution phase, and the hydrates did not expand to fill the gas region of the cell, as shown in Figure 5.2 (a). At this time, with pressure-temperature conditions of 842 psig and 3.2°C, a GC sample showed a gas phase composed of 56.7% CH_4 and 43.3% CO_2. The pressure drop due to hydrate formation was 72 psig, which corresponded to 7.8% conversion of gas into hydrates. Thirty minutes later, 339 mL of CH_4 gas was added to the cell, increasing cell pressure to 866 psig, to agitate the system and to make sure that all of the solution in the cell had formed gas hydrates. Unsurprisingly, when CH_4 was added to the system, the gas had to make a path through what were clearly solid gas hydrates, as shown in Figure 5.2 (b). A GC sample taken after this gas addition showed a gas phase that was identical to the sample taken prior to adding this gas to the cell. This indicated that all CH_4 added to the cell instantly formed hydrates. The cell was left cooling for over two hours, and at a pressure of 862 psig at 3.3°C, the gas phase of the cell was found to be 57.2% CH_4 and 42.8% CO_2. Since the gas composition and pressure had not changed much and such a solid hydrate plug had formed in the system, at this time cooling was ended, and the cell was allowed to warm up to room temperature for three days to dissociate the hydrates formed. Once the cell had reached room temperature (24°C), GC samples were taken as the cell was depressurized in steps. Prior to depressurizing the cell, at 975 psig and 24.1°C, the cell was composed of 60.3% CH_4 and 39.7% CO_2. As the cell was depressurized in several pressure drops, the amount of CO_2 in the gas phase drastically increased as CO_2 evolved from the 5 wt% $BaCl_2$ solution, as shown by the GC data plotted in Figure 5.3 (b). At 510 psig and 23.8°C, gas in the cell was made up of 59.8% CH_4 and 40.2% CO_2. At 102 psig and 23.6°C, the gas phase was composed of 54.1% CH_4 and 45.9% CO_2, while at 50 psig and 23.8°C, the cell contained 24.2% CH_4 and 75.8% CO_2. A last GC sample taken at 15 psig and 23.9°C indicated 16.1% CH_4 and 83.9% CO_2.

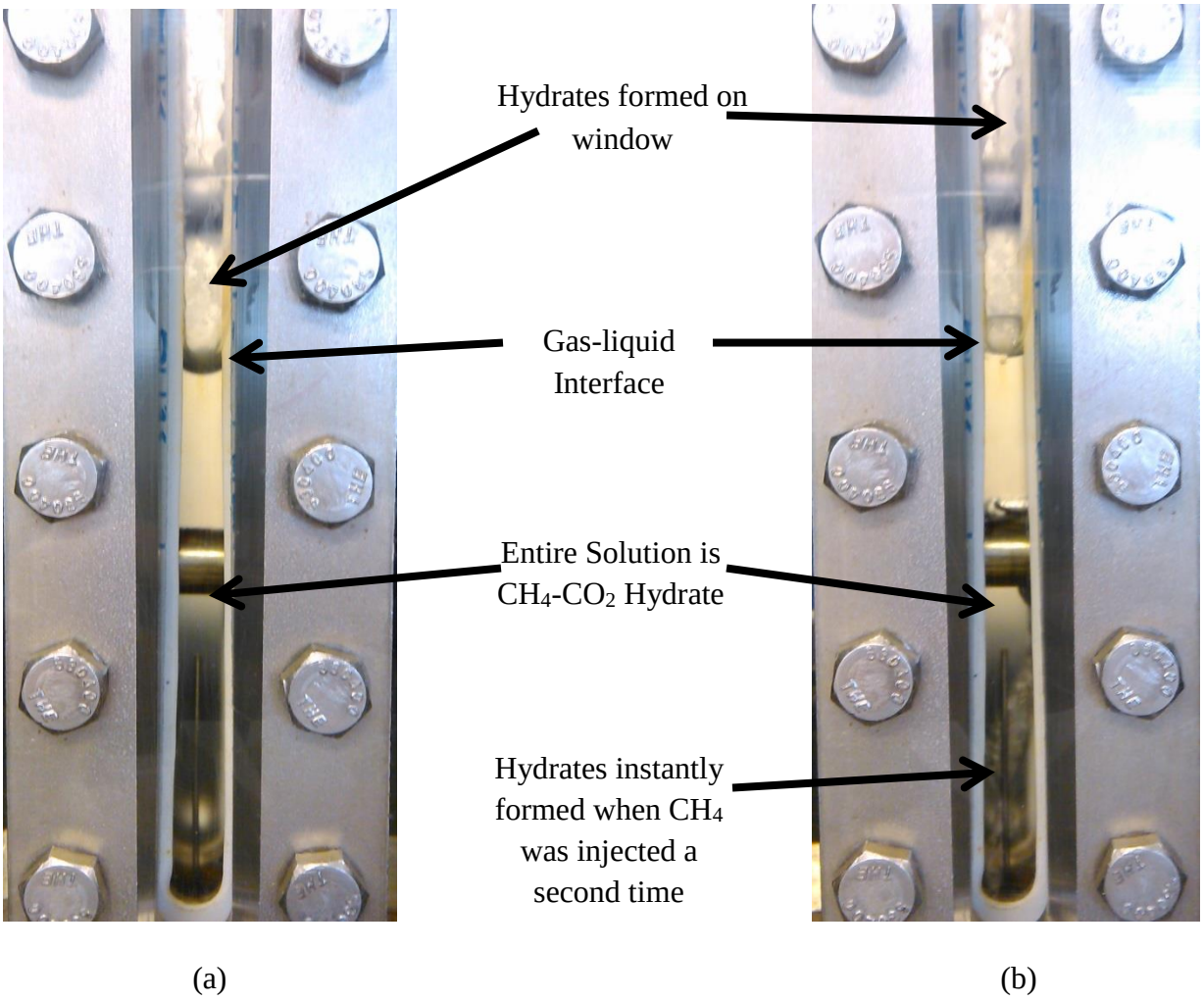

Figure 5.2: *(a) Run 11 gas hydrates initially viewed in cell 47.9 h after cell pressurization, at 840 psig and 3.0°C. GC samples indicated that the composition of the gas phase was 56.7% CH_4 and 43.4% CO_2. (b) Gas hydrates in cell after second CH_4 gas injection at 48.5 h. The cell was at 866 psig and 3.0°C, and the gas phase composition was identical to (a).*

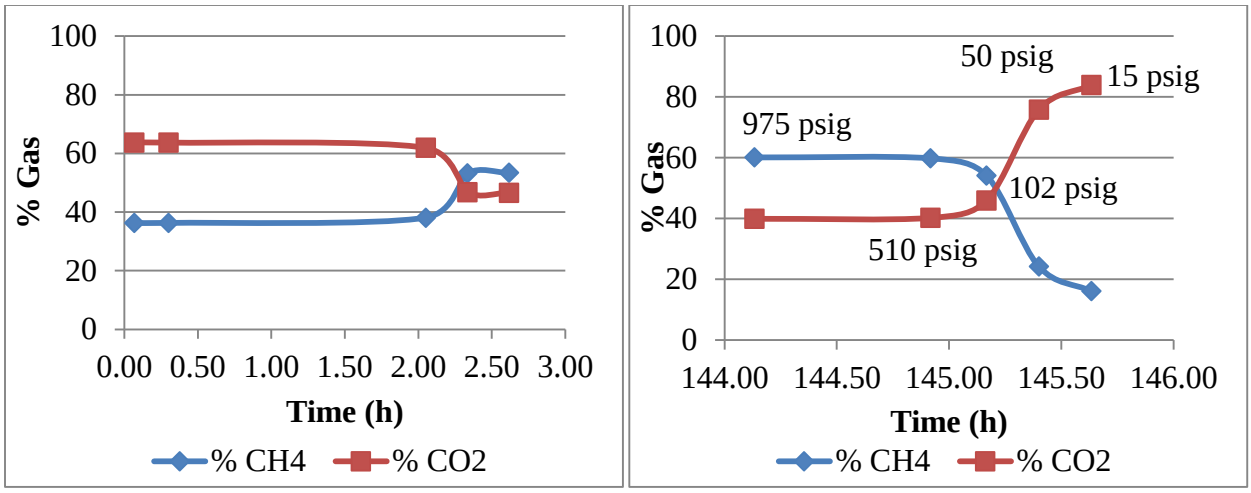

(a) (b)

Figure 5.3: *(a) Initial gas phase compositions upon cell pressurization for Run 11. GC samples indicated that the composition of the gas phase was nearly constant until hydrate dissociation. (b) Gas phase compositions during depressurization of the cell in steps. The cell pressure values at each GC sample are indicated, and the cell was at room temperature (24°C) for all samples.*

For Run 12, CH_4 hydrates were formed, followed by a CO_2 gas injection into the system. The same 75 mL of 5 wt% $BaCl_2$ used in the previous experiment was utilized again for this experiment. In between experiments, the system was warmed up to room temperature (23°C), and nitrogen gas was flushed through the cell. The cell was pressurized to 962 psig with CH_4 gas at 23.6°C, and then cooling was begun. Figure 5.4 plots cell pressure and temperature over time through hydrate formation and dissociation. After 21.3 h of cooling at 896 psig and 6.4°C, hydrates were visible in the cell at the gas-liquid interface. Hydrates did not change noticeably in appearance over the next 22 hours, and a 20 psig pressure drop was attributed to hydrate formation, resulting in a 2.2% conversion of CH_4 into hydrates. An image of CH_4 hydrates in the cell is shown in Figure 5.5 (a).

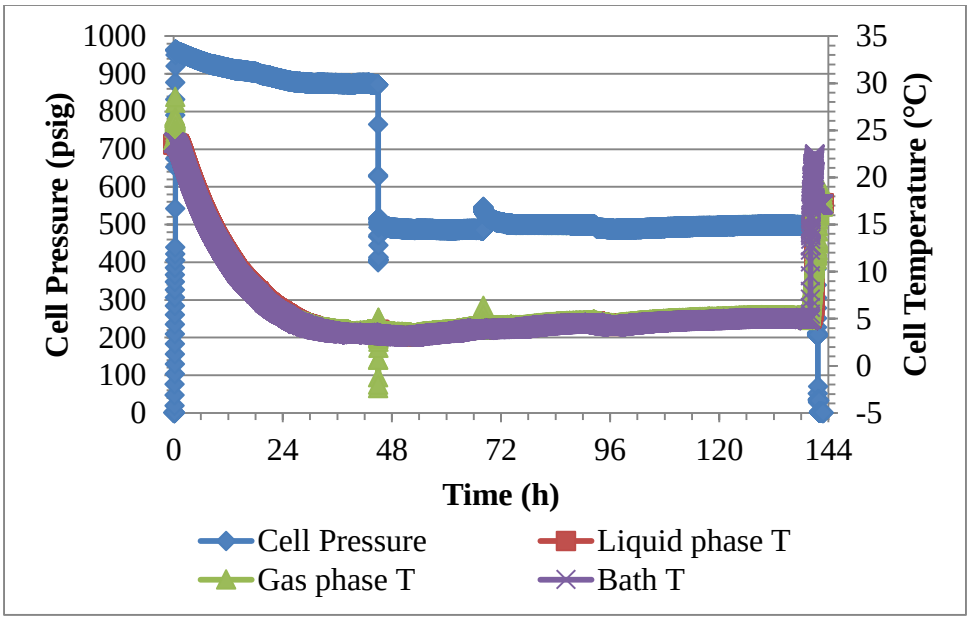

Figure 5.4: *Cell pressure and temperature data over time during Run 12*

At this point, CO_2 was introduced into the system. Prior to adding CO_2, the cell was depressurized to 409 psig at 3.4°C, and then CO_2 from the Hoke reactor was allowed to mix with CH_4 in the Jerguson cell. All CH_4 hydrates dissociated when cell pressure was lowered to allow for the addition of gaseous CO_2. Pressure increased to 524 psig at 3.7°C, and hydrates instantly formed around CO_2 gas bubbles. Figure 5.5 shows images of the hydrates that formed in the cell over time, and Figure 5.6 (a) plots gas composition data directly after CO_2 was added to the cell. GC samples indicated a pure CH_4 gas phase for the next two hours, but after 22 hours, the gas phase was composed of 97.5% CH_4 and 2.5% CO_2. Cell pressure had dropped to 491 psig at 4.2°C, corresponding to a 6.2% conversion of gas into hydrates. Next, CO_2 from the Hoke reactor was allowed to mix with the gases in the system for a second time. Pressure in the Jerguson cell increased to 549 psig at 4.1°C, and once again, hydrates instantly formed around gas bubbles. A GC sample taken at this time indicated 93.8% CH_4 and 6.2% CO_2. Over the next two days, the percentage of CO_2 in the gas phase continued to increase, reaching 16.1% CO_2 at 493 psig and 5.3°C. This pressure drop indicated that an additional 9.9% of gas in the cell was converted into hydrates, making total gas conversion at this time 16.1%. A subsequent GC sample indicated that the composition of the gas phase did not change, therefore cell cooling was ended and the water bath cooling the Jerguson cell was drained and refilled with warm water.

All hydrates dissociated quickly, and once the cell reached 17°C, the system was depressurized in steps. Three gas samples were taken, and GC data is plotted in Figure 5.6 (b). An initial sample at 551 psig and 16.9°C indicated a gas phase composition of 81.2% CH_4 and 18.8% CO_2. At 210 psig and 16.5°C, the gas phase was 64.9% CH_4 and 35.1% CO_2, while the final sample taken at 35 psig and 17.3°C indicated 1.9% CH_4 and 98.1% CO_2 in the gas phase. It was clear that large quantities of CO_2 had been solubilized in the 5 wt% $BaCl_2$ solution.

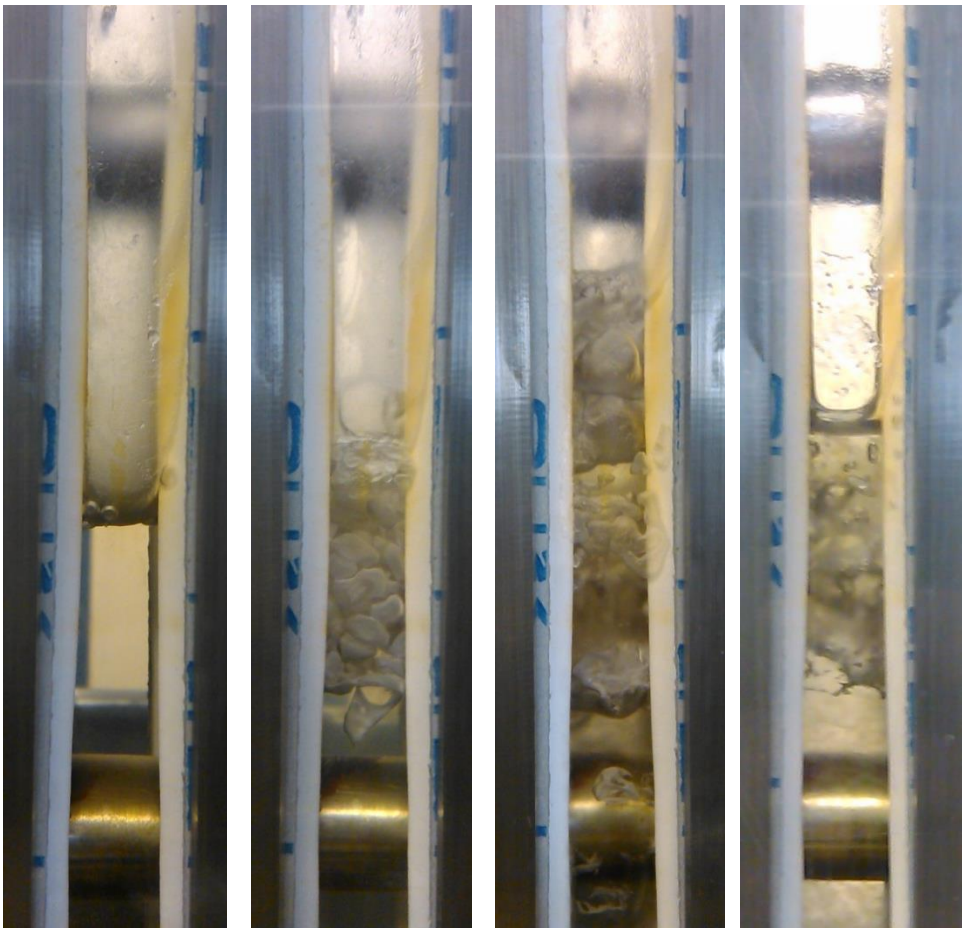

(a) (b) (c) (d)

Figure 5.5: *Hydrate formation at the gas-liquid interface. (a) CH_4 hydrates viewed in the cell during Run 12, 44.5 h after cell pressurization with CH_4 at 876 psig and 3.4°C. (b) At 44.8 h, the cell was partially depressurized and CO_2 was introduced into the cell. At 520 psig and 3.7°C, the gas phase consisted of pure CH_4 gas. (c) At 72.3 h, after a second CO_2 gas mixing at 510 psig and 4.1°C, the gas phase of the cell was 92.5% CH_4 and 7.5% CO_2. (d) After 139.5 h, at 493 psig and 5.3°C, the gas phase was composed of 81.2% CH_4 and 16.1% CO_2.*

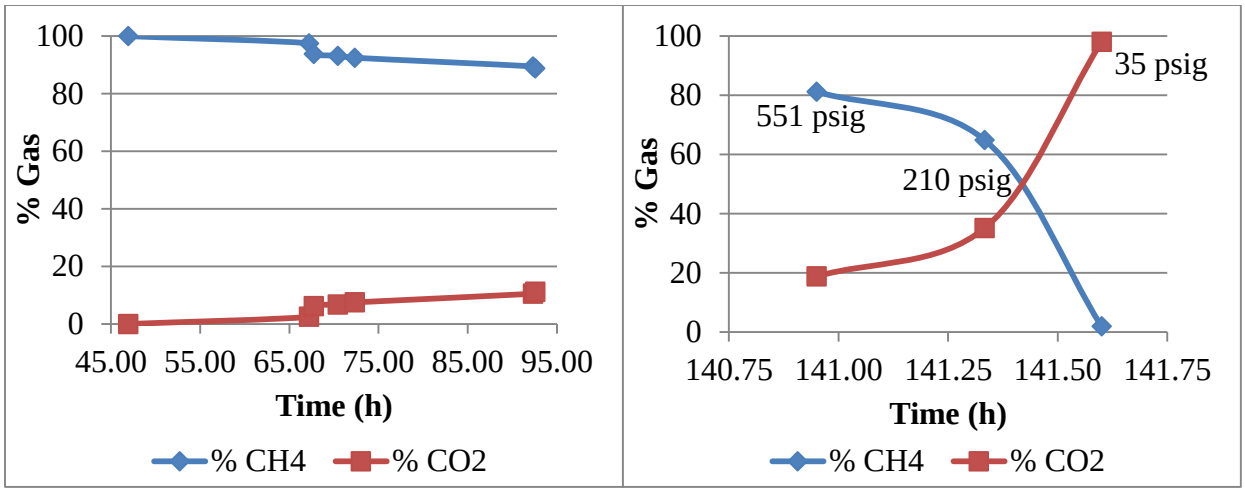

(a) (b)

Figure 5.6. *(a) Gas phase compositions after CO_2 injection for Run 12. While the gas phase remained of pure CH_4 for a while, over time, the amount of CO_2 in the gas phase increased. (b) Gas phase compositions during depressurization of the cell in steps. The cell pressure values at each GC sample are indicated, and the cell was at room temperature (17°C) for all samples.*

Prior to Run 13, the bath water had been drained, and the bath was refilled with water at room temperature. Nitrogen gas was also flushed through the cell, and the same 75 mL of 5 wt% $BaCl_2$ used in the previous two runs was used to form CO_2 hydrates. The cell was pressurized up to 605 psig with CO_2 gas at 17.9°C. Cell pressure and temperature over time are plotted in Figure 5.7. CO_2 hydrates formed in less than 24 hours, and a pressure drop to 516 psig indicated a 10.5% conversion of CO_2 gas into hydrates. At 24 h, a second batch of CO_2 gas was injected into the cell, and hydrates formed instantly around gas bubbles as they entered the reactor. Figure 5.8 shows CO_2 hydrates formed before and after the second CO_2 gas injection. CO_2 hydrates formed prior to the second CO_2 gas injection at the gas-liquid interface remained intact, and additional hydrates accumulated below, though there was a region of solution between the two sets of hydrates formed. This second CO_2 charging led to an additional 1.7% gas conversion into hydrates.

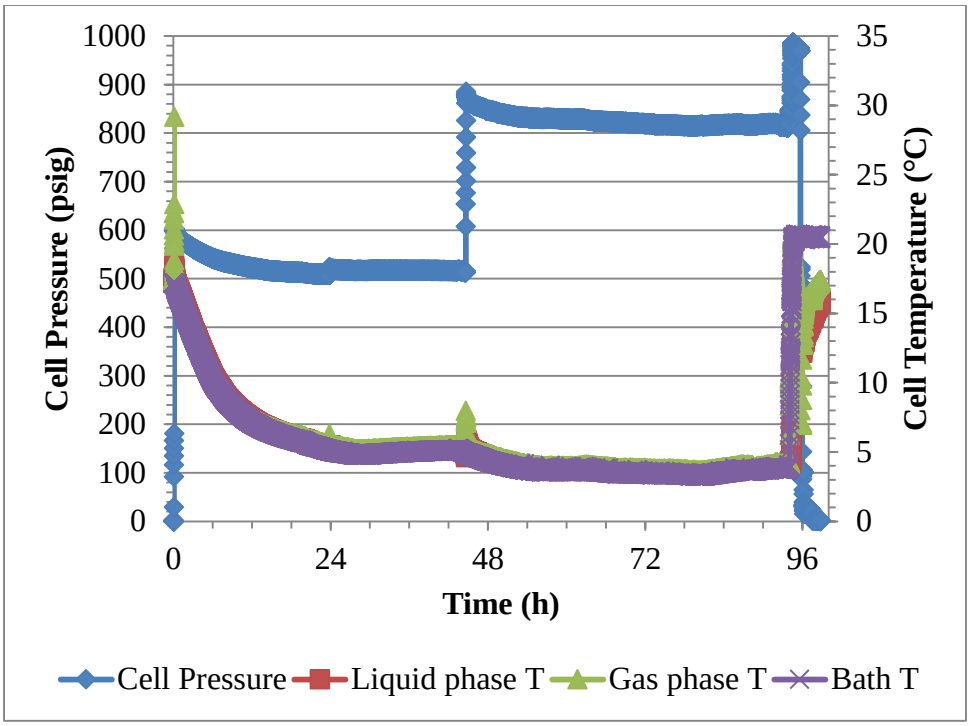

Figure 5.7: *Cell pressure and temperature data over time during Run 13*

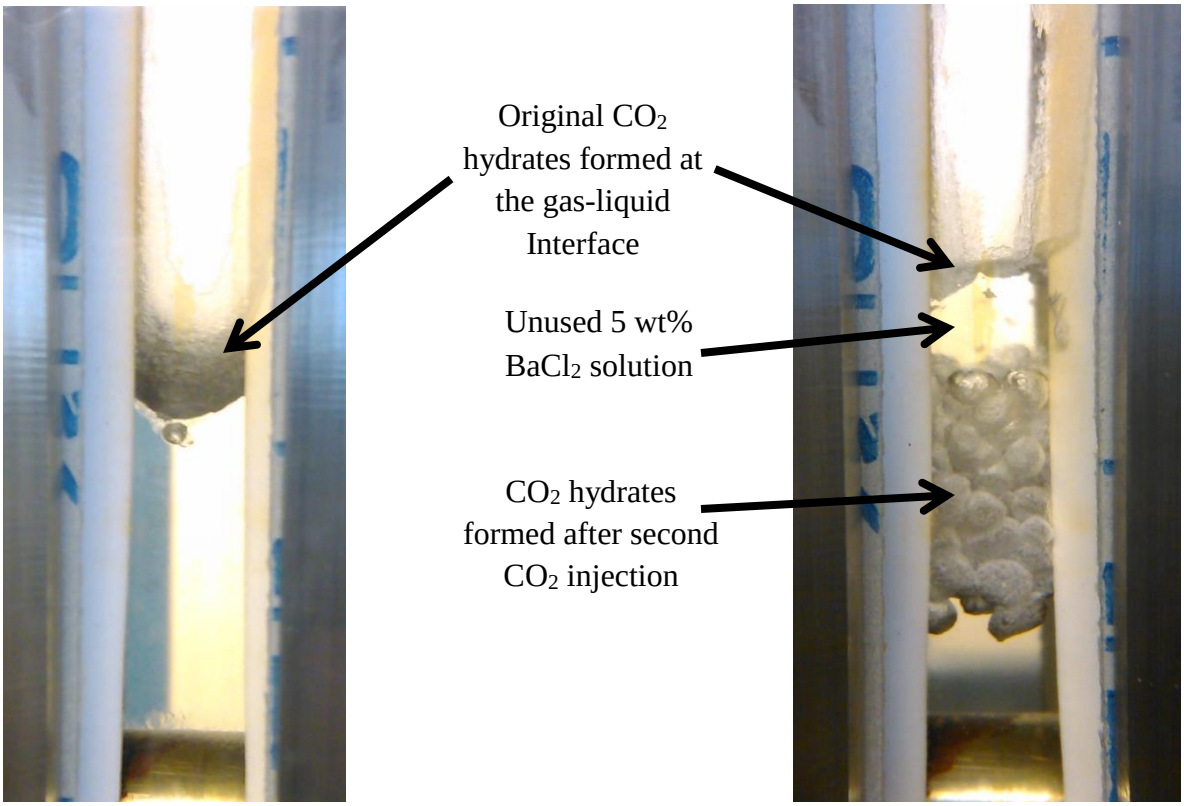

Figure 5.8: *(a) CO_2 hydrates from Run 13 at the gas-liquid interface 19.8 h after cell pressurization at 519 psig and 5.9°C. (b) At 23.8 h, the cell was pressurized a second time with CO_2, and CO_2 hydrates formed instantly at 530 psig and 5.4°C, though they accumulated beneath the original gas-liquid interface with unused 5 wt% $BaCl_2$ solution in between.*

The following day, 44.7 h after cell pressurization with CO_2, CH_4 was injected into the cell to raise cell pressure to 882 psig at 5.6°C. Figure 5.10 (a) plots gas composition values during the initial stages of the CH_4 injection. GC samples taken at this time indicated a CO_2 rich gas phase composed of 12.6% CH_4 and 87.4% CO_2, but over the next several days, as GC samples were taken, the amount of CH_4 slowly increased in the gas phase, until cell pressure stabilized at 93.5 h at 820 psig at 3.9°C. At this point, the gas phase comprised of 22.3% CH_4 and 77.7% CO_2, and the pressure drop witnessed corresponded to a 5.3% conversion of gas into hydrates. The partial pressure of CH_4 in the system increased over time, while the partial pressure for CO_2 decreased, indicating that more CO_2 hydrates formed as CH_4 and CO_2 exchanged in the gas hydrate phase. Photographs of hydrates in the cell were also taken over time in Figure 5.9, but there was no clear hydrate growth over time. At 94.0 h, cell cooling was ended, and the cell was allowed to warm up to dissociate gas hydrates. Once all hydrates had dissociated, the system was depressurized in steps, and five GC samples were taken and plotted in Figure 5.10 (b). At 95.5 h, at 974 psig and 16.2°C, the gas phase was made up of 29.0% CH_4 and 71.0% CO_2. When the cell was depressurized to 487 psig at 15.6°C, the gas phase was 45.0% CH_4 and 55.0% CO_2, while at 104 psig and 15.3°C, the gas phase was similar at 43.3% CH_4 and 56.7% CO_2. Once the cell was depressurized to 26 psig at 15.4°C, the gas in the cell was composed of mostly CO_2 gas, at 12.4% CH_4 and 87.6% CO_2. The cell was allowed to stabilize and warm up for an additional hour at 26 psig and 16.4°C, and a GC sample taken at that time indicated a gas phase of 9.8% CH_4 and 90.2% CO_2.

(a) (b) (c)

Figure 5.9: *(a) Taken during Run 13 right after the cell was injected with CH_4 at 44.7 h after cell pressurization with CO_2, at 877 psig and 5.8°C. The gas phase of the cell at this time was 12.6% CH_4 and 87.4% CO_2. (b) At 69.1 h, at 828 psig and 3.6°C, the gas phase consisted of 22.3% CH_4 and 77.7% CO_2. (c) At 92.5 h, at 822 psig and 4.0°C, the gas phase of the cell was 22.2% CH_4 and 77.8% CO_2. Shortly after this image was taken, cell cooling ended to dissociate gas hydrates.*

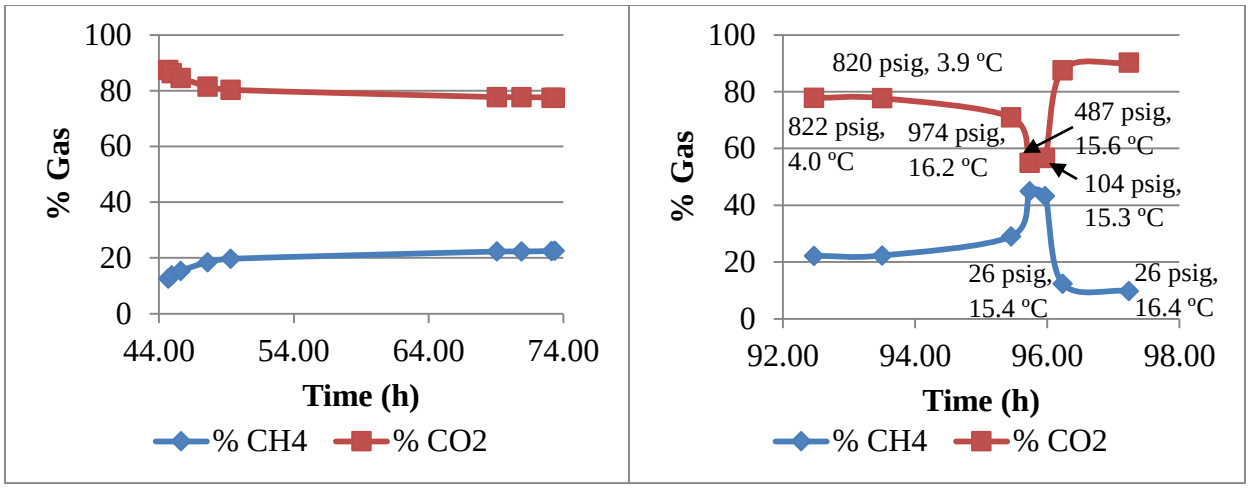

(a) (b)

Figure 5.10: *(a) Gas phase compositions after CH_4 injection during Run 13. While the gas phase was composed of a majority of CO_2, over time, the amount of CH_4 in the gas phase increased. (b) Gas phase compositions during depressurization of the cell in steps. The cell pressure and temperature values at each GC sample point are indicated.*

5.1.1 Macroscale CH_4-CO_2 Hydrate Formation in 5 wt% $BaCl_2$ Discussion

Three hydrate formation experiments were performed in the Jerguson cell to compare macroscale hydrate growth in 5 wt% $BaCl_2$ to hydrate growth on a microscale during CMT imaging at the NSLS. A summary of the experimental conditions, induction times, and gas conversions into hydrates is listed in Table 5.1.

Table 5.1: *Macroscale CH_4-CO_2 Hydrate Formation Run Summary*

Run	Gas	Initial Pressure	Cell Temperature	Initial Induction Time	Conversion
		psig	°C	H	%
11	CH_4-CO_2	976	3	<48	7.8±0.6
12	CH_4	962	4	<21	2.2±0.6
	CH_4-CO_2	524			6.2±0.6
	CH_4-CO_2 (second CO_2 charge)	549			9.9±0.6
13	CO_2	605	4	<24	10.5±0.6
	Second CO_2 charge	530			1.7±0.6
	CH_4-CO_2	882			5.3±0.6

It is clear that gas hydrates formed in large volumes in less than two days in these experiments. Gas hydrates were similar in appearance for Runs 12 and 13 where they formed initially at the gas-liquid interface, and then, when a secondary gas was injected into the system, hydrates formed around incoming gas bubbles. Hydrates formed in Run 11 had the appearance of solid ice, though the temperature of the system was above the ice stability regime, and the hydrates formed did not expand noticeably beyond the initial volume of the salt solution in the cell. The hydrates formed in Run 11 were similar in appearance to the pure CO_2 hydrates formed in Runs 2 and 3 in Chapter 3. The percentage of CO_2 in the gas phase during this run was reduced by 20% once hydrates were viewed in the cell. It is likely that mostly CO_2 hydrates had formed in Run 11, which is why their appearance was similar to previous pure CO_2 hydrates.

As seen in Runs 4 and 5 in Chapter 3, the gas phase of the mixed CH_4-CO_2 Run 11 was initially mostly composed of CO_2 gas. As with those previous runs, the percentage of CO_2 in the gas phase decreased with time in Run 11, however CH_4 became the majority component of the gas phase much more quickly for Run 11 (2 h) than for Run 4 (between 170-284 h) and Run 5 (between 96-119 h). As 300 ppm SDS, a hydrate promotor solution, was used for Runs 4 and 5, it is surprising that the induction time for CH_4-CO_2 hydrates formed in Run 11 with 5 wt% $BaCl_2$, a hydrate inhibitor, was shorter. It is possible that the longer induction times for Runs 4 and 5 were due to SDS precipitation.

As seen in Runs 6-10 in Chapter 4, in Runs 12 and 13, the gas that was injected first to form hydrates initially made up a majority of the system's gas phase immediately after the secondary gas was bubbled into the system. Still, in Runs 12 and 13, the first gas in the system was found to make up a majority of the gas phase until stepwise system depressurization was begun.

In all of these runs, the system was warmed up to >15°C prior to the stepwise depressurization of the system. Interestingly, the composition of the gas phase of the cooled hydrate system was very similar to the gas phase of the warmed up cell once hydrates were no longer present. It was not until pressure was reduced in the system that the composition of the gas phase changed, and in all systems, the proportion of CO_2 in the system increased. This seems to suggest that the proportion of CH_4 and CO_2 in gas hydrates in these systems scaled with the composition of the gas phase prior to hydrate dissociation.

As the cell was depressurized in steps for each of these runs, the composition of CO_2 in the gas phase increased. As discussed in Chapter 4, this is likely due to CO_2 evolving from the 5 wt% $BaCl_2$ solution and CO_2 hydrates. CO_2 is more soluble in water at high pressures and low temperatures, so by reducing the pressure and increasing the temperature of the system, some CO_2 will be released from the hydrate forming solution.

5.2 Small Volume Test Cell Runs

Before imaging was attempted at the NSLS, preliminary hydrate formation runs were performed to ensure that gas hydrates would form in these smaller diameter cells. In these experiments, 1", ½", and ¼" OD stainless steel cells, described in Chapter 2, were used to form gas hydrates. In addition, a CMT cell, made from ¼" OD aluminum tubing, also described in Chapter 2, was used in these test runs. Each of the sample cells and the CMT cell can be attached to a top assembly containing a pressure transducer.

In these experiments, various amounts of 5 wt% $BaCl_2$ or 300 ppm SDS solution were syringed into the different cells. Salt solution was used as a surrogate to simulate seafloor conditions and as a contrasting agent for CMT imaging. SDS is a known hydrate promoter used to encourage hydrate formation. These cells were then evacuated and pressurized to the experimental pressure; for CO_2 hydrates, a pressure of 450-650 psig (3.2-4.6 MPa) was used and for CH_4 hydrates, a pressure of 950 psig (6.7 MPa) was used. The cell was then either placed horizontally into a water bath with an isothermal temperature above freezing that was controlled by an ethylene glycol-water cooled refrigerated circulator set at varying temperatures, or the cell was positioned at an angle directly into the ethylene glycol-water cooling bath of the refrigerated circulator. A more detailed experimental procedure can be found in Chapter 2.

In 24 hours to 1 week, a pressure drop occurred, indicating the formation of gas hydrates. Pressure and temperature values over time were recorded. Once a run was completed, the cell was depressurized slowly, and pressure drop data was used to determine the percentage of gas that was converted into gas hydrates. This analysis has shown that mass transfer area (tube diameter), temperature, gas-liquid ratio, and system agitation have a significant effect on the percent conversion of gas into gas hydrates.

Many CH_4 hydrate and CO_2 hydrate formation runs were attempted, and Tables 5.2 and 5.3 list the parameter ranges for the experiments performed. Detailed summaries of the

experimental conditions and conversions for all of the runs performed are listed in Tables 5.4 and 5.5 at the end of this chapter. As 80 small cell runs were performed (40 to form CH_4 hydrates and 40 to form CO_2 hydrates), runs will be discussed in groups. Throughout all of these runs, the experimental cell was tapped or shaken to agitate the solution to promote further gas hydrate formation.

Table 5.2. *CH_4 Hydrate Formation Runs*

Cell	Solution	# of Runs	Solution Volume	Gas-Liquid Volume Ratio	Bath T	Charging Pressure	Pressure Drop	Conversion
			mL		ºC	psig	psi	%
1/4"	300 ppm SDS	9	1.5-4	1.3-5.1	3.7 – 4.5	922-976	0-241	0 - 9.7
	300 ppm SDS + Ottawa Sand	1	4	1.2	4.5	944	12	0.5
	300 ppm SDS + 5 wt% $BaCl_2$ + Ottawa Sand	3	4	1.3	4	936-949	18-111	0.7 - 4.5
	5 wt% $BaCl_2$	8	2-4	1.3-4.2	0 – 5.7	914-950	0-43.7	0-3.9
1/2"	5 wt% $BaCl_2$	4	4-5	2.5-3.4	3.5-3.9	942-950	77-105	7.6-11.1
		5	6	1.9	2-3.5	942-944	16-234	1.0-14.0
		3	8-10	0.8-1.2	4-5	937-941	9-194	0.2-5.6
1"	300 ppm SDS	2	20	2.6	4.1-4.8	930-936	300-319	24.2 - 25.6
	5 wt% $BaCl_2$	5	20	2.6	2-4.5	933-942	100-185	8.1 - 15.0

Table 5.3: *CO_2 Hydrate Formation Runs*

Cell	Solution	# of Runs	Solution Volume	Gas-Liquid Volume Ratio	Bath T	Charging Pressure	Pressure Drop	Conversion*
			mL		ºC	psig	psi	%
1/4"	300 ppm SDS	3	2-2.5	2.6-3.3	1.7-2	651-696	29-200	2.5-21.4
	300 ppm SDS + Glass Beads	3	0.75-1.5	3.6-7.5	2-3.4	690-699	84-122	13.5-29.5
	5 wt% $BaCl_2$	7	2.5	2-2.6	2-6.6	404-639	60-166	4.9-13.9
	5 wt% $BaCl_2$ + Glass Beads	2	2	2.9	2-4.5	672-783	104-152	5.3-9.9
	5 wt% $BaCl_2$ + Ottawa Sand	5	1.4-2.5	2.1-4.5	1.7-2	602-662	16-110	2.3-7.9
1/2"	300 ppm SDS	1	6	3.2	2	652	70	7.2
	Distilled Water	1	6	3.2	2	651	55	5.6
	5 wt% $BaCl_2$	9	4-6	1.9-5.2	1.9-6.5	369-665	3-133	0.2-20.2
1"	300 ppm SDS	1	20	2.6	2	656	105	8.9
	Distilled Water	2	20	2.6	2	649-657	95-129	8.0-10.9
	5 wt% $BaCl_2$	6	15-25	1.9-3.8	2-3.7	388-460	39-140	4.8-11.7

*Conversion of CO_2 gas into hydrates was calculated using the same conversion calculation methods described in Chapter 2. However, as CO_2 is very soluble in water, and CO_2 solubility increases with decreasing temperature, it is likely that some of the pressure drop used to determine conversion was due to CO_2 solubility; therefore, actual conversion values are likely to be slightly below those reported.

5.2.1 CH_4 Hydrate Runs

Runs to form CH_4 hydrates in a ¼" OD tube were performed in either a ¼" stainless steel cell or in the ¼" aluminum CMT cell, with volumes ranging from 7.4-10.3 mL. CH_4 hydrate Run 3 was performed in the ¼" CMT cell using the same 4 mL of 300 ppm SDS solution and CH_4 gas as the previous Run 2, with an initial pressure of 922 psig. After ~48 hours, pressure had dropped 55 psig below the expected pressure drop due to cell cooling at 4.5ºC (866 psig). This indicated a 2.2% conversion of CH_4 gas into hydrates. Studies[54] have shown that hydrates nucleate at a faster rate if they are formed in solutions that have been previously depleted of hydrates, but in this run, this hydrate memory effect was not seen, as the previous Run 2 had resulted in a 6.6% conversion of gas into hydrates. As discussed in Chapter 3, the SDS used as a promoter has a tendency to precipitate out of aqueous solutions. Lee et al.[108] verified that when higher concentrations of SDS are placed under higher pressures, SDS was found to precipitate out earlier than at lower concentrations. In addition, the memory effect for hydrate growth will not occur if the solution is warmed above 25[54] or 28°C[17] or for too long a time period (several hours[17]). During the week that the cell was left at room temperature, it is possible that the temperature of the cell reached 28ºC. Another issue that emerged in the first few hydrate formation runs was heat transfer. The CMT cell is jacketed by a polypropylene tube, and during Runs 1-4 the tube was empty and only filled with air, so it is possible that, since heat transfer is slower through plastic, the temperature of the cell was not as low as the bath temperature. In subsequent runs using the CMT cell, the cooling jacket of the cell was filled with ethylene glycol and connected to the refrigerated circulator for better heat transfer.

CH_4 hydrate Runs 5-9 were performed similarly in the ¼" CMT cell with 300 ppm SDS solution. In these runs, two small stainless steel balls were added into the cell. Throughout all hydrate formation runs, the cell was agitated by shaking or tapping the cell to encourage hydrate nucleation, and the presence of these spheres helped disturb the solution further. Run 8 was performed similarly to the previous Runs 5-7, but this time a fresh 300 ppm SDS solution was made. For the previous runs, a bulk 300 ppm SDS solution created at the start of Run 1 was used, and the bulk solution was shaken to redissolve any precipitated SDS prior to loading solution into the cell. Since SDS precipitation is known to be an issue, the creation of fresh solution each time that a run was performed ensured that SDS was newly dissolved in the solution. In this run, 4 mL of 300 ppm SDS solution with an initial pressure of 943 psig was

cooled, and after less than 24 hours, cell pressure had decreased to 644 psig at 4ºC. This 241 psig pressure drop corresponded to a 9.7% conversion of CH_4 into hydrates. This was the largest pressure drop and conversion seen in ¼" CH_4 hydrate formation runs, indicating that the presence of the stainless steel balls and fresh SDS solution was beneficial to hydrate formation.

While conversions of gas into hydrates were achieved for CH_4 hydrate Runs 11-13, these runs were overall unsuccessful. For these runs, CMT imaging at the NSLS was attempted to view hydrates formed in a 4 mL 300 ppm SDS / 5 wt% $BaCl_2$ solution in Ottawa sand in the ¼" CMT cell. When CMT imaging was attempted, bright spots were seen that complicated the viewing of the images obtained. At this time, it was discovered that when SDS and $BaCl_2$ were used together to create a solution, $BaCl_2$ precipitates out. $BaCl_2$ is very dense and has high x-ray attenuation, which creates bright spots on CMT images, making it difficult to determine the other phases present in the cell. From this point on, only 5 wt% $BaCl_2$ solutions were used for imaging attempts.

Eight experiments were performed to form CH_4 hydrates in a 5 wt% $BaCl_2$ solution. These experiments did not result in significant conversion of CH_4 into hydrates (0-3.9%). Salt inhibits hydrate formation, and the combination of salt and low gas volume in the cell for some of the experiments might have made hydrate nucleation more difficult. Due to the small volume of the ¼" cell, it is difficult to have a large enough gas-liquid surface area to promote hydrate formation, as CH_4 hydrates accumulate at the gas-liquid interface. After hydrates have formed at this interface, hydrate formation ends as the hydrates that have formed block any remaining CH_4 gas from reaching the solution left in the cell. For these reasons, several experiments were also performed to form CH_4 hydrates in ½" and 1" cells.

In a ½" cell, twelve runs were performed employing different volumes (4-10 mL) of 5 wt% $BaCl_2$ solution to form CH_4 hydrates. The runs with the highest percent conversion of gas into hydrates were those performed with 6 mL of solution. The most successful run, CH_4 hydrate Run 31, was performed in the ½" cell with 6 mL of 5 wt% $BaCl_2$ and 2 stainless steel balls. The cell was pressurized up to 943 psig and was cooled in a secondary bath at 4ºC. To initiate hydrate formation, after one day of cooling, the temperature of the refrigerated circulator was lowered slightly, resulting in a bath temperature of 2ºC for about 2 hours. Once this time had passed, the bath temperature was returned to 4ºC. After 4 days, pressure dropped 234 psig

which corresponded to a 14.0% conversion of CH_4 into hydrates. Overall, smaller gas-liquid volume ratios resulted in lower conversions of gas into hydrates. This is likely due to the fact that all of these runs had gas as the limiting reagent, so the addition of more solution to the cell did not further encourage hydrate nucleation. When 4-6 mL of solution were used, higher conversions of CH_4 into hydrate were achieved (up to 14.0%), while 8-10 mL of solution resulted in lower conversions (up to 5.6%). In addition, the run that resulted in the lowest conversion of gas into hydrate was quickly quenched from room temperature down to a bath temperature of 2°C. The cell cooling method used for all of the other experiments, where the cell was slowly cooled from room temperature to the selected temperature, was found to be a better method.

Seven experiments were performed in the 1" cell. CH_4 hydrate Run 19, performed with 20 mL of 5 wt% $BaCl_2$ solution and 939 psig of CH_4 gas at 2ºC, resulted in a 14.4% conversion of gas into hydrates. Run 21 was performed using the same $BaCl_2$ solution as Run 19, but the cell was repressurized up to 942 psig with fresh CH_4 gas and cooled directly in the refrigerated circulator at 2ºC. After a little less than 4 days, pressure dropped 692 psig which corresponded to a 15.0% conversion of CH_4 into hydrates. Though the increase was small, the hydrate memory effect could be seen. CH_4 hydrate Run 25 took place in a 1" SS cell with 20 mL of 300 ppm SDS and 2 stainless steel balls. The cell was pressurized up to 930 psig and cooled in a secondary bath at 4ºC. After 2 days, pressure dropped 556 psig which corresponded to a 25.6% conversion of CH_4 into hydrates. In the 1" SS cell, it was clear that a 300 ppm SDS solution was beneficial to CH_4 hydrate formation. The largest conversions (24.2-25.6%) of gas into hydrate were achieved with 20 mL of SDS solution in the 1" cell. Comparable conversions, ranging from 8.1–15.0% of gas into hydrate were also achieved with 5 wt% $BaCl_2$ solution. While SDS is beneficial to hydrate formation, this solution will not work for NSLS imaging as it has an x-ray attenuation coefficient equal to that of water and thereby too close to the attenuation value for CH_4 hydrates to be able to distinguish between hydrates and unused solution in the cell.

5.2.1.1 CH_4 Hydrate Runs Discussion

The memory effect was not seen in several runs performed with 300 ppm SDS solution, likely due to the fact that the SDS used as a promoter in these runs has been found to precipitate out of aqueous solutions and the temperature of the cell may have reached above 28ºC for

extended periods of time, thereby nullifying the memory effect. In many runs, two stainless steel spheres were placed inside the cell to help agitate the solution, and this additional source of agitation was found to increase the conversion of gas into hydrates. The use of solution mixtures of 300 ppm SDS and 5 wt% $BaCl_2$ together in the cell are not beneficial to hydrate formation, as $BaCl_2$ was found to precipitate out of the solution. Solutions of 300 ppm SDS resulted in higher conversions of gas into hydrates than 5 wt% $BaCl_2$ solution. This is not surprising, as SDS is a hydrate promoter and $BaCl_2$ is a hydrate inhibitor. In addition, higher gas to liquid volume ratios, and thereby lower volumes of solution in the cell, resulted in higher conversions of gas into hydrates. Overall, the conversion of gas into hydrates varied as these runs were performed at slightly different pressures and bath temperatures.

5.2.2 CO_2 Hydrate Runs

Several attempts to form CO_2 hydrates in a ¼" cell were attempted with 300 ppm SDS solution or 5 wt% $BaCl_2$ solution, with or without glass beads or Ottawa sand as a porous media. As noted in Table 5.3, the conversion values reported are likely to be slightly higher than actual CO_2 gas into hydrate conversions achieved in these experiments due to the effects of increased CO_2 solubility at lower temperatures.

For CO_2 hydrate Runs 1-11, the system was pressurized up to 450 psig with CO_2 to remain well within the CO_2 vapor phase stability region. CO_2 hydrate Run 5 was performed in a 1" cell with 20 mL of 5 wt% $BaCl_2$ solution and 2 stainless steel balls. The cell was pressurized up to 455 psig and then shaken to solubilize CO_2 in the solution, as CO_2 is quite soluble in water. This caused cell pressure to decrease, so the cell was charged again up to near 450 psig and shaken. This was repeated until cell pressure remained at 455 psig and did not decrease with shaking. Many other runs were performed similarly as to solubilize CO_2 at room temperature to maintain the initial charging pressure in the system. Then the cell was cooled in a secondary bath at 3.3ºC. After 4 days, pressure dropped 139 psig which corresponded to an 11.7% conversion of CO_2 into hydrates.

CO_2 hydrate Run 11 was performed in the ½" cell with 4 mL of 5 wt% $BaCl_2$ solution and 2 stainless steel balls. The cell was pressurized up to 454 psig and cooled to 4.2ºC. The cell was agitated by shaking it several times throughout hydrate formation. After 3 days of cell cooling, similar to CH_4 hydrate Run 31, the temperature of the bath was reduced to 3.4ºC for

three hours in an attempt to initiate hydrate formation. After this time, the bath temperature was returned to 4.2ºC. This change in temperature was found to cause a 12 psi pressure drop, and an overall pressure drop of 87 psig was achieved for this run, resulting in a 14.6% conversion of gas into hydrate.

These low pressure experiments (436-454 psig) resulted in 0.2-14.6% conversion of CO_2 into CO_2 hydrates in the ½" cell and 4.8-11.7% conversion in the 1" cell. As higher pressures encourage larger gas conversions into hydrates, for the subsequent runs, cells were pressurized to about 650 psig, which is just below the liquid-gas equilibrium curve for CO_2 at room temperature (22ºC). CO_2 hydrate Run 12 was performed in the ½" cell with 6 mL of 5 wt% $BaCl_2$ solution and two stainless steel balls. The cell was pressurized and agitated until pressure remained at 642 psig, and then the cell was cooled in a secondary bath at 4ºC. After three days, pressure dropped 131 psig, which resulted in a 12.8% conversion of CO_2 into hydrates. Similarly, CO_2 hydrate Run 15, performed with 4 mL of 5 wt% $BaCl_2$ solution and 2 stainless steel balls, was pressurized up to 640 psig and cooled to 6.5ºC. After four days, a pressure drop of 120 psig resulted in a 20.2% conversion of gas into hydrates. It is clear that a higher initial pressure and lower solution volume produce better gas conversions.

CO_2 hydrate Run 20 was performed in the ¼" CMT cell with 0.75 mL of 300 ppm SDS solution and 4.37 g of 0.5 mm glass beads. The cell was pressurized to 699 psig with CO_2 gas and cooled at 3.4ºC. After less than 24 hours, a 122 psig pressure drop had occurred, indicating a 29.5% conversion of CO_2 into hydrates. This run resulted in the highest achieved conversion of gas into hydrates in the small cells. Of all of the experiments performed, the three performed with 300 ppm SDS solution and glass beads had the highest conversion values (13.5-29.5%). Of course, these runs were performed with lower liquid and gas volumes due to the presence of glass beads, so while percent conversions are higher, larger volumes of hydrates may have formed in other experiments. A solution of 300 ppm SDS is known for being a better hydrate former, and the presence of glass beads must have led to the availability of more hydrate nucleation sites. These runs were also performed with the largest gas-liquid volume ratio. These experiments are in agreement with previously performed experiments with CH_4 or CO_2 gas which indicated that higher gas-liquid volume ratios are better for hydrate formation.

CO_2 hydrate Run 25 was performed using 2.5 mL of 5 wt% $BaCl_2$ solution in the ¼" cell and 2.05 g of Ottawa sand. The cell was pressurized to 644 psig and cooled to 2ºC. After cooling the cell for 1 day, a pressure drop of 93 psig resulted in a 6.4% conversion of gas into hydrates. At this point, the cell was warmed up to room temperature and left uncooled for two days. After two days, the cell was recooled to 2ºC for Run 25.5. After two days of cooling for Run 25.5, a pressure drop of 110 psig indicated a 7.6% conversion of CO_2 into hydrate. As the second run to form hydrates using the same gas and solution resulted in more hydrate formation, the memory effect was seen to occur, though run 25.5 was cooled for one day longer than Run 25.

The CO_2 hydrate formation runs performed with 5 wt% $BaCl_2$ solution and porous media (glass beads or Ottawa sand) resulted in the lowest gas conversion values (2.3-9.9%). The presence of porous media and solution volumes of 1.4 – 2.5 mL in these runs limited the volume of the cell available for CO_2 gas, which led to an excess solution system. The 300 ppm SDS solution with glass beads runs that resulted in such high conversions of gas into hydrates were performed with lower solution volumes (0.75 – 1.5 mL), thereby allowing for more CO_2 gas to be present in the cell.

5.2.2.1 CO_2 Hydrate Runs Discussion

As was expected, the runs performed with higher pressures resulted in higher conversions of gas into hydrates in all of the reactors used. Experiments with higher gas-liquid volume ratios and smaller volumes of solution were also found to have higher conversions of gas into hydrates. As was true with CH_4 hydrates, this CO_2 system was limited by the volume of CO_2 gas, therefore adding more solution to the system did not help initiate hydrate formation. Similar to CH_4 experiments, solutions of 300 ppm SDS resulted in higher conversions of gas into CO_2 hydrates than 5 wt% $BaCl_2$ solutions.

5.3 Conclusions

CH_4 and CO_2 hydrates did form on a macroscale in the Jerguson cell in 5 wt% $BaCl_2$ solutions. As most hydrates in Runs 11-13, as well as Runs 6-10 reported in Chapter 4, were witnessed to accumulate at the gas-liquid interface, CMT imaging, especially for experiments without a sand pack, will be focused at the gas-liquid interface.

Overall, it was found that both CH_4 and CO_2 hydrates will form in small volume cells. While the pressure drop and conversion of gas into hydrates varied from run to run, factors that were found to best encourage hydrates to form were: 1) Using higher gas pressures, 2) Using lower liquid volumes, and 3) Agitating the cell, using stainless steel balls and shaking. While larger percentages of hydrates were generally found to form in the ½" and 1" cells, the diameters of those reactors are too large for CMT imaging, therefore a ¼" CMT cell was utilized for the CMT imaging experiments performed and described in Chapters 6 and 7. In addition, though the 300 ppm SDS solution was better for hydrate formation, since a contrasting agent is needed to increase the x-ray attenuation coefficient for the hydrate forming solution, solutions containing varying proportions of $BaCl_2$ were utilized for CMT imaging.

Table 5.4: *Summary of all Small Cell CH_4 Hydrate Formation Experiments*

Run #	Cell	Media	Solution	V_{total}	V_{liquid}	V_{sand}	V_{gas}	$T_{chiller}$	T_{bath}	P_i at RT	P_i at T_{bath}	P_f	ΔP_{Hyd}	Conversion
				mL	mL	mL	mL	°C	°C	psig	psig	psig	psi	%
1	1/4" NSLS	none	300 ppm SDS	9.18	1.5	0	7.68	2	4	976	915.6	929	0.0	0
2	1/4" NSLS	none	300 ppm SDS	9.18	4	0	5.18	2	4.5	932	875.9	710	165.9	6.6
3	1/4" NSLS	none	300 ppm SDS (same as 2)	9.18	4	0	5.18	2	4.5	922	866.5	811	55.5	2.2
4	1/4" NSLS	Ottawa sand	300 ppm SDS	9.18	4	0.38	4.8	2	4.5	944	887.2	875	12.2	0.5
5	1/4" NSLS	2 SS balls	300 ppm SDS	9.18	4	0	5.18	2	3.7	932	873.3	842	31.3	1.3
6	1/4" NSLS	2 SS balls	300 ppm SDS (same as 5)	9.18	4	0	5.18	2	4	924	866.8	791	75.8	3
7	1/4" NSLS	2 SS balls	300 ppm SDS	9.18	4	0	5.18	2	4	939	867.9	871	0.0	0
8	1/4" NSLS	2 SS balls	300 ppm SDS	9.18	4	0	5.18	2	4	943	884.6	644	240.6	9.7
9	1/4" NSLS	2 SS balls	300 ppm SDS	9.18	4	0	5.18	2	4	945	886.5	803	83.5	3.3
10	1/4" NSLS	none	300 ppm SDS	9.18	4	0	5.18	2	4	944	885.5	862	23.5	0.9
11	1/4" NSLS	Ottawa sand	300 ppm SDS and 5 wt% $BaCl_2$	9.18	4	5	5.18	2	4	949	890.2	779	111.2	4.5
12	1/4" NSLS	Ottawa sand	300 ppm SDS and 5 wt% $BaCl_2$	9.18	4	5	5.18	2	4	945	886.5	868	18.5	0.7

13	1/4" NSLS	Ottawa sand	300 ppm SDS and 5 wt% $BaCl_2$	9.18	4	5	5.18	2	4	936	878.0	840	38.0	1.5
14	1/4" NSLS	none	5 wt% $BaCl_2$	9.18	4	0	5.18	2	0	929	858.7	815	43.7	1.8
15	1/4" NSLS	none	5 wt% $BaCl_2$	9.18	2	0	7.18	2	0	936	865.1	862	3.1	0.4
16	1/4" NSLS	none	5 wt% $BaCl_2$	9.18	2.5	0	6.68	2	0	940	868.8	843	25.8	2.2
17	1/4" SS	none	5 wt% $BaCl_2$	7.41	2.5	0	4.91	2	3	914	854.2	877	0.0	0
18	1/4" SS	none	5 wt% $BaCl_2$	7.41	2.5	0	4.91	2	2	943	878.1	859	19.1	1.2
19	1" SS	none	5 wt% $BaCl_2$	72	20	0	52	2	2	939	874.4	697	177.4	14.4
20	1/4" SS	none	5 wt% $BaCl_2$	7.41	2.5	0	4.91	2	2	950	884.6	891	0.0	0
21	1" SS	none	5 wt% $BaCl_2$ (same soln as 19)	72	20	0	52	2	2	942	877.2	692	185.2	15.0
22	1/2" SS	none	5 wt% $BaCl_2$ (quenched)	17.6	6	0	11.6	2	2	944	879.0	863	16.0	1.0
23	1" SS	2 SS balls	5 wt% $BaCl_2$	72	20	0	52	2	2	942	877.2	763	114.2	9.3
24	1/2" SS	2 SS balls	5 wt% $BaCl_2$	17.6	6	0	11.6	2	2	944	879.0	807	72.0	4.3
23.5	1" SS	2 SS balls	5 wt% $BaCl_2$ (same gas and soln as 23)	72	20	0	52	2	2	942	877.2	777	100.2	8.1
24.5	1/2" SS	2 SS balls	5 wt% $BaCl_2$ (same gas and soln as 24)	17.6	6	0	11.6	2	2	944	879.0	805	74.0	4.5

25	1" SS	2 SS balls	300 ppm SDS	72	20	0	52	2	4.8	930	875.0	556	319.0	25.6
26	1" SS	2 SS balls	300 ppm SDS	72	20	0	52	2	4.1	936	878.3	578	300.3	24.2
27	1" SS	2 SS balls	5 wt% $BaCl_2$	72	20	0	52	2	4.5	933	876.8	735	141.8	11.4
28	1/2" SS	2 SS balls	5 wt% $BaCl_2$	17.6	10	0	7.6	2	5	940	885.0	876	9.0	0.2
29	1/2" SS	2 SS balls	5 wt% $BaCl_2$	17.6	5	0	12.6	2	3.9	950	890.8	793	97.8	7.6
30	1/2" SS	2 SS balls	5 wt% $BaCl_2$	17.6	10	0	7.6	2	4	937	879.0	685	194.0	4.6
31	1/2" SS	2 SS balls	5 wt% $BaCl_2$	17.6	6	0	11.6	2	3.5	943	883.0	649	234.0	14.0
32	1/2" SS	2 SS balls	5 wt% $BaCl_2$	17.6	8	0	9.6	2	4	941	882.7	733	149.7	5.6
33	1/2" SS	2 SS balls	5 wt% $BaCl_2$	17.6	4	0	13.6	2	3.5	942	882.0	777	105.0	11.1
34	1/2" SS	2 SS balls	5 wt% $BaCl_2$	17.6	6	0	11.6	2	3.5	942	882.0	771	111.0	6.7
35	1/2" SS	2 SS balls	5 wt% $BaCl_2$	17.6	4	0	13.6	2	3.5	945	884.9	808	76.9	8.1
36	1/2" SS	2 SS balls	5 wt% $BaCl_2$	17.6	4	0	13.6	2	3.5	947	886.7	802	84.7	8.9
37	1/4" NSLS	none	5 wt% $BaCl_2$	10.31	2	0	8.31	2	4	944	885.5	861	24.5	3.2
38	1/4" NSLS	2 SS balls	5 wt% $BaCl_2$	10.31	2	0	8.31	2	5.7	942	889.2	859	30.2	3.9

Table 5.5: *Summary of all Small Cell CO_2 Hydrate Formation Experiments*

Run #	Cell	Media	Solution	V_{total}	V_{liquid}	V_{sand}	V_{gas}	T_{bath}	P_i at RT	P_i at T_{bath}	P_f	ΔP_{Hyd}	Conversion without solubility
				mL	mL	mL	°C	°C	psig	psig	psig	psi	%
1	1" SS	none	5 wt % $BaCl_2$	72	20	0	52	2	388	360.7	255	105.7	9.0
2	1/4" SS	none	5 wt % $BaCl_2$	7.41	2.5	0	4.91	2	404	375.6	299	76.6	4.9
3	1/2" SS	none	5 wt % $BaCl_2$	17.6	6	0	11.6	4	369	345.6	303	42.6	2.7
4	1/2" SS	none	5 wt % $BaCl_2$	17.6	6	0	11.6	4	442	414.1	411	3.1	0.2
5	1" SS	2 SS balls	5 wt % $BaCl_2$	72	20	0	52	3.3	455	425.2	286	139.2	11.7
6	1" SS	2 SS balls	5 wt % $BaCl_2$	72	25	0	47	3.3	460	429.9	290	139.9	8.5
7	1" SS	2 SS balls	5 wt % $BaCl_2$	72	20	0	52	3.7	452	423.1	308	115.1	9.7
8	1" SS	2 SS balls	5 wt % $BaCl_2$	72	15	0	57	3.3	454	424.3	385	39.3	4.8
9	1/2" SS	none	5 wt% $BaCl_2$	24.91	6	0	18.91	3.5	438	409.6	317	92.6	9.5
10	1/2" SS	2 SS balls	5 wt% $BaCl_2$	24.91	6	0	18.91	4	436	408.5	338	70.5	7.2
11	1/2" SS	2 SS balls	5 wt% $BaCl_2$	24.91	4	0	20.91	4.2	454	425.7	339	86.7	14.6
12	1/2" SS	2 SS balls	5 wt% $BaCl_2$	24.91	6	0	18.91	4	642	602.0	471	131.0	12.8
13	1/2" SS	2 SS balls	5 wt% $BaCl_2$	24.91	6	0	18.91	6.2	640	605.0	472	133.0	13.4
14	1" SS	2 SS balls	5 wt% $BaCl_2$	72	20	0	52	6	638	602.6	442	160.6	13.4
15	1/2" SS	2 SS balls	5 wt% $BaCl_2$	24.91	4	0	20.91	6.5	644	609.4	489	120.4	20.2
16	1/4" SS	2 SS balls	5 wt% $BaCl_2$	7.41	2.5	0	4.91	6.6	635	601.1	471	130.1	8.2
17	1/4" SS	Glass Beads	5 wt% $BaCl_2$	8.96	2	1.18	5.78	2	783	728.9	577	151.9	9.9
18	1/4" SS	Glass Beads	5 wt% $BaCl_2$	8.96	2	1.18	5.78	4.5	672	631.3	527	104.3	5.3
19	1/4" NSLS	Glass Beads	300 ppm SDS	8.1	1.5	1.18	5.42	2.8	690	644.2	529	115.2	13.5
20	1/4"	Glass	300 ppm SDS	8.1	0.75	1.75	5.6	3.4	699	654.0	532	122.0	29.5

	NSLS	Beads											
21	1/4" SS	Glass Beads	300 ppm SDS	8.96	1	1.18	6.78	2	695	646.9	563	83.9	18.5
22	1/4" SS	2 SS balls	5 wt% $BaCl_2$	8.96	2.5	0	6.46	2	639	594.7	435	159.7	13.4
23	1/4" SS	2 SS balls	5 wt% $BaCl_2$	8.96	2.5	0	6.46	2	638	593.8	428	165.8	13.9
24	1/4" SS	2 SS balls	5 wt% $BaCl_2$	8.96	2.5	0	6.46	4.6	638	599.5	540	59.5	5.0
25	1/4" SS	Ottawa sand	5 wt% $BaCl_2$	8.96	2.5	1.2	5.26	2	644	599.4	506	93.4	6.4
25.5	1/4" SS	Ottawa sand	5 wt% $BaCl_2$ (same gas & soln from 25)	8.96	2.5	1.2	5.26	2	602	560.2	450	110.2	7.6
26	1/4" SS	Ottawa sand	5 wt% $BaCl_2$	8.96	2.5	1.2	5.26	2	646	601.2	540	61.2	4.2
27	1/4" SS	Ottawa sand	5 wt% $BaCl_2$	8.96	1.5	2.4	5.06	2	662	616.1	544	72.1	7.9
28	1/4" SS	none	300 ppm SDS	8.56	2	0	6.56	2	651	605.9	406	199.9	21.4
29	1/4" SS	none	300 ppm SDS	8.96	2.5	0	6.46	1.7	673	625.7	532	93.7	7.9
30	1/4" SS	none	5 wt% $BaCl_2$	8.96	2.5	0	6.46	1.7	688	639.7	598	41.7	3.5
31	1/4" SS	none	300 ppm SDS	8.96	2.5	0	6.46	1.7	696	647.1	618	29.1	2.5
32	1/4" SS	none	5 wt% $BaCl_2$	8.96	2.5	0	6.46	1.7	648	602.4	570	32.4	2.7
33	1/4" SS	Ottawa sand	5 wt% $BaCl_2$	8.96	1.4	1.3	6.26	1.7	642	596.8	581	15.8	2.3
34	1/2" SS	none	300 ppm SDS	24.91	6	0	18.91	2	652	606.8	537	69.8	7.2
35	1/2" SS	none	5 wt% $BaCl_2$	24.91	6	0	18.91	1.9	665	618.7	567	51.7	5.3
36	1/2" SS	none	Distilled water	24.91	6	0	18.91	2	651	605.9	551	54.9	5.6
37	1" SS	none	Distilled water	72	20	0	52	2	649	604.0	475	129.0	10.9
38	1" SS	none	300 ppm SDS	72	20	0	52	2	656	610.6	506	104.6	8.9
39	1" SS	none	Distilled water	72	20	0	52	2	657	611.5	517	94.5	8.0

Chapter 6

6.0 CMT Experiments – CH_4, CO_2 and CH_4-CO_2 Hydrate Formation without Porous Media

In previous chapters we focused on macroscale experiments to understand CH_4, CO_2, and CH_4-CO_2 hydrate formation. This chapter describes runs that were conducted at BNL at the NSLS. Gas hydrates were formed in a ¼" [6.35 mm] OD reactor with a total volume of about 10 mL. A portion of the cell (3.5 mL) consisted of x-ray transparent aluminum tubing and was covered with a cooling jacket to maintain the low temperatures needed for gas hydrate formation. This cell was utilized to image hydrate formation and growth using CMT at the X2B beamline. The cell, CMT facilities, and experimental procedure are described in detail in Chapter 2. An x-ray energy of 30 keV was used to view gas hydrates, and the pixel size on the images obtained was 7.68 μm.

6.1 Distinguishing Between Phases

In CMT imaging, different phases can be distinguished based on their x-ray attenuation coefficients. These attenuation coefficients are related to the amount of x-rays each material absorbs. Table 6.1 lists x-ray attenuation coefficients for all of the materials potentially present in CMT scans. X-ray attenuation values for each chemical at 30 keV were obtained from the National Institute of Standards and Technology (NIST)[131] website and, by multiplying these attenuations by the density of the chemical species, x-ray attenuation coefficients could be calculated for each chemical.

Table 6.1: *X-ray Attenuation Coefficients for the Phases Present during Experiments*

Material	**X-ray Attenuation @ 30 keV[131]**	**Densities**	**Attenuation Coefficient**	**Attenuation Coefficient**
	cm^2/g	g/cm^3	cm^{-1}	$pixel^{-1}$
CH_4 gas	0.2815	0.00066	0.0002	0
CO_2 gas	0.3447	0.0865	0.0298	24
CH_4 Hydrate	0.3633	0.9	0.3270	262
CO_2 Hydrates	0.3666	1.1	0.4033	323
Water	0.3756	1	0.3756	300
5 wt% $BaCl_2$	0.7246	1.02	0.7391	591
10 wt% $BaCl_2$	1.074	1.08	1.1599	928
15 wt% $BaCl_2$	1.423	1.13	1.6080	1286
20 wt% $BaCl_2$	1.772	1.17	2.0732	1659
Ethylene Glycol	0.3288	1.11	0.3650	292
Glass Beads (SiO_2 - Na_2O)	1.027	2.53	2.5983	2079
Ottawa sand (SiO_2)	0.8726	2.6476	2.3103	1848
Aluminum	1.128	2.7	3.0456	2436

To identify phases present in the cell, once a scan was complete, raw .prj files could be processed to create 2D image slices, similar to the one shown in the background of Figure 6.1. Using ImageJ, a plot profile of linear attenuation along a line drawn across the cell was taken, and a normalized graph, as shown in Figure 6.1, was obtained. This plot has been normalized as the experimental attenuation coefficients obtained for all materials were below those expected for the x-ray energy used. This is likely due to error in beamline energy calibration, and the attenuation coefficients obtained for materials are closer to those expected when using an energy of 34-35 keV rather than 30 keV. This slice contains CO_2 hydrates, 20 wt% $BaCl_2$ solution, and Al tubing. The yellow line drawn shows the parts of the cell being identified while the red line shows the linear attenuation coefficient at each pixel location across the yellow line. The ends of the red line show the attenuation coefficient for aluminum tubing (white in color on the image), which is around 2.8 to 3.0 cm^{-1} and in agreement with the theoretical attenuation coefficient value (3.05 cm^{-1}). The light gray regions on the image show 20 wt% $BaCl_2$ solution, with attenuation values between 1.5 and 2.0 cm^{-1}, in agreement with the calculated value of 2.1 cm^{-1}. Finally, CO_2 hydrates are the darker gray regions on the image slice. They have an attenuation value around 0.5 cm^{-1}, which is in agreement with the theoretical value of 0.4 cm^{-1} for CO_2 hydrates.

Similarly, the average experimental x-ray attenuation coefficient value obtained from the data could be plotted versus theoretical attenuation data. If the phases present in the cell have been correctly identified and gas hydrates have formed, the plot of this data will form a near straight line with an R^2 value near 1 as seen in Figure 6.2.

In addition, the histograms depicting the frequency (count) of each x-ray attenuation coefficient value ($pixel^{-1}$) can be obtained in ImageJ for a region of a 2D image slice. As the attenuation coefficient values for all of the phases present in the cell are close in value, peaks for each material in a histogram overlap, making it difficult to determine the phases present in the cell from histograms alone. The PeakFit program can be used to estimate the various material peaks that create a histogram plot to get an idea of the phases present in the cell. For each run series, a histogram of at least one of the CMT scans performed was analyzed in PeakFit to help indicate the presence or absence of gas hydrates.

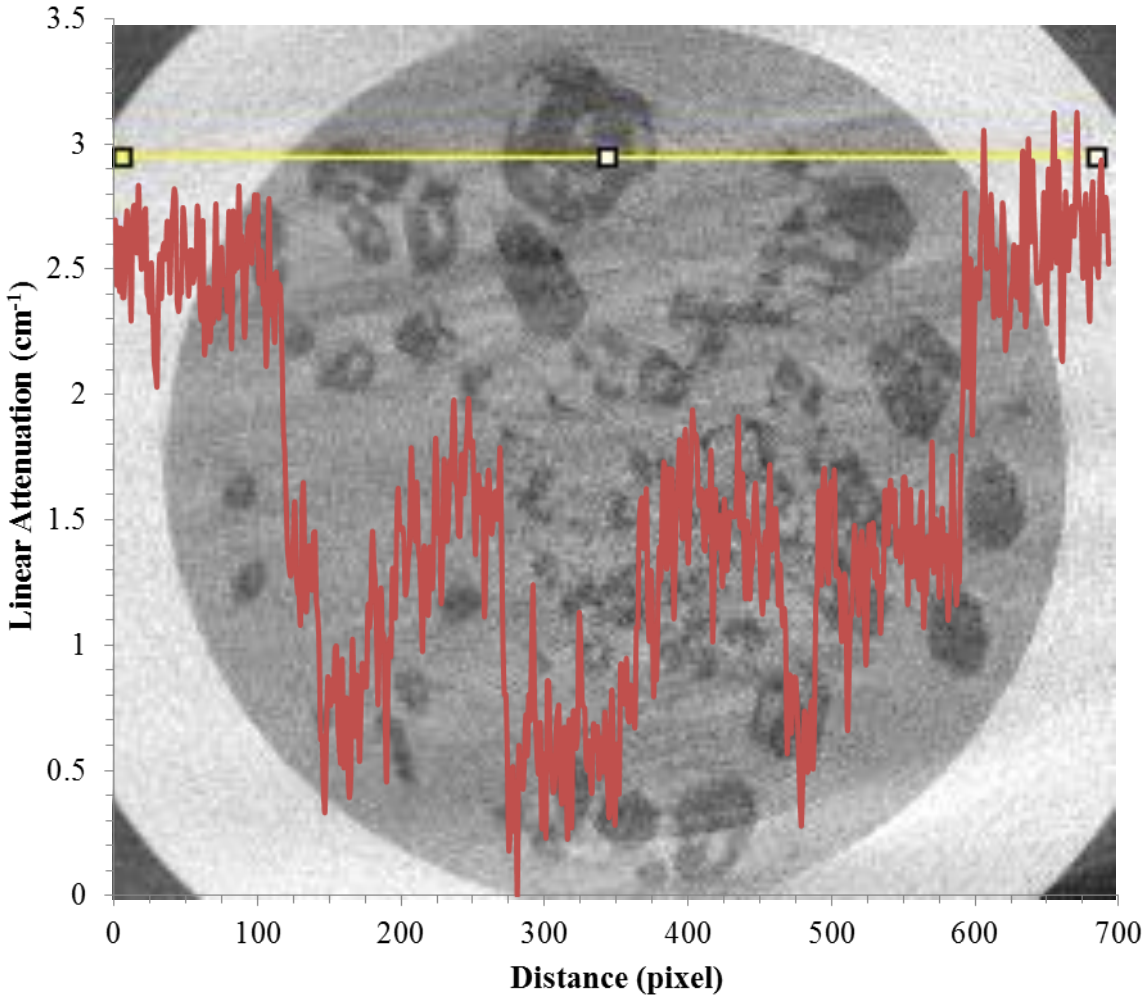

Figure 6.1: *A normalized plot of x-ray attenuation across the pixels of the 2D image slice. The yellow line touches the parts of the cell being identified while the red line shows the linear attenuation coefficient at each pixel location across the yellow line. Aluminum tubing (white), 20 wt% $BaCl_2$ solution (light gray), and CO_2 hydrates (dark gray) have experimental x-ray attenuation coefficients in agreement with theoretical values.*

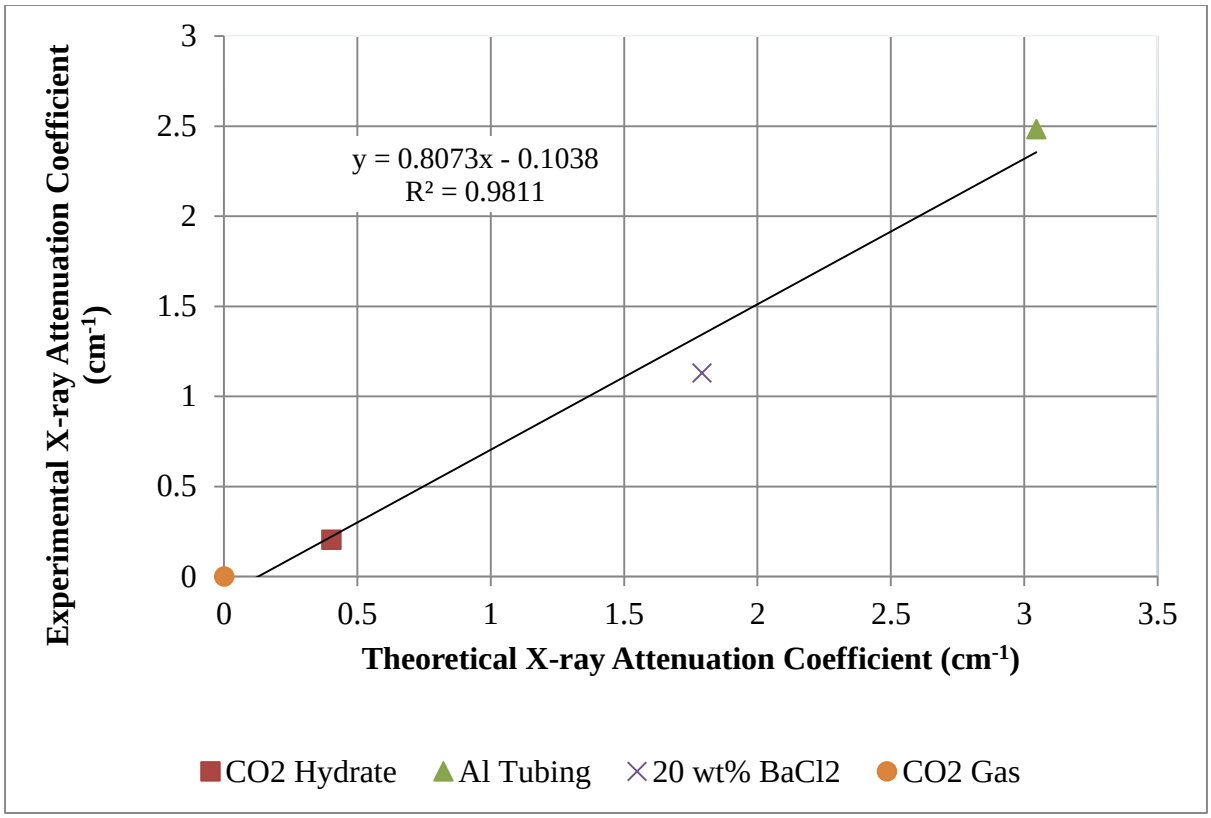

Figure 6.2: *Plot of theoretical x-ray attenuation coefficients versus normalized experimental x-ray attenuation coefficient values for the phases present in an experiment. The data created a straight line when plotted with a R^2 value near 1, indicating that phases in the cell have been properly identified and gas hydrates have indeed formed.*

6.2 CMT Experiments without Porous Media

A series of experiments were performed to grow CH_4, CO_2, and mixed CH_4-CO_2 hydrates. In all experiments, a salt solution with either 10, 15, or 20 wt% $BaCl_2$ was used to attempt to form hydrates. Salt is a hydrate inhibitor, but in this experiment it is a necessary contrast agent for CMT. Table 6.2 lists the conditions for these experiments. All pressure and temperature conditions used were within the hydrate stability zone, and temperatures were above the freezing point of the salt solution used, as shown in Figure 6.3. For all experiments, it is likely that the temperature of the cell during imaging was slightly higher than the temperature of the refrigerated circulator due to heat lost as coolant traveled through the cooling lines. Tests indicated that there was roughly a 2ºC temperature difference between the cell and the refrigerated circulator, therefore temperatures listed in the table reflect this difference. Unless noted, at the end of each imaging day, the cell was placed back into the refrigerated circulator for overnight cooling. In all runs where hydrate dissociation was monitored, hydrates disappeared within 10 minutes of ending cell cooling.

Table 6.2: *CMT Experimental Conditions*

Run #	Solution	Charging Pressure (psig)	Temperature (°C)	Duration of Experiment (days)
1	10 wt% $BaCl_2$	965 psig CH_4	0	3
2	10 wt% $BaCl_2$	965 psig CH_4	1 - 0	4
3	10 wt% $BaCl_2$	966 psig CH_4	0	21
4	20 wt% $BaCl_2$	658 psig CO_2	-1.5	13
5	15 wt% $BaCl_2$	647 psig CO_2	2 - 0	3
6	15 wt% $BaCl_2$	668 psig CO_2	2 - 0	28
7	15 wt% $BaCl_2$	960 psig (50% CH_4-50% CO_2)	1 - 0	7
8	15 wt% $BaCl_2$	945 psig (32% CH_4-68% CO_2)	0	4
9	15 wt% $BaCl_2$	961 psig (68% CH_4-32% CO_2)	0	5

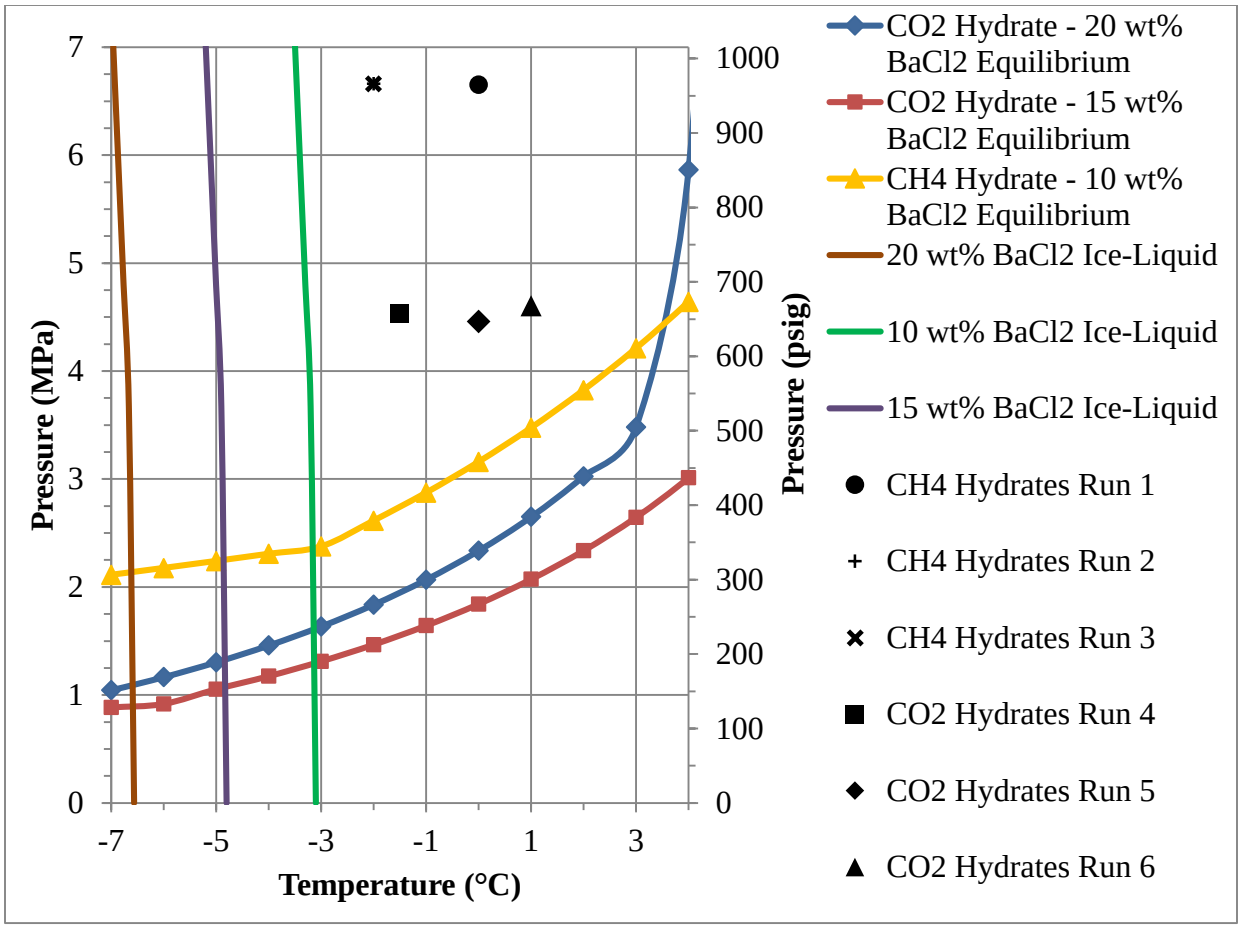

Figure 6.3: *Hydrate stability curves for the different gases and solutions used, along with water-ice stability lines. All experiments performed were within the hydrate stability zone.*

6.2.1 CH_4 Hydrates (Runs 1-3)

This first CH_4 hydrate formation experiment was performed using 2.2 mL of 10 wt% $BaCl_2$ solution ($T_{Freezing}$: -3.1°C) and 965 psig of CH_4 gas (Run 1). Once the cell was placed in the X2B beamline hutch, imaging began while the cell cooled down to about 0°C. Figure 6.4 shows only the volume of hydrates present in the cell over time. The cell was continuously imaged over 3 days throughout hydrate formation and growth. All images were taken at the gas-liquid interface, therefore all regions above the red hydrates were composed of CH_4 gas, and all regions below and surrounding the lower CH_4 hydrates were 10 wt% $BaCl_2$. Hydrates were viewed to coat the gas-liquid interface for the first time around 16.5 h after cell cooling had begun, and over the next two days, hydrates grew downwards into the solution phase, forming many smaller spherical CH_4 hydrates. Figure 6.4 clearly shows small spheres present below the gas-liquid interface at 46.4 h, and by 68.8 h, the number of CH_4 hydrates had multiplied. These hydrate spheres did not appear to be solid hydrates, rather a hydrate coating had formed surrounding a CH_4 gas bubble, similar to the hydrate coated gas-liquid interface. It is not surprising that hydrates accumulated at the gas-liquid interface, as the density of CH_4 hydrates (0.9 g/cm^3) is lower than the density of the salt solution (1.08 g/cm^3). CH_4 hydrates may also be found at the gas-liquid interface because the largest concentration of dissolved CH_4 gas would be located at this interface[112].

The presence of CH_4 hydrates was confirmed in the histograms shown in Figure 6.5. Figure 6.5(a) shows a histogram taken from a 2D image slice of the cell at room temperature prior to beginning cooling. Three clear, distinct peaks can be seen for CH_4 gas, 10 wt% $BaCl_2$, and aluminum tubing. At the first sign of hydrate formation, a histogram was taken at 16.5 h in Figure 6.5(b). Three peaks located at the same attenuation coefficients can be seen, but at this time, the gas and solution peaks overlap more. This is because a small peak for CH_4 hydrates is located in between those two larger peaks, and as the attenuation coefficients for gas, gas hydrates, and solution are close together, their peaks in the histogram overlap. The PeakFit program was used to separate these peaks so that the three phases can be better identified. Figure 6.5(c) shows the histogram of the 2D slice shown on the right from a CMT scan performed at 68.8 h. Histogram values near zero are attributed to gases, though in all experiments performed, experimental attenuation values obtained for all materials present in the cell were slightly lower in value than the theoretical x-ray attenuation coefficient values calculated from NIST. This is

possibly due to an underestimate of the beam energy calibrated at the X2B beamline. Since our experimental attenuations are slightly below what is to be expected, it is fair to attribute peaks with attenuation values above 0 $pixel^{-1}$ to gas hydrate existence. Since the center of the peak for CH_4 hydrates in Figure 6.5 has an attenuation value above 0 $pixel^{-1}$, CH_4 hydrates are indeed present in this CMT run. Figure 6.6 is a plot profile across the region of the cell highlighted in the yellow box that further confirms CH_4 hydrate formation. The gray value (which is related to x-ray attenuation in units of $pixel^{-1}$) corresponds well to each of the phases present across the yellow box.

The 2D image slices shown beneath the 3D volumes in Figure 6.4 show what one horizontal slice of the cell appeared like over time. Histograms for each 2D slice are shown below, and it is clear to see how colors were defined in the image slices. The hydrates (red) inside the aluminum tubing (green) match ethylene glycol – water coolant that surrounds the aluminum, as to be expected due to similar x-ray attenuation coefficient values. In these images, yellow represents salt solution and blue is CH_4 gas. It is interesting to note that at 16.5 h, hydrates are seen mostly coating the gas phase with some spots in the solution, but in later scans, the hydrates appear to be potentially forming a scaffold in the gas phase. This can also be seen at the top of the 3D volume images at 46.4 and 68.8 h in the gas region above the hydrates. Figure 6.7 shows an enlarged image of CH_4 hydrates in the cell at 68.8 h. It is clear that the CH_4 hydrates formed are very spherical and coating gas bubbles, though there is much surface structure to the hydrates.

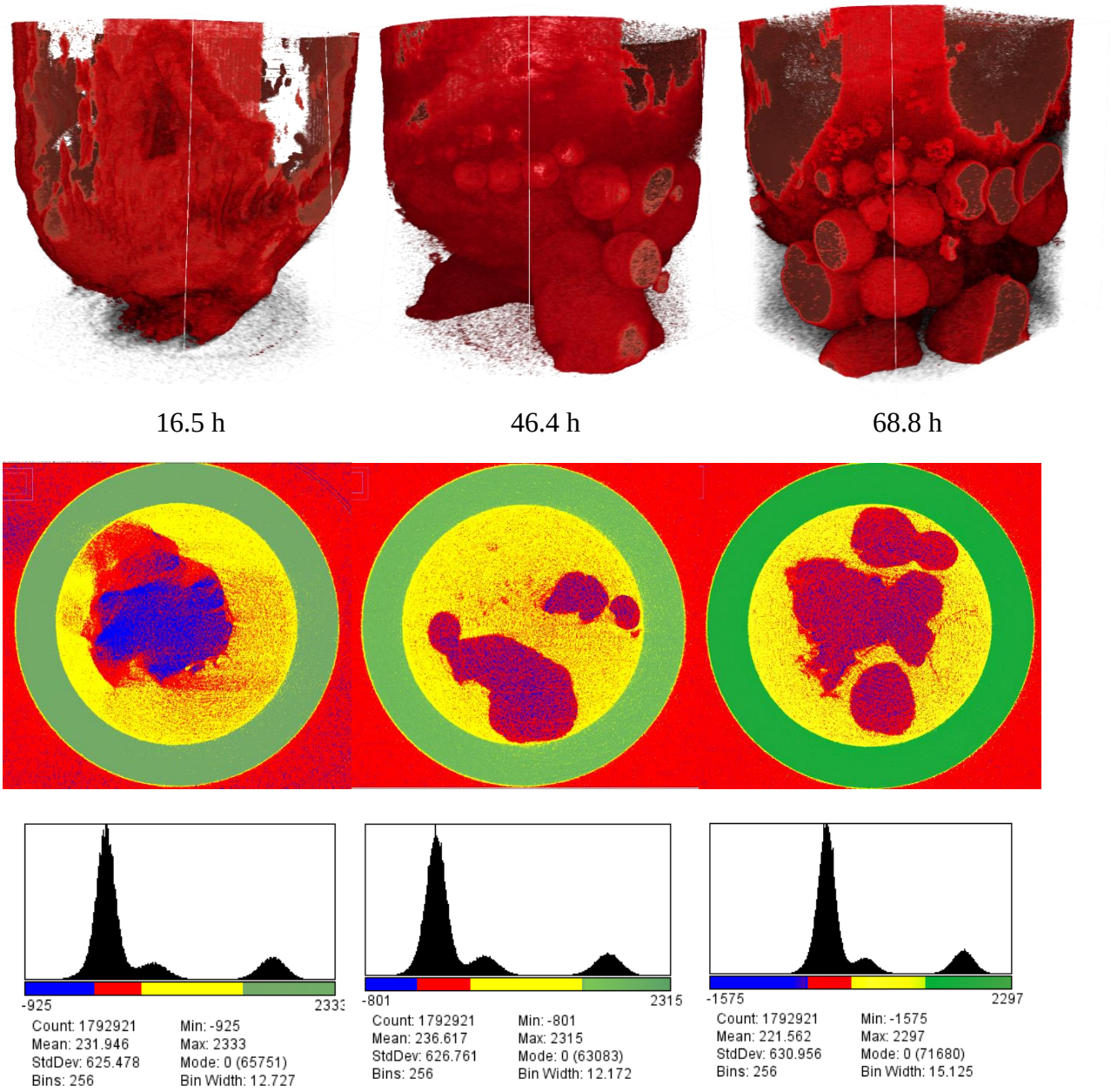

Figure 6.4: *Time-Resolved CMT images of Run 1 CH_4 hydrate growth from an aqueous solution of 10 wt% $BaCl_2$. Time resolved hydrate growth is shown in 3D volumes, where red indicates CH_4 hydrates and all other phases present in the cell have been made transparent. The 2D image slices represent slice 450 of the 3D images. In the 2D images, red indicates CH_4 hydrates, blue is CH_4 gas, yellow is 10 wt% $BaCl_2$ solution, and green is aluminum tubing. The OD of the green aluminum tubing is 0.25" and the ID is 0.18". The histograms of the different phases in the 2D images are also shown. The growth of hydrates extends downwards into the liquid phase from the gas-liquid interface.*

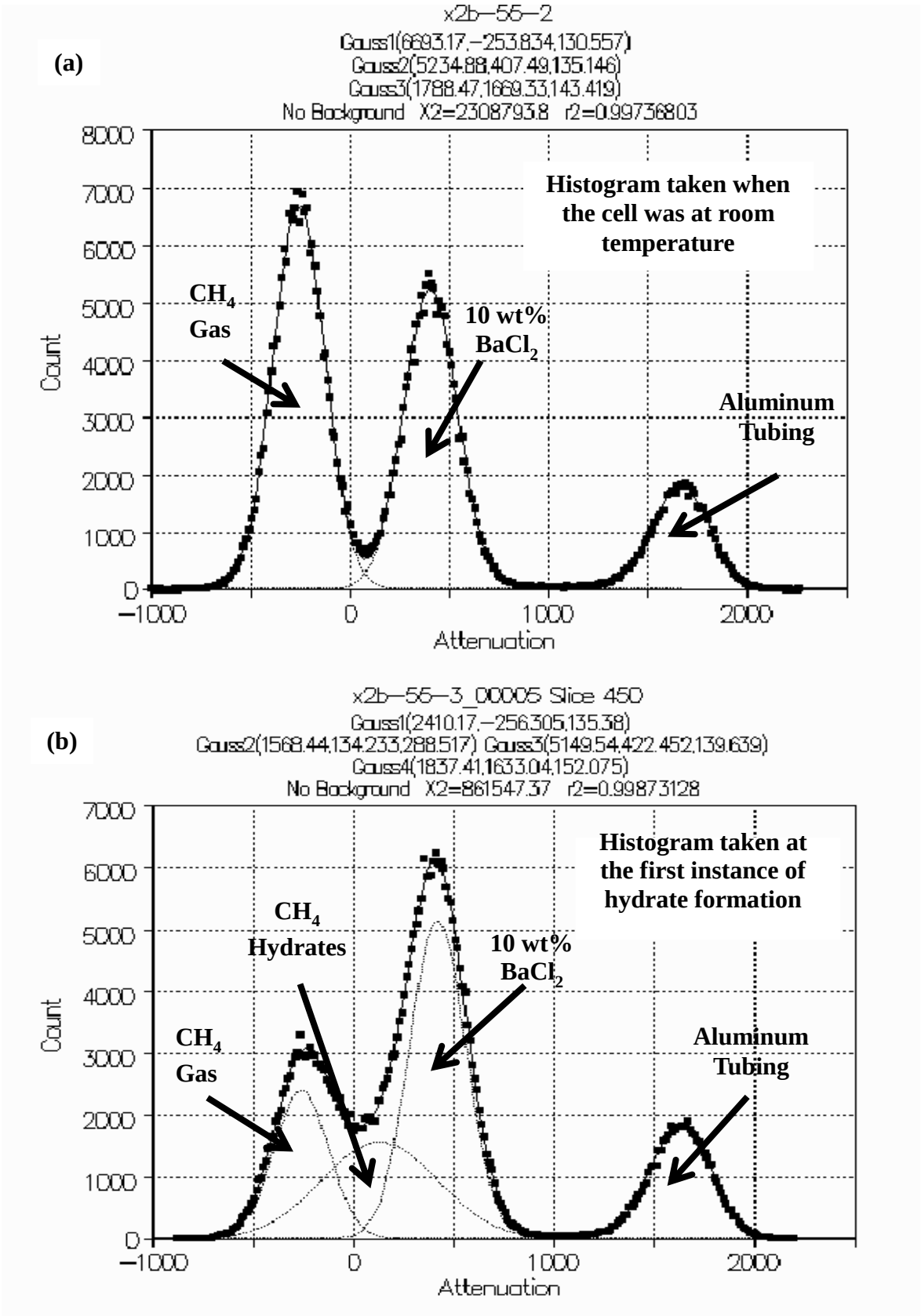
(a)
x2b—56—2
Gauss1(6693.17,−253.834,130.557)
Gauss2(5234.88,407.49,135.146)
Gauss3(1788.47,1669.33,143.419)
No Background X2=23087938 r2=0.99736803
Histogram taken when the cell was at room temperature
CH4 Gas
10 wt% BaCl2
Aluminum Tubing
Count
Attenuation
(b)
x2b—56—3_00005 Slice 450
Gauss1(2410.17,−256.305,135.38)
Gauss2(1568.44,134.233,288.517) Gauss3(5149.54,422.452,139.639)
Gauss4(1837.41,1633.04,152.075)
No Background X2=861547.37 r2=0.99873128
Histogram taken at the first instance of hydrate formation
CH4 Hydrates
10 wt% BaCl2
CH4 Gas
Aluminum Tubing
Count
Attenuation

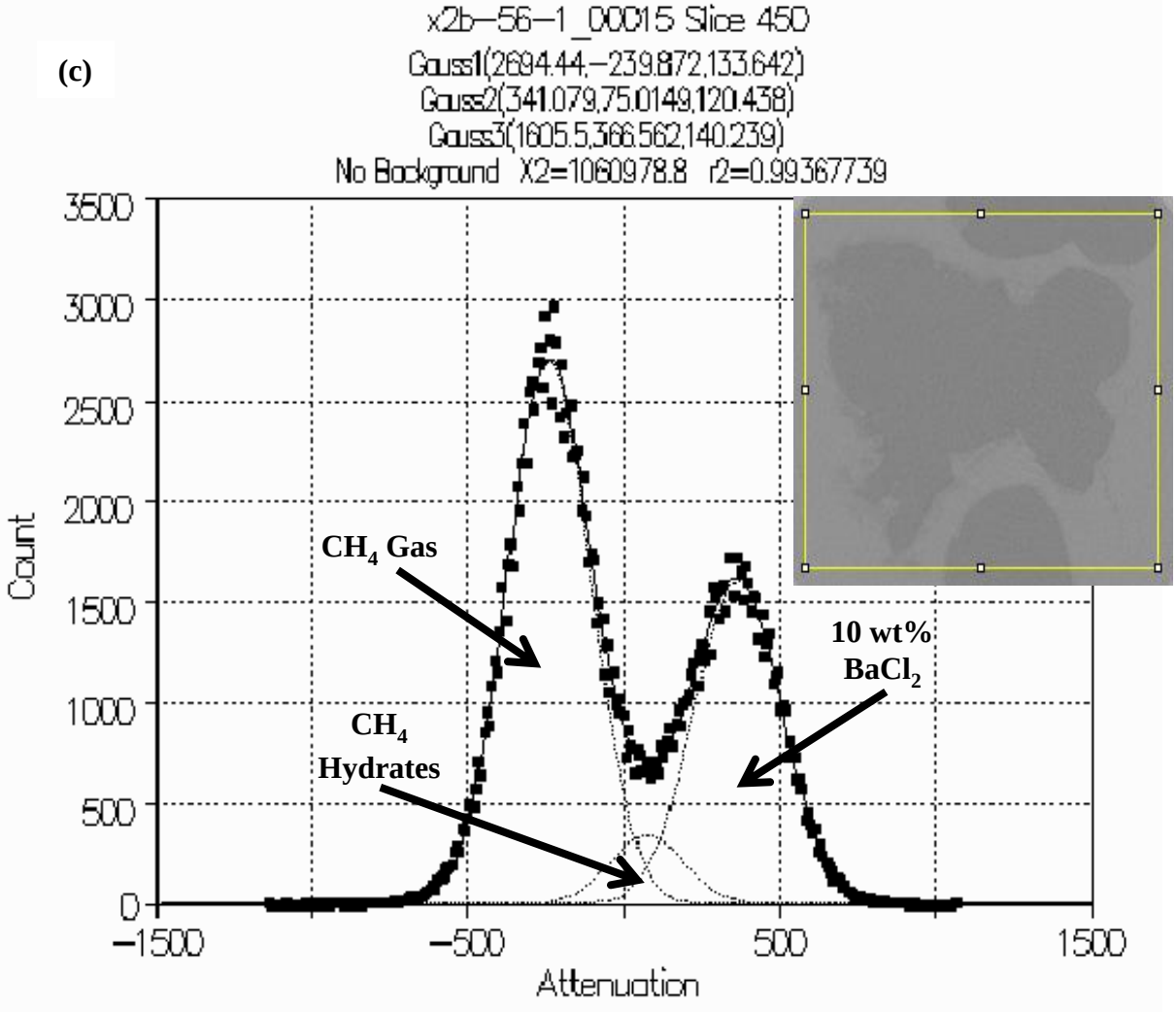

Figure 6.5: *(a) Histogram of the cell at room temperature, where there is clear distinction between CH_4 gas, 10 wt% $BaCl_2$ solution, and aluminum tubing. (b) Histogram of the cell at the first instance of CH_4 hydrates. The peaks seen at room temperature in (a) are still visible at similar attenuation values, but a peak for CH_4 hydrates can be found between the gas and solution peaks, which causes an overlap of peaks in the histogram. (c) Histogram with attenuation values of pixel^{-1} for slice 450 of the CMT scan performed during Run 1 at 68.8 h. The PeakFit program was used to distinguish between the different peaks in the histogram created by the various materials present inside the cell. The image inside the yellow box above the plot shows the region of the cell used to create this histogram, and in the image, darker gray regions are gas, lighter gray regions are solution, and gray colors in between gas and solution are gas hydrates. Since the peak attributed to CH_4 hydrates is centered above 0 pixel^{-1}, CH_4 hydrates are present in this experiment.*

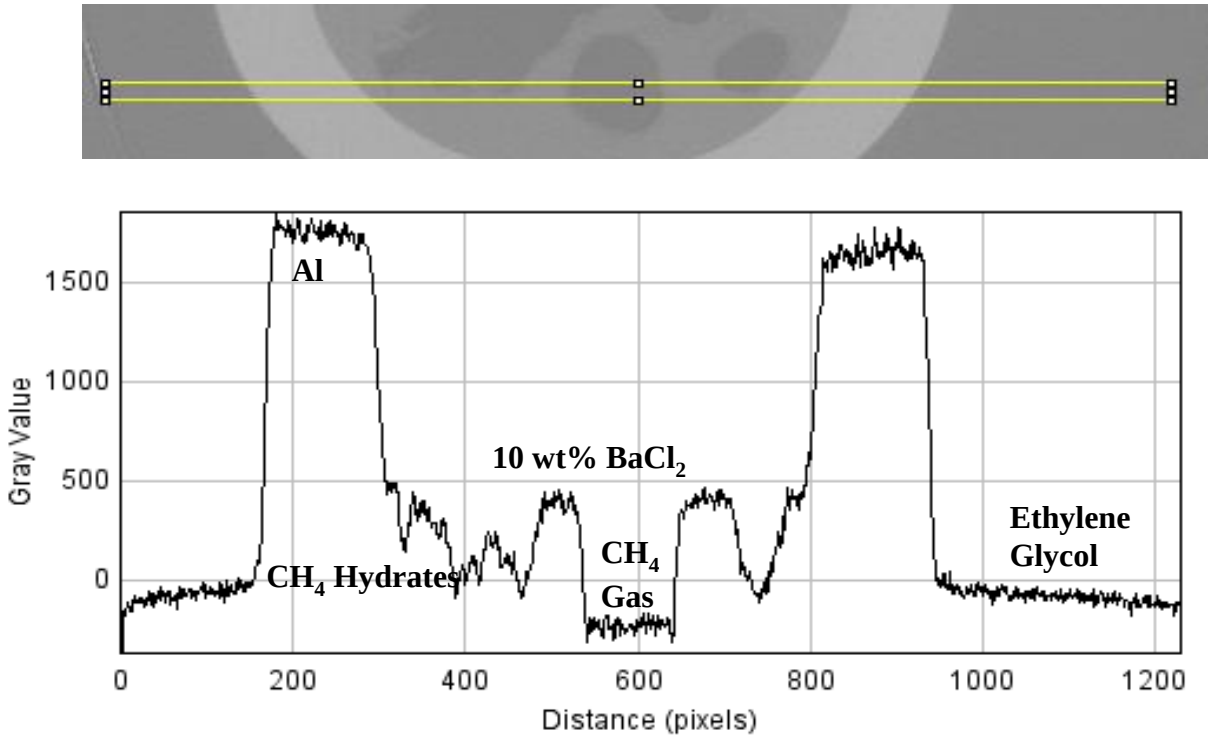

Figure 6.6: *A plot profile was taken across a 2D image slice of the cell at 68.8 h containing aluminum tubing, 10 wt% $BaCl_2$ solution, CH_4 hydrates, CH_4 gas, and ethylene glycol-water coolant. A profile of the gray value (related to attenuation) across the yellow box was taken and plotted to show where the phases are defined.*

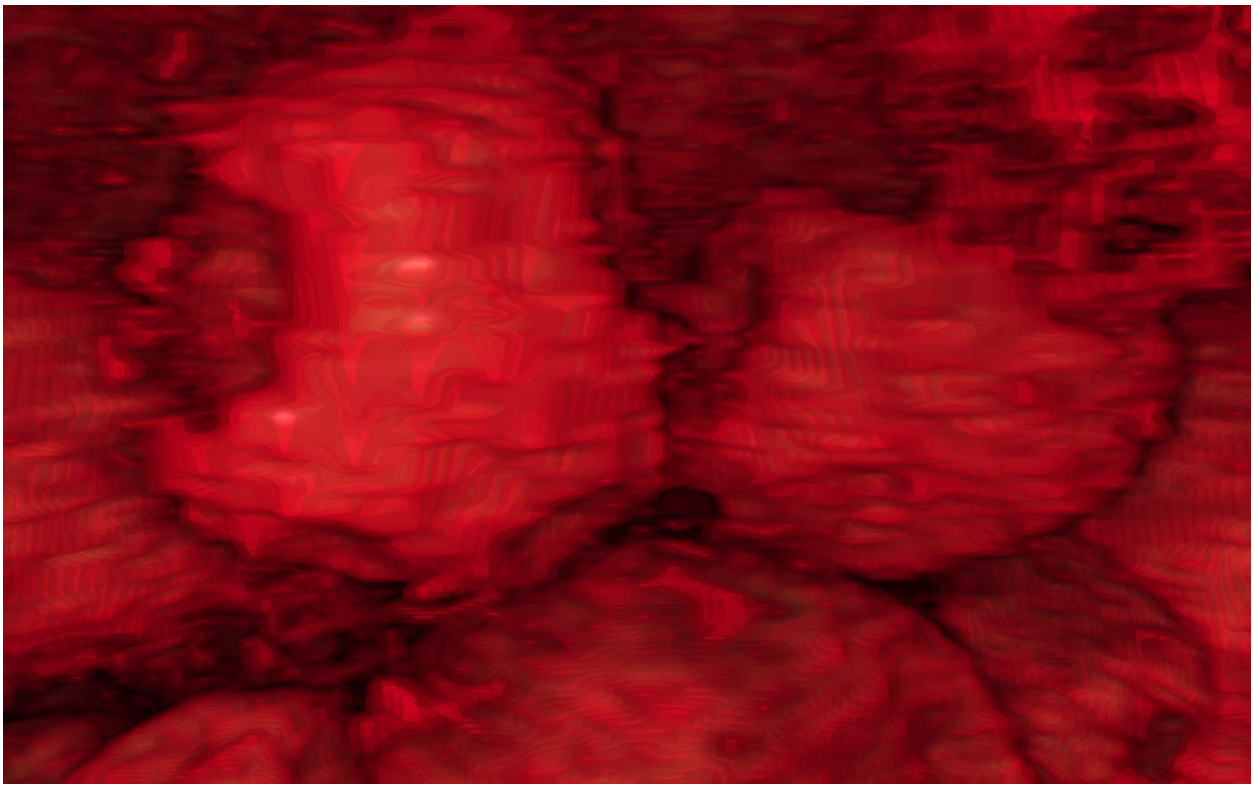

Figure 6.7: *Zoom in of the CH_4 hydrates formed at 68.8 h in Run 1.*

Another run was performed to form CH_4 hydrates from a solution containing 2.4 mL of 10 wt% $BaCl_2$ under 965 psig of CH_4 gas (Run 2). The cell was monitored for four days, and the cell was cooled to 0°C. When the scans showed no hydrate growth two days after cell cooling had begun, the cell was vigorously shaken and many CH_4 gas bubbles formed. Once the cell was shaken, the region imaged was no longer at the gas-liquid interface, but instead it was within the solution phase. The gas-liquid interface location in the cell changed several times during this experiment, but it is doubtful that CH_4 hydrates formed. The presence of CH_4 hydrates was negated in the histogram shown in Figure 6.8. The PeakFit program was used to separate the material peaks present in the histogram taken of one of the 2D slices of the CMT scan performed at 70.3 h, shown at the top of Figure 6.8. Since the center of the peak for CH_4 hydrates has an attenuation value below 0 $pixel^{-1}$, CH_4 hydrates are most likely not present in this CMT run. If this is a hydrate phase, not enough was formed in an appreciable amount to be detected in the histogram peaks. The plot profile shown in Figure 6.9 also does not show as clear of a CH_4 hydrate phase as the other runs described herein show; it is likely that the upper peaks in between the two aluminum tubing peaks are due to 10 wt% $BaCl_2$ while the bottom peaks in that region could be indicating an initial hydrate stage.

Images of the cell near the gas-liquid interface are shown in Figure 6.10. After 65.8 h of cooling, while CH_4 hydrates were not definitely found, the red colored regions in Figure 6.8 have attenuations slightly lower than that expected for hydrates, but higher than the attenuation values for CH_4 gas. These regions covering the gas-liquid interface and several gas bubbles in the solution may indicate the early stages of hydrate nucleation in the solution, though hydrates were not found to grow much during the nearly four days of CMT imaging. Over the following day, the individual gas bubbles in the solution became more spherical at 70.3 h, and by 89.8 h, some gas bubbles agglomerated into the larger, spherical bubble on the left, while many small, amorphous gas bubbles were located near the gas-liquid interface with a possible extremely thin CH_4 hydrate coating.

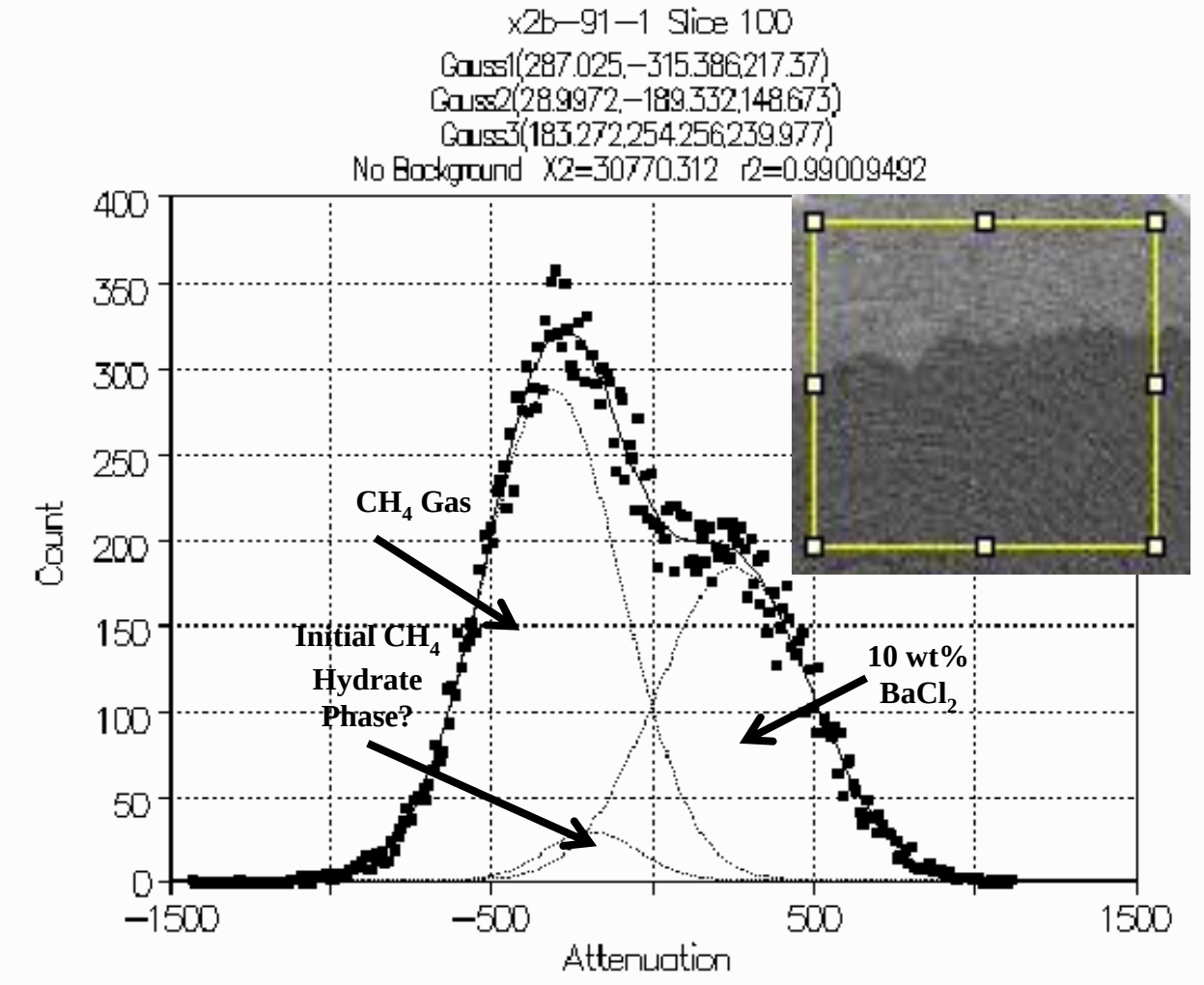

Figure 6.8: *Histogram with attenuation values of pixel^{-1} for slice 100 of the CMT scan performed during Run 2 at 70.3 h. The PeakFit program was used to distinguish peaks in the histogram created by the various materials present inside the cell. The image inside the yellow box above the plot shows the region of the cell used to create this histogram, and in the image, darker gray regions are gas, lighter gray regions are solution, and gray colors in between gas and solution are potential initial gas hydrate structures. The peak possibly attributed to CH_4 hydrates is centered below 0 pixel^{-1}, so it is likely that CH_4 hydrates are not present in this experiment in appreciable amounts.*

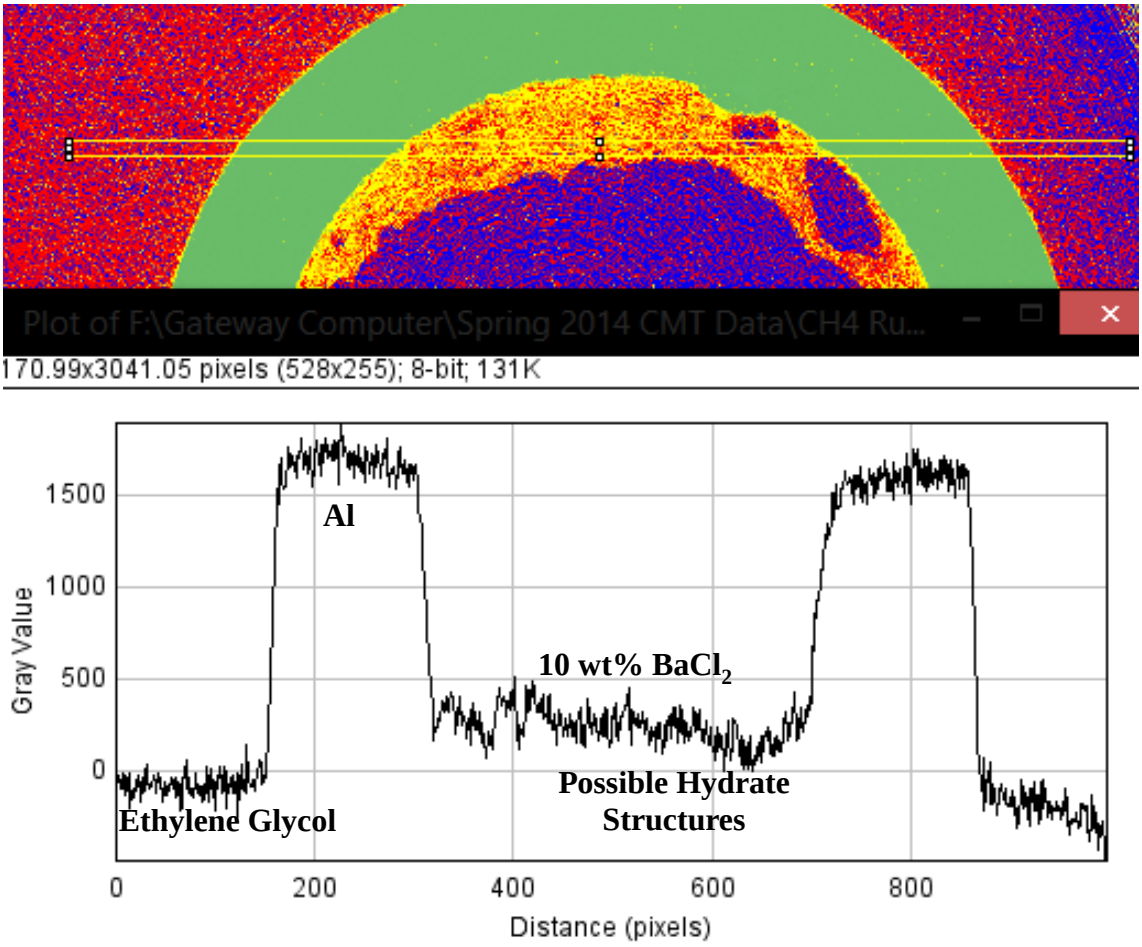

Figure 6.9: *A plot profile was taken across a 2D image slice of the cell at 70.3 h containing aluminum tubing, 10 wt% $BaCl_2$ solution, possible CH_4 hydrate structures, and ethylene glycol-water coolant. A profile of the gray value (related to attenuation) across the yellow box was taken and plotted to show where the phases are defined.*

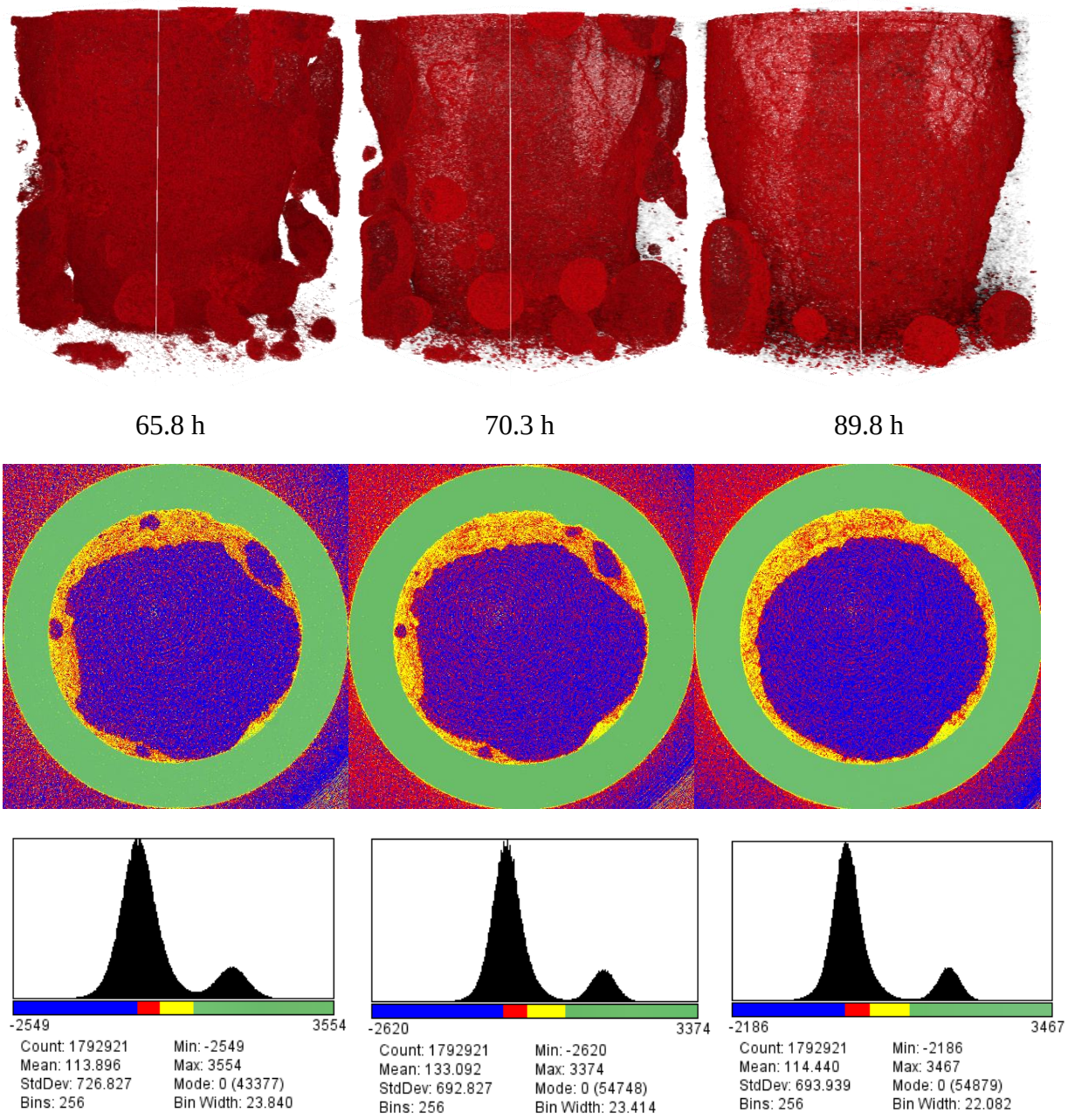

Figure 6.10: *Time-Resolved CMT images of Run 2 potential CH_4 hydrate structures from an aqueous solution of 10 wt% $BaCl_2$. Time resolved hydrate growth is shown in 3D volumes, where red indicates potential early stages of CH_4 hydrate structures and all other phases present in the cell have been made transparent. The 2D image slices represent slice 100 of the 3D images. In the 2D images, red indicates potential early CH_4 hydrate structures, blue is CH_4 gas, yellow is 10 wt% $BaCl_2$ solution, and green is aluminum tubing. The OD of the green aluminum tubing is 0.25" and the ID is 0.18". Histograms of the different phases in the 2D images are also shown.*

Run 3 was performed similarly, using 2.4 mL of 10 wt% $BaCl_2$ solution and 966 psig of CH_4 gas. For this experiment, the cell was cooled to -2°C for sixteen days prior to CMT imaging, when the cell temperature was maintained around 0°C. Initial images at 381.2 h in Figure 6.11 show that CH_4 hydrates had formed at and below the gas-liquid interface, as well as surrounding a CH_4 gas bubble. Images taken a day later at 405.0 h indicated similar hydrate presence. Hydrates found branching off of the gas-liquid interface after 503.9 h of cooling formed rounded shapes, similar to previous experiments, though there is much structure to the hydrates formed in this run. The presence of CH_4 hydrates was confirmed in the histogram of one of the 2D slices of the CMT scan performed at 381.2 h shown in Figure 6.12. Since the center of the peak for CH_4 hydrates has an attenuation value above 0 $pixel^{-1}$, CH_4 hydrates are indeed present in this CMT run. Similarly, the plot profile taken in Figure 6.13 shows distinct regions where CH_4 hydrates must be present.

The 2D image slices in Figure 6.11 show much cluster hydrate growth within the 10 wt% $BaCl_2$ solution, away from the gas-liquid interface. In these clusters, smaller individual hydrates appeared to conglomerate together in spherical groupings. Hydrates formed mostly within the solution near the center of the cell, rather than on the walls of the reactor. This is true for most of the experiments; there always appeared to be a liquid layer between the aluminum tubing and hydrates formed. Upon zooming in more closely to hydrates formed after 503.9 h in Figure 6.14, there is much structure to the hydrate surface, and their spherical nature can be seen.

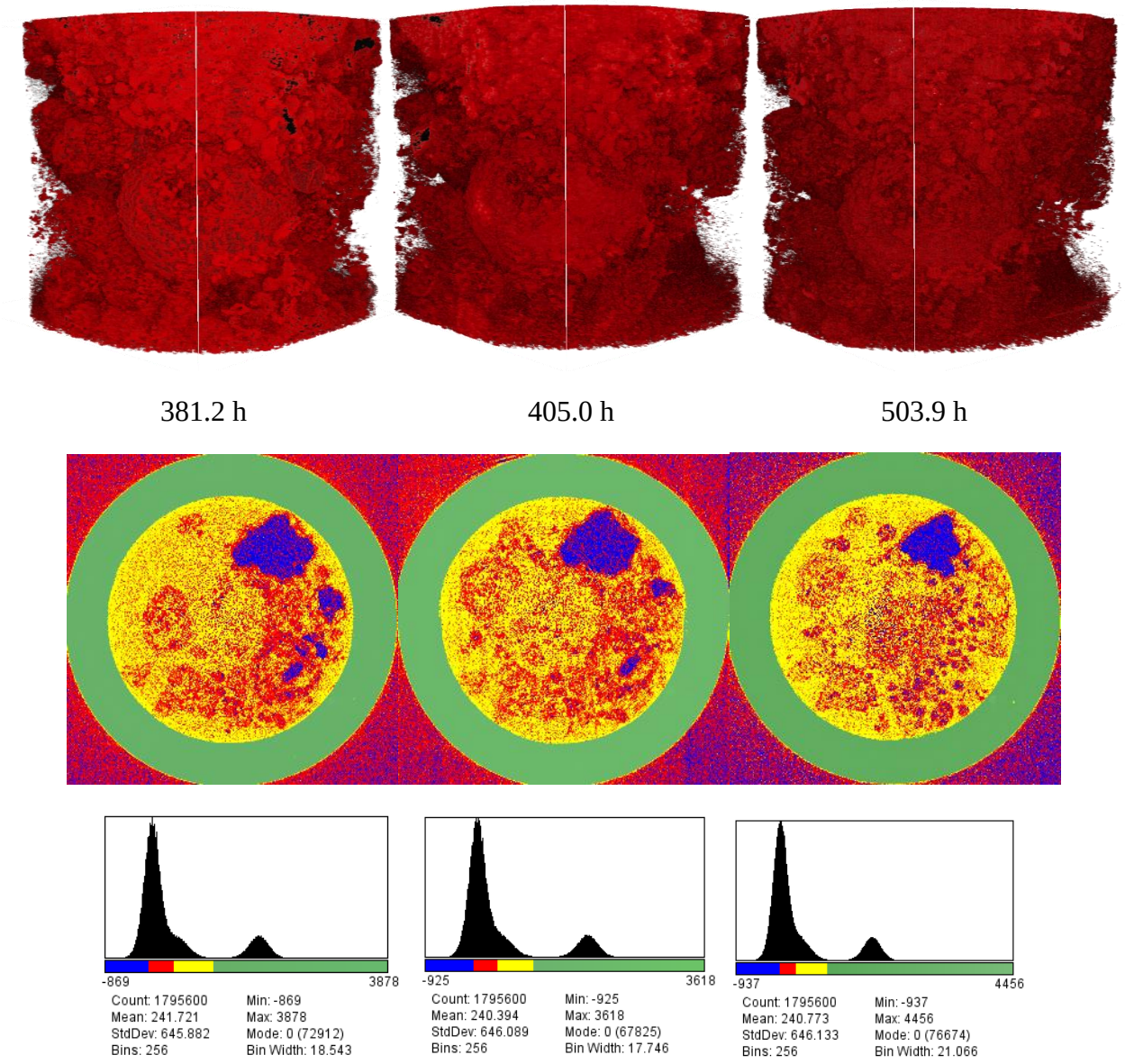

Figure 6.11: *Time-Resolved CMT images of Run 3 CH_4 hydrate growth from an aqueous solution of 10 wt% $BaCl_2$. Time resolved hydrate growth is shown in 3D volumes, where red indicates CH_4 hydrates and all other phases present in the cell have been made transparent. The 2D image slices represent slice 250 of the 3D images. In the 2D images, red indicates CH_4 hydrates, blue is CH_4 gas, yellow is 10 wt% $BaCl_2$ solution, and green is aluminum tubing. The OD of the green aluminum tubing is 0.25" and the ID is 0.18". Histograms of the different phases in the 2D images are also shown. The growth of hydrates extends downwards into the liquid phase from the gas-liquid interface.*

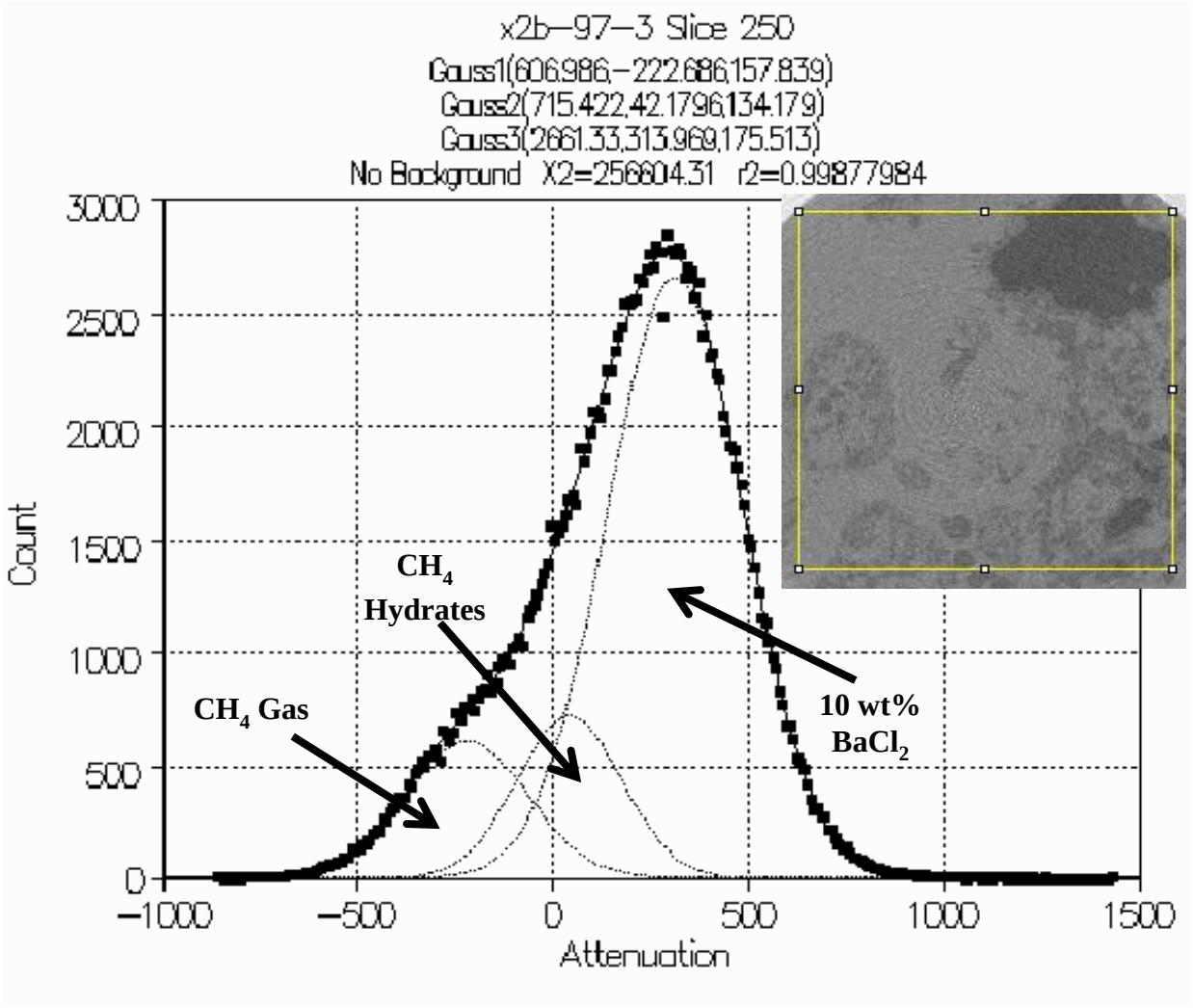

Figure 6.12: *Histogram with attenuation values of pixel^{-1} for slice 250 of the CMT scan performed during Run 3 at 381.2 h. The PeakFit program was used to distinguish between the different peaks in the histogram created by the various materials present inside the cell. The image inside the yellow box above the plot shows the region of the cell used to create this histogram, and in the image, darker gray regions are gas, lighter gray regions are solution, and gray colors in between gas and solution are gas hydrates. Since the peak attributed to CH_4 hydrates is centered above 0 pixel^{-1}, CH_4 hydrates are present in this experiment.*

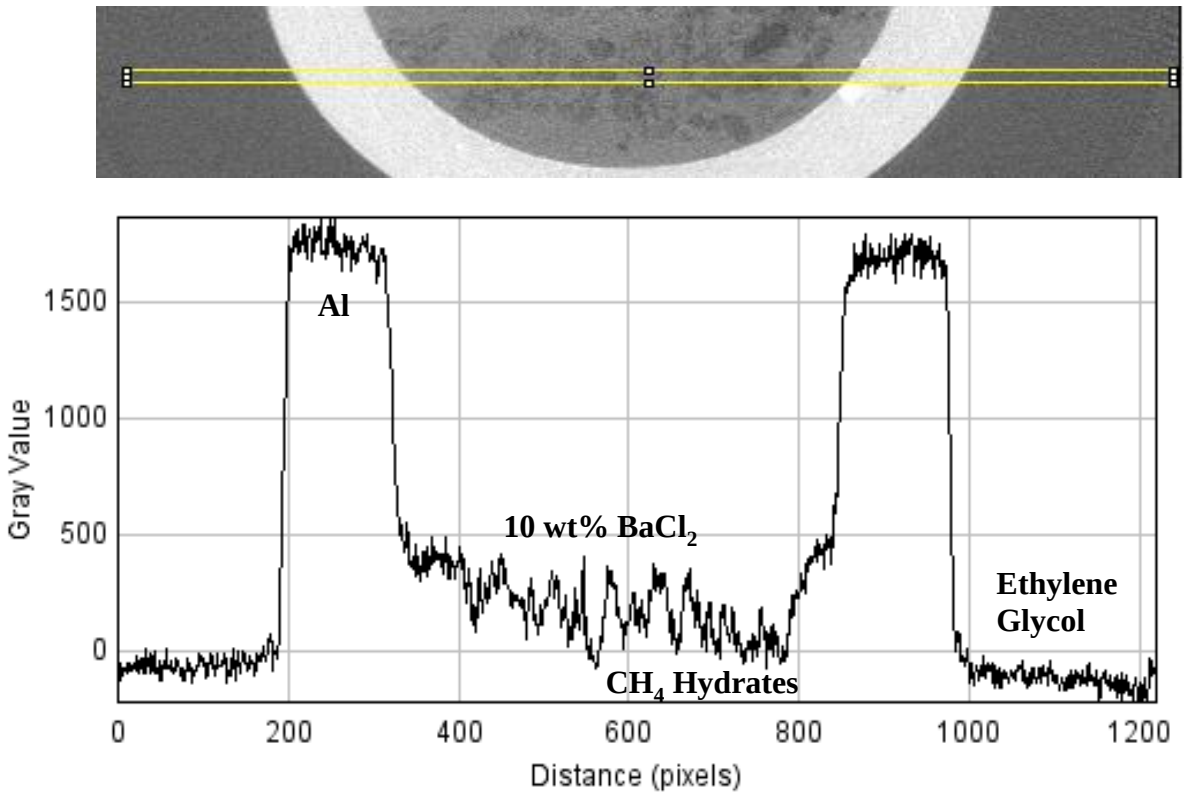

Figure 6.13: *A plot profile was taken across a 2D image slice of the cell at 381.2 h containing aluminum tubing, 10 wt% $BaCl_2$ solution, CH_4 hydrates, and ethylene glycol-water coolant. A profile of the gray value (related to attenuation) across the yellow box was taken and plotted to show where the phases are defined.*

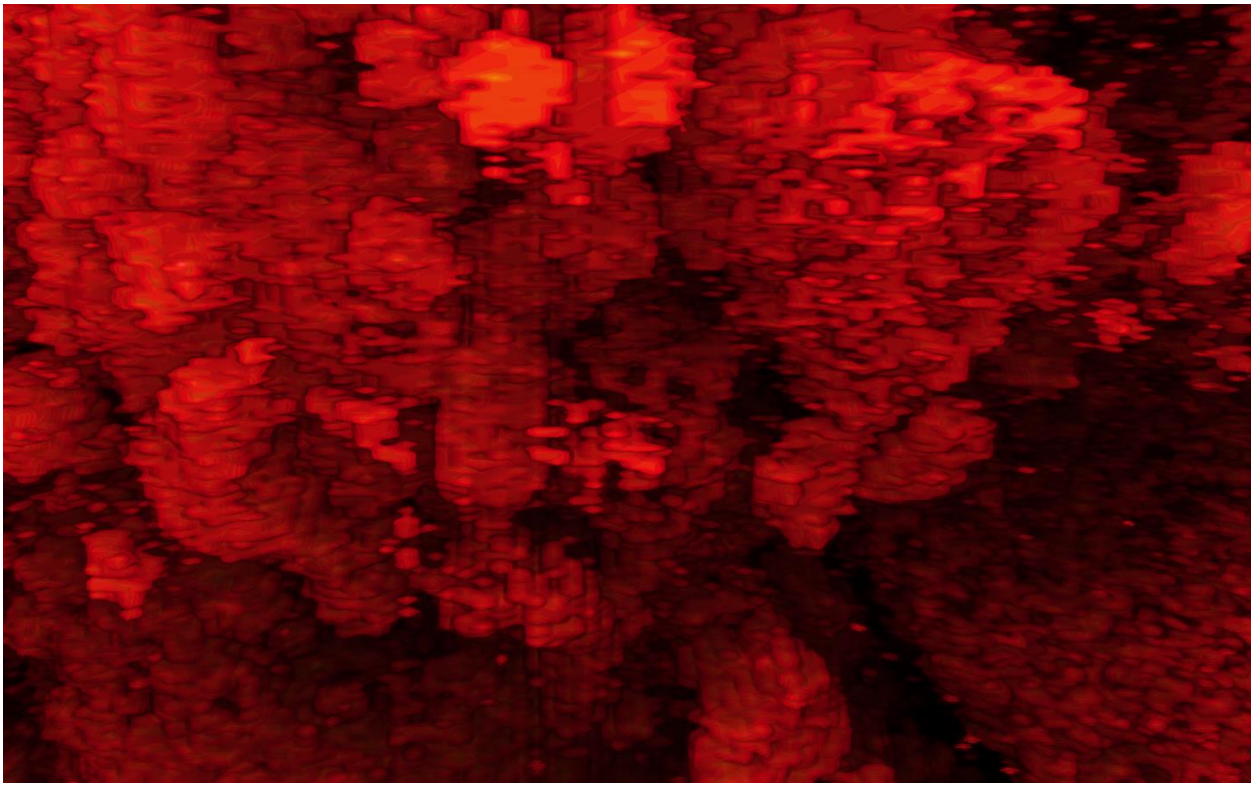

Figure 6.14: *Zoom in of the CH_4 hydrates formed at 503.9 h in Run 3.*

6.2.2 CO_2 Hydrates (Runs 4-6)

Runs 4-6 focused on hydrates of CO_2. Run 4 was performed using 2.2 mL of 20 wt% $BaCl_2$ solution ($T_{Freezing}$: -6.6°C, ρ: 1.17 g/cm^3) and 658 psig of CO_2 gas. The cell was cooled down to -1.5°C for 10 days, and then CMT imaging scans were taken to monitor CO_2 hydrate (ρ: 1.1 g/cm^3) growth at the gas-liquid interface. Initially after 241.0 h of cooling, CO_2 hydrates were found to coat the gas-liquid interface, as well as exist in the liquid phase, as shown in Figure 6.15. Oval, rod-like branched hydrates were found to continue to thicken and grow over time from the gas-liquid interface into the liquid phase until 300.0 h when most of the imaging region was filled with CO_2 hydrates. CO_2 hydrate existence was confirmed in the histogram of one of the 2D slices of the CMT scan performed at 381.2 h shown in Figure 6.16. Since the center of the peak for CO_2 hydrates has an attenuation value above 0 pixel^{-1}, CO_2 hydrates were indeed present in this CMT run. In Figure 6.17, CO_2 hydrates have a gray value on the plot profile very similar to and slightly above the ethylene glycol-water coolant, which further confirms hydrate presence.

The 2D image slices (Figure 6.15) show that, unlike CH_4 hydrates, CO_2 hydrates are mostly solid, though the larger hydrates do appear to have regions of gas enclosed by hydrate. A zoom in (Figure 6.18) shows that these rod-like hydrates have much surface structure and some branching.

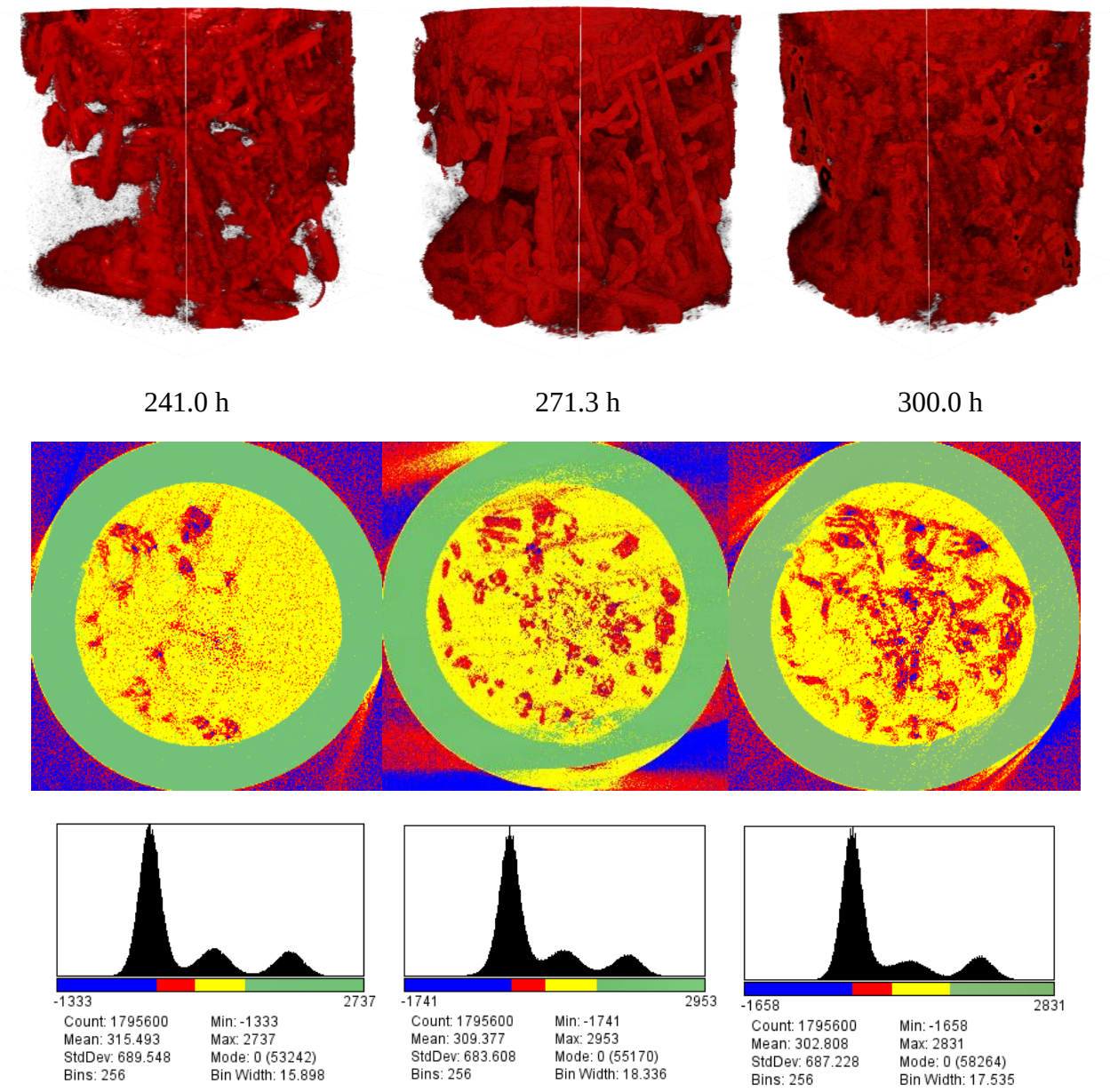

Figure 6.15: *Time-Resolved CMT images of CO_2 hydrate growth from an aqueous solution of 20 wt% $BaCl_2$ in Run 4. Time resolved hydrate growth is shown in 3D volumes, where red indicates CO_2 hydrates and all other phases present in the cell have been made transparent. The 2D image slices represent slice 150 of the 3D images. In the 2D images, red indicates CO_2 hydrates, blue is CO_2 gas, yellow is 20 wt% $BaCl_2$ solution, and green is aluminum tubing. The OD of the green aluminum tubing is 0.25" and the ID is 0.18". Histograms of the different phases in the 2D images are also shown. The growth of hydrates extends downwards into the liquid phase from the gas-liquid interface.*

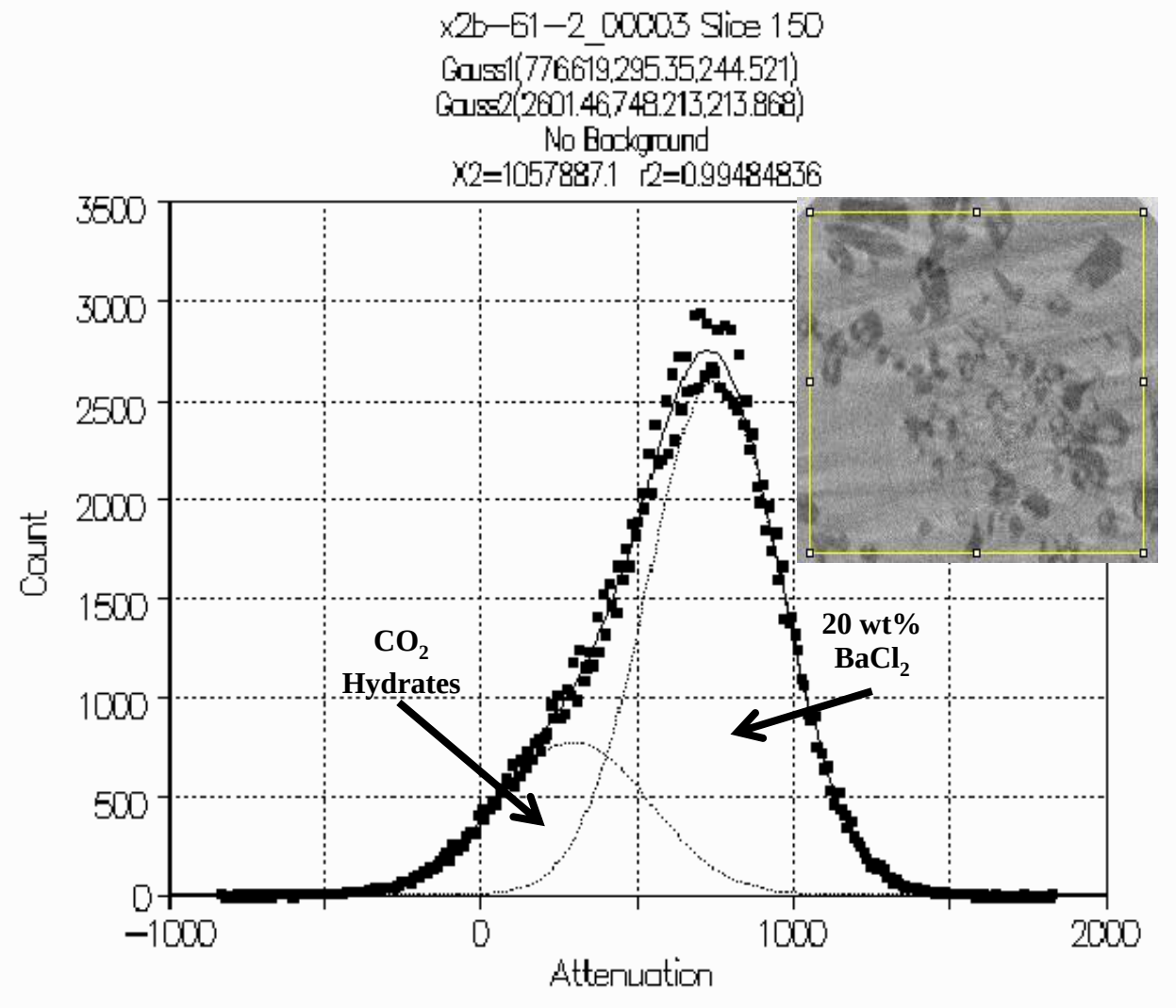

Figure 6.16: *Histogram with attenuation values of pixel^{-1} for slice 150 of the CMT scan performed during Run 4 at 271.3 h. The PeakFit program was used to distinguish between the different peaks in the histogram created by the various materials present inside the cell. The image inside the yellow box above the plot shows the region of the cell used to create this histogram, and in the image, light gray regions are solution and darker gray colors are gas hydrates. Since the peak attributed to CO_2 hydrates is centered above 0 pixel^{-1}, CO_2 hydrates are present in this experiment.*

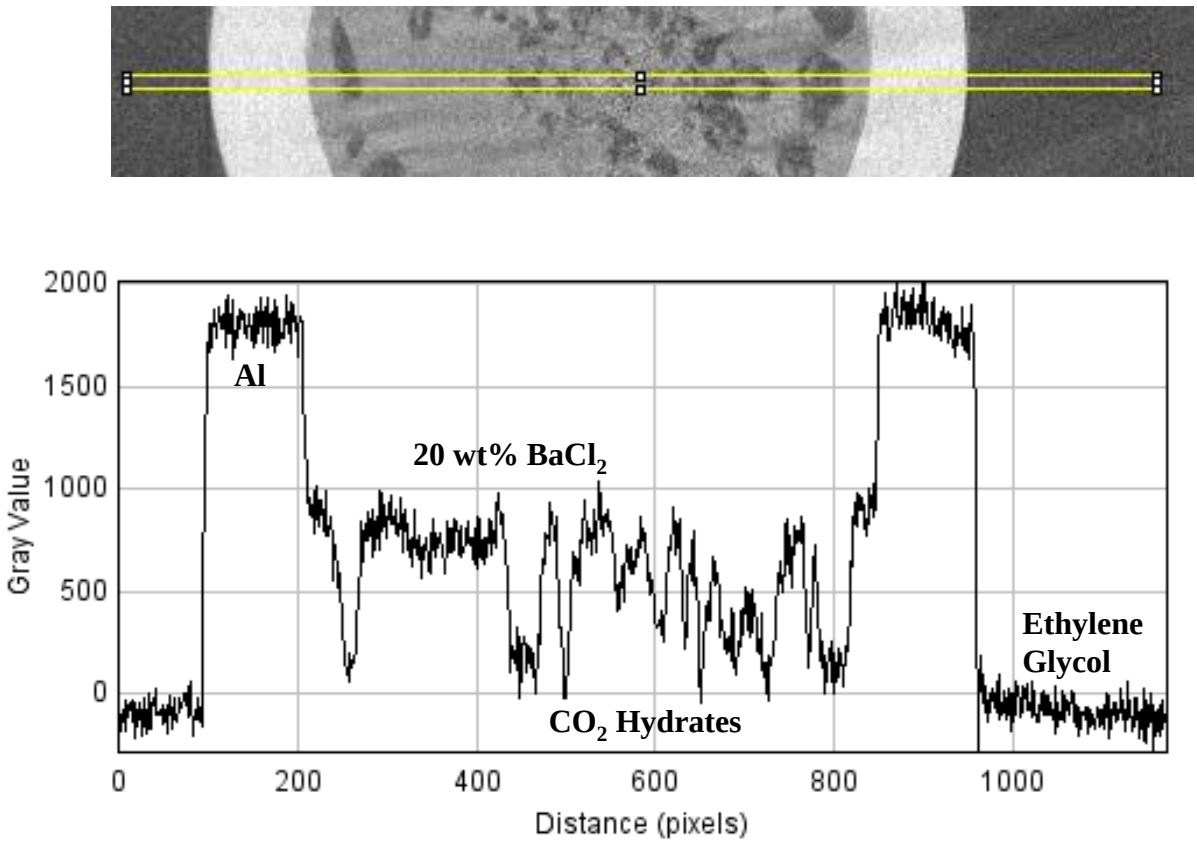

Figure 6.17: *A plot profile was taken across a 2D image slice of the cell at 271.3 h containing aluminum tubing, 20 wt% $BaCl_2$ solution, CO_2 hydrates, and ethylene glycol-water coolant. A profile of the gray value (related to attenuation) across the yellow box was taken and plotted to show where the phases are defined.*

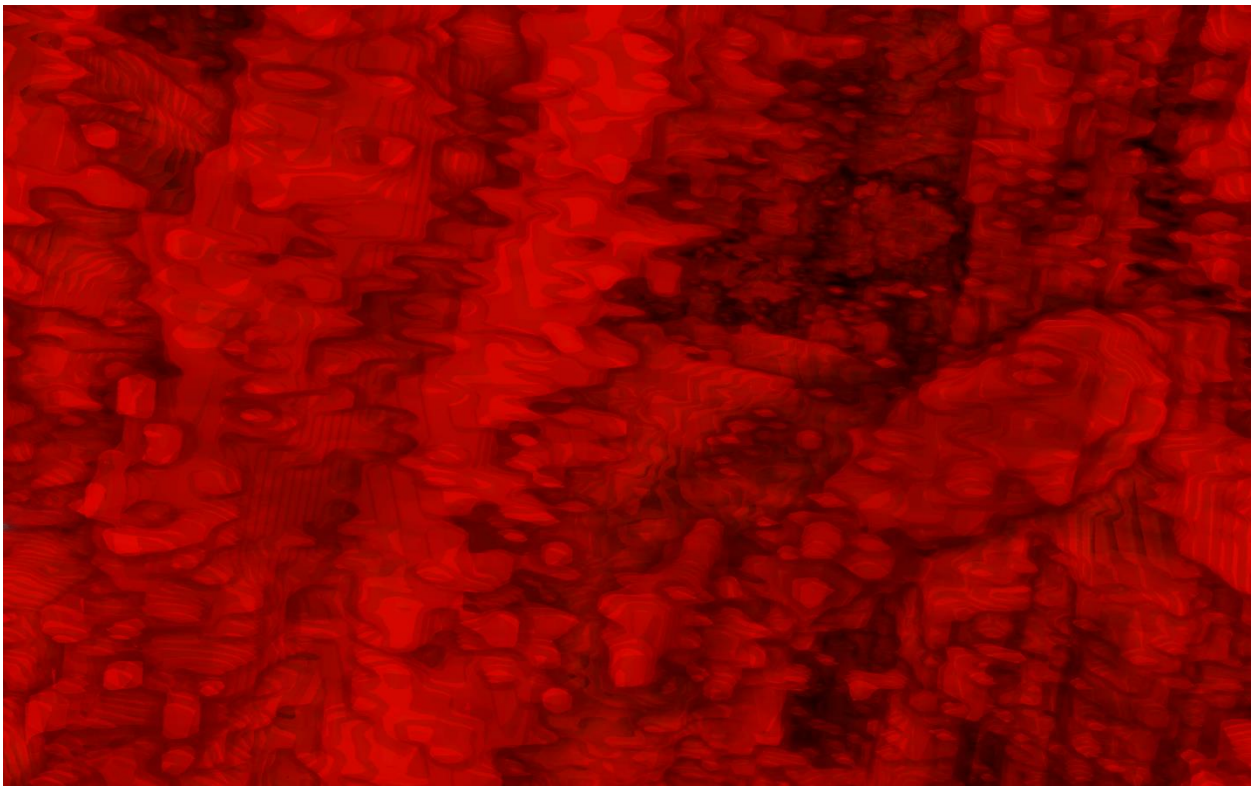

Figure 6.18: *Zoom in of the CO_2 hydrates formed at 300.0 h in Run 4.*

Run 5 was performed using 2.3 mL of 15 wt% $BaCl_2$ solution ($T_{Freezing}$: -4.8°C, ρ: 1.13 g/cm^3) and 647 psig of CO_2 gas while the cell was cooled down to about 0°C. Over a 3 day period, continuous CMT imaging scans were taken at the gas-liquid interface as the cell reached the target experimental temperature. Hydrates were visible after only 12.3 h of cooling when they formed a thin coating on the gas-liquid interface and around a CO_2 gas bubble that migrated below this interface. As shown in Figure 6.19, over the next two days, further CO_2 hydrate branches grew off of the gas-liquid interface, some of which appear to have dendritic branches. Gas hydrates have been found to form a dendritic structure[132], and dendritic crystal growth has been well studied[133]. It is clear that large volumes of very structured, dendritic branched CO_2 hydrates were formed. As seen by Ohmura et al.[44], in a system like this with 3-6 K sub-cooling, many hydrates were found to grow from the gas-liquid interface down into the salt solution, and these hydrates had dendritic shapes. CO_2 hydrate existence was confirmed in the histogram of one of the 2D slices of the CMT scan performed at 381.2 h shown in Figure 6.20. Since the center of the peak for CO_2 hydrates has an attenuation value above 0 $pixel^{-1}$, CO_2 hydrates are indeed present in this CMT run. The plot profile in Figure 6.21 was taken across a region containing both CO_2 gas and CO_2 hydrates, and it is clear in the plot that there is a lower peak for CO_2 gas that is distinguishable from the many CO_2 hydrate peaks.

The 2D image slice at 34.7 h in Figure 6.19 shows several solid, round hydrate structures at the top of the slice. By 61.0 h, these circles are gone as hydrates have formed a thicker layer around the gas-liquid interface and around several gas pockets at the bottom of the image slice. The structure in these dendritic branches at 61.0 h can be seen in Figure 6.22. Hydrate branches are distinct, but each seems to consist of several shorter, perpendicular branches.

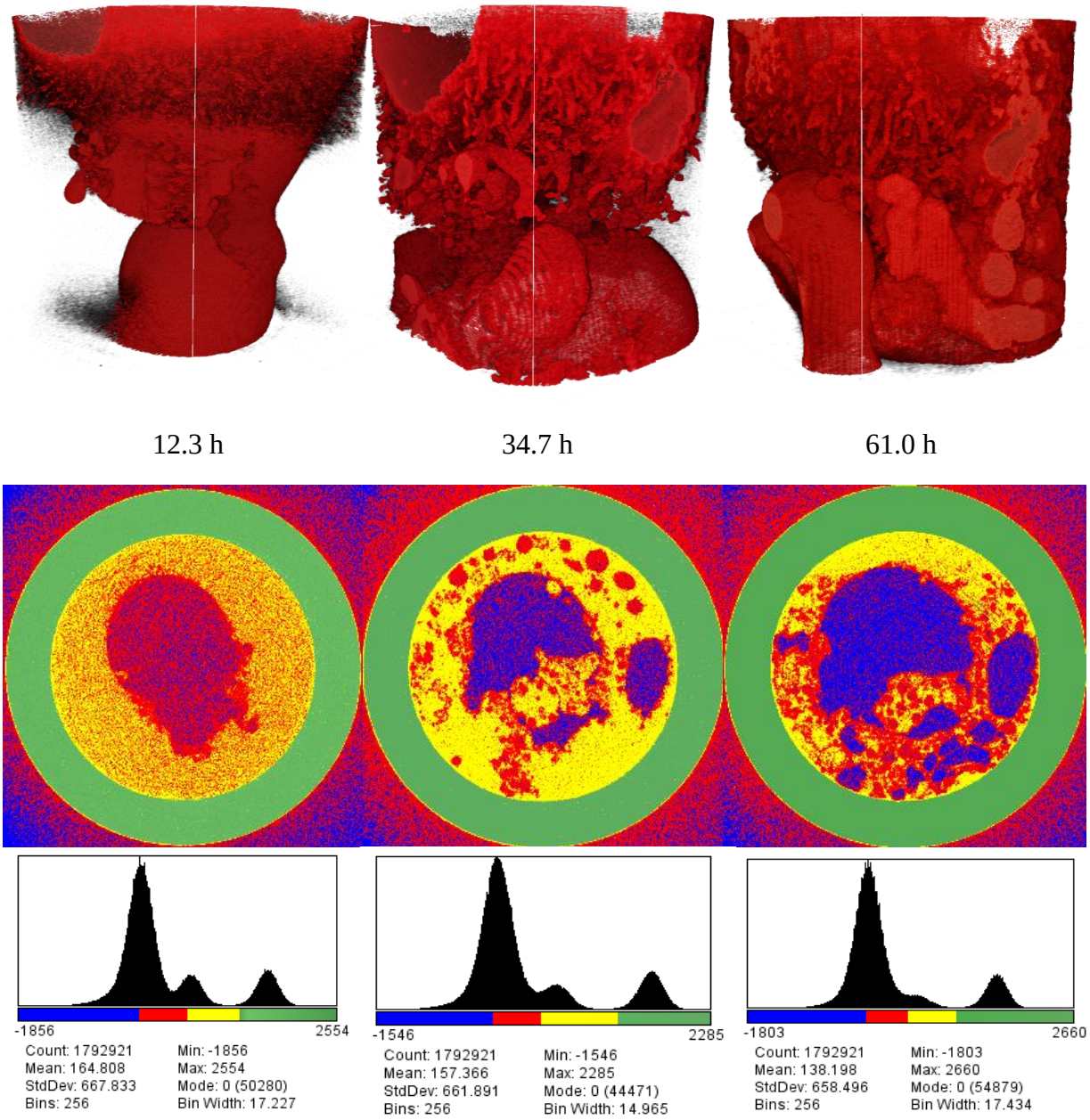

Figure 6.19: *Time-Resolved CMT images of CO_2 hydrate growth from an aqueous solution of 15 wt% $BaCl_2$ in Run 5. Time resolved hydrate growth is shown in 3D volumes, where red indicates CO_2 hydrates and all other phases present in the cell have been made transparent. The 2D image slices represent slice 450 of the 3D images. In the 2D images, red indicates CO_2 hydrates, blue is CO_2 gas, yellow is 15 wt% $BaCl_2$ solution, and green is aluminum tubing. The OD of the green aluminum tubing is 0.25" and the ID is 0.18". Histograms of the different phases in the 2D images are also shown. The growth of hydrates extends downwards into the liquid phase from the gas-liquid interface.*

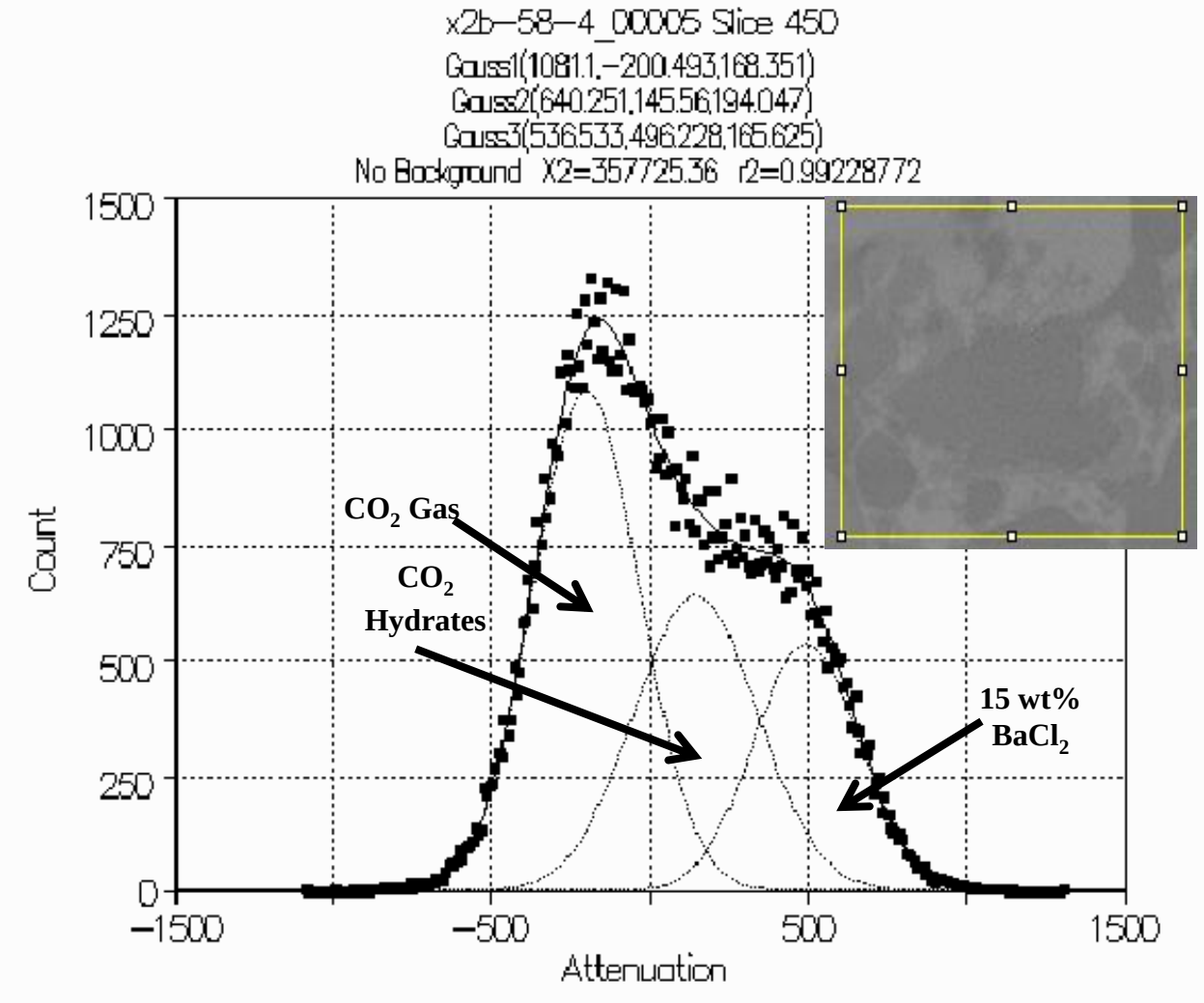

Figure 6.20: *Histogram with attenuation values of pixel^{-1} for slice 450 of the CMT scan performed during Run 5 at 61.0 h. The PeakFit program was used to distinguish between the different peaks in the histogram created by the various materials present inside the cell. The image inside the yellow box above the plot shows the region of the cell used to create this histogram, and in the image, darker gray regions are gas, lighter gray regions are solution, and gray colors in between gas and solution are gas hydrates. Since the peak attributed to CO_2 hydrates is centered above 0 pixel^{-1}, CO_2 hydrates are present in this experiment.*

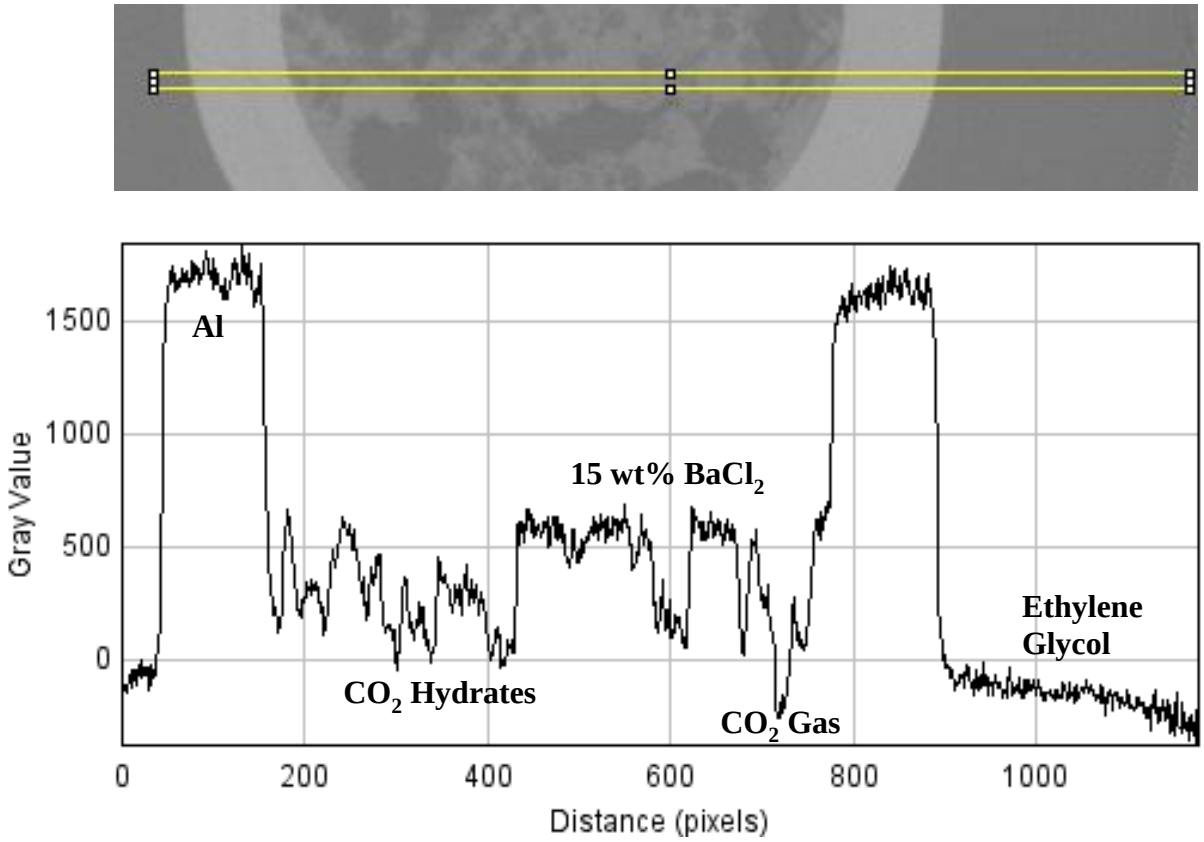

Figure 6.21: *A plot profile was taken across a 2D image slice of the cell at 61.0 h containing aluminum tubing, 15 wt% $BaCl_2$ solution, CO_2 hydrates, CO_2 gas, and ethylene glycol-water coolant. A profile of the gray value (related to attenuation) across the yellow box was taken and plotted to show where the phases are defined.*

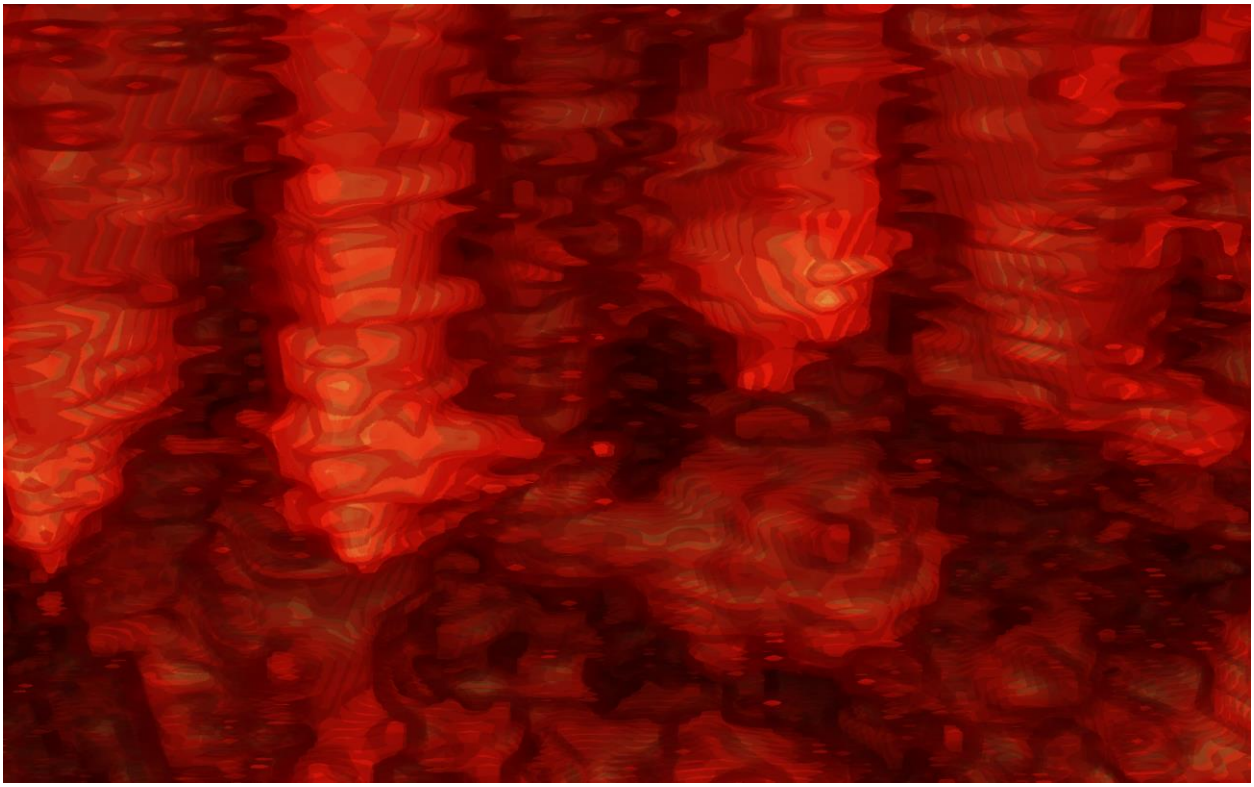

Figure 6.22: *Zoom in of the CO_2 hydrates formed at 61.0 h in Run 5.*

The third run to form CO_2 hydrates was performed using 2.4 mL of 15 wt% $BaCl_2$ solution and 668 psig of CO_2 gas (Run 6). This was the longest running experiment, lasting for 28 days, and there was much hydrate growth over time. At 238.6 h, two regions with the same attenuation as the $BaCl_2$ solution separated by a thin layer of CO_2 hydrates were found to exist; the lower liquid phase consisted of a scaffold-like network of CO_2 hydrates, while the upper liquid phase was pure liquid with few hydrates, as shown in Figure 6.23. This separation of the $BaCl_2$ solution phase was seen for two days and then disappeared. In all runs taken from this point onwards, there was a very heterogeneous mixture of many gas bubbles, gas hydrates, and liquid areas in the regions viewed. Areas of CO_2 gas were found to move, and over time, hydrates thickened to consume a large portion of space in the reactor, thus moving the gas-liquid interface to higher locations in the cell as hydrates took up larger volumes. Two areas of the cell were imaged over the next 18 days – the region where the $BaCl_2$ solution liquid-liquid separation was originally found (Figure 6.23), and the initial gas-liquid interface in the cell (Figure 6.24). At 263.1 h in Figure 6.23, it is clear that dendritic branch structures had formed. The 2D image slice in Figure 6.23 at 450.0 h shows a structure where there are four gas regions coated in CO_2 hydrates, as well as hydrate bands circling around these gas regions near the aluminum tubing. Figure 6.25 shows what these hydrate branches look like up close at 450.0 h at the liquid-liquid interface region; these branches look very similar to those in Figure 6.22 for Run 5, though these branches are less straight and more random in direction.

Similar to the hydrates found to form in the solution, hydrates at the gas-liquid interface in Figure 6.24 were branching hydrates that thickened over time. As hydrates grew, the gas-liquid interface was raised such that it was out of the field of view for this scanning sequence, as seen at 453.0 h. A close-up view of CO_2 hydrates located in the liquid-liquid interface region shown in Figure 6.25 look identical to those shown in Figure 6.26 near the gas-liquid interface.

The existence of CO_2 hydrates was confirmed in the histogram of one of the 2D slices of the CMT scan performed at 381.2 h and is shown in Figure 6.27(a). Since the center of the peak for CO_2 hydrates has an attenuation value above 0 $pixel^{-1}$, CO_2 hydrates are indeed present in this CMT run. This run showed very clear hydrate formation that could easily be observed across 2D image slices. Figure 6.27(b) shows a yellow box region that was profiled in the plot shown in 6.27(c). A clear phase separation of gray values (related to x-ray attenuation) can be seen among

the phases present in the cell, where the highest gray values indicate aluminum tubing, followed by 15 wt% $BaCl_2$ solution, CO_2 hydrates, ethylene glycol-water coolant, and the lowest gray values represent CO_2 gas. Figure 6.28 shows another plot profile taken across a region with CO_2 hydrates, CO_2 gas, and 15 wt% $BaCl_2$ solution. There is distinct separation of the phases present in the cell across the 2D image slice.

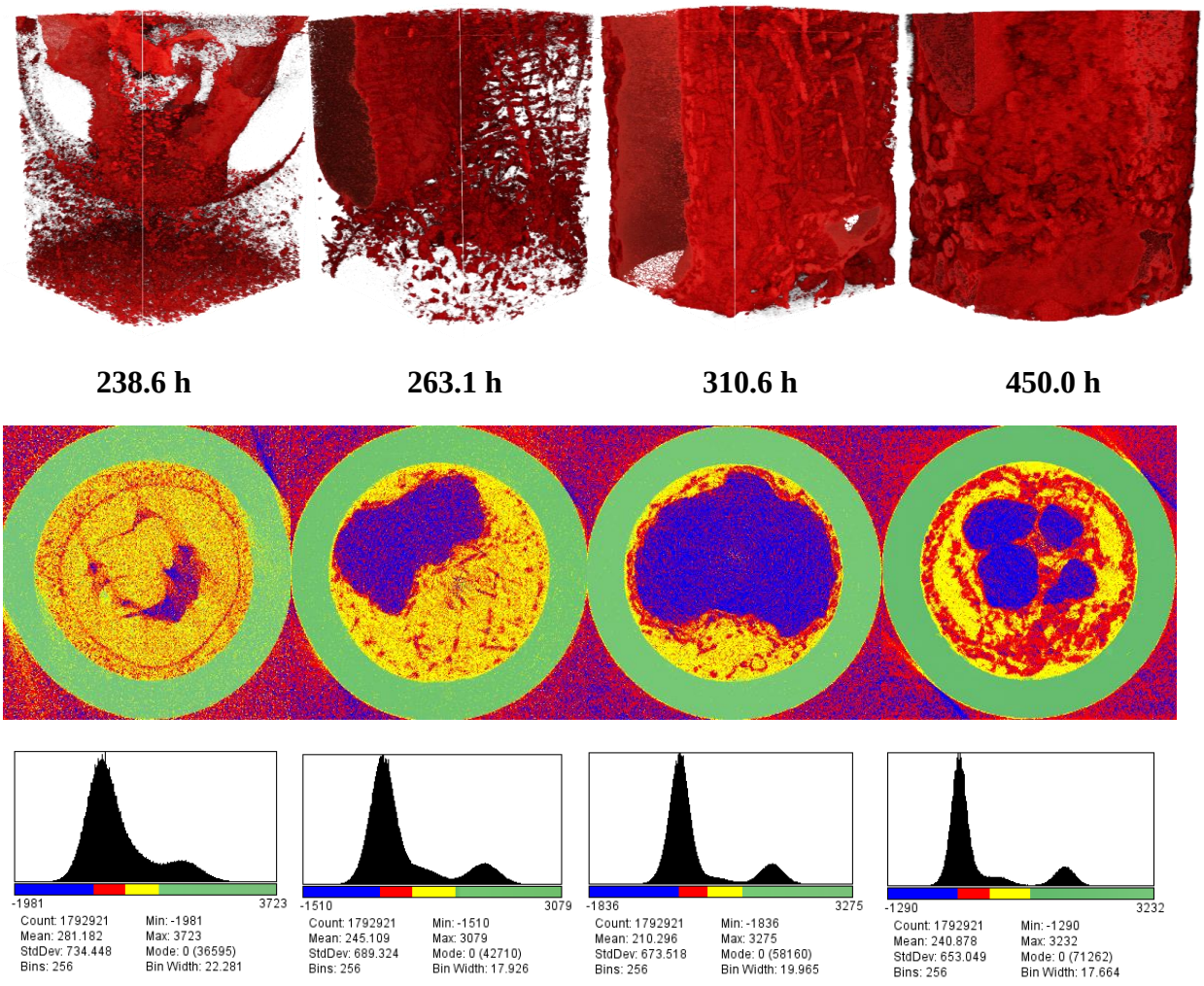

Figure 6.23: *Time-Resolved CMT images of CO_2 hydrate growth from an aqueous solution of 15 wt% $BaCl_2$ at the liquid-liquid interface in Run 6. Time resolved hydrate growth is shown in 3D volumes, where red indicates CO_2 hydrates and all other phases present in the cell have been made transparent. The 2D image slices represent slice 300 of the 3D images. In the 2D images, red indicates CO_2 hydrates, blue is CO_2 gas, yellow is 15 wt% $BaCl_2$ solution, and green is aluminum tubing. The OD of the green aluminum tubing is 0.25" and the ID is 0.18". Histograms of the different phases in the 2D images are also shown.*

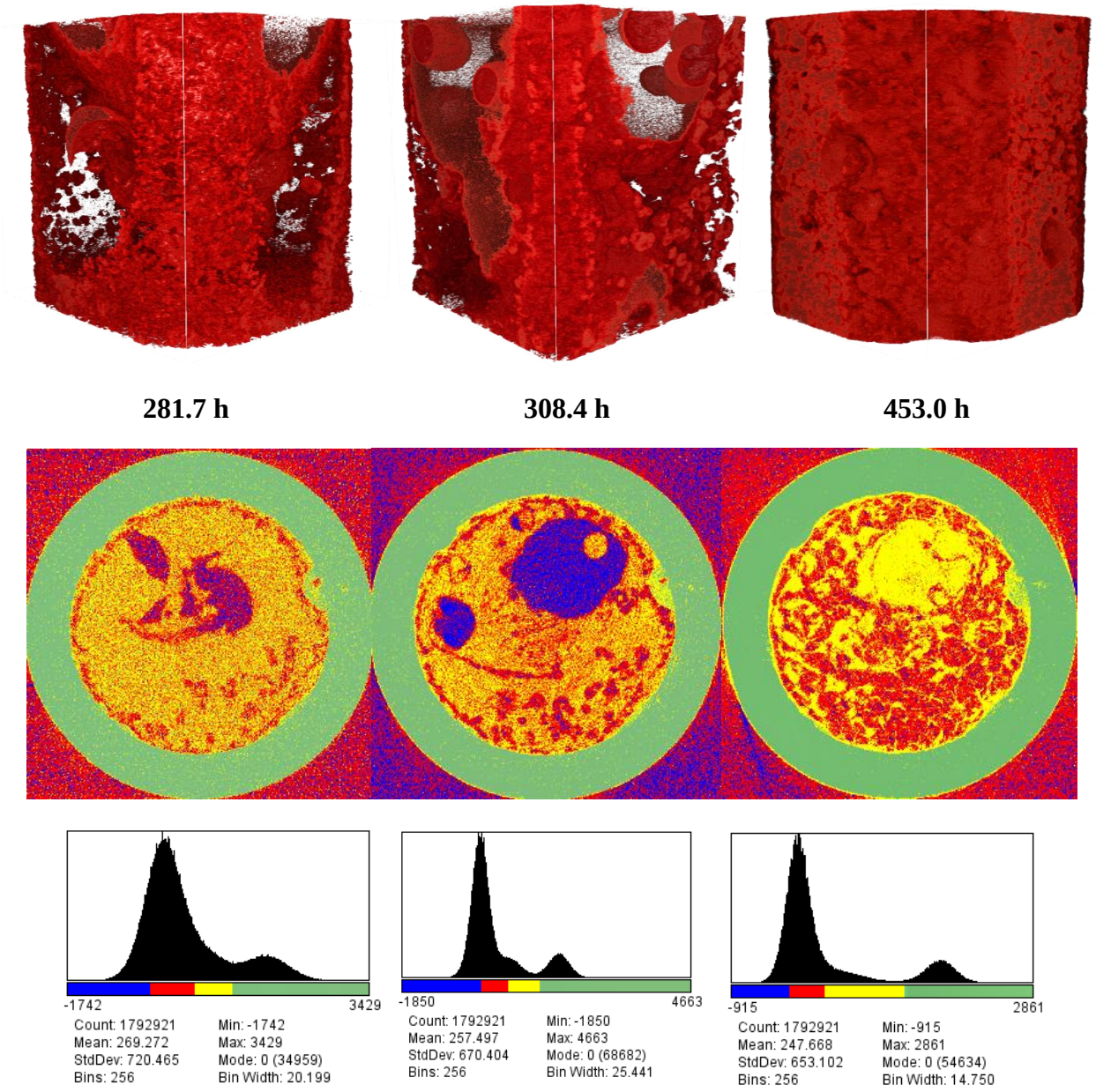

Figure 6.24: *Time-Resolved CMT images of CO_2 hydrate growth from an aqueous solution of 15 wt% $BaCl_2$ at the gas-liquid interface in Run 6. Time resolved hydrate growth is shown in 3D volumes, where red indicates CO_2 hydrates and all other phases present in the cell have been made transparent. The 2D image slices represent slice 350 of the 3D images. In the 2D images, red indicates CO_2 hydrates, blue is CO_2 gas, yellow is 15 wt% $BaCl_2$ solution, and green is aluminum tubing. The OD of the green aluminum tubing is 0.25" and the ID is 0.18". Histograms of the different phases in the 2D images are also shown.*

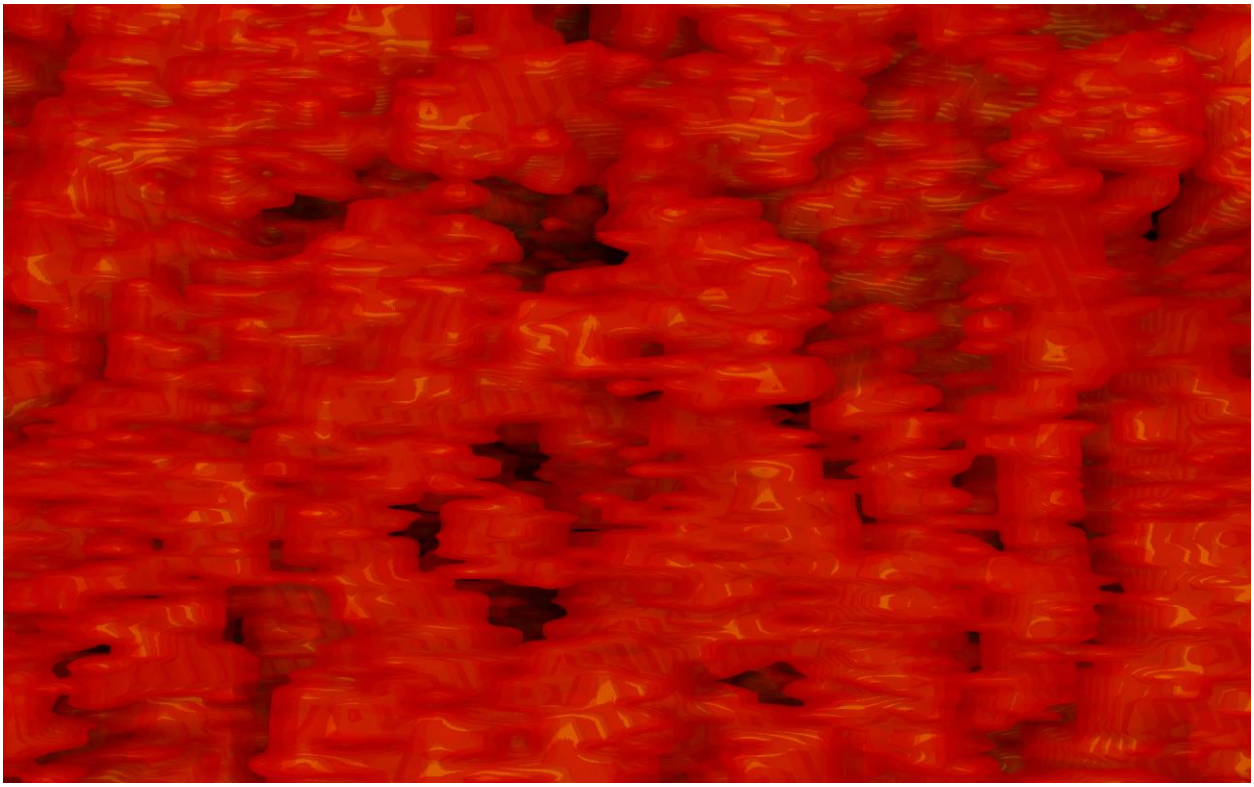

Figure 6.25: *Zoom in of the CO_2 hydrates formed at 450.0 h in Run 6 at the liquid-liquid interface region.*

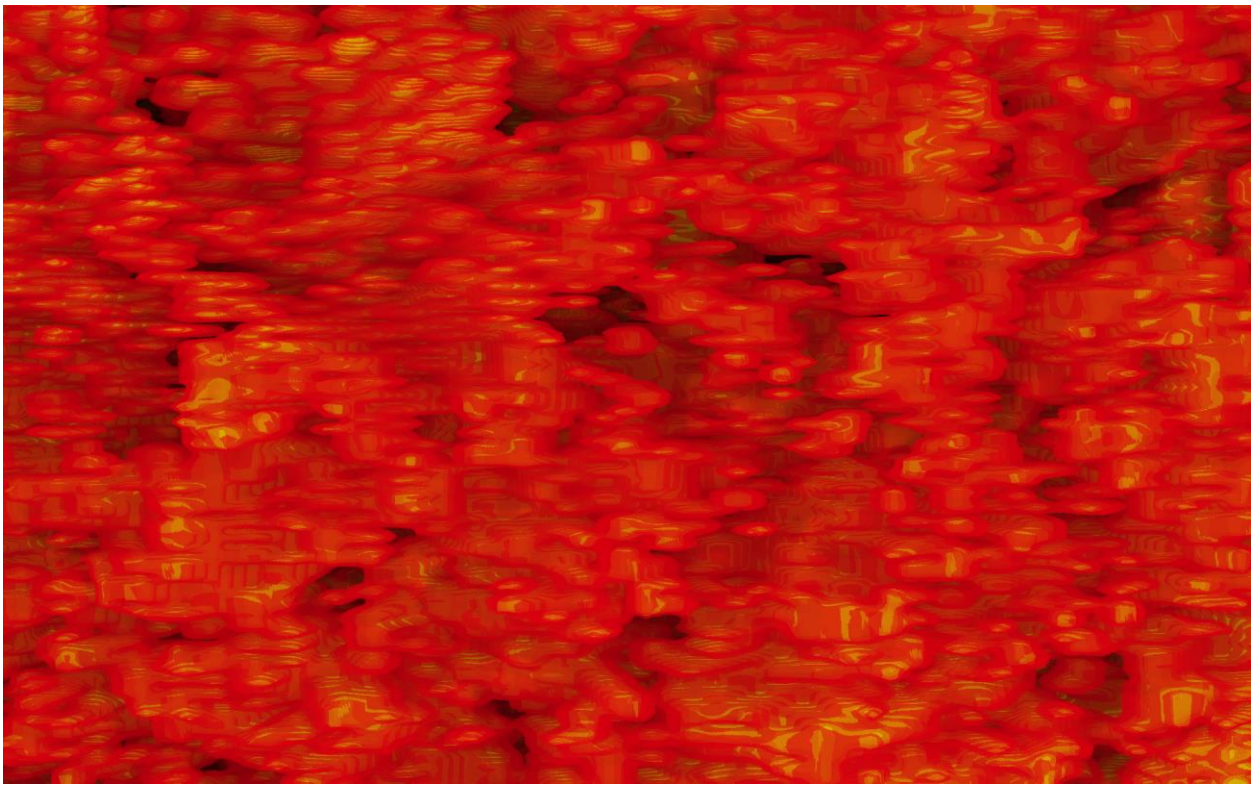

Figure 6.26: *Zoom in of the CO_2 hydrates formed at 453.0 h in Run 6 at the gas-liquid interface region.*

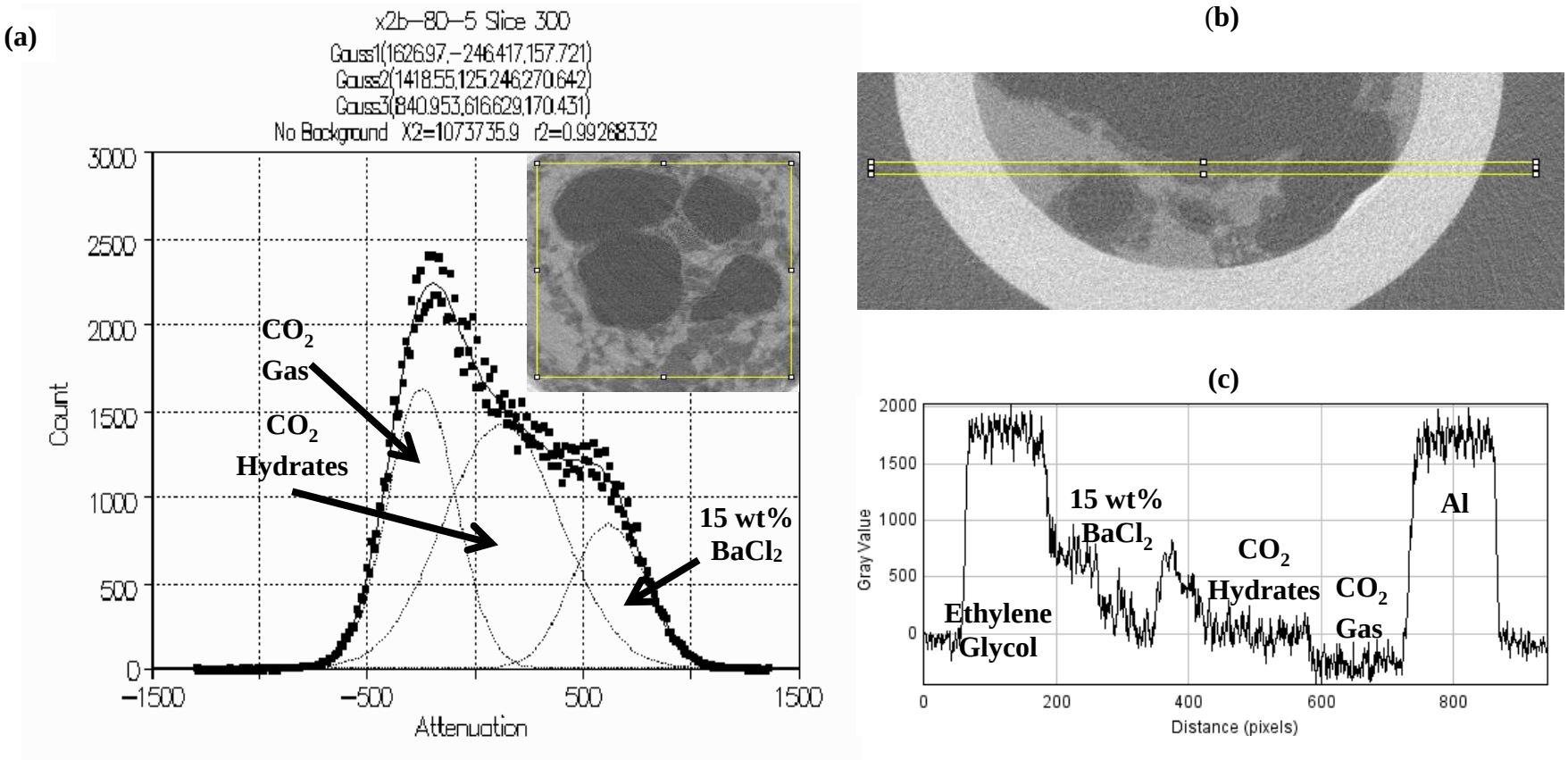

Figure 6.27: (a) *Histogram with attenuation values of pixel^{-1} for slice 300 of the CMT scan performed during Run 6 at 450.0 h. The PeakFit program was used to distinguish between the different peaks in the histogram created by the various materials present inside the cell. The image inside the yellow box above the plot shows the region of the cell used to create this histogram, and in the image, darker gray regions are gas, lighter gray regions are solution, and gray colors in between gas and solution are gas hydrates. Since the peak attributed to CO_2 hydrates is centered above 0 pixel^{-1}, CO_2 hydrates are present in this experiment. (b) A plot profile box was drawn across a 2D image slice of the cell at 669.1 h containing aluminum tubing, 15 wt% $BaCl_2$ solution, CO_2 hydrates, CO_2 gas, and ethylene glycol-water coolant. (c) A plot of the gray value (related to attenuation) across the yellow box where the phases are defined.*

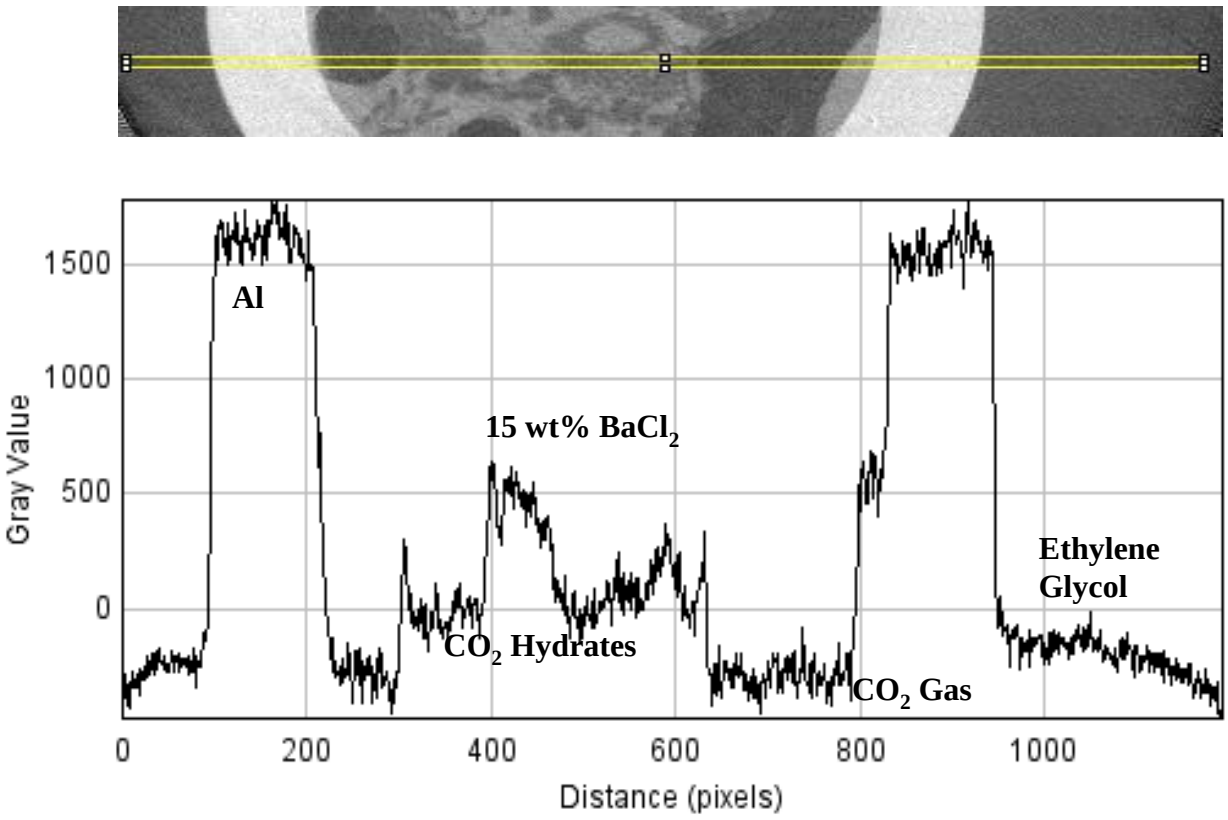

Figure 6.28: *A plot profile was taken across a 2D image slice of the cell at 450.0 h containing aluminum tubing, 15 wt% $BaCl_2$ solution, CO_2 hydrates, CO_2 gas, and ethylene glycol-water coolant. A profile of the gray value (related to attenuation) across the yellow box was taken and plotted to show where the phases are defined.*

A later scan taken at a different height than those shown in Figures 6.23 and 6.24 is presented in Figure 6.29 for Run 6. A different color scheme was used, such that pink is CO_2 hydrates, purple is CO_2 gas, orange is 15 wt% $BaCl_2$ solution, and yellow is aluminum tubing. In Figure 6.29 (a), all of the phases in the cell are colored, whereas in Figure 6.29 (b), only the hydrate phase is highlighted, and a histogram shows how colors are defined for both images. Figure 6.29 (b) indicates the presence of a material with the same attenuation coefficient as the CO_2 hydrates forming a scaffold network in the CO_2 gas region of the system. No previous studies have described the possibility of a hydrate network in the gas phase of a hydrate system. A few other experiments described herein appeared to have a similar scaffold, though the network depicted in Figure 6.29 was the most clear.

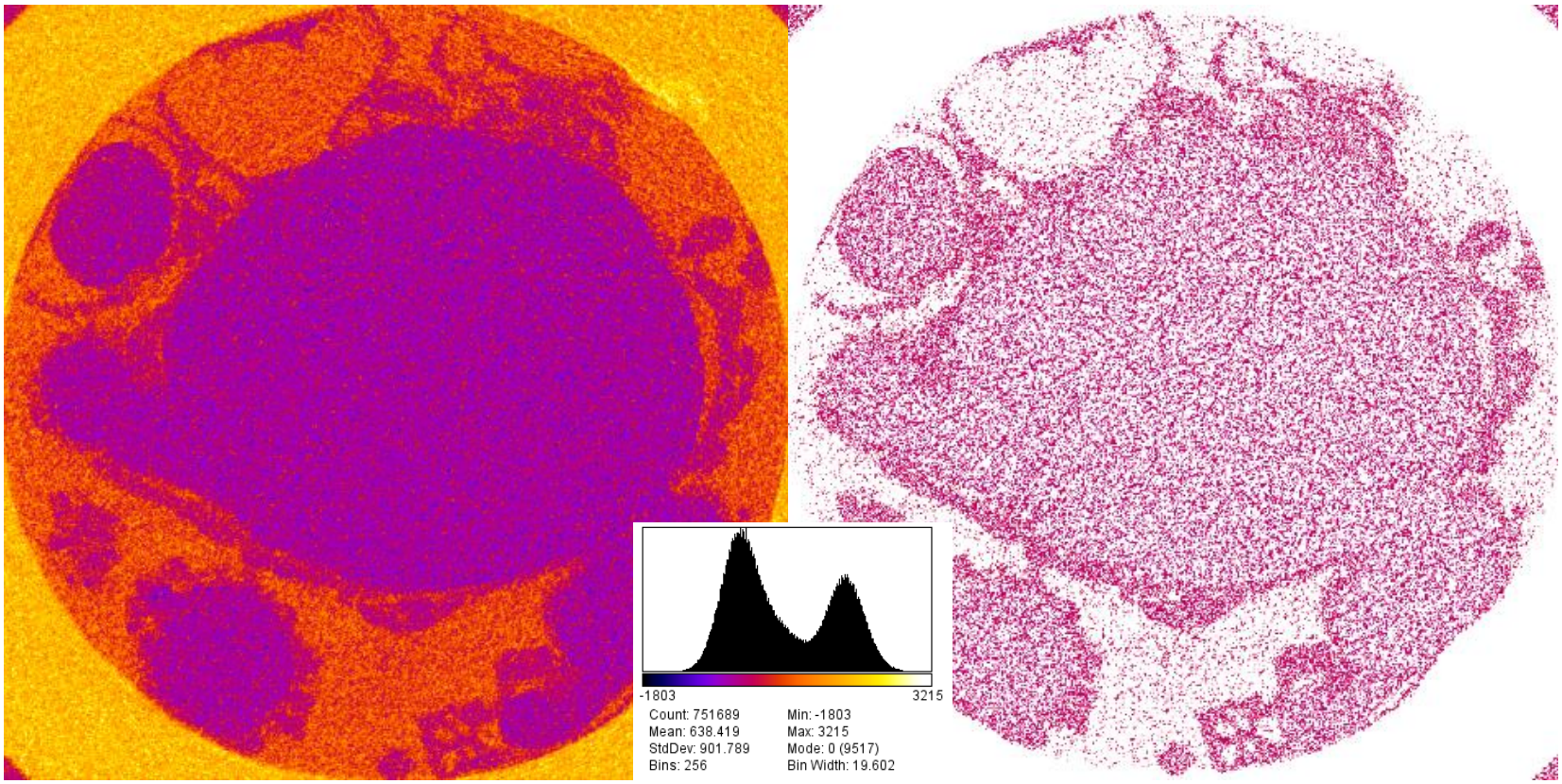

(a) **(b)**

Figure 6.29: *One image slice from a scan taken at the gas-liquid interface at 669.1 h for Run 6, which is above the previous gas-liquid interface shown in Figure 6.24. Under this color scheme, pink represents CO_2 hydrates, purple is CO_2 gas, orange is 15 wt% $BaCl_2$ solution, and yellow is aluminum tubing. (a) shows all of the phases present in the cell while (b) highlights CO_2 hydrates only.*

6.2.3 Mixed CH_4 - CO_2 Hydrates (Runs 7-9)

Next, mixed CH_4-CO_2 gas hydrate experiments were performed to determine hydrate morphology differences based on gas composition. In the first mixed gas run (Run 7), a 50%-50% mixture of CH_4 and CO_2 was used to form hydrates in 2.4 mL of 15 wt% $BaCl_2$ solution. The cell was first pressurized to 484 psig with CO_2 gas, then up to 960 psig with CH_4 gas. The system was cooled directly in the refrigerated circulator at -2.0°C, and after 5 hours of cooling, cell pressure reached 885 psig at -2.1°C. However, 20 h after cooling began, the cell was at 946 psig and -2.1°C. The refrigerated circulator was checked and found to be working properly, and an image taken at the gas-liquid interface at this time indicated only the presence of a gas bubble. After 74.0 h when the system was at 953 psig and -2.1°C, the cell was imaged at about 0ºC, and gas hydrates were found to be coating the gas-liquid interface and gas bubbles in the solution, as shown in Figure 6.30. This is a peculiar finding, as usually a drop in system pressure indicates hydrate formation, while in Run 7, an increase in pressure was found to result in hydrate formation. The cell was imaged again after 141.5 h and 167.8 h which both showed further hydrate growth extending from the gas-liquid interface in amorphous shapes. Mixed gas hydrate presence was confirmed in the histogram of one of the 2D slices of the CMT scan performed at 381.2 h shown in Figure 6.31. Since the center of the peak for mixed gas hydrates has an attenuation value above 0 $pixel^{-1}$, mixed gas hydrates are indeed present in this CMT run. The plot profile shown in Figure 6.32 depicts the clear phase separation for this run that confirms hydrate formation.

The zoom in shown in Figure 6.33 indicates that there is a mixture of individual, small hydrate spheres, as well as some larger hydrate branches. The hydrate growth witnessed appeared to be a combination of the structures seen for pure CH_4 hydrate formation in Runs 1 and 3 and pure CO_2 hydrate formation in Runs 4-6.

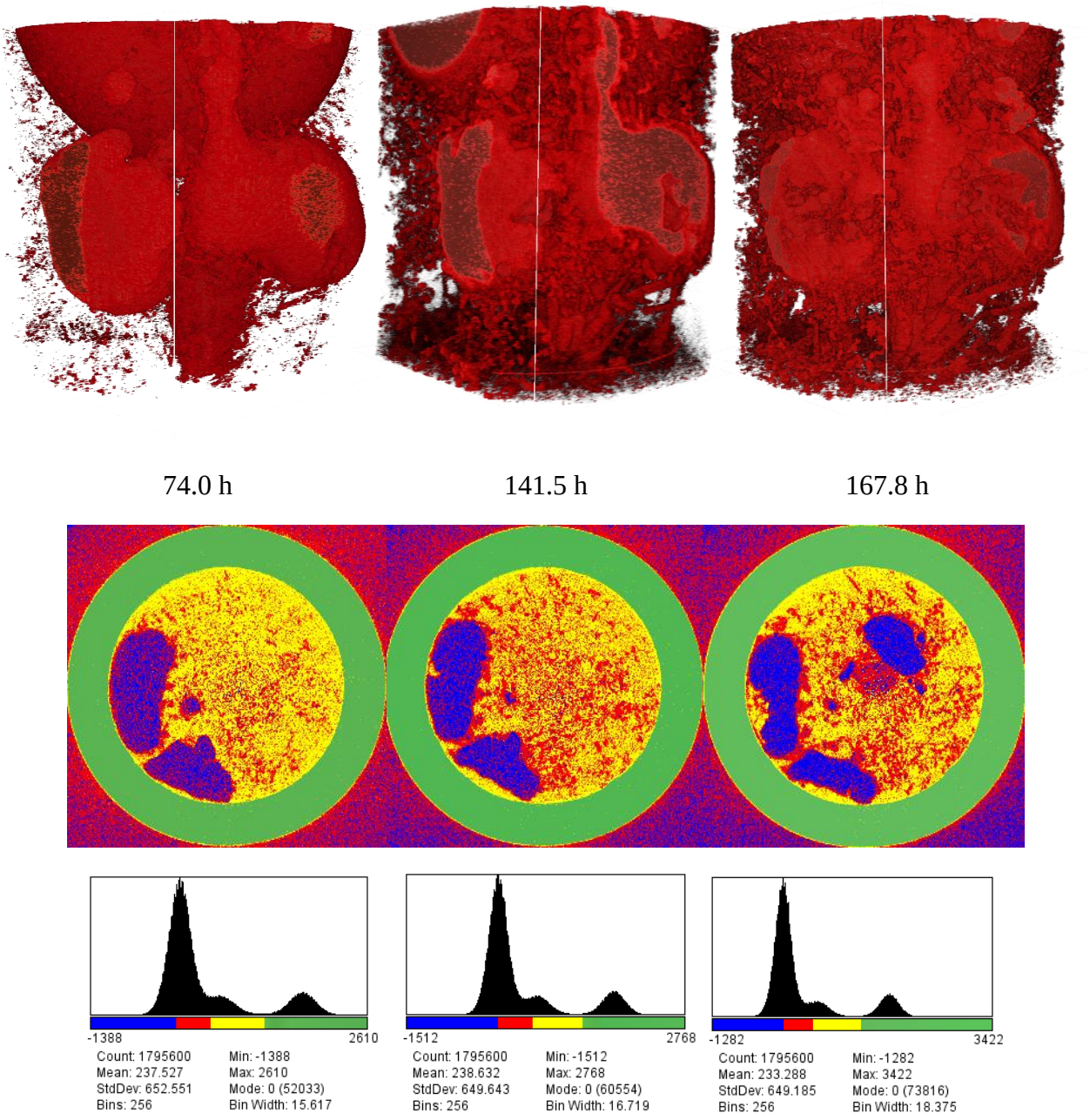

Figure 6.30: *Time-Resolved CMT images of hydrate growth in a 50%-50% CH_4-CO_2 gas mixture from an aqueous solution of 15 wt% $BaCl_2$ in Run 7. Time resolved hydrate growth is shown in 3D volumes, where red indicates CH_4-CO_2 hydrates and all other phases present in the cell have been made transparent. The 2D image slices represent slice 250 of the 3D images. In the 2D images, red indicates CH_4-CO_2 hydrates, blue is CH_4-CO_2 gas, yellow is 15 wt% $BaCl_2$ solution, and green is aluminum tubing. The OD of the green aluminum tubing is 0.25" and the ID is 0.18". Histograms of the different phases in the 2D images are also shown. The growth of hydrates extends downwards into the liquid phase from the gas-liquid interface.*

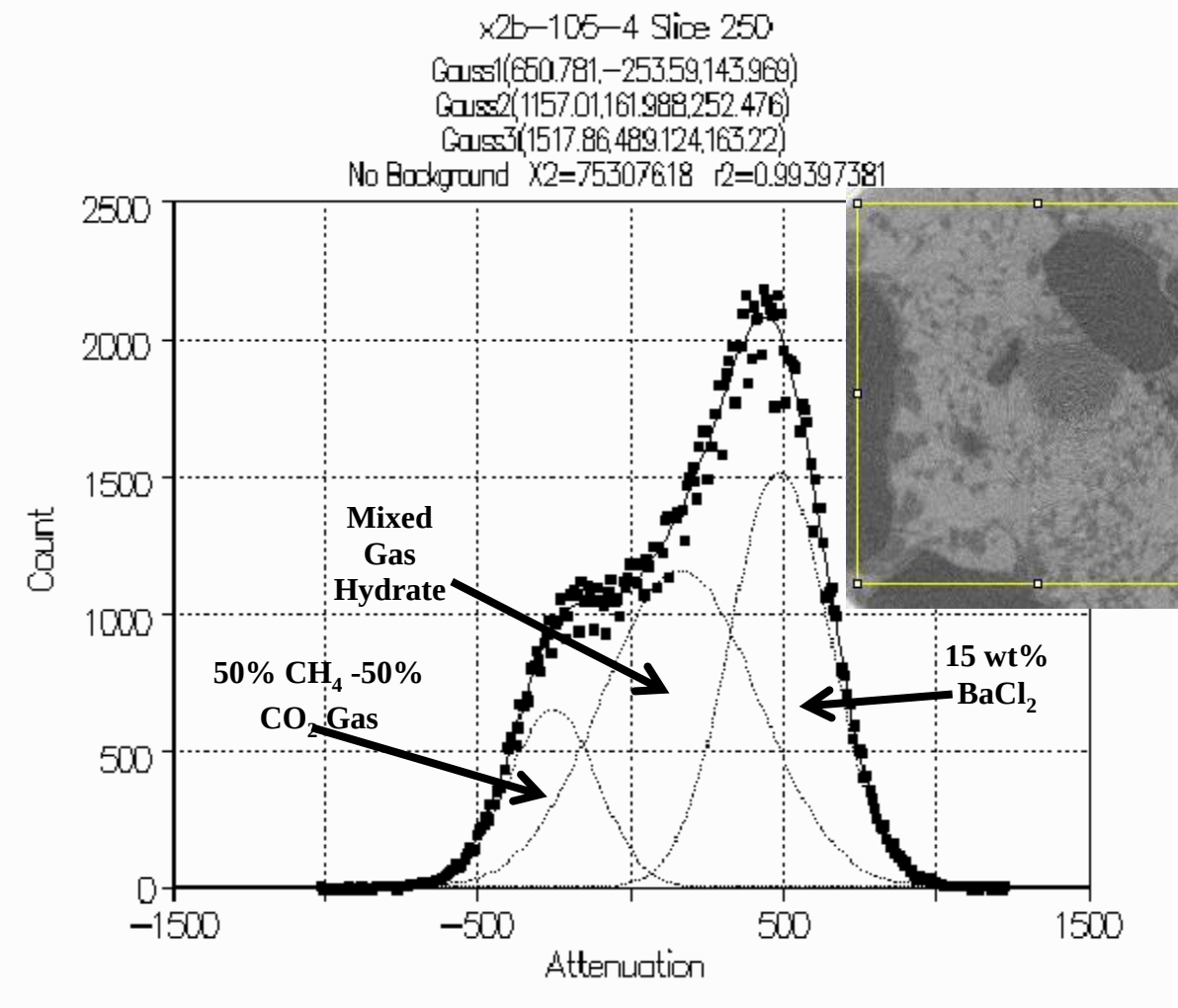

Figure 6.31: *Histogram with attenuation values of pixel^{-1} for slice 250 of the CMT scan performed during Run 7 at 167.8 h. The PeakFit program was used to distinguish different peaks in the histogram created by the various materials present inside the cell. The image inside the yellow box above the plot shows the region of the cell used to create this histogram, and in the image, darker gray regions are gas, lighter gray regions are solution, and gray colors in between gas and solution are gas hydrates. Since the peak attributed to CH_4-CO_2 hydrates is centered above 0 pixel^{-1}, CH_4-CO_2 hydrates are present in this experiment.*

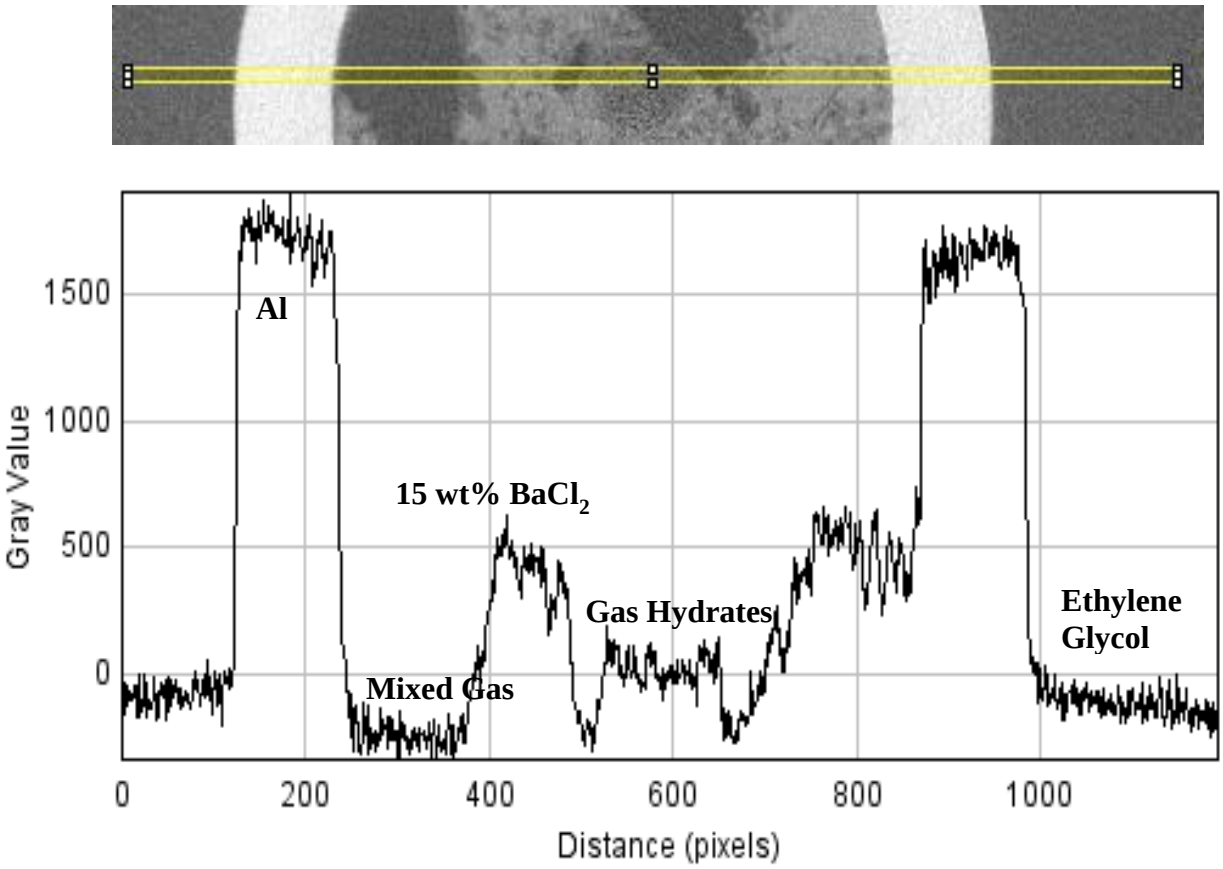

Figure 6.32: *A plot profile was taken across a 2D image slice of the cell at 167.8 h containing aluminum tubing, 15 wt% $BaCl_2$ solution, mixed gas hydrates, CH_4-CO_2 gas, and ethylene glycol-water coolant. A profile of the gray value (related to attenuation) across the yellow box was taken and plotted to show where the phases are defined.*

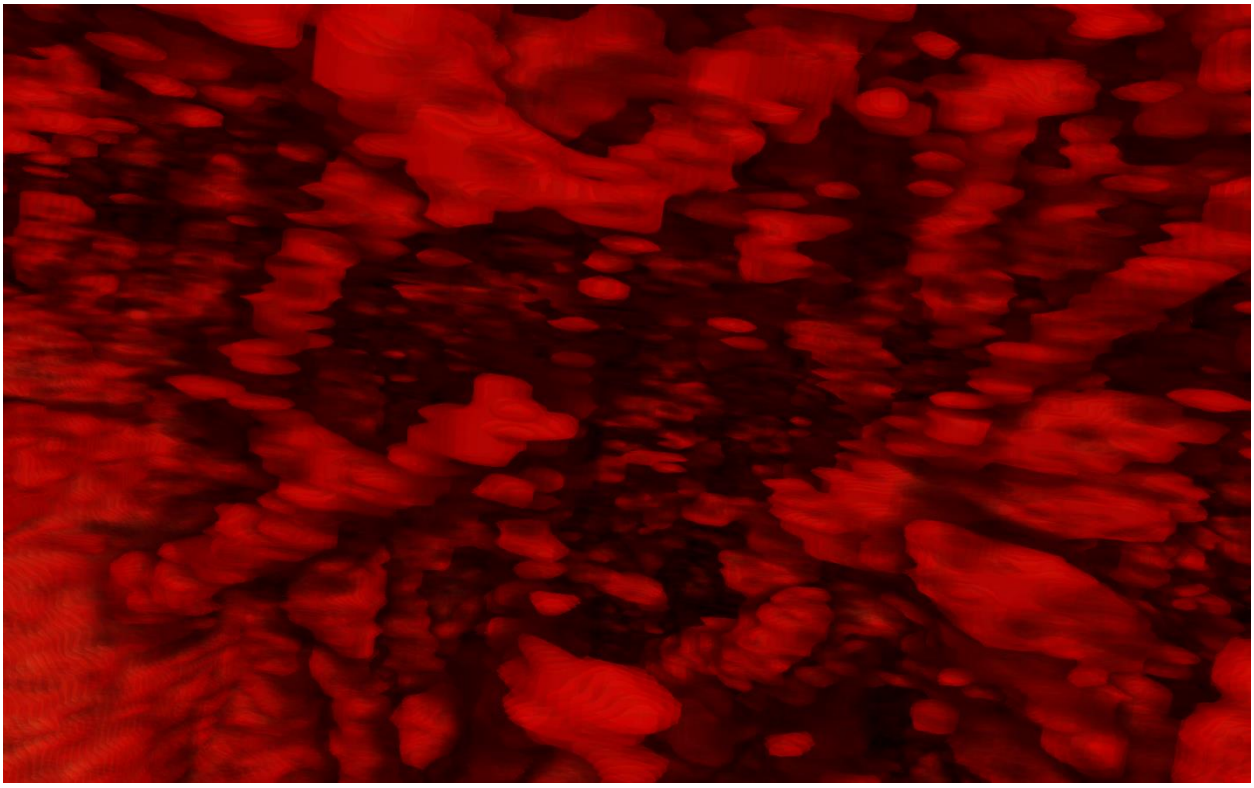

Figure 6.33: *Zoom in of the CH_4-CO_2 hydrates formed from a 50% CH_4-50% CO_2 gas mixture at 167.8 h in Run 7.*

In Run 8, a mixture of 32% CH_4 and 68% CO_2 was used to form hydrates in 2.5 mL of 15 wt% $BaCl_2$ solution. The cell was first pressurized to 638 psig with CO_2 gas, then up to 945 psig with CH_4 gas. The cell was continuously imaged as it was cooled from room temperature, and after about 3 hours of cooling to around 0ºC, hydrates were found to form at the gas-liquid interface. Cell pressure cannot be monitored once CMT scans are begun, so the behavior of pressure during cell cooling for this run was not monitored. CH_4 hydrates have been found to be stabilized by the presence of CO_2[71], so the speedy formation of mixed gas hydrates could be due to this effect. Needle-like hydrates were observed growing downwards from the interface, and more hydrates grew and thickened over three days as shown in Figure 6.34. Mixed gas hydrate presence was confirmed in the histogram of one of the 2D slices of the CMT scan performed at 381.2 h shown in Figure 6.35. Since the center of the peak for mixed gas hydrates has an attenuation value above 0 $pixel^{-1}$, mixed gas hydrates are indeed present in this CMT run. As the needles on these hydrates are very thin and interspersed in the solution, the plot profile shown in Figure 6.36 has very sharp and choppy peaks in the solution-hydrate region of the image slice. When the 3D volume of the hydrates at 70.4 h was zoomed in on for Figure 6.37, it was clear that there were rounded hydrate branches that formed the thin needles seen.

At the end of this run, several GC samples were taken to determine the composition of the gas phase in the cell. GC samples taken prior to depressurization, when the cell was still cold, indicated a gas phase of 2% CH_4 and 98% CO_2. After the cell was warmed up to room temperature, the gas phase was composed of less than 1% CH_4 and almost entirely CO_2. Before and after the cell was warmed up to room temperature, the composition of the gas phase in the cell was similar, indicating that the concentration of gas in hydrates was similar to the composition of gas in the gas phase. These results are similar to Jerguson Runs 11-13 described in Chapter 5 for mixed gas hydrates.

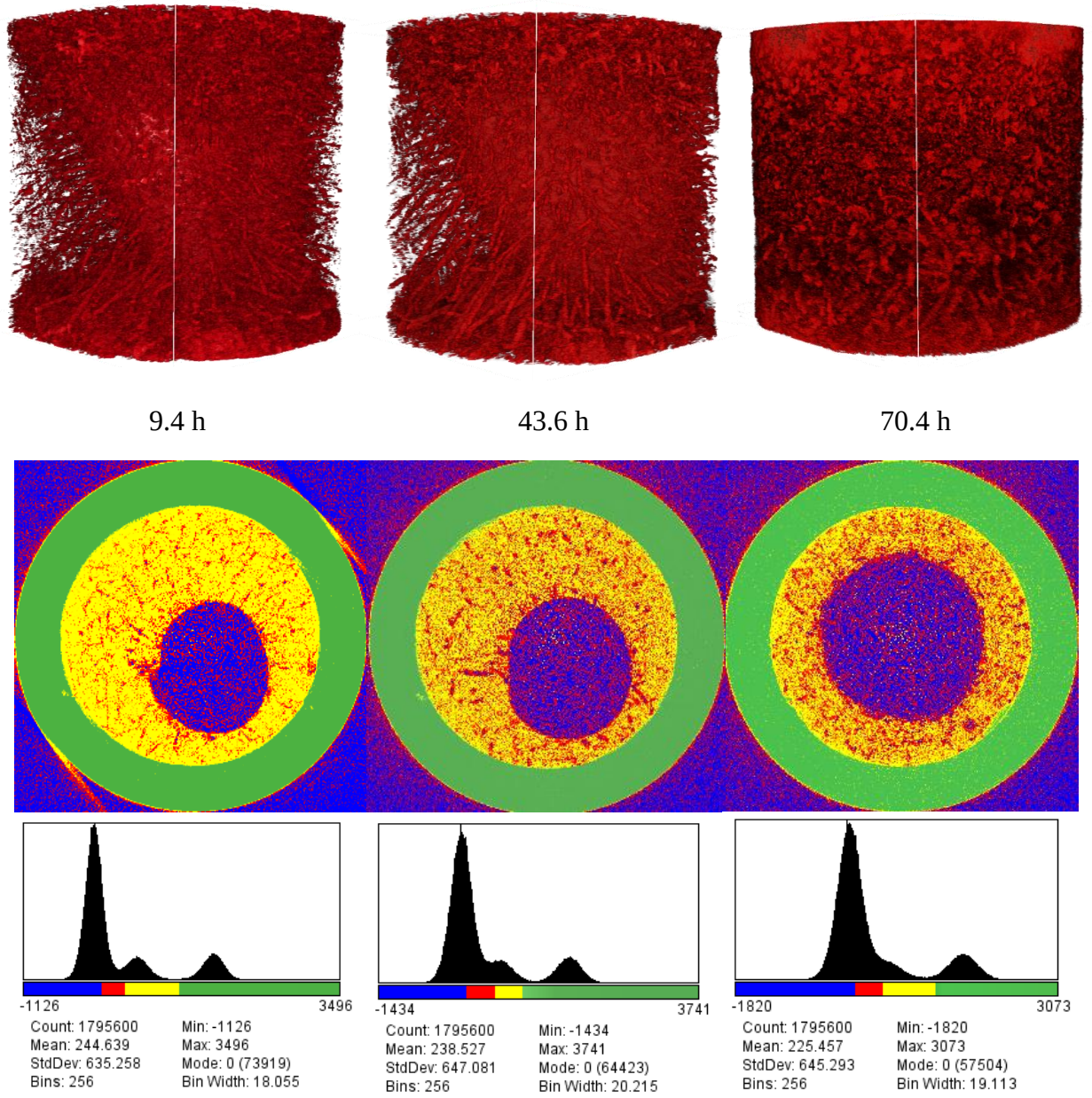

Figure 6.34: *Time-Resolved CMT images of hydrate growth in a 32% CH_4 – 68% CO_2 gas mixture from an aqueous solution of 15 wt% $BaCl_2$ in Run 8. Time resolved hydrate growth is shown in 3D volumes, where red indicates CH_4-CO_2 hydrates and all other phases present in the cell have been made transparent. The 2D image slices represent slice 450 of the 3D images. In the 2D images, red indicates CH_4-CO_2 hydrates, blue is CH_4-CO_2 gas, yellow is 15 wt% $BaCl_2$ solution, and green is aluminum tubing. The OD of the green aluminum tubing is 0.25" and the ID is 0.18". Histograms of the different phases in the 2D images are also shown. The growth of hydrates extends downwards into the liquid phase from the gas-liquid interface.*

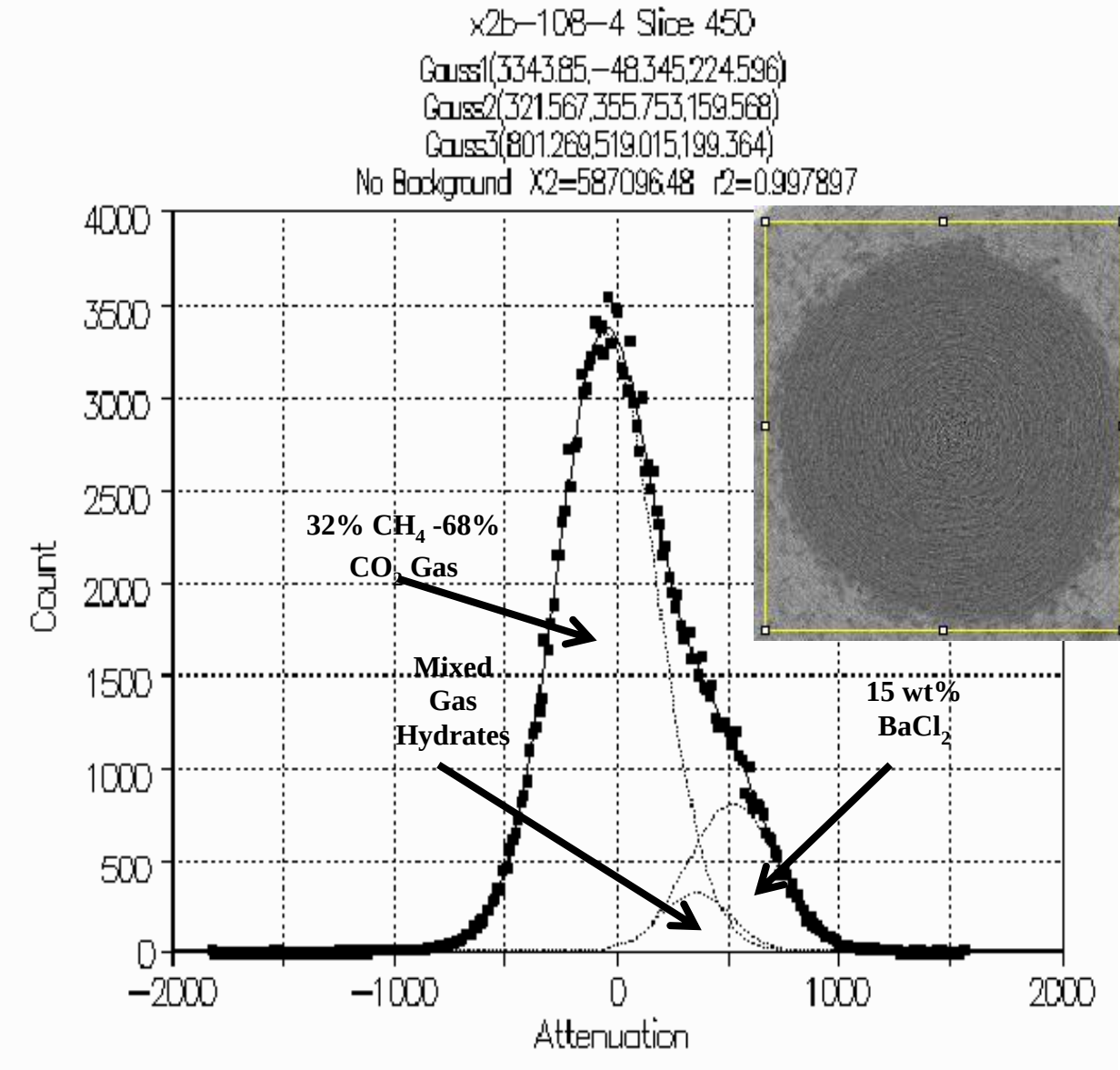

Figure 6.35: *Histogram with attenuation values of pixel^{-1} for slice 450 of the CMT scan performed during Run 8 at 70.4 h. The PeakFit program was used to distinguish between the different peaks in the histogram created by the various materials present inside the cell. The image inside the yellow box above the plot shows the region of the cell used to create this histogram, and in the image, darker gray regions are gas, lighter gray regions are solution, and gray colors in between gas and solution are gas hydrates. Since the peak attributed to CH_4-CO_2 hydrates is centered above 0 pixel^{-1}, CH_4-CO_2 hydrates are present in this experiment.*

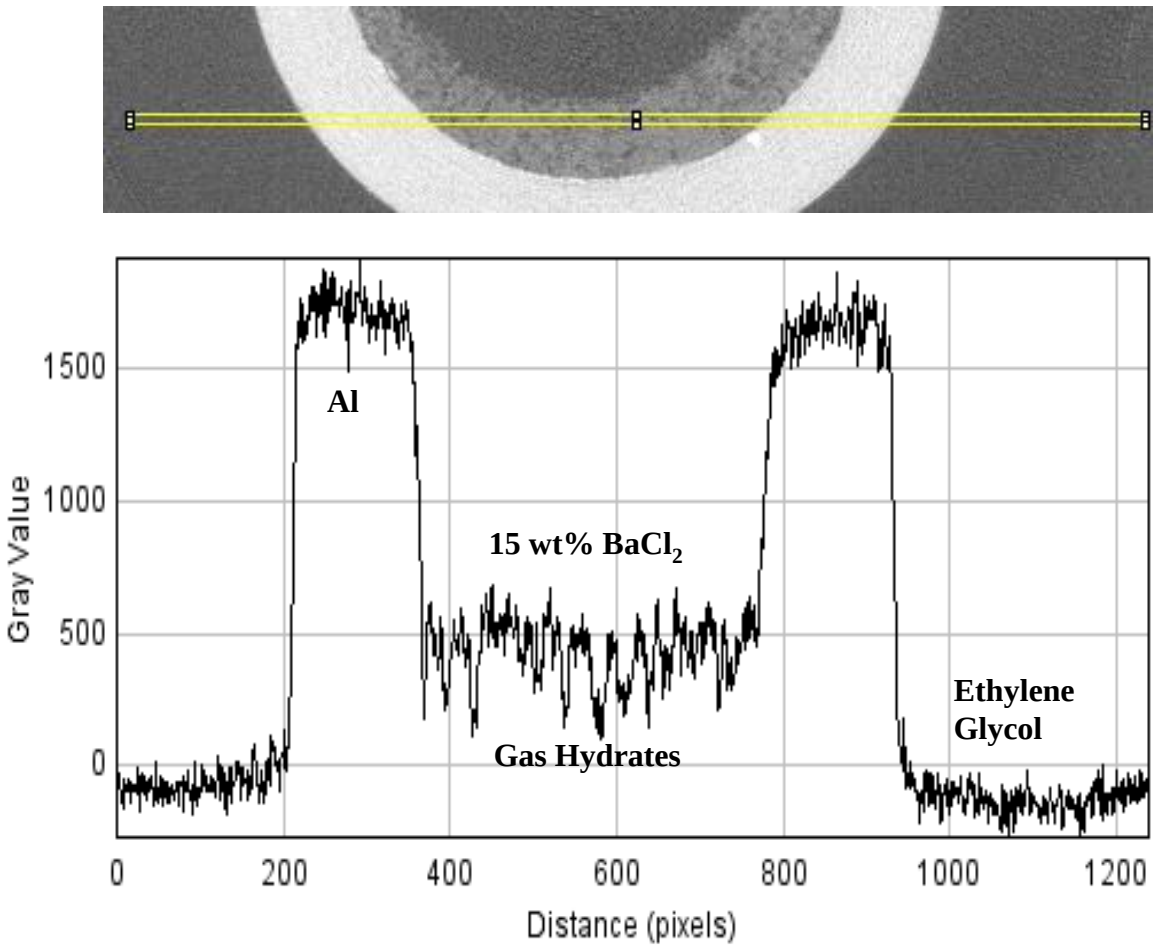

Figure 6.36: *A plot profile was taken across a 2D image slice of the cell at 70.4 h containing aluminum tubing, 15 wt% $BaCl_2$ solution, mixed gas hydrates, and ethylene glycol-water coolant. A profile of the gray value (related to attenuation) across the yellow box was taken and plotted to show where the phases are defined.*

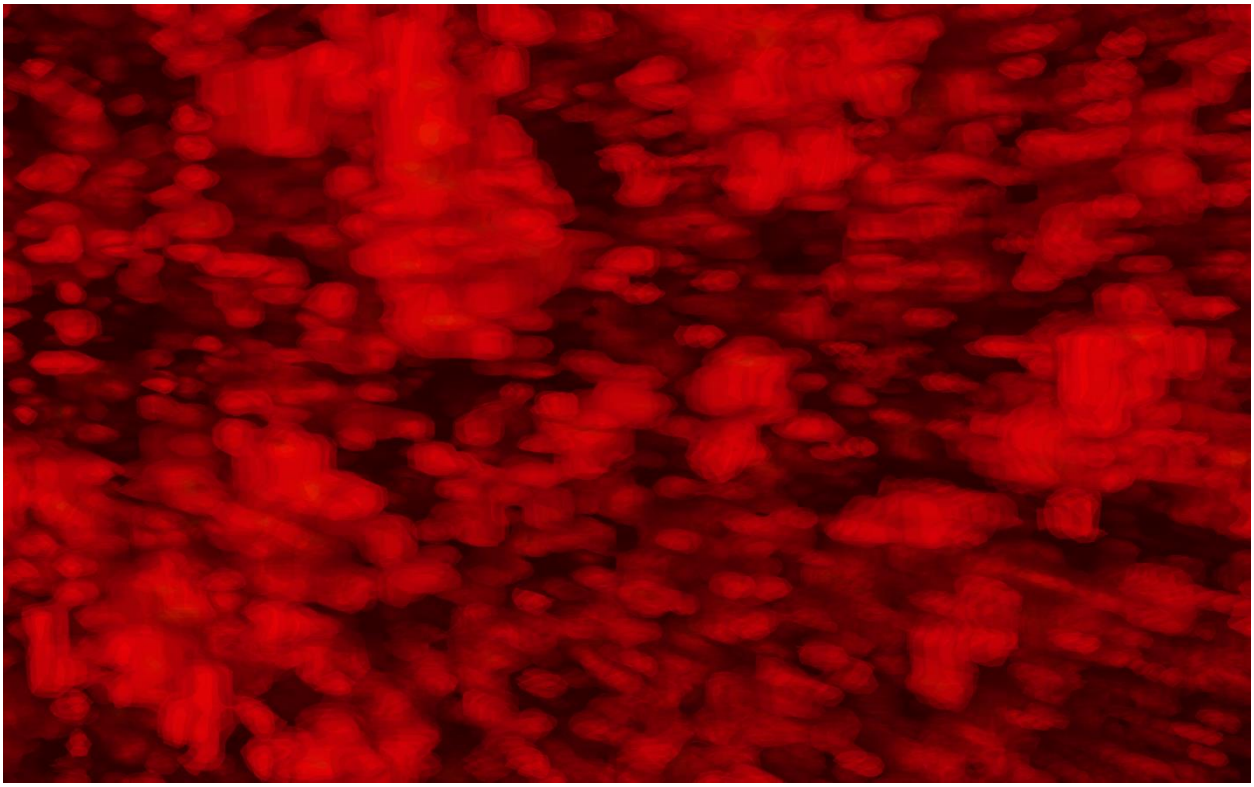

Figure 6.37: *Zoom in of the CH_4-CO_2 hydrates formed from a 32% CH_4-68% CO_2 gas mixture at 70.4 h in Run 8.*

In Run 9, a mixture of 68% CH_4 and 32% CO_2 was used to form hydrates in 2.5 mL of 15 wt% $BaCl_2$ solution. The cell was first pressurized to 338 psig with CO_2 gas, then up to 1052 psig with CH_4 gas. GC samples taken initially at room temperature analyzed the gas phase to be 87% CH_4 and 13% CO_2. After GC sampling, the cell pressure was 961 psig at 21.3°C. After about 1.5 h when the cell was cooled to 0.7°C, cell pressure reached 919 psig, and after 20.3 h of cooling, cell pressure was found to be 941 psig at -2.1°C. As was seen in the first mixed gas run, pressure decreased and then increased during cell cooling. At 20.2 h, the gas-liquid interface was imaged at around 0ºC, and a coating of hydrates was found along the gas-liquid interface while some needle-like hydrates formed in the solution phase, perpendicular to the gas-liquid interface. The growth of hydrates in this run over time can be seen in Figure 6.38. This hydrate morphology was similar to Run 8 as needle-like hydrates grew downwards from the interface and thickened over time. Mixed gas hydrate presence was confirmed in the histogram of one of the 2D slices of the CMT scan performed at 381.2 h shown in Figure 6.39. Since the center of the peak for mixed gas hydrates has an attenuation value above 0 $pixel^{-1}$, mixed gas hydrates are indeed present in this CMT run. The plot profile in Figure 6.40 shows the clear separation of phases across a 2D image slice. Figure 6.41 shows a zoom in of these needle-like hydrates; unlike the hydrates formed in Run 8, these hydrate branches are thinner and less rounded.

Prior to depressurization, while the cell was still chilled, GC samples indicated a gas phase composition of 55% CH_4 and 45% CO_2. GC samples taken when the cell was warmed back up to room temperature indicated a similar gas phase – 54% CH_4 and 46% CO_2. Similar to the previous run, the composition of the gas phase before and after the cell was warmed up to room temperature was the same.

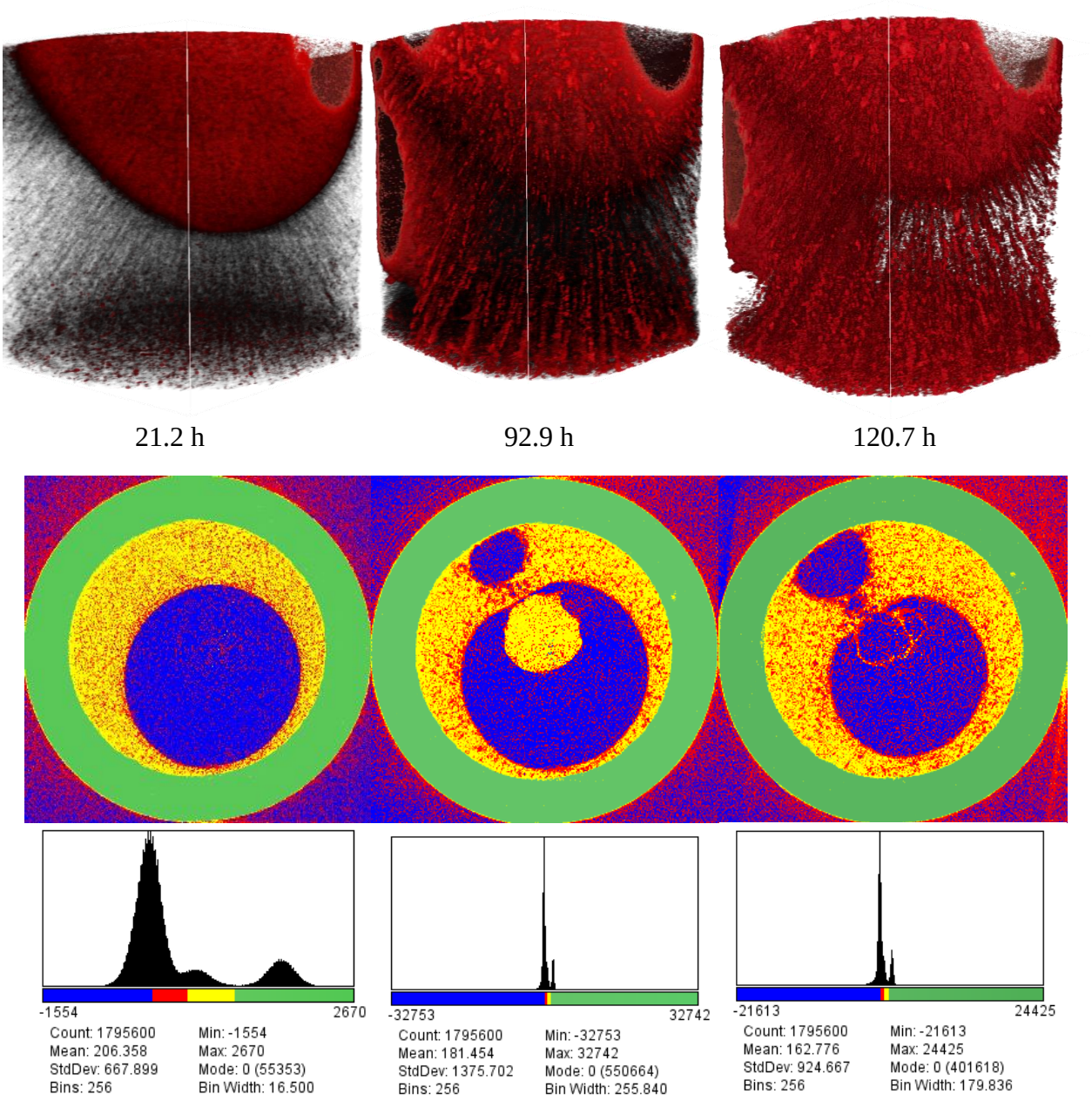

Figure 6.38: *Time-Resolved CMT images of hydrate growth in a 68% CH_4 – 32% CO_2 gas mixture from an aqueous solution of 15 wt% $BaCl_2$ in Run 9. Time resolved hydrate growth is shown in 3D volumes, where red indicates CH_4-CO_2 hydrates and all other phases present in the cell have been made transparent. The 2D image slices represent slice 200 of the 3D images. In the 2D images, red indicates CH_4-CO_2 hydrates, blue is CH_4-CO_2 gas, yellow is 15 wt% $BaCl_2$ solution, and green is aluminum tubing. The OD of the green aluminum tubing is 0.25" and the ID is 0.18". Histograms of the different phases in the 2D images are also shown. The growth of hydrates extends downwards into the liquid phase from the gas-liquid interface.*

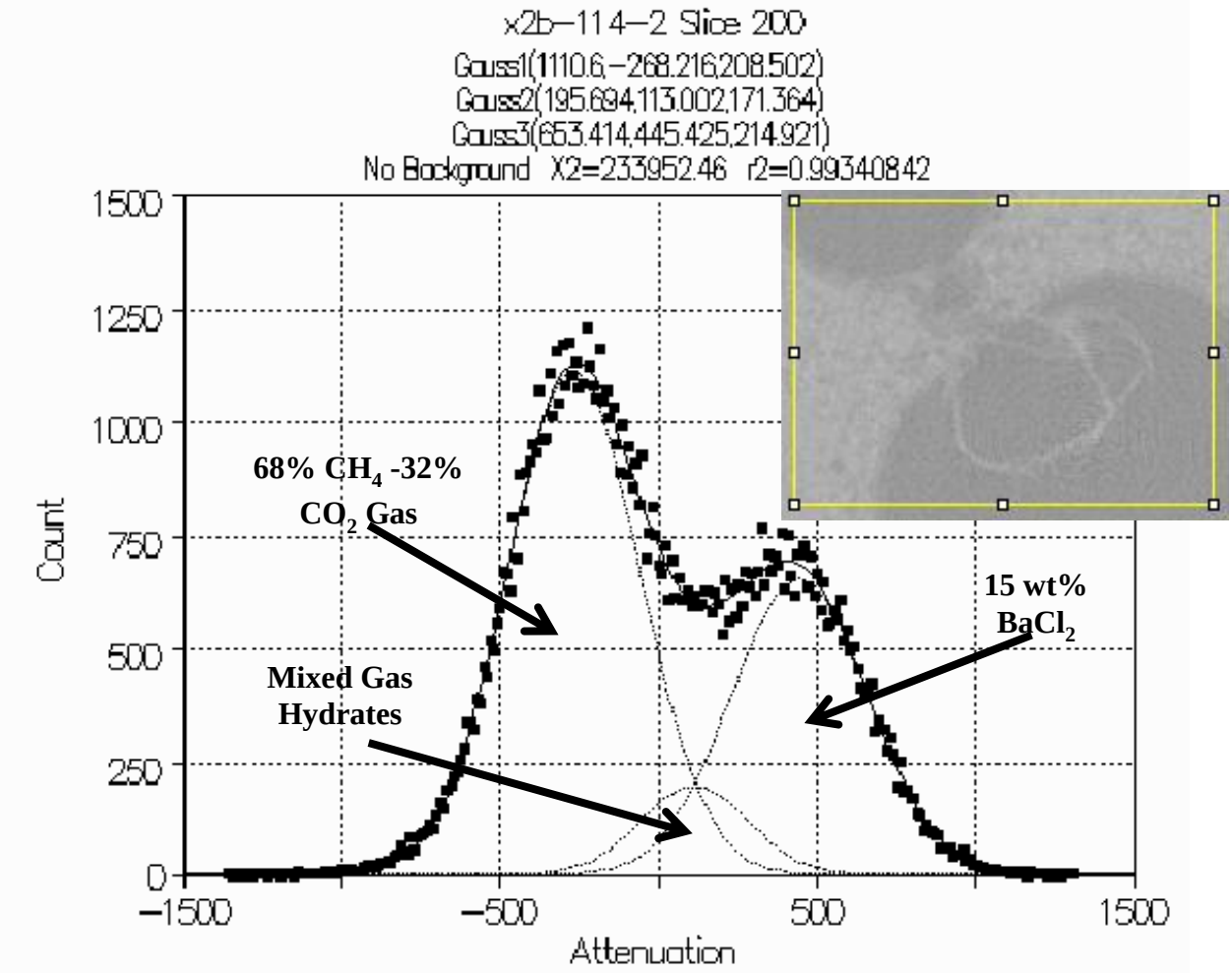

Figure 6.39: *Histogram with attenuation values of pixel^{-1} for slice 200 of the CMT scan performed during Run 9 at 120.7 h. The PeakFit program was used to distinguish between the different peaks in the histogram created by the various materials present inside the cell. The image inside the yellow box above the plot shows the region of the cell used to create this histogram, and in the image, darker gray regions are gas, lighter gray regions are solution, and gray colors in between gas and solution are gas hydrates. Since the peak attributed to CH_4-CO_2 hydrates is centered above 0 pixel^{-1}, CH_4-CO_2 hydrates are present in this experiment.*

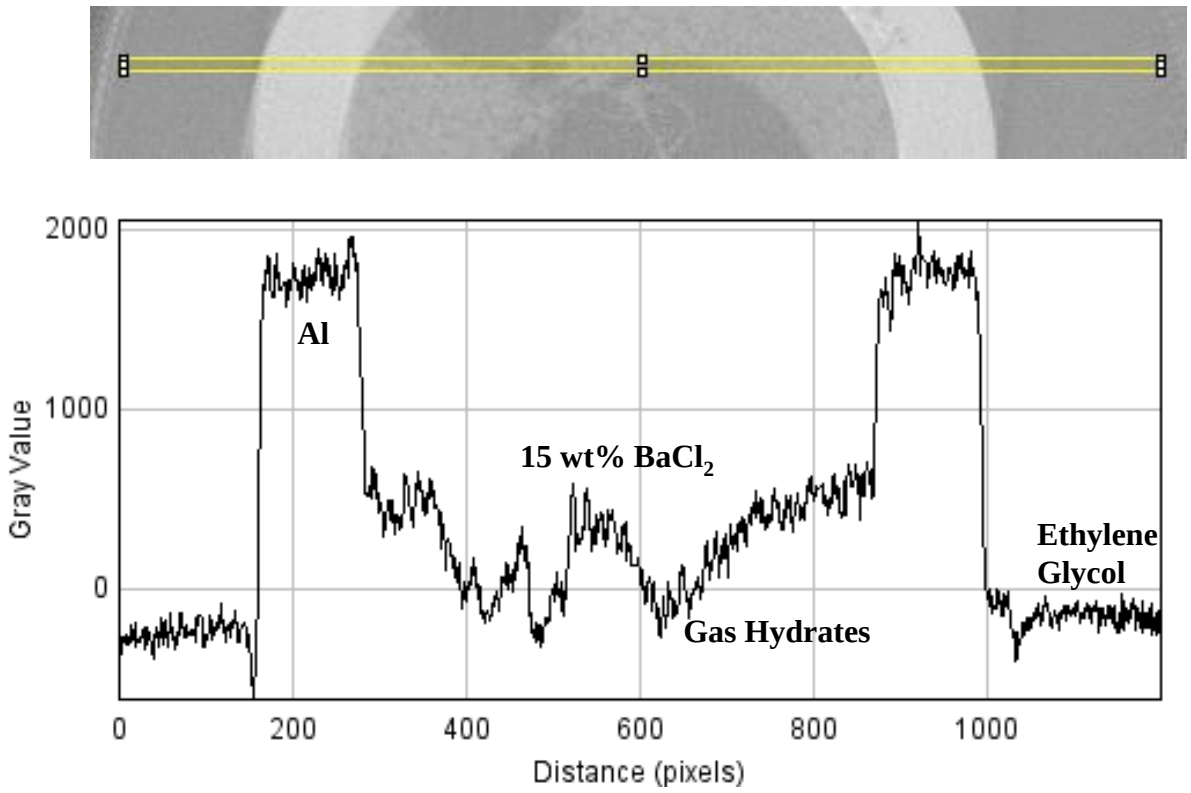

Figure 6.40: *A plot profile was taken across a 2D image slice of the cell at 120.7 h containing aluminum tubing, 15 wt% $BaCl_2$ solution, mixed gas hydrates, and ethylene glycol-water coolant. A profile of the gray value (related to attenuation) across the yellow box was taken and plotted to show where the phases are defined.*

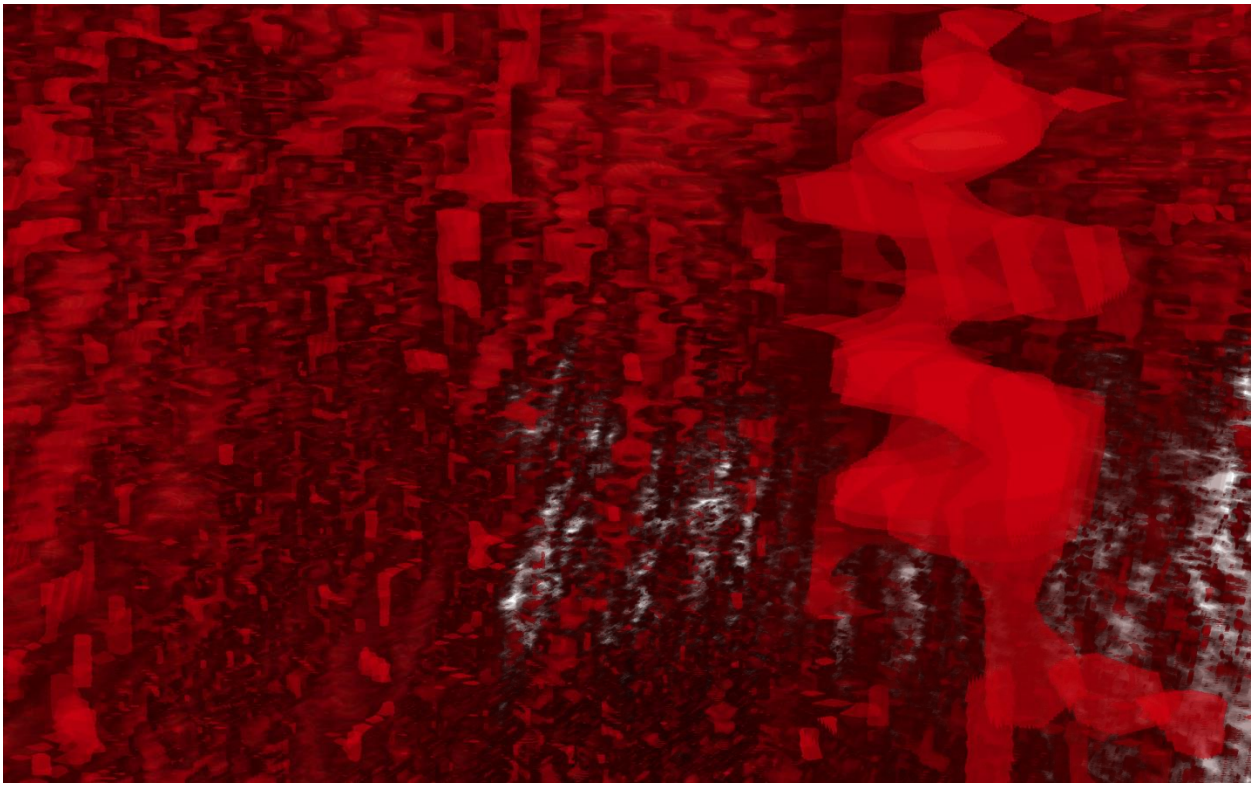

Figure 6.41: *Zoom in of the CH_4-CO_2 hydrates formed from a 68% CH_4-32% CO_2 gas mixture at 120.7 h in Run 9.*

6.3 Comparing Pure CH_4, Pure CO_2, and Mixed CH_4-CO_2 Hydrates

The formation of gas hydrates at the gas-liquid interface, and shorter induction times for CO_2 hydrates can be explained by gas diffusion in the cell. The correlation for determining the diffusion coefficients for CO_2 and CH_4 derived by Lu et al.[34] and Guo et al.[33] respectively is listed in Chapter 1 (Equation 1.3). Using this correlation, the diffusion coefficients for CO_2 and CH_4 gas within a temperature range of 0-6°C would be 910.4 – 1122.7 $\mu m^2/s$ and 692.4 – 883.9 $\mu m^2/s$ respectively. This would indicate that it would take between 4.1 h at 6°C or 5.0 h at 0°C for CO_2 and 5.2 h at 6°C or 6.6 h at 0°C for CH_4 to diffuse through the 1.64 x 10^7 μm^2 (0.025 in^2) cross sectional area of the CMT cell. Since the entire volume of hydrate forming solution in the cell is about 2.5 cm^3, it would take a considerable amount of time for gas to fully diffuse through the solution. The faster rate of diffusion and higher solubility of CO_2 in water suggest a mechanism for the generally shorter induction times that were observed for CO_2 hydrates over CH_4 hydrates. In addition, the fact that hydrates in all successful experiments were seen to initially form at the gas-liquid interface indicates the effect of diffusion on hydrate formation.

It is clear that both CO_2 and CH_4 hydrates initially accumulate and grow from the gas-liquid interface into the liquid phase. However, the structure of hydrate growth in the liquid solution phase varied among CH_4, CO_2, and mixed gas hydrates. A summary of the hydrate structures seen during Runs 1-9 are listed in Table 6.3. While pure CH_4 formed more spherical, gas coating separate hydrates and CO_2 formed dendritic branches, mixed gas hydrates tended to form more needle-like hydrates. These varying morphologies are likely due to differing driving forces for hydrate formation as a result of gas composition[134], gas concentration in the solution[39], and degree of subcooling[134]. Servio and Englezos[48] studied the difference in hydrate morphology when a high or a low driving force was applied to a water droplet, and it was found that a higher driving force results in several needle-like hydrates while hydrates formed under a lower driving force were smooth, covering the water droplet. Generally, when driving forces are low, gas hydrates are likely to grow as single crystals[17]. Free energy has been found to play a large role in hydrate morphology: small free energy differences between the gas hydrate and the original phase result in spherical and slurry-like hydrates, while large free energy differences result in branched crystals that are less likely to form individual hydrate crystals[135].

Table 6.3: *Summary of CMT Hydrate Structures*

Run #	Gas Composition	Hydrate Shape
1	CH_4	Spherical / gas coating
2	CH_4	None
3	CH_4	Sphere shaped clusters / gas coating
4	CO_2	Rods / gas coating
5	CO_2	Dendritic branches / gas coating
6	CO_2	Dendritic branches / ring clusters / gas coating
7	50% CH_4-50% CO_2	Dendritic branches / small amorphous particles / gas coating
8	32% CH_4-68% CO_2	Needles / gas coating
9	68% CH_4-32% CO_2	Needles / gas coating

In CH_4 hydrate Run 1 and CO_2 hydrate Run 5, the cell was imaged as it was cooled from room temperature to near 0°C, and it was found that induction times for either gas hydrate were similar, though CO_2 hydrates formed 4 hours sooner than CH_4 hydrates. The thermodynamic driving forces (distance from equilibrium pressure-temperature) for the CH_4 hydrate experiments were higher than that for CO_2 hydrates. At the same time, CO_2 is much more soluble in water than CH_4, therefore the results seen in Runs 1 and 5 confirm that gas solubility and the concentration of gas dissolved in the solution play a major role in hydrate nucleation[39]. It appears that thermodynamic effects are less pertinent to hydrate formation than kinetic driving forces. It is also noticeable that CH_4 hydrates and CO_2 hydrates formed the fastest during these two runs, and mixed CH_4-CO_2 hydrates formed more quickly during Run 8. As these three runs were the only runs where the cell was imaged continuously as the cell was cooled, the cell was bombarded with x-rays throughout hydrate formation. It is possible that the presence of x-ray radiation shortened the induction time for gas hydrate formation.

Overall, gas hydrate growth seems comparable to snow crystal growth as described by Libbrecht[136]. System temperature and humidity greatly affected snow particle morphology. Just below the freezing point of water, dendritic or plate-like snow crystals formed, and as temperature decreased to -10°C, prism and needle structures were observed. As temperature

decreased further to between -10°C and -22°C, dendritic and plate-like structures were observed once again, and below -22°C, column and plate-like crystals formed. Under high water saturations, dendritic crystals were seem while at low saturations thin plate-like structures formed[136]. While the temperature of the gas hydrate formation experiments described herein did not vary a great deal, the water saturation snow crystal morphology differences are akin to the different pure CO_2 and pure CH_4 hydrates. As CO_2 is more soluble in solutions than CH_4, the higher saturation of CO_2 in $BaCl_2$ solutions likely led to the dendritic structures seen. More spherical, coating CH_4 hydrates are comparable to the simpler, plate-like snow crystals seen at lower saturations.

While Run 2 lacked definitive CH_4 hydrate formation, it seems possible that an initial hydrate structure may have formed, as the attenuation coefficient values for certain regions coating gas-liquid interfaces were higher than the coefficient expected for CH_4 gas. Molecular dynamic simulations have found that the clusters of hydrate-like cages only exist on the order of picoseconds[17], so this region may not be initial hydrate cages, but perhaps it is an effect of a supercooled solution in the cell or CH_4 diffusion into the solution.

When experiments are performed at higher pressures involving CO_2, it is possible for liquid CO_2 to form in the cell. The presence of liquid CO_2 could make it difficult to differentiate between liquid CO_2 and CO_2 hydrates, as their attenuation coefficients are 0.315 cm^{-1} and 0.403 cm^{-1} respectively. While these values are close together, CO_2 hydrate formation was verified by comparing the attenuation coefficient of the hydrate phase to that of ethylene glycol – water coolant. The attenuation coefficient for the ethylene glycol – water coolant in the cooling jacket was between 0.365 – 0.376 cm^{-1} (depending on the concentration of water in the mixture), thereby regions with attenuations near ethylene glycol – water, but slightly larger, must be CO_2 hydrates, while regions slightly below ethylene glycol must be liquid or gaseous CO_2. It is clear in the plot profiles shown in Figures 6.17, 6.21, 6.27, and 6.28 that CO_2 hydrate regions consisted of attenuations higher than the ethylene glycol – water mixture, and no obvious evidence of liquid CO_2 formation was found in these three runs.

The hydrate scaffold witnessed in the gas phase of the cell above the gas-liquid interface during Run 6 was an original finding. Many resources[17] have discussed hydrogen bonded networks in the water phase, but not in the gas phase. Several additional scans taken during

other runs indicated the possibility of such a network of hydrates in the gas phase. It is possible that gas hydrates formed at the gas-liquid interface could form very fine, thin branch upwards into the gas phase. Further investigation of hydrate growth in the gas phase with a more powerful x-ray source could be beneficial.

Hydrates created in mixed gas Runs 8 and 9 formed similar needle-like structures, while those formed in Run 7 were more of an agglomeration of smaller hydrate amorphous branches and spherical, hydrate-coated gas bubbles. This is a peculiar finding, as a 50% CH_4-50% CO_2 mixture was used in Run 7, while 32% CH_4-68% CO_2 and 68% CH_4-32% CO_2 mixtures were used for Runs 8 and 9 respectively. This way, a 50%-50% CH_4-CO_2 mixture formed gas hydrates that had the appearance of both pure CH_4 and pure CO_2 hydrates, but unequal CH_4-CO_2 ratios formed entirely different hydrate structures. Upon magnifying the hydrates formed in Runs 8 and 9, it is clear that more spherical structures created the hydrate branches in Run 8, whereas the hydrate branches in Run 9 were thinner and more rigid. Perhaps these morphology differences are due to the cage occupancy of CH_4 and CO_2 in hydrates cavities. Both CO_2 and CH_4 form hydrates of the same known structure, sI, and CO_2 molecules prefer the larger $5^{12}6^2$ cages while CH_4 molecules easily fit in smaller 5^{12} cages[27]. It is also possible that the partial pressure of CH_4 and CO_2 in the system affected the structure of hydrates formed.

In addition, in mixed gas Runs 8 and 9, gas samples of the cell at the end of the experiment before and after hydrate dissociation indicated that the composition of the gas phase of the cell was the same, whether or not hydrates were present. Similar to Jerguson Runs 11-13 described in Chapter 5, this indicates that the composition of hydrates in the system was comparable to the gas phase composition in the cell. Both Runs 8 and 9 showed a higher percentage of CO_2 in the gas phase at the end of the experiment than the initially input composition of CO_2 gas into the system (i.e. Run 8 was performed by adding 68% CO_2 while GC samples found 98-99% CO_2 in the gas phase, and Run 9 was performed with 32% CO_2 yet GC samples indicated 45-46% CO_2 in the gas phase). When gas hydrates form, water is consumed to form the hydrate cage, but salt is excluded from the hydrate structure[137], therefore the salinity of the solution in the cell increases as more hydrates form. Increasing salinity results in decreasing CO_2 solubility[138], hence the larger percentage of CO_2 gas in the gas phase when hydrates had formed implies that some CO_2 had desolublized from the 15 wt% $BaCl_2$ solution, and upon

warming up to room temperature, it did not have enough time to resolublize. These GC values could also indicate the possibility that these mixed gas hydrates were made up of predominantly CH_4. The small volume of the CMT cell and the lack of pressure measurement on the reactor after CMT imaging makes GC sampling difficult. The taking of one 0.5 mL gas sample for GC analysis will reduce the pressure of the system greatly, thereby it is difficult to better quantify these results.

At temperatures above 0°C, hydrate dissociation is similar for CO_2 or CH_4 hydrates[139]. Dissociation during all of these runs happened within minutes of ending coolant flow through the cell cooling jacket, therefore in these experiments CH_4 and CO_2 hydrate dissociation was found to be comparable.

6.4 Analyzing the Pressure Phenomena Seen During Mixed Gas CMT Runs: CH_4-CO_2 Hydrate Formation in the CMT Cell Connected to LabVIEW without X-ray Imaging

The pressure decrease and subsequent pressure increase seen during CH_4-CO_2 CMT runs was peculiar and not noted elsewhere in literature, nor was it seen during pure gas CMT runs or mixed gas macroscale Jerguson experiments. When CMT experiments are performed at the NSLS, it is not possible to monitor cell pressure and temperature while CMT imaging is taking place, so two experiments were performed to connect the CMT cell to LabVIEW to record pressure-temperature conditions throughout a hydrate formation experiment without x-ray imaging.

LabVIEW CMT Run 1 was performed using 2.4 mL of 15 wt% $BaCl_2$. To add a 50%-50% CH_4-CO_2 gas mixture to the cell, first the cell was pressurized to 525 psig with CO_2 gas, then to 1047 psig with CH_4 gas. Initial GC samples indicated that the gas phase was composed of 80.7% CH_4 and 19.3% CO_2. This seems to indicate that initially CO_2 was partially solubilized in the $BaCl_2$ solution as gas was charged into the cell. After this gas sample was taken and cell pressure was at 961 psig, the cell was cooled from room temperature slowly to -2°C, as the freezing point of 15 wt% $BaCl_2$ is -4.8°C. It took about 4 hours for the cell to reach -2°C, and at this time, cell pressure was at 831 psig. After this low pressure was achieved, the pressure of the system increased until it reached near 950 psig 29 h after cell cooling had begun, as seen in

Figure 6.42(b). From this point on, cell pressure was constant near 950 psig, as shown in the entire run's pressure-temperature conditions over time plotted in Figure 6.42(a).

Prior to ending the experiment, while the cell was still cold, GC samples were taken that indicated 49.5% CH_4 and 50.5% CO_2 in the gas phase. Upon warming the cell up to room temperature (27°C), the gas composition was similar, with 49.3% CH_4 and 50.7% CO_2. GC data and cell pressure at the end of the run are plotted over time in Figure 6.43.

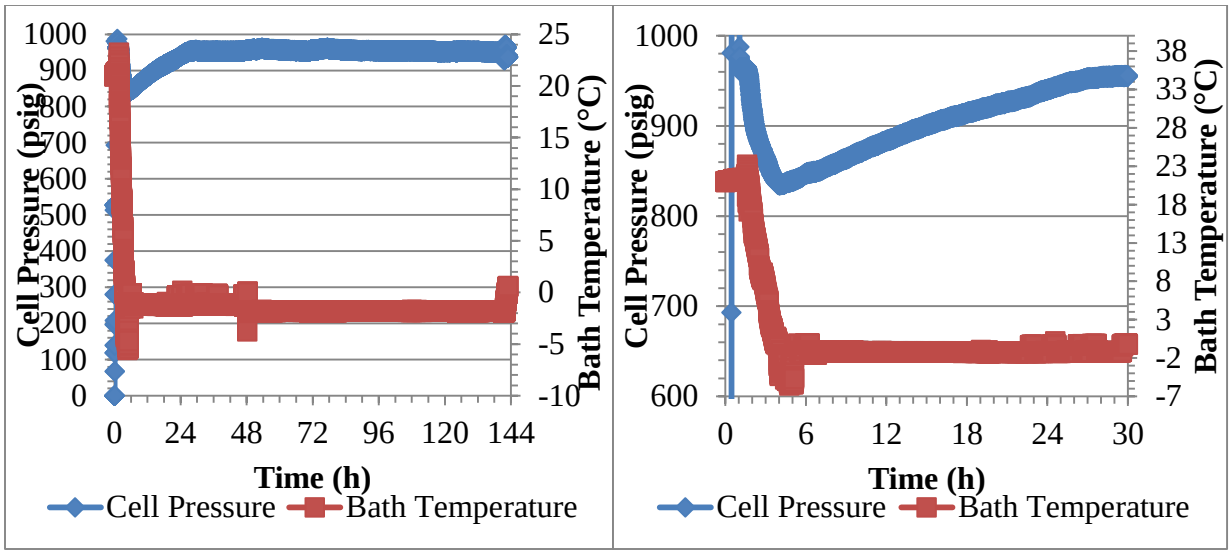

Figure 6.42: *Pressure and temperature conditions over time for LabVIEW CMT Run 1. (a) shows pressure-temperature conditions for the entire run and (b) is a close up of the pressure drop and increase that occurred initially during the experiment.*

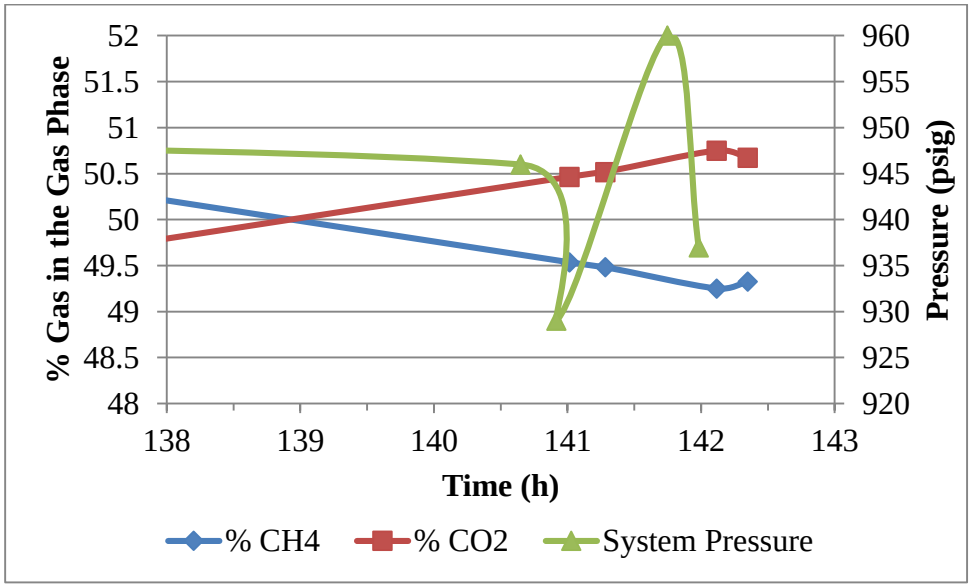

Figure 6.43: *Gas composition and pressure data at the end of LabVIEW CMT Run 1.*

The second experiment, LabVIEW CMT Run 2, was performed similarly, using 2.4 mL of fresh 15 wt% $BaCl_2$ solution and a 50%-50% CH_4-CO_2 gas composition. The cell was pressurized to 528 psig with CO_2 gas and then up to 1050 psig with CH_4 gas. Comparable to the previous run, initial GC samples indicated that the gas phase was composed of 81.1% CH_4 and 18.9% CO_2. Once this gas sample was taken and the cell was at 1016 psig, cell cooling was begun. Again, it took about 4 hours for the cell to be cooled to -2°C, and the cell reached a pressure of 860 psig (with some pressure lost to GC sampling). GC samples taken at this pressure indicated the same 81.1% CH_4 and 18.9% CO_2 gas composition that was seen initially. After this low pressure was achieved, the pressure of the system increased until it reached about 940 psig 22 h after cell cooling had begun, as seen in Figure 6.44(b). It is important to note that the sudden pressure decrease seen near 4 h was due to gas lost during a GC sample collection. From this point on, cell pressure was fairly constant near 940 psig, as shown in the entire run's pressure-temperature conditions over time plotted in Figure 6.44(a). While it appears as though cell pressure did not back up as high as the previous run, each GC sample resulted in several psig pressure drops in the system and more GC samples were taken during this experiment, therefore cell pressure was indeed found to increase considerably during this experiment.

Prior to ending the experiment after two days, while the cell was still cold at -1.84ºC and 944 psig, GC samples were taken that indicated 57.1% CH_4 and 42.9% CO_2 in the gas phase. Upon warming the cell up to room temperature (26°C), the gas composition at 868 psig changed slightly to be 51.6% CH_4 and 48.4% CO_2. While at room temperature, the cell was depressurized in several steps to determine the gas phase composition of the cell at lower pressures. At 781 psig, the gas phase of the cell was 51.3% CH_4 and 48.7% CO_2, while at 412 psig, the gas phase was composed of 46.8% CH_4 and 53.2% CO_2. A final sample taken at 203 psig indicated 45.1% CH_4 and 54.9% CO_2. GC data and cell pressure at the end of the run are plotted over time in Figure 6.45.

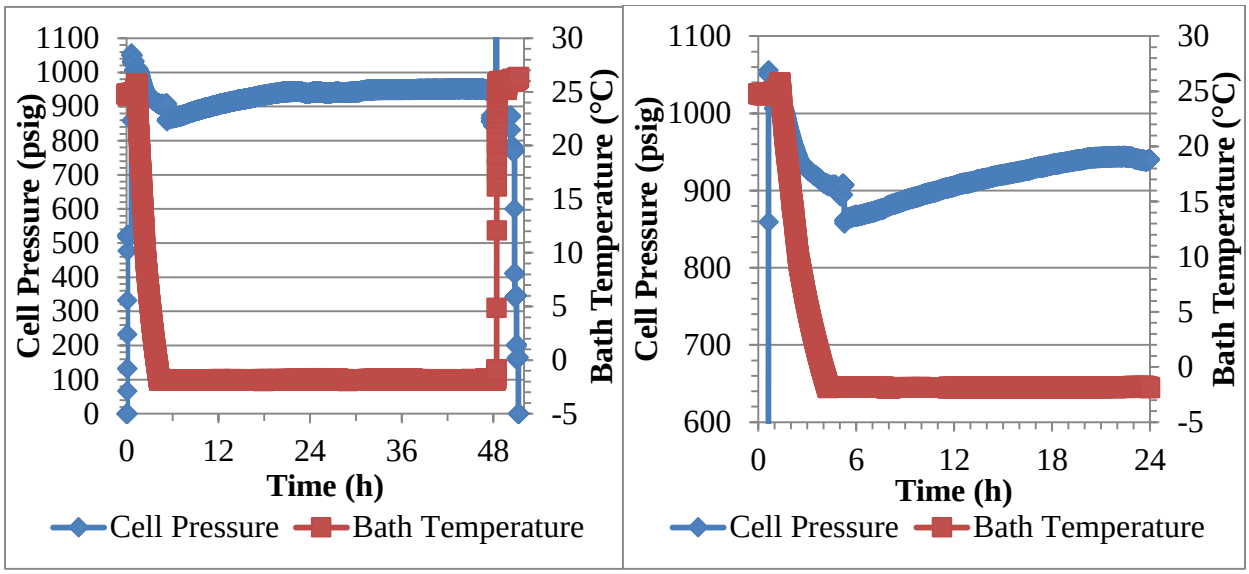

Figure 6.44: *Pressure and temperature conditions over time for LabVIEW CMT Run 2. (a) shows pressure-temperature conditions for the entire run and (b) is a close up of the pressure drop and increase that occurred initially during the experiment.*

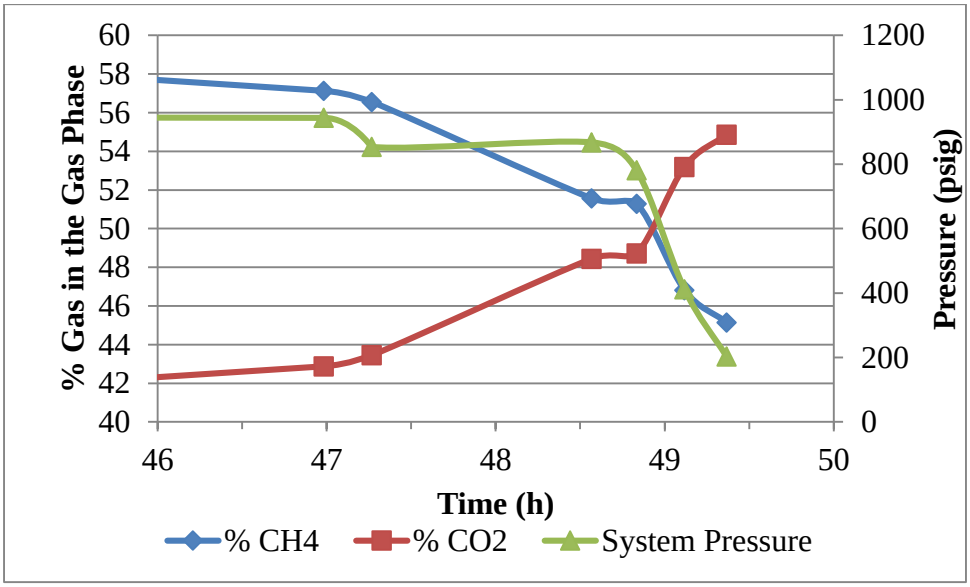

Figure 6.45: *Gas composition and pressure data at the end of LabVIEW CMT Run 2.*

6.4.1 CMT Hydrate Discussion

Gas composition values for these two LabVIEW CMT runs were very consistent. Even though gas was added to the cell to create a 50%-50% pressure ratio, both runs indicated a room temperature gas composition of 81% CH_4 and 19% CO_2. This was likely due to the higher solubility of CO_2 in water and the order in which gas was added to the cell, as CH_4 was added last. Gas samples taken at the lowest pressure reading during LabVIEW CMT Run 2 resulted in the same 81% CH_4 and 19% CO_2 gas composition, which suggests that either no hydrates had formed yet upon the cell reaching this pressure or that hydrates of a composition proportional to the gas phase composition had formed. Final GC samples taken before and after dissociating gas hydrates by warming the cell up to room temperature were very similar for LabVIEW CMT Cell Runs 1 and 2, as was also seen in CMT Runs 8 and 9.

As was seen in CMT Runs 7 and 9, LabVIEW CMT Runs 1 and 2 also began with a pressure drop followed by a pressure rise. For CMT Runs 7 and 9, cell pressure increased back to within 20 psi of the original starting pressure at room temperature, while for LabVIEW CMT Run 1, pressure rose to be 5 psi below the cell's pressure prior to cooling initiation. As more GC samples were taken during LabVIEW CMT Run 2 that reduced the overall pressure of the system, pressure did not back up as far as LabVIEW CMT Run 1, though a clear pressure decrease and increase was seen.

Since CO_2 is more soluble than CH_4 in water, it seems as though initially CO_2 gas in the cell solubilized as a result of the addition of CH_4 gas to the cell, leading to a deceivingly higher initial ratio of CH_4 in the gas phase. It is possible that the pressure increase seen once the cell was cooled to -2°C may have been a result of CO_2 gas dissolving out of the salt solution as gas hydrates formed. While no other studies with this pressure increase have been found, it is known that adding salt to water lowers the water's activity[140], and when water activity is lowered, the system's pressure needs to increase[141]. As salt is not included in the structure of a gas hydrate[137], the formation of hydrates in a salt system would absorb water, thereby increasing the salinity of the remaining salt solution. The pressure increase observed likely represents an increase in system salinity due to gas hydrate formation. It is clear from CMT images that hydrates can grow to fill a majority of the experimental cell, leaving behind very little free water with a thereby resultantly high salinity. The finding of a larger percentage of CO_2 in the gas phase of

the cell at the end of the experiments in comparison to the initial percentage of CO_2 in the cell correlates well with this idea. It is likely that the small volume of the CMT reactor pronounced this pressure effect.

The fact that this effect was not witnessed during either the pure CH_4 or the pure CO_2 CMT hydrate formation experiments indicates that gas composition plays a key role in this pressure effect. A combination of salinity increases and the interaction of CH_4 and CO_2 gas in gas hydrates must lead to this pressure increase. Since this was not witnessed during any of the pure or mixed gas macroscale experiments in the Jerguson cell, it is clear that this phenomenon is also related to the small volume in the CMT cell. It is also possible that the gas trapped in hydrate cages reconfigures, leading to the expulsion of some gas from the hydrate structure, thereby increasing system pressure. It is clear that further experiments utilizing additional analysis tools could lead to a better understanding of this phenomenon.

6.5 Conclusions

CMT was used to image gas hydrates formed in salt solutions. Pure CH_4, pure CO_2, and mixed CH_4-CO_2 hydrates formed without porous media accumulated in large volumes near the gas-solution interface. Hydrate morphology was unique for different gases and gas compositions, due to differences in the driving forces for hydrate formation. Under the conditions used, CH_4 formed more spherically shaped, gas bubble-coating hydrates, CO_2 formed dendritic branched hydrates, 50%-50% CH_4-CO_2 mixtures formed a combination of amorphous shaped and branched hydrates, and unequal proportions of CH_4-CO_2 gas resulted in needle-like hydrates. In addition, a pressure drop during cell cooling, followed by a pressure increase during hydrate formation in mixed CH_4-CO_2 systems was likely to be a result of a salinity increase in the system due to hydrate formation and CH_4-CO_2 interactions in hydrates. The fact that CO_2 and CH_4 hydrates grew differently under similar temperatures but different pressures and gas compositions could have implications on the extraction of CH_4 and sequestration of CO_2 on the ocean floor.

Chapter 7

7.0 CMT Experiments – CO_2 and CH_4-CO_2 Hydrate Formation within Porous Media

A series of experiments were performed to grow CO_2 or CH_4-CO_2 hydrates with 500 µm glass beads or 180-250 µm Ottawa sand. In all experiments, a salt solution with either 10, 15, or 20 wt% $BaCl_2$ was used to form hydrates. Salt is a hydrate inhibitor, but in this experiment it was a necessary contrast agent for CMT. Table 7.1 lists the conditions for these experiments. All of the pressure-temperature conditions used were within the hydrate stability zone, and temperatures were above the freezing point of the salt solution used. The temperature values reported are an estimate of the cell temperature based on correlations that there is about a 2ºC difference between the refrigerated circulator and cell temperatures during CMT scans. While the conditions described are representative of the ocean floor, there was a lack of hydrostatic pressure that is present naturally. Hydrostatic pressure can affect hydrate stability as well[142].

Table 7.1: *Experimental Conditions*

Run #	Porous Media	Solution	Charging Pressure (psig)	Temperature (°C)	Duration of Experiment (days)
10	Glass Beads (500 µm)	20 wt% $BaCl_2$	662 psig CO_2	-2.5	10
11	Ottawa Sand (180-250 µm)	10 wt% $BaCl_2$	664 psig CO_2	-3 to -2	44
12	Ottawa Sand (180-250 µm)	15 wt% $BaCl_2$	660 psig CO_2	0 to 2	7
13	Ottawa Sand (180-250 µm)	15 wt% $BaCl_2$	960 psig (50% CH_4-50% CO_2)	-2 to 0	6

The presence of gas hydrates in all of these experiments was confirmed by comparing theoretical x-ray attenuation coefficients to the x-ray attenuation coefficients calculated from experimental results, as explained in Chapter 6. A histogram of a slice of the cell can also be used to distinguish between phases, though since the x-ray attenuation coefficients for all of the phases present in the cell are very close together, histogram peaks tend to overlap. The PeakFit program was utilized to estimate the various peaks that make up a histogram for the scans performed, as described in Chapter 6.

7.1 CO_2 Hydrates in Glass beads (Run 10)

Run 10 was performed using 1.5 mL of 20 wt% $BaCl_2$ solution ($T_{Freezing}$: -6.6°C, ρ: 1.17 g/cm^3) and 3.79 g of glass beads (500 µm diameter obtained from Biospec). The cell was charged to 662 psig with CO_2 gas and then cooled to -2.5°C. CMT images were taken over seven days, beginning after the cell had been cooled for three days. The first 3D image in Figure 7.1 and 2D image in Figure 7.2 were taken at 74.1 h at the gas-liquid-glass beads interface. CO_2 hydrates were found to form at this interface and in the pore space between glass beads near the interface, most likely due to gas diffusion as described in Chapter 6. These hydrates filled much of the pore space, but did not wet the glass beads. A clear 20 wt% $BaCl_2$ solution layer can be found between hydrates and glass beads. Figure 7.3 shows two areas in yellow boxes where corresponding plot profiles were taken. These profiles indicate the gray value (related to x-ray attenuation in units of pixel^{-1}) of the phases present across the yellow box. The plot profile taken at the bottom of the cell goes across a glass bead (gray) to 20 wt% $BaCl_2$ solution (blue) to another glass bead. It is clear that there is a sharp change in gray value when traveling from a glass bead into solution. The plot profile taken at the top of the image traverses a CO_2 hydrate region (red) to 20 wt% $BaCl_2$ solution to a glass bead. Similarly to the profile at the bottom of the image, there is a change in slope when traveling across these three phases, but unlike the sharp change in slope when transitioning from glass bead to solution in the bottom profile, this upper profile has a more gradual change, and the slope across this region is not constant. This indicates the presence of a phase in between the CO_2 hydrate and glass bead. If there was no phase in between the hydrate and glass bead, the slope for gray value between these points would be sharper and more constant, rather than broad with changing slopes.

After this imaging scan, the cell was warmed up to room temperature to 1) test the gas hydrate memory effect and 2) verify that the x-ray attenuation coefficients for CO_2 gas and CO_2 hydrate are distinctly different enough to confirm hydrate formation in porous media. A CMT scan taken at room temperature at 97.0 h showed a noticeable attenuation difference between these room temperature gas bubbles and the chilled gas hydrates imaged at 74.1 h. CO_2 hydrates at 74.1 h had x-ray attenuation coefficient values near 40 $pixel^{-1}$, which is slightly above those for ethylene glycol coolant (near -100 $pixel^{-1}$). On the other hand, the CO_2 bubbles at 97.0 h had attenuation values near -170 $pixel^{-1}$, which is below the coolant (near -120 $pixel^{-1}$). All of these attenuation values correlate well with expected attenuation trends, thus confirming hydrate formation at lower temperatures and CO_2 gas presence at room temperatures. After this scan, cell recooling was begun.

It is clear from Figure 7.1 that initially, prior to warming the cell up to room temperature, there are many CO_2 hydrates present, especially at the top of the glass bead pack at the gas-liquid interface. Once the cell was recooled, the gas-liquid interface was no longer in the field of view, possibly due to the formation of more CO_2 hydrates in the glass bead pore space. Instead, 20 wt% $BaCl_2$ solution filled the region above the glass bead pack, as shown in the vertical image slice in Figure 7.4. CO_2 hydrates did grow back in the cell, but they did not form in the same locations. They no longer formed a thick coat at the top of the glass bead pack, and these newly reformed hydrates were more spherical, smaller, and more numerous than the hydrates seen initially. The CO_2 hydrates shown in Figures 7.1 and 7.2 at 168.8 h and 217.8 h respectively also did not fill a majority of the glass bead pore spaces as the hydrates initially did at 74.1 h.

The validity of CO_2 hydrate formation was confirmed using the PeakFit program to match peaks for the various phases present in the histogram of a region of the cell shown in Figure 7.5(a). Figure 7.5(c) shows a plot profile of the yellow boxed region shown in Figure 7.5(b). It is clear that the various phases present in the cell can be distinctly seen at different gray values (attenuation coefficients). In addition, the gray values for CO_2 hydrates are slightly above those for ethylene glycol-water coolant, further confirming the presence of gas hydrates in the cell. Finally, Figure 7.6 plots the theoretical x-ray attenuation coefficients versus experimentally obtained attenuation values. It is evident that the attenuated regions assigned to each material are correct as the points create a line with an R^2 value very near to 1.

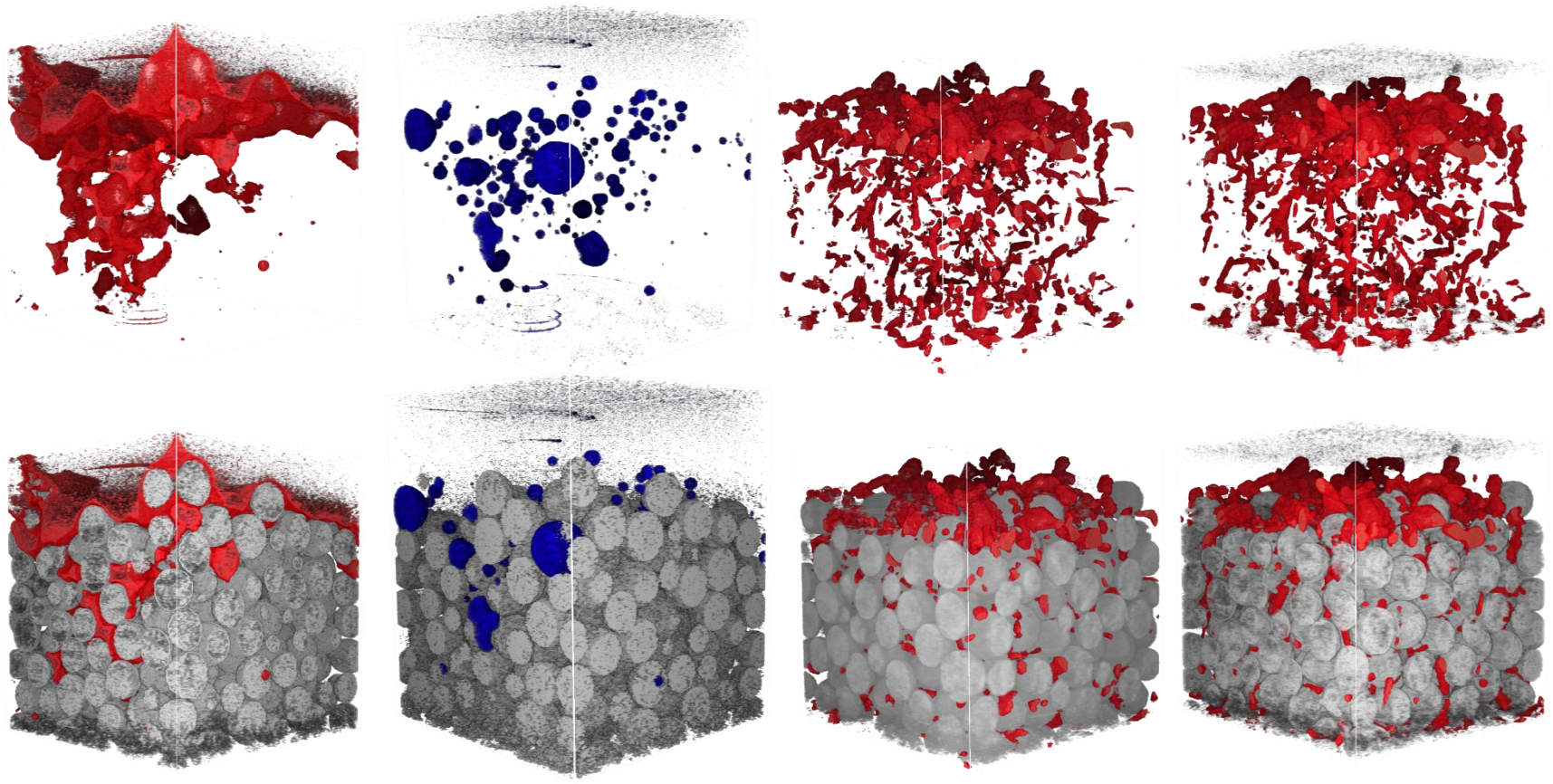

Figure 7.1: *Time resolved CO_2 hydrate formation in glass beads during Run 10. In these 3D volume images, red represents CO_2 hydrates, blue is CO_2 gas, and gray is glass beads. The top 3D volumes only show images of CO_2 hydrates or CO_2 gas in the cell, while the bottom images show how these CO_2 hydrates or CO_2 gas bubbles are located within glass bead particles. The solution phase is not shown in these images. At 74.1 h, hydrates were found to fill the pore space between glass beads. At 99.1 h, the cell was warmed up to room temperature, which is why only CO_2 gas bubbles are present in the scan. Once cell cooling was begun again, hydrates formed slowly in smaller sizes, mostly at the top of the glass bead pack and within the glass bead pore space.*

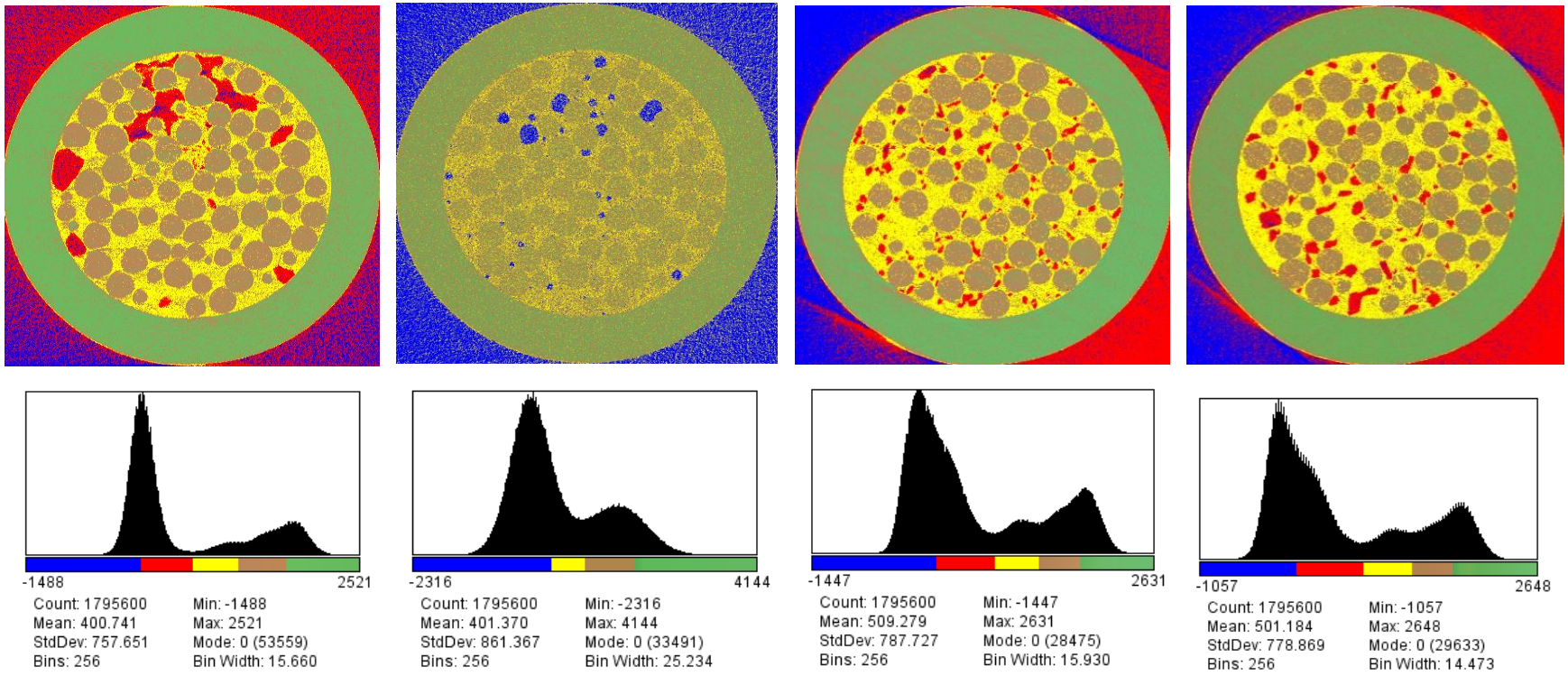

74.1 h 97.0 h 168.8 h 217.8 h

Figure 7.2: *Time resolved image slices from slice 306 of Run 10 where red indicates CO_2 hydrates, blue is CO_2 gas, yellow is 20 wt% $BaCl_2$ solution, brown is glass beads, and green is aluminum tubing. Histograms of these 2D slices are shown below.*

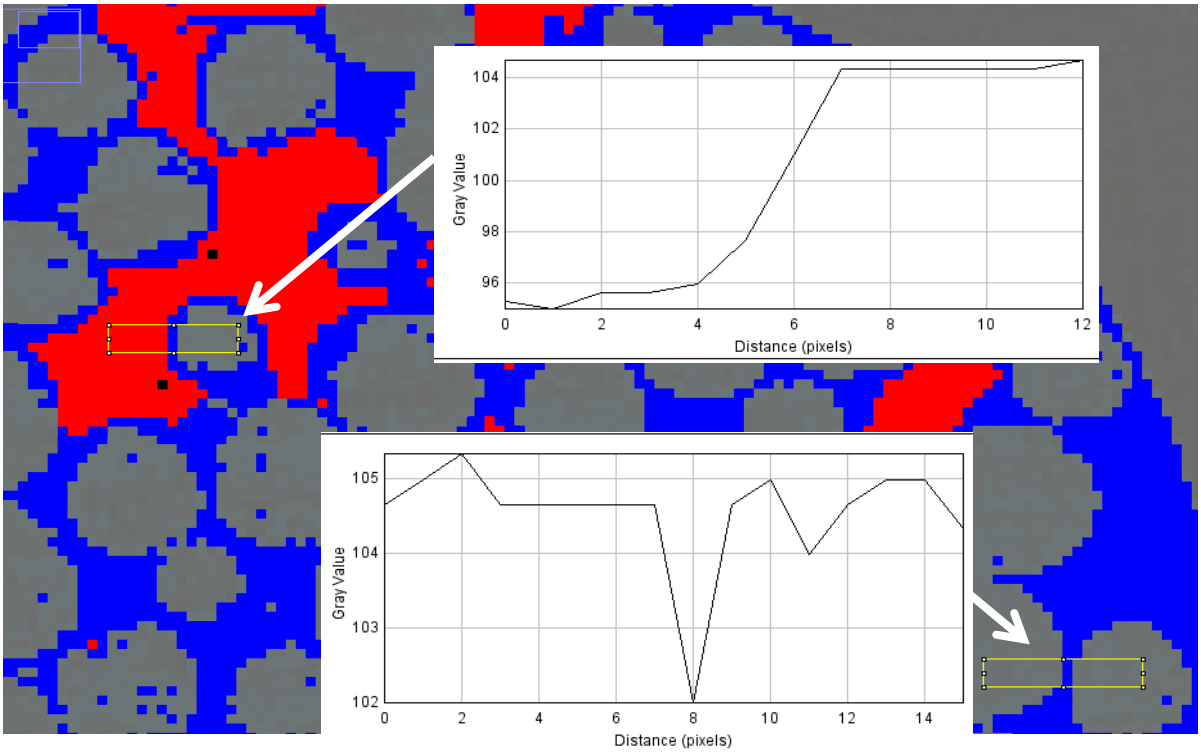

Figure 7.3: *Plot profiles indicating the presence of a solution layer (blue) between glass beads (gray) and CO_2 hydrates (red). The plot profile of the yellow box at the bottom of the image shows a distinct, sharp change in slope between glass beads with a 20 wt% $BaCl_2$ solution layer in the middle. On the other hand, the profile of the yellow box at the top shows a gradual transition between hydrates and glass beads, with a change of slope occurring across this transition, indicating the presence of another phase in between the glass bead and the hydrate.*

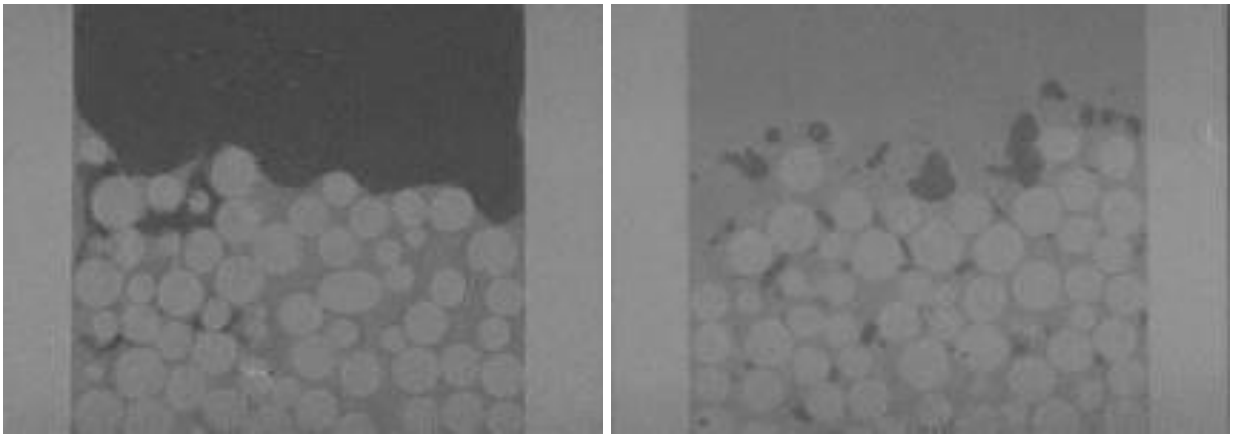

74.1 h 217.8 h

Figure 7.4: *Vertical image slices of the cell at 74.1 and 217.8 h where the blackest region above the glass beads is CO_2, dark colored shapes are CO_2 hydrates, the gray vertical lines on the left and right of each image represent aluminum tubing, the light gray spheres are glass beads, and the gray regions surrounding the glass beads and above the beads at 217.8 h represent 20 wt% $BaCl_2$ solution. At 74.1 h, the gas-liquid interface is at the top of the glass bead pack. After the imaging scan at 74.1 h, the cell was warmed up to room temperature, and upon recooling the cell, the gas-liquid interface was no longer in the field of view, as at 217.8 h 20 wt% $BaCl_2$ solution fills the cell above and in between glass beads.*

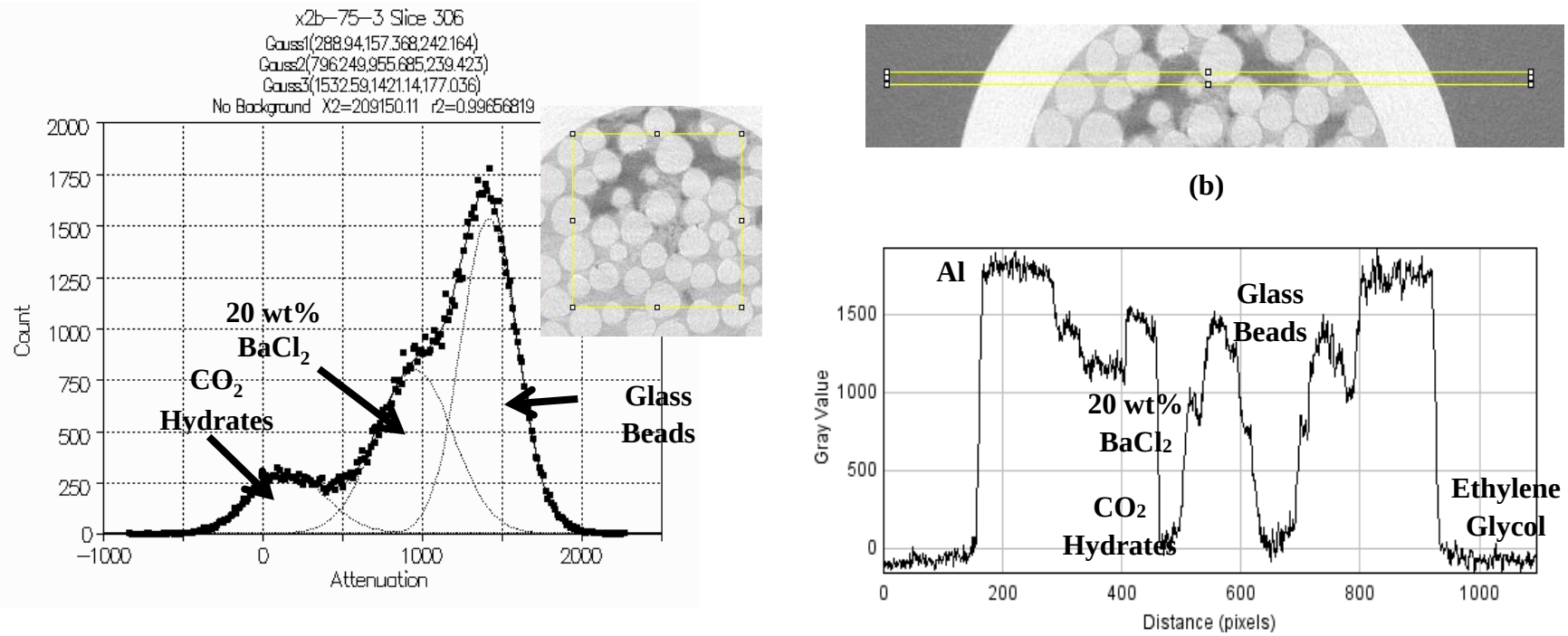

Figure 7.5: *(a) Histogram with attenuation values of pixel^{-1} for slice 306 of the CMT scan performed during Run 10 at 74.1 h. The PeakFit program was used to distinguish the different peaks in the histogram created by the various materials present inside the cell. The image inside the yellow box above the plot shows the region of the cell used to create this histogram, and in the image, darker gray regions are gas hydrates, lighter gray regions are solution, and the white spheres are glass beads. Since the peak attributed to CO_2 hydrates is centered above 0 pixel^{-1}, CO_2 hydrates are present in this experiment. (b) A plot profile box was drawn across a 2D image slice of the cell at 74.1 h containing aluminum tubing, 20 wt% $BaCl_2$ solution, CO_2 hydrates, glass beads, and ethylene glycol-water coolant. (c) A plot of the gray value (related to attenuation) across the yellow box where the phases are defined.*

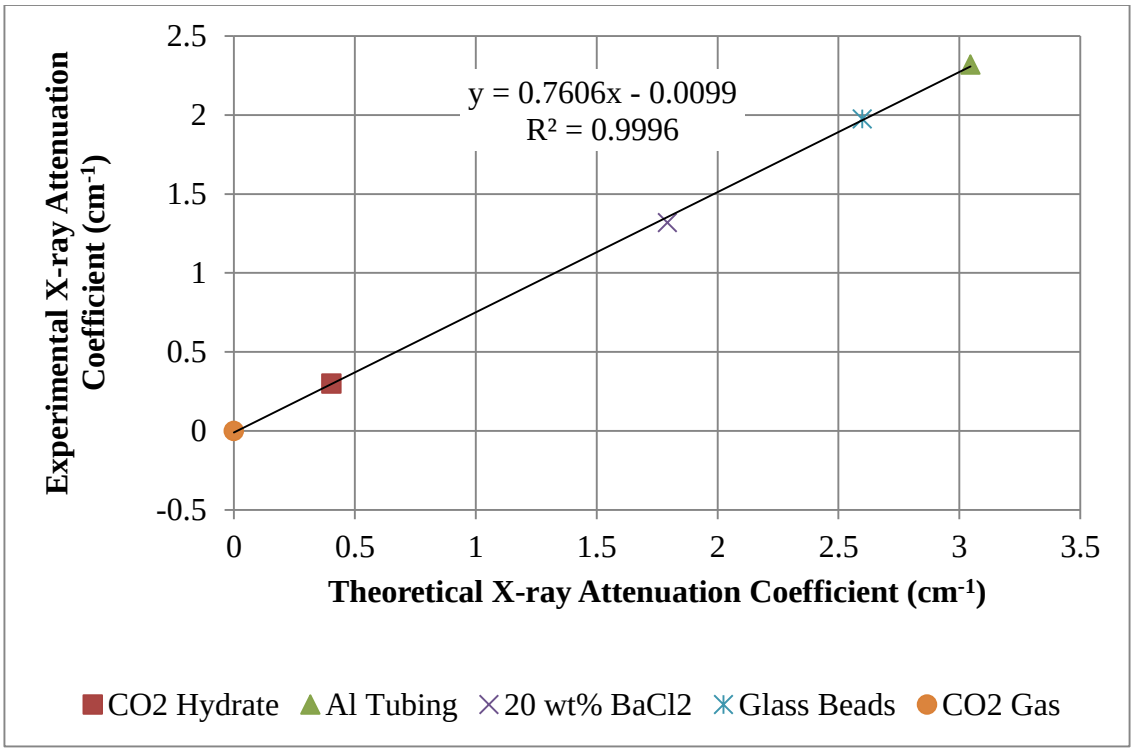

Figure 7.6: *Plot of theoretical vs. experimentally obtained x-ray attenuation coefficients for Run 10, indicating a good fit between theoretical and experimental data.*

7.2 CO_2 Hydrates in Ottawa Sand (Run 11-12)

Run 11 was performed using 1.2 mL of 10 wt% $BaCl_2$ solution ($T_{Freezing}$: -3.1°C, ρ: 1.08 g/cm^3) and 4.20 g of Ottawa sand (sieved 180-250 μm diameter particles used; obtained from the United States Geological Survey). The cell was charged with CO_2 gas up to 664 psig and cooled to -1.3°C in the bath of the ethylene glycol-water refrigerated circulator. CMT images were taken over time after the cell had been cooled for fifteen days. The time-resolved scans taken for this run were within the sand pack, but additional CMT scans were taken at a meniscus found above the sand pack in the gas phase of the cell. The top of this interface had attenuation coefficient values clearly corresponding to CO_2 gas, but the denser phase had attenuation values much lower than those for 10 wt% $BaCl_2$ solution. Upon deeper investigation, it is likely that the denser phase seen was liquid CO_2. A plot profile for a 2D image slice depicting this interface is shown in Figure 7.7. It is possible, based on run starting conditions, for liquid CO_2 to be stable in the cell during this run; as it is not possible to monitor system pressure during CMT scans, the exact final pressure at the estimated cell temperature is unknown. The attenuation coefficient for liquid CO_2 (0.315 cm^{-1}) has values in between those from CO_2 gas (0.030 cm^{-1}) and ethylene glycol-water coolant (0.365 – 0.376 cm^{-1}). Attenuation values for CO_2 hydrates (0.403 cm^{-1}) are near to those for liquid CO_2, but the attenuation coefficient range for ethylene glycol-water coolant is in between both of these phases, thereby the presence of hydrates in all of the CO_2 hydrate formation runs described herein and in Chapter 6 was confirmed by verifying that the attenuation coefficient for CO_2 hydrates was above the value for coolant. However, the Run 11 imaging series contained structured regions that consisted of attenuation coefficients closer to those for liquid CO_2, yet some areas of these regions had higher attenuation values that indicate the possibility of CO_2 hydrates. Figures 7.8 and 7.9 are plot profiles across regions of the cell imaged at 359.7 and 381.5 h respectively. In all of these profiles, there are some regions that match the liquid CO_2 peaks in Figure 7.7, but there are also some regions with gray values between 0 – 200 pixels^{-1} that have the potential to be CO_2 hydrates. Edges surrounding the larger dark shape in these images particularly had regions that could be hydrates, so it is possible that the liquid CO_2 bubbles are coated in CO_2 hydrates.

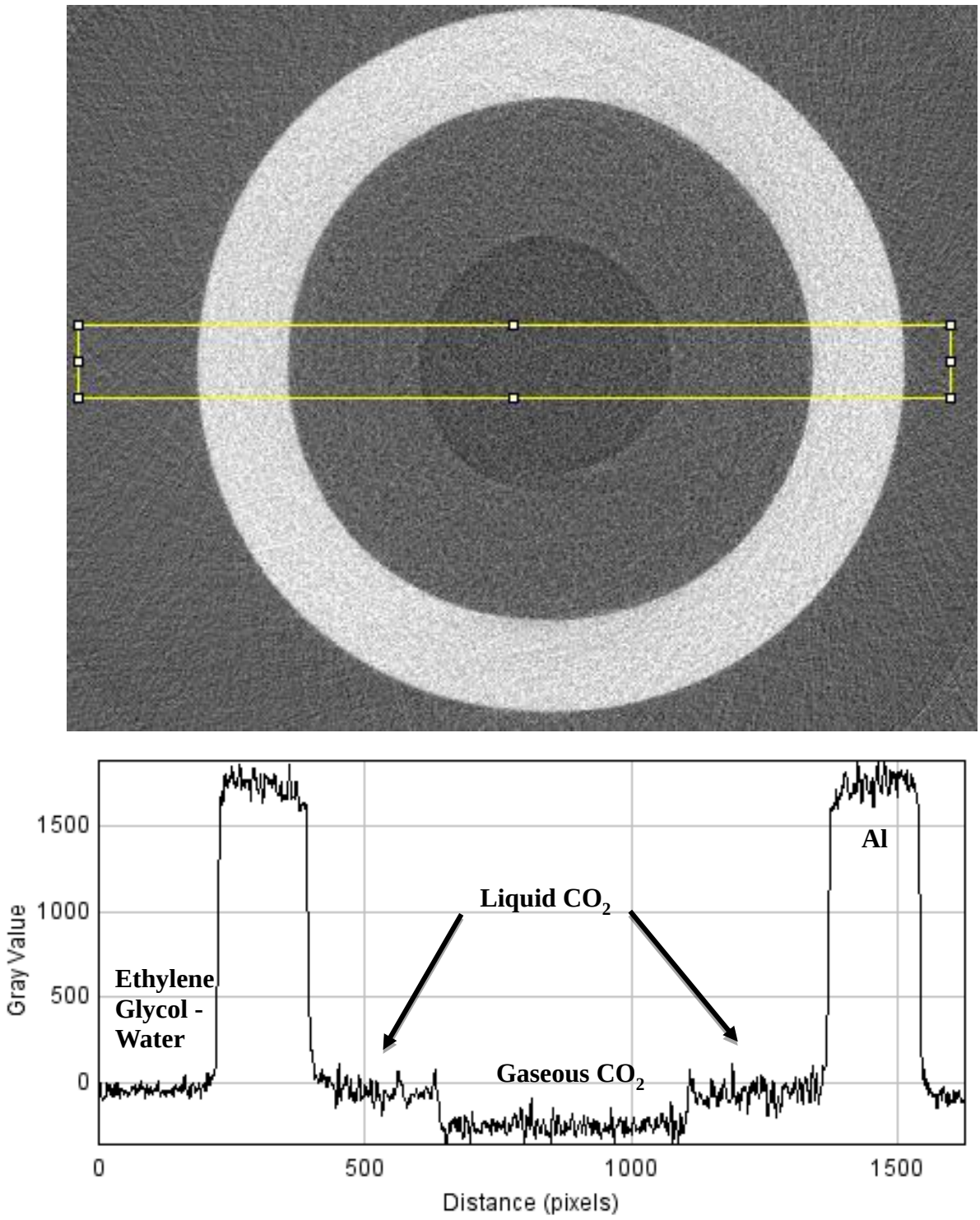

Figure 7.7: *Plot profile of the region highlighted in the yellow box of the 2D image slice at the gaseous CO_2-liquid CO_2 interface found high above the sand pack.*

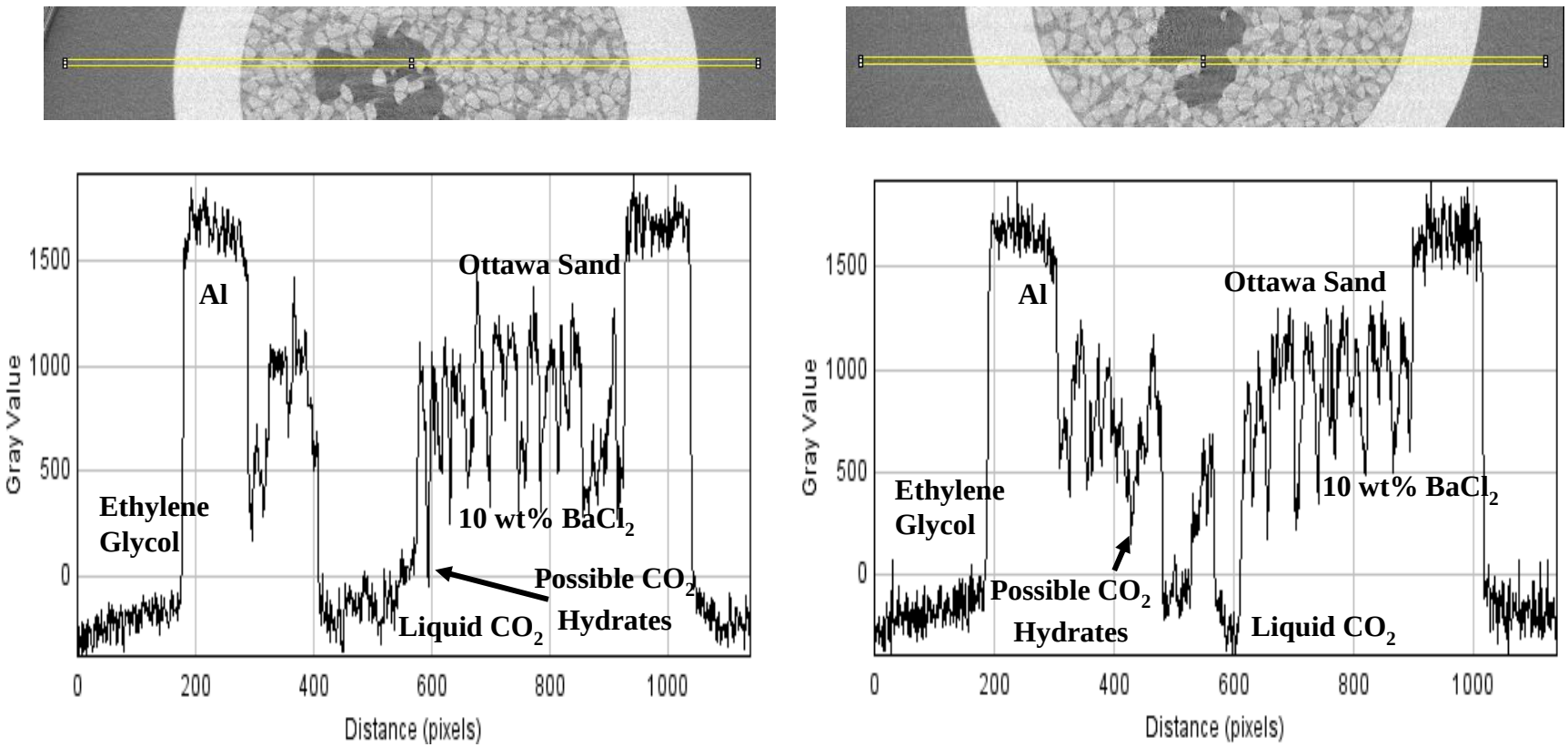

Figure 7.8: *Plot profiles of the regions highlighted in the yellow boxes of the 2D image slices at 359.7 h. These profiles show the possible regions for CO_2 hydrates.*

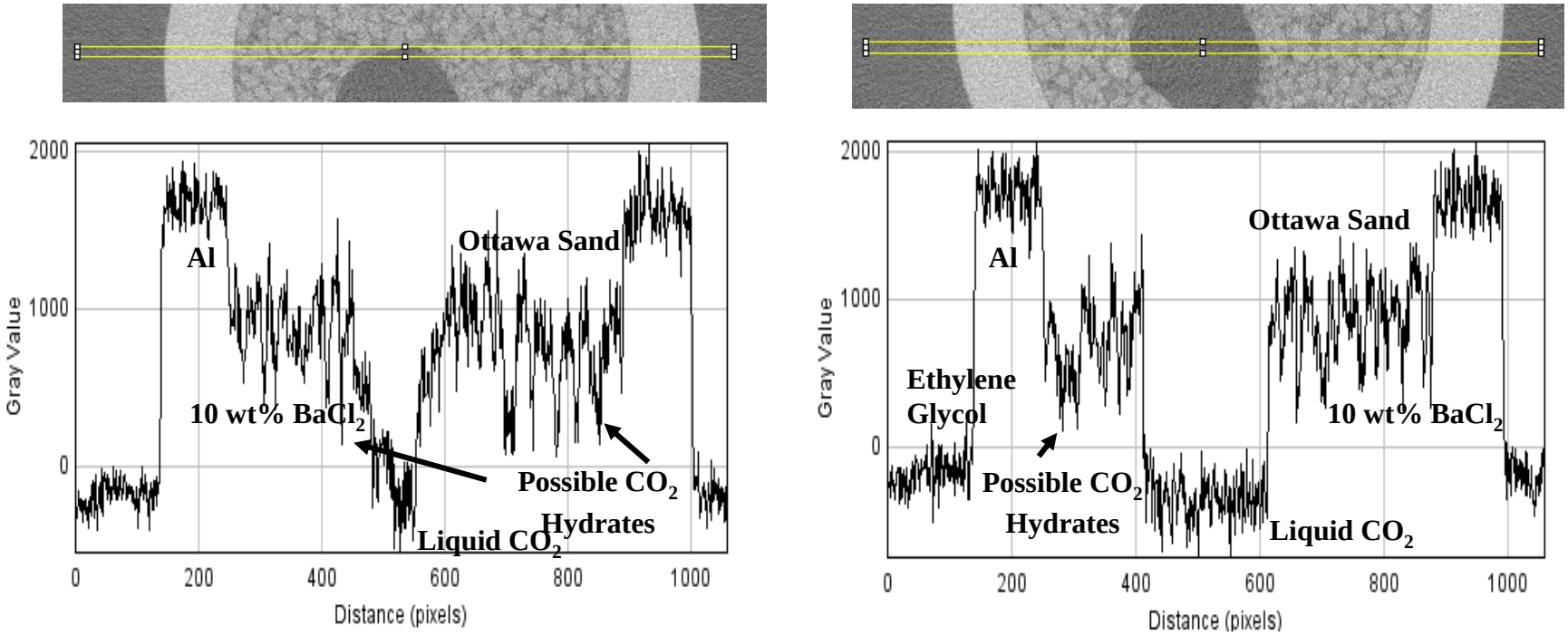

Figure 7.9: *Plot profiles of the regions highlighted in the yellow boxes of the 2D image slices at 381.5 h. These profiles show the possible regions for CO_2 hydrates.*

The time resolved CMT images taken during Run 11 shown in 3D in Figure 7.10 and in 2D in Figure 7.11, were taken in a region where the Ottawa sand was saturated with 10 wt% $BaCl_2$ solution. Initially, structures found to form at 359.7 h appeared to be forming in the pore spaces between the sand grains, but in a scan taken one day later at 381.5 h, the structures seemed to take on a more oval-like shape that appeared to have displaced sand grains. The following scan at 407.3 h shows that the structures restructured into nearly perfect spheres, which are the most energy efficient shape that a phase can form. After this scan, the NSLS was shut down for maintenance for 26 days, but the CMT cell was left cooling in the bath of the refrigerated circulator during this time. When the cell was imaged next at 1033.3 h, it was clear that structures remained stable in nearly the exact same places within the sand pack with the same spherical morphology. It is likely that the large structures in Figures 7.10 and 7.11 are mostly composed of liquid CO_2 (black), but the smaller ones are possible CO_2 hydrates (red).

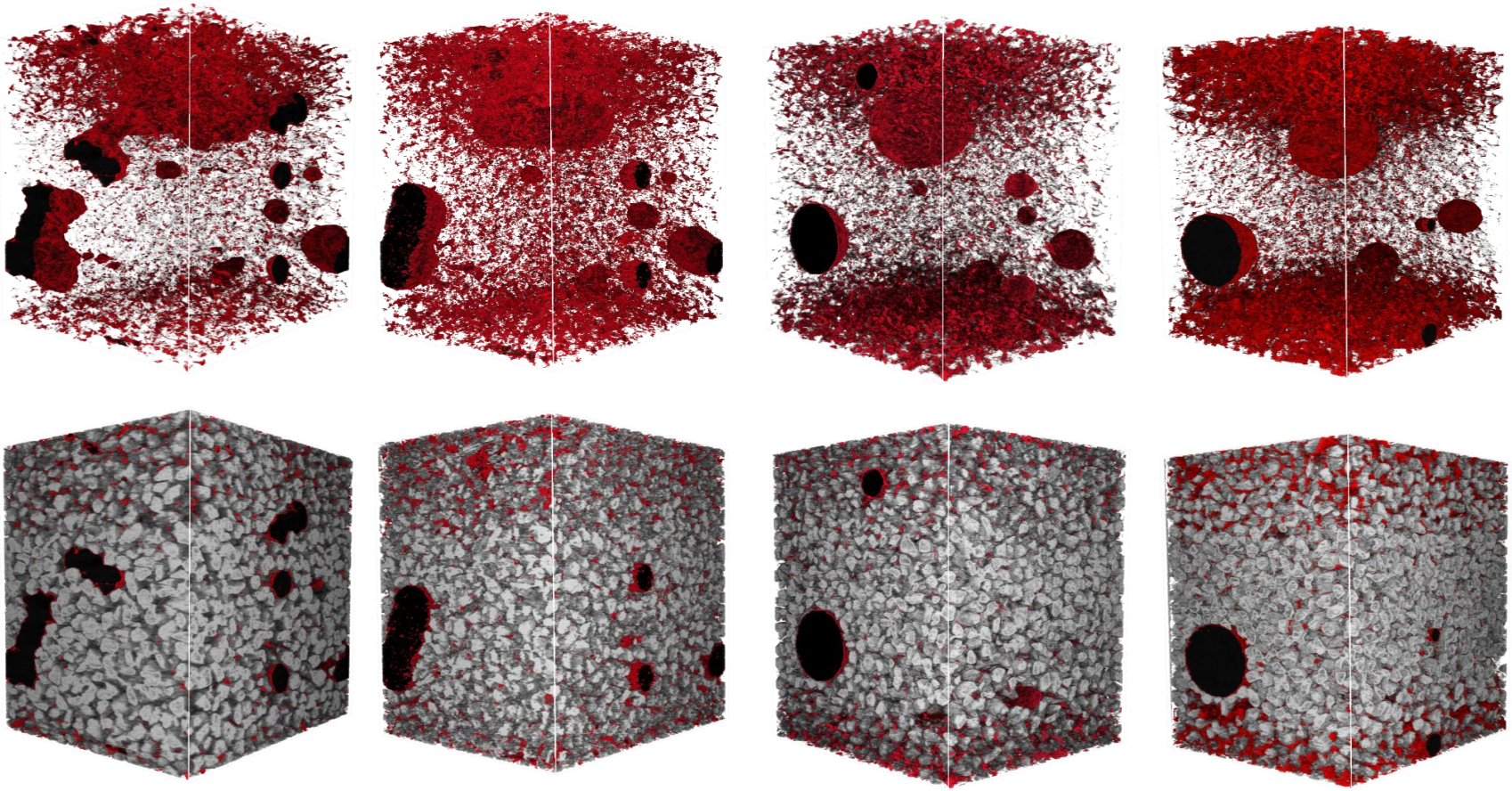

Figure 7.10: *Time resolved CO_2 hydrate formation in Ottawa Sand during Run 11. In these 3D volume images, red represents potential CO_2 hydrates, black is liquid CO_2, and gray is Ottawa sand. The top 3D volumes only show images of CO_2 hydrates in the cell, while the bottom images show how these CO_2 hydrates are located within Ottawa sand particles. The solution phase is not shown in these images.*

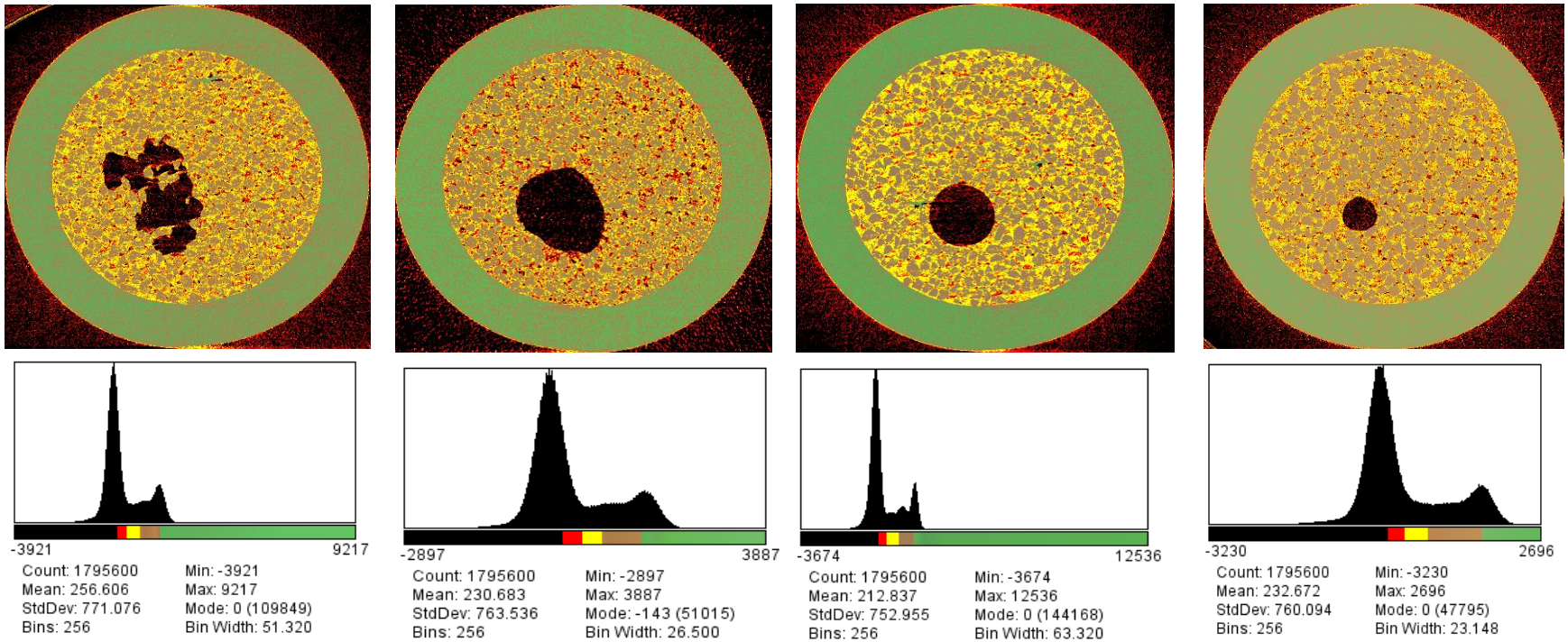

359.7 h 381.5 h 407.3 h 1033.3 h

Figure 7.11: *Time resolved image slices from slice 156 of Run 11 where red indicates potential CO_2 hydrates, black is liquid CO_2, yellow is 10 wt% $BaCl_2$ solution, brown is Ottawa sand, and green is aluminum tubing. Histograms of these 2D slices are shown below.*

Run 12 was performed using 0.95 mL of 15 wt% $BaCl_2$ ($T_{Freezing}$: -4.8°C, ρ: 1.13 g/cm^3) in 4.84 g of 180-250 µm Ottawa sand. The cell was pressurized with CO_2 gas to 660 psig, and the cell was imaged continuously as it was cooled to 0ºC. CO_2 hydrates formed in the cell are shown as 3D volumes in Figure 7.12 and as 2D image slices in Figure 7.13. Hydrates were witnessed in the cell after 17.7 h. Similar to the later CMT scans of Run 10, CO_2 hydrates were found to form in small shapes in the pore space between Ottawa sand particles. Over the seven days that the cell was imaged, hydrates grew to fill more pore spaces in the cell. It is clear from Figure 7.13 that there was more 15 wt% $BaCl_2$ solution visible in the pore spaces at 17.7 h than in the later scans. As hydrates formed, more solution was utilized to form hydrate cages. While this run had the least amount of hydrate forming solution injected in the cell, the solution seemed to be the wetting phase of the Ottawa sand rather than the CO_2 hydrates, as seen in Figure 7.14. There is a noticeable change of gray value slope when traveling from CO_2 hydrate to Ottawa sand, which indicates the presence of a solution phase in between the hydrate and sand particle. This is consistent with the results of Run 10.

Figure 7.15 shows histograms of the cell at 17.7 h and 77.5 h with peaks representing each phase fit into the overall image histogram using PeakFit. It is noticeable that at 17.7 h, the histogram for the cell was wider on the right side into the negative attenuation region. As attenuations were more negative, it was clear that there was a CO_2 gas phase presence in the cell. Later at 77.5 h, the histogram did not reach as far into the negative attenuation region, which indicated that CO_2 gas had further converted into CO_2 hydrates, and PeakFit no longer could find a peak for CO_2 gas. Figure 7.16 shows a plot profile across an image slice of the cell at 119.6 h. Each phase can be seen distinctly in the cell based on gray value (attenuation).

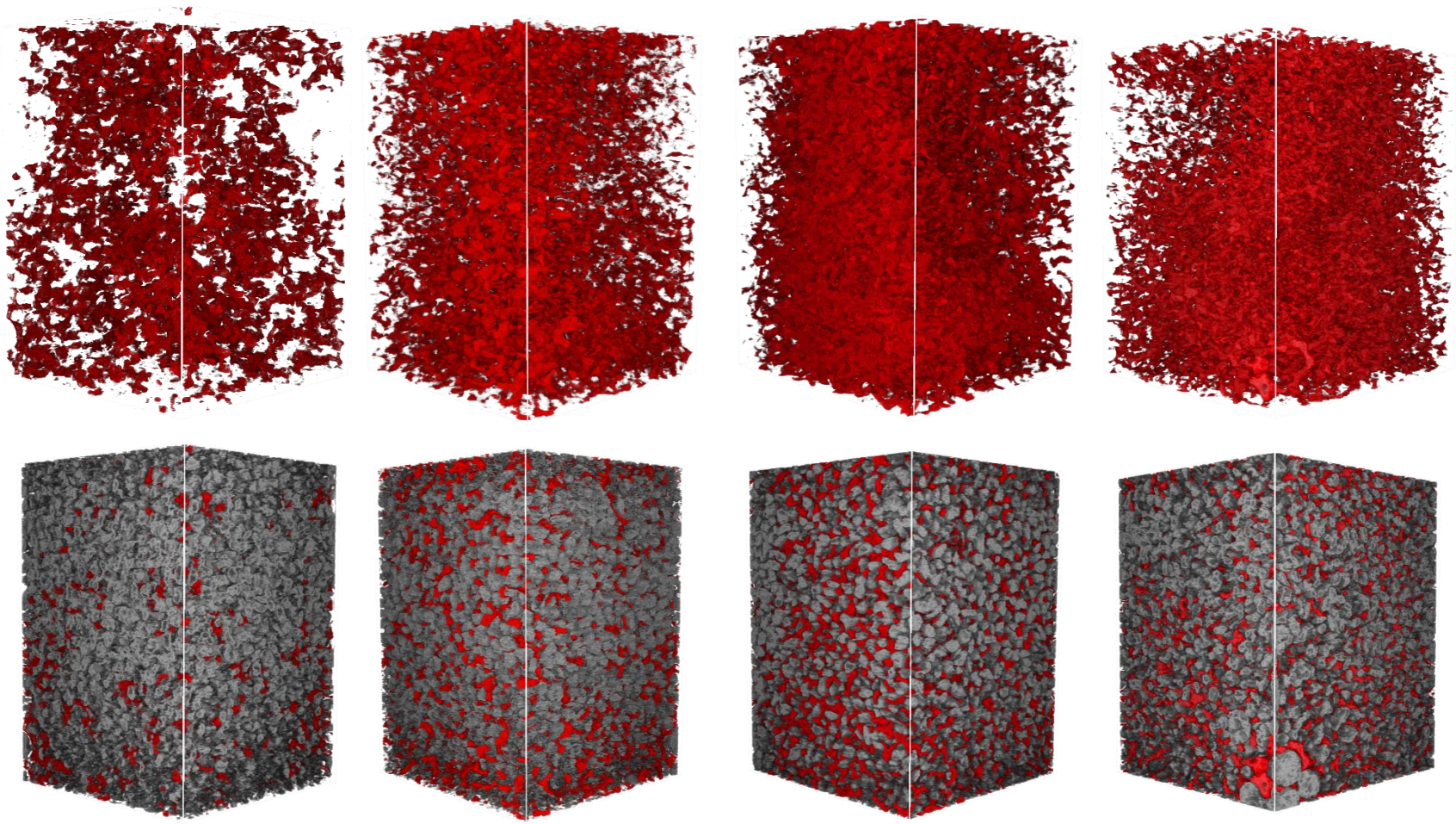

Figure 7.12: *Time resolved CO_2 hydrate formation in Ottawa Sand during Run 12. In these 3D volume images, red represents CO_2 hydrates and gray is Ottawa sand. The top 3D volumes only show images of CO_2 hydrates in the cell, while the bottom images show how these CO_2 hydrates are located within Ottawa sand particles. The solution and gas phases are not shown in these images.*

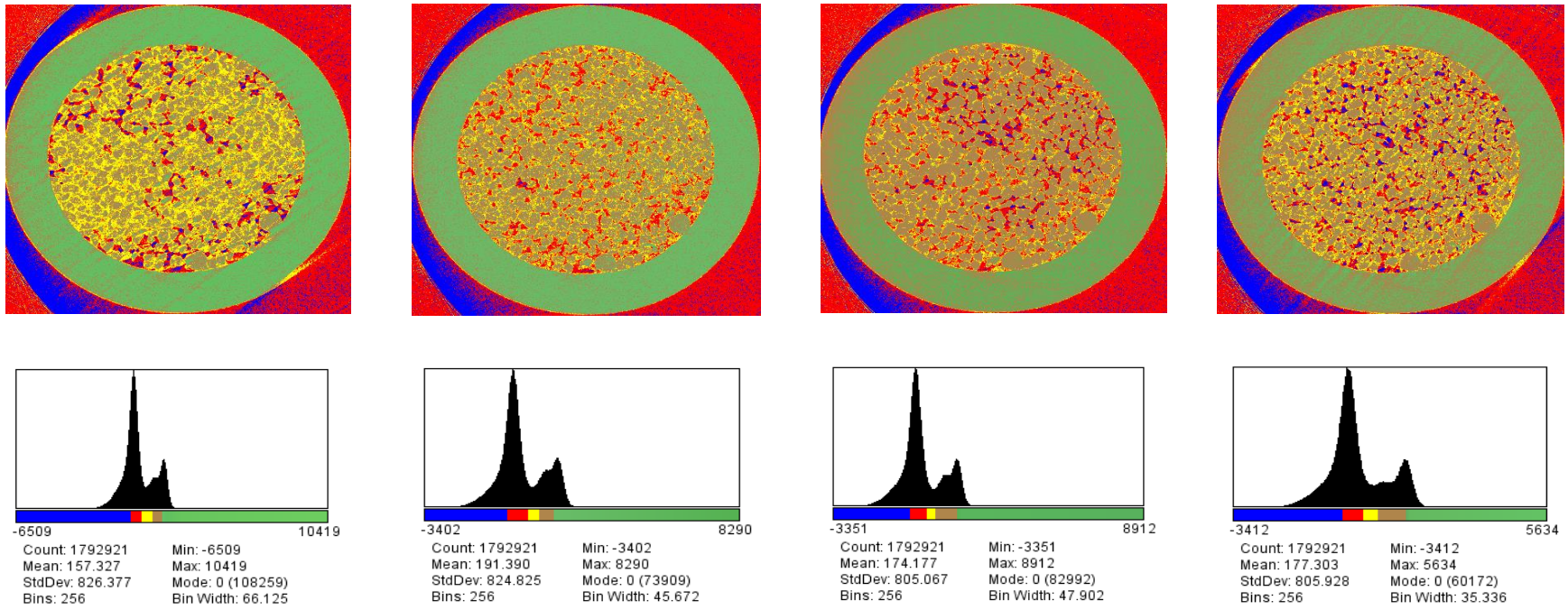

17.7 h 77.5 h 119.6 h 159.3 h

Figure 7.13: *Time resolved image slices from slice 233 of Run 12 where red indicates CO_2 hydrates, blue is CO_2 gas, yellow is 15 wt% $BaCl_2$ solution, brown is Ottawa sand, and green is aluminum tubing. Histograms of these 2D slices are shown below.*

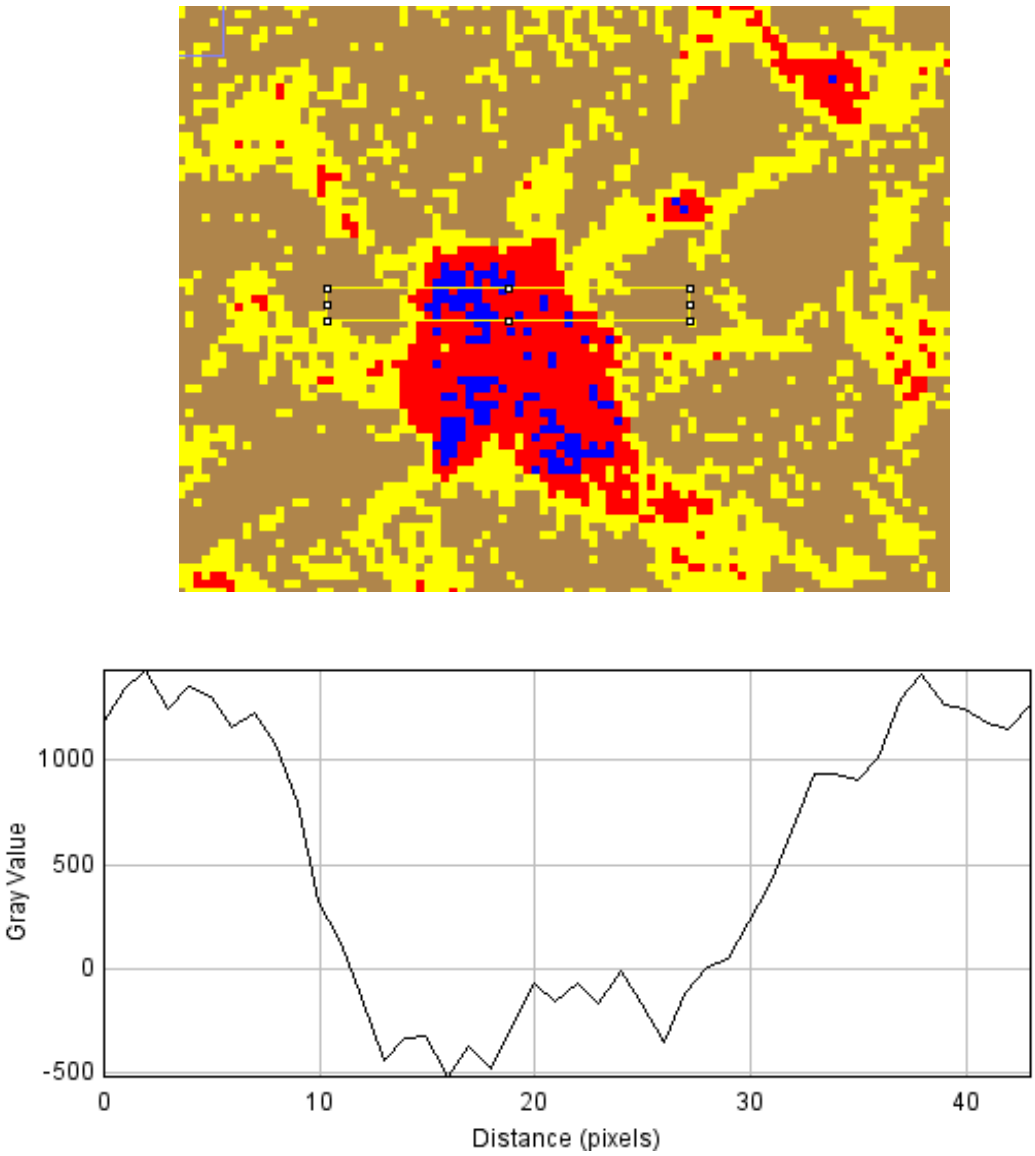

Figure 7.14: *Plot profiles indicating the presence of a solution layer (yellow) between Ottawa sand (brown) and hydrates (red). The plot profile of the yellow box in the above image slice shows a gradual transition between hydrates and Ottawa sand, with changes of slope occurring across this transition near gray values of 500 pixel^{-1}, indicating the presence of another phase in between the glass beads and hydrates.*

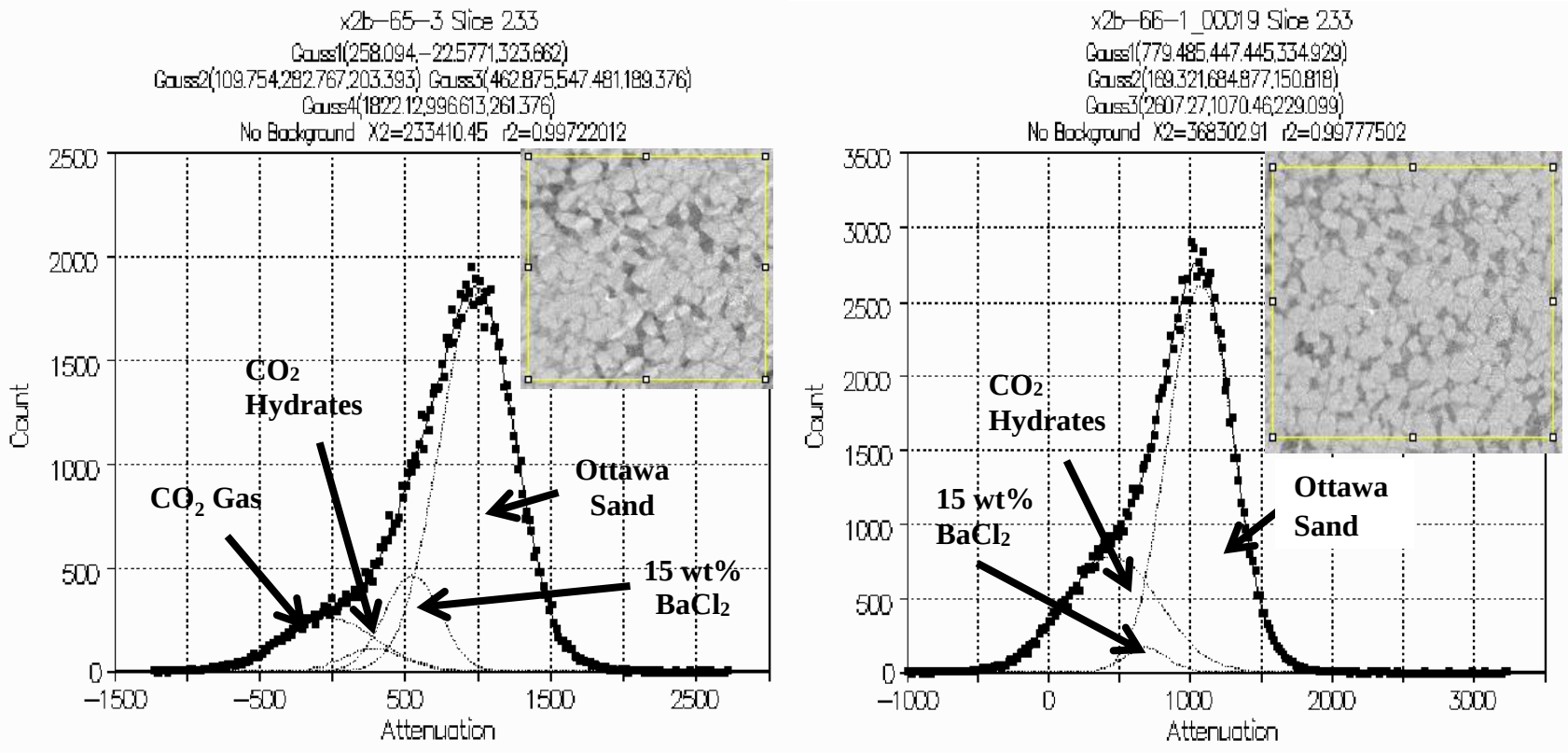

Figure 7.15: *(a) Histogram with attenuation values (pixel^{-1}) of slice 233 of the CMT scan performed during Run 12 at (a) 17.7 h and (b) 77.5 h. The PeakFit program was used to distinguish between the different peaks in the histogram created by the various materials present inside the cell. The image inside the yellow box above the plots show the region of the cell used to create these histograms, and in the image, darker gray regions are CO_2 gas, medium gray regions are CO_2 hydrates, lighter gray regions are 15 wt% $BaCl_2$ solution, and the whiter shapes are Ottawa sand particles. Since the peak attributed to CO_2 hydrates is centered above 0 pixel^{-1}, CO_2 hydrates are present in this experiment. Based on attenuation, it is clear that the CO_2 gas present at 17.7 h was absorbed to form further CO_2 hydrates by 77.5 h due to the lack of a CO_2 gas peak in (b).*

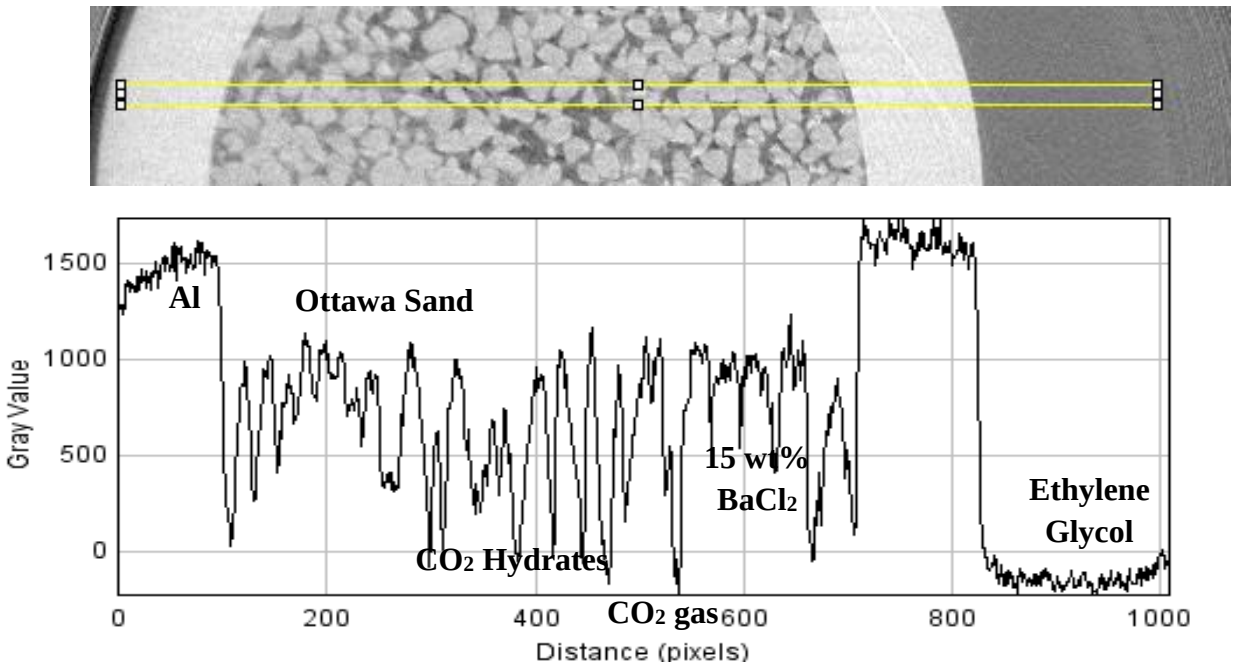

Figure 7.16: *A plot profile was taken across the yellow box in a 2D image slice of the cell at 119.6 h containing aluminum tubing, 15 wt% $BaCl_2$ solution, CO_2 gas, CO_2 hydrates, Ottawa sand, and ethylene glycol-water coolant. A plot of the gray value (related to attenuation) across the yellow box is shown below that defines the phases present.*

7.3 50% CH_4 – 50% CO_2 Hydrates in Ottawa Sand (Run 13)

Once it was clear that pure hydrates could form and be imaged in the CMT cell in porous media, an experiment was attempted to form gas hydrates from a 50% CH_4 - 50% CO_2 gas mixture in Ottawa sand. For Run 13, 4.65 g of 180-250 µm Ottawa sand was loaded into the cell, and then 1.1 mL of 15 wt% $BaCl_2$ solution was added. The cell was first pressurized to 526 psig with CO_2 gas and then up to 1049 psig with CH_4 gas. GC samples taken at room temperature indicated about 81% CH_4 and 19% CO_2 in the gas phase, even though the cell was loaded with a 50%-50% CH_4-CO_2 gas mixture based on cell pressure. Much of the CO_2 gas added to the cell most likely initially solubilized in the solution as CH_4 was added to the cell. After gas was removed from the cell for GC samples, cell pressure was down to 960 psig at 21.4°C. The cell was cooled to -2.0ºC, and after 4 h when the cell had reached -2.1°C, cell pressure was at 891 psig. After 18 h of cooling, cell pressure was found to be 907 psig at -2.1°C, and after cooling for an additional day, cell pressure was at 920 psig at -2.1°C. As was seen in the mixed gas experiments of Chapter 6, pressure decreased and then increased during cell cooling. At this time, the top assembly was depressurized and disconnected, and different regions of the sand pack were imaged during each CMT scan.

As shown in 3D volumes in Figure 7.17 and 2D image slices in Figure 7.18, hydrates were found to grow in the pore space between sand particles. As with the previous run, there appeared to be less 15 wt% $BaCl_2$ solution in the cell as time went on, suggesting that the solution was used to form gas hydrates. There were also large regions of a highly attenuating phase that must be precipitated $BaCl_2$ (attenuation coefficient of 28 cm^{-1}), further confirming that as water was absorbed into the hydrate structure, $BaCl_2$ was left behind. The wetting phase of the Ottawa sand appeared to be the solution again in several locations in the cell, but regions that had a very thin layer of solution phase between hydrates and Ottawa sand were found as well. The plot profiles in Figure 7.19(a) and (b) illustrate these different regions. The thin solution wetting layer is likely due to the fact that the sand was not as saturated in this run due to hydrate formation and a low initial solution volume. Each of the images in Figures 7.17 and 7.18 were taken at different heights in the sand pack, indicating hydrate growth all over the cell during the six days of CMT imaging.

Figure 7.20 shows histograms with PeakFit analysis for regions in two image slices taken during the 50.1 h scan. The slice analyzed in Figure 7.20(a) has attenuation values that are too high to suggest a large presence of CH_4-CO_2 gas, whereas the slice shown in 7.20(b) does have lower attenuation values that are likely due to gas existence in this slice. Figure 7.21 shows a plot profile taken of an image slice from a CMT scan at 140.3 h. Each phase can be seen distinctly in the cell based on gray value (attenuation), and in this run, there were several bright white spots on the image slice of Figure 7.21 that are precipitated $BaCl_2$.

Prior to depressurization, while the cell was still chilled, GC samples indicated a gas phase of 47% CH_4 and 53% CO_2. GC samples taken when the cell was warmed back up to room temperature indicated 40% CH_4 and 60% CO_2 initially, and the last sample indicated 30% CH_4 and 70% CO_2. This indicates the likelihood that the mixed gas hydrates formed were composed of more CO_2 than CH_4, and CO_2 gas had indeed been initially solubilized in the hydrate forming solution.

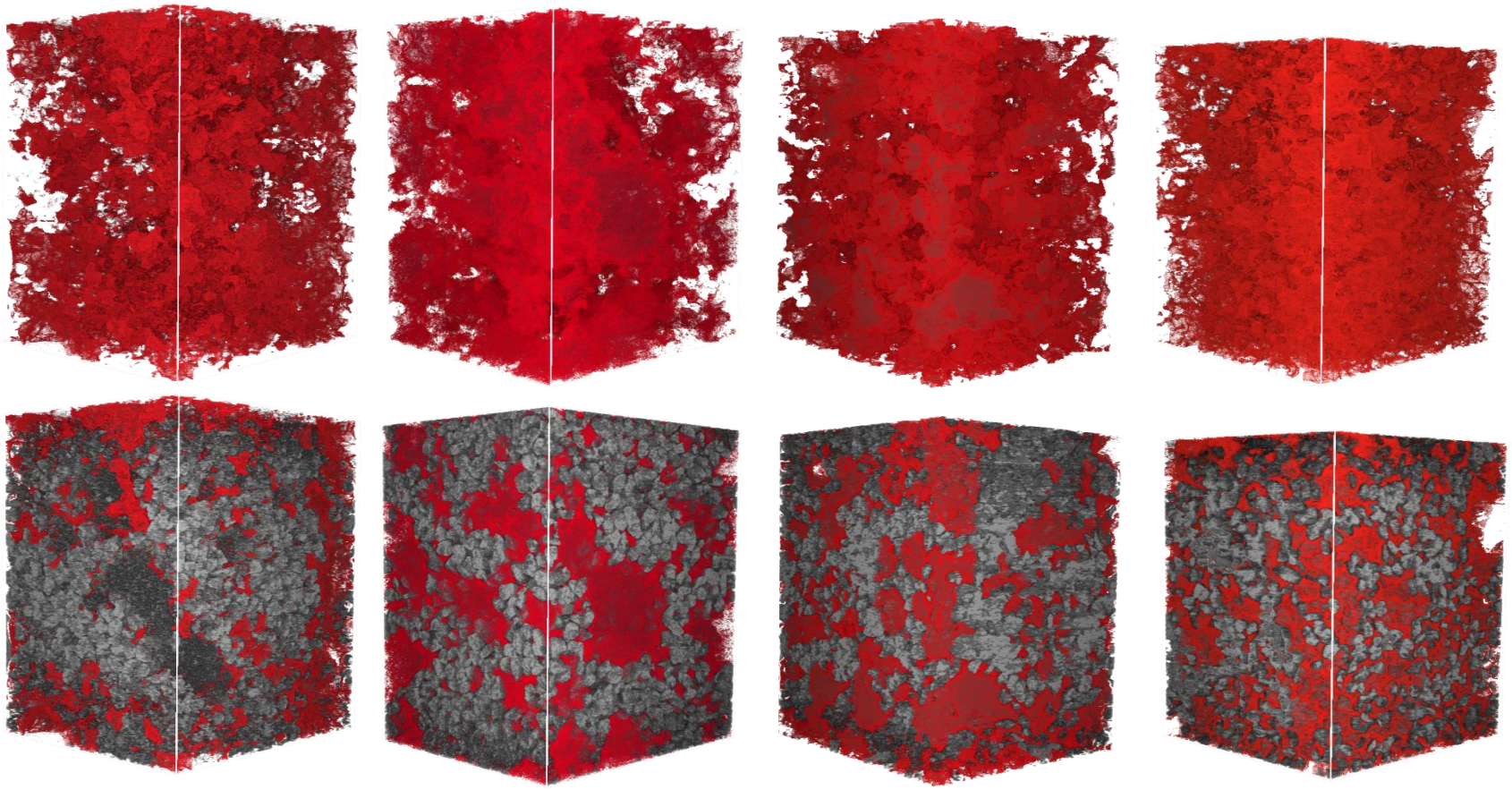

42.5 h 45.7 h 50.1 h 140.3 h

Figure 7.17: *CH_4-CO_2 hydrate formation at different regions within the Ottawa sand pack at different times during Run 13. In these 3D volume images, red represents mixed gas hydrates and gray is Ottawa sand. The top 3D volumes only show images of gas hydrates in the cell, while the bottom images show how these gas hydrates are located within Ottawa sand particles. The solution and gas phases are not shown in these images.*

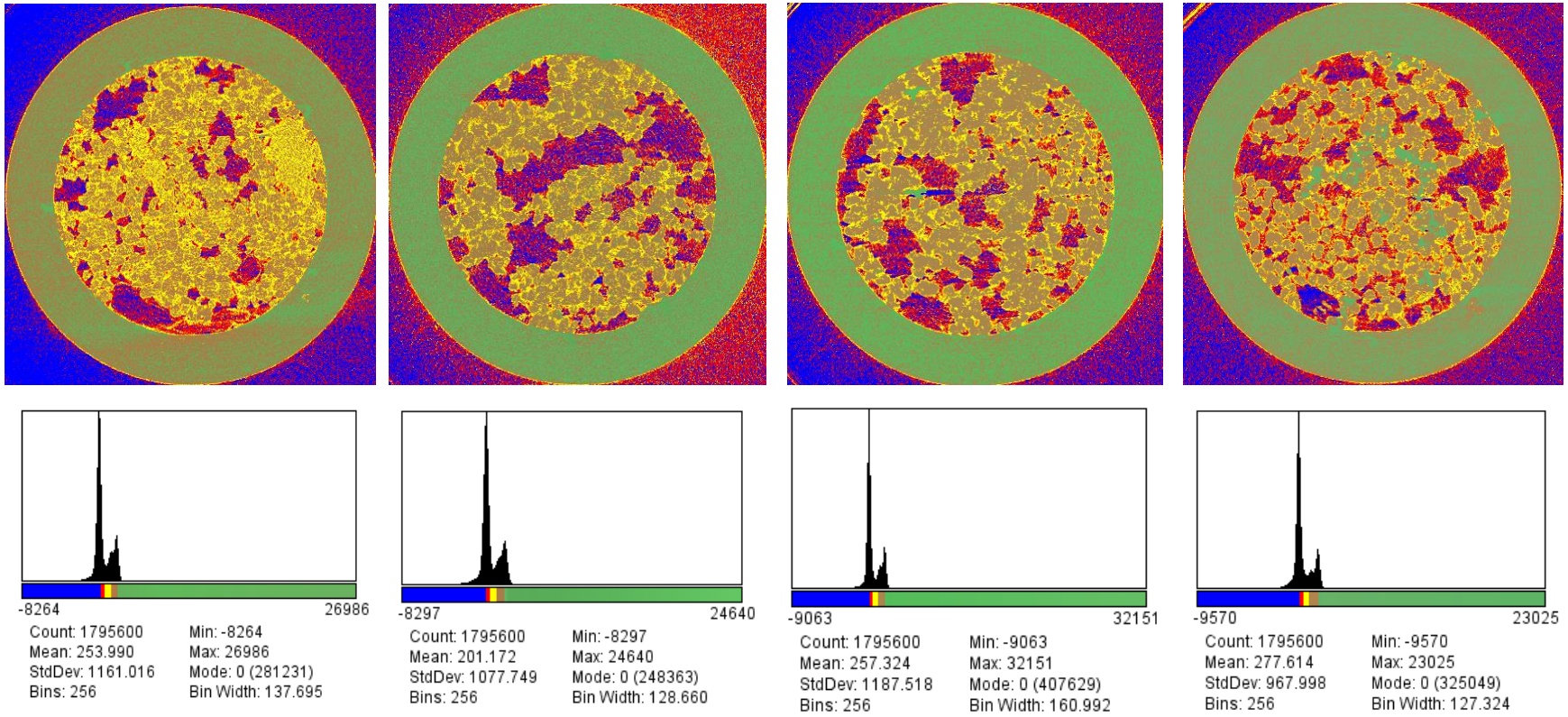

42.5 h 45.7 h 50.1 h 140.3 h

Figure 7.18: *Image slices from slice 300 or 430 of Run 13 where red indicates gas hydrates, blue is CH_4-CO_2 gas, yellow is 15 wt% $BaCl_2$ solution, brown is Ottawa sand, and green is aluminum tubing and precipitated $BaCl_2$. Each of these image slices is from a different region of the CMT cell imaged at different times. Histograms of these 2D slices are shown below.*

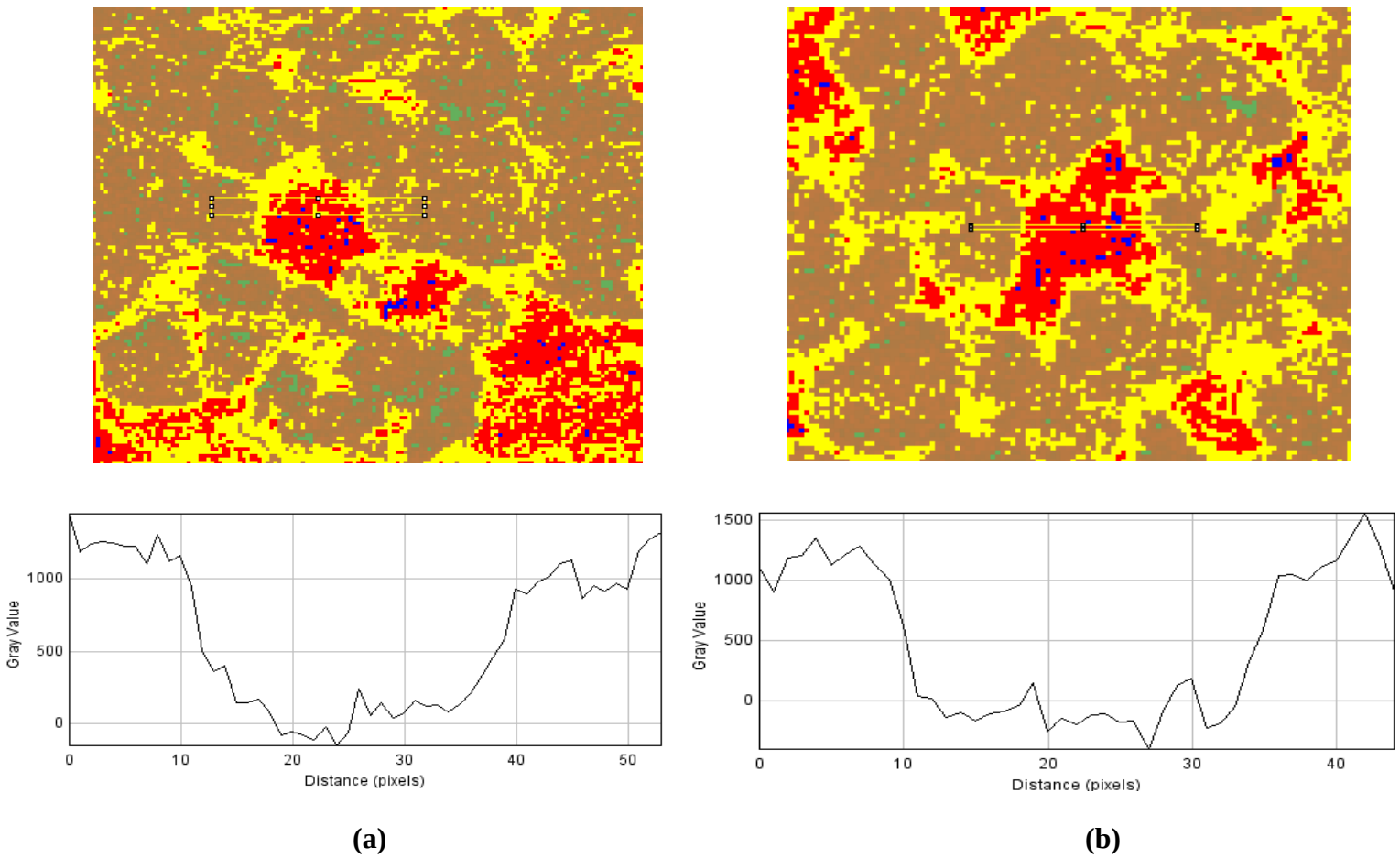

Figure 7.19: *(a) Plot profile indicating the presence of a solution layer (yellow) between Ottawa sand (brown) and hydrates (red), as there is a gradual transition between the hydrates and Ottawa sand, with slope changes occurring across this transition near gray values of 500 pixel^{-1}. (b) Plot profile in another region of the cell that has a very small change in slope between the Ottawa sand and the mixed gas hydrate, indicating the possibility of a very thin solution layer.*

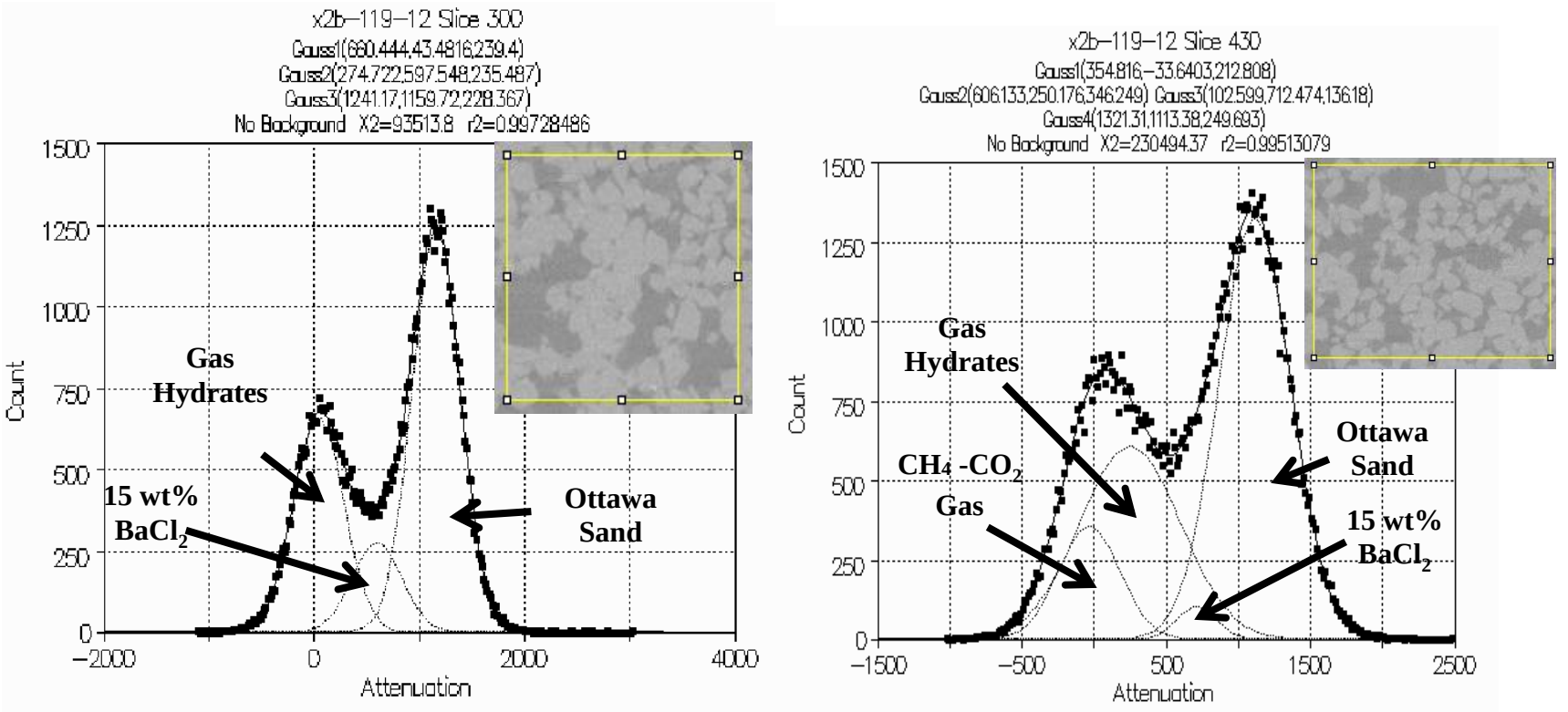

(a) **(b)**

Figure 7.20: *(a) Histogram with attenuation values (pixel^{-1}) of the CMT scan performed during Run 13 at 50.1 h at image slice (a) 300 and (b) 430. The PeakFit program was used to distinguish between the different peaks in the histogram created by the various materials present inside the cell. The images inside the yellow box above the plots show the region of the cell used to create each histogram, and in the images, the darkest regions are CH_4-CO_2 gas, dark gray regions are gas hydrates, lighter gray regions are solution, and the whiter shapes are Ottawa sand particles. Since the peak attributed to CO_2 hydrates is centered above 0 pixel^{-1}, CO_2 hydrates are present in this experiment. (a) shows that at image slice 300 in this imaging scan, there was minimal CH_4-CO_2 gas present, as there is no peak in the histogram negative enough to be gas while (b) taken at slice 430 does have a histogram that has a very negative peak that must represent gas presence.*

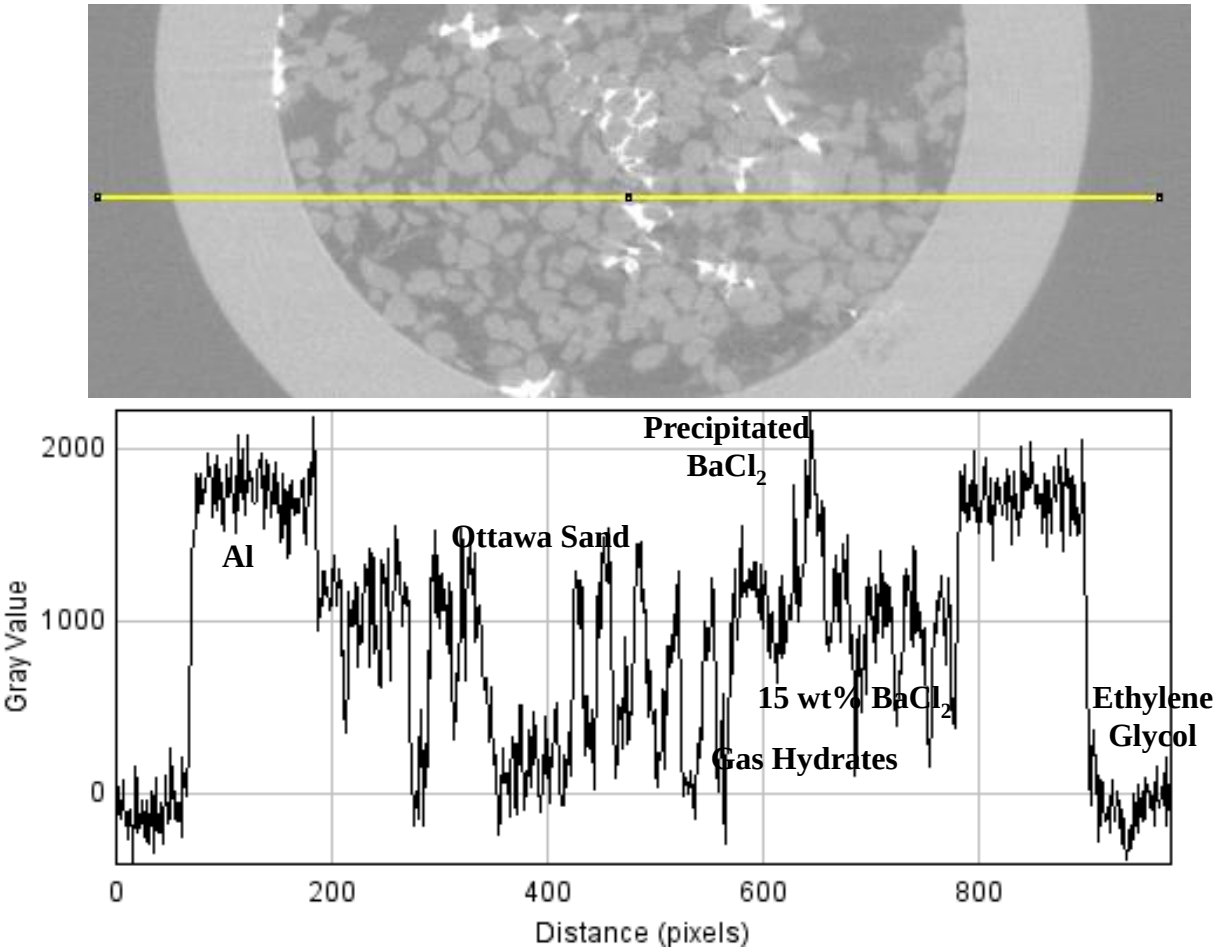

Figure 7.21: *A plot profile was taken across the yellow box in a 2D image slice of the cell at 140.3 h containing aluminum tubing, 15 wt% $BaCl_2$ solution, mixed gas hydrates, Ottawa sand, precipitated $BaCl_2$, and ethylene glycol-water coolant. A plot of the gray value (related to attenuation) across the yellow box is shown below that defines the phases present.*

7.4 Hydrate Growth in Porous Media Discussion

The hydrate memory effect, a theory which hypothesizes that reforming hydrates in a system that had previously held hydrates should occur faster with a higher conversion of gas into hydrates, was not seen during Run 10. Since the average temperature of the X2B experimental hutch is about 25-27°C, during dissociation it is quite likely that the temperature of the cell rose above 25°C, which is why the memory effect was not seen[54]. The hydrates that grew the second time were more spherical and smaller than the pore spaces between glass beads. These reformed hydrates were not found to form in the same locations in the sand pack as the original hydrate formation event. This is consistent with Rees et al.[128] which found that hydrate morphology and growth location was not repeatable among hydrate formation in the same sand pack and hydrate forming solution.

In these 3D reconstructions, it is clear that $BaCl_2$ solutions, not CO_2 hydrates, are the wetting phase of the porous media in Runs 10 and 12. This is in agreement with past studies of THF[129] and CH_4[130] hydrates performed by our group and verifies hydrate models that assume the solution to be the wetting phase of the porous media[143,144]. Run 13 consisted of regions with a visible solution wetting phase, as well as areas with a very thin solution wetting phase for the Ottawa sand. This is likely due to a lack of solution in the cell after much hydrate formation and $BaCl_2$ precipitation.

In Runs 10, 12, and 13, gas hydrates formed in the pore spaces between glass beads or Ottawa sand particles, and they did not appear to have affected the position of the porous media. On the other hand, the structures formed in Run 11 were initially found to have a pore filling morphology that reconfigured and displaced sand grains to form a grain displacing morphology. This rearrangement is likely due to Ostwald ripening, a phenomenon where smaller orders of a substance combine into larger ones to minimize the free energy of the system[145]. While it is likely that these structures were mostly composed of liquid CO_2, plot profiles across these regions did have some locations with attenuations near that of CO_2 hydrates. Studies[146,128] have shown that, initially upon formation, hydrate morphology can be dendritic. These high surface area hydrates have unstable surface energies, so over time (2-5 hours), the hydrates will reconfigure into more energy efficient shapes. Clennell et al.[71] explained that a hydrate will grow in a pore space until it reaches a certain size in the pore. After that critical size has been

reached, the hydrate will have a surface curvature that allows it to displace porous media, rather than the hydrate growing into smaller pores. When this occurs, the hydrate will take on a larger surface curvature as these pore throats are overcome. More gas, lower temperatures, or higher pressures are needed for hydrate growth of this nature. The pressure of this experiment was high, and temperature was very low, thereby this effect may have contributed to the rearrangement of these liquid CO_2/hydrate regions. In addition, the presence of liquid CO_2 may have contributed to this structure's change in morphology. The liquid CO_2 formed during Jerguson Run 7 described in Chapter 4 did bring about hydrate formation, which is another reason to indicate the likelihood of hydrate presence near these liquid CO_2 regions.

Hydrate morphology is dependent on the porous media in which they have formed, formation conditions, and the ratio and types of chemical components in the system[147]. As pore filling hydrates may or may not cement sediment grains, it is difficult to characterize how it will affect seafloor stability[147]. Kingston et al.[148] found that when CH_4 hydrates were formed in fully water-saturated sand, hydrates formed on the interface of gas bubbles trapped in water. When hydrates form this way, a large amount of hydrates would be needed to cement sand in place. As hydrates formed, sand grains were still free to move.[148] In CMT reconstructions small volumes of CO_2 gas can be found near hydrates in the sand pores, and sand grains appear to have moved slightly between subsequent imaging scans, so it is likely that the hydrates formed were not cementing.

Mixed gas hydrates in Run 13 were found to form randomly throughout the sand pack. This mixed CH_4-CO_2 hydrate system in porous media also exhibited a pressure drop followed by a pressure increase during cell cooling, which suggests that this phenomenon is greatly related to the presence of two gases in a hydrate forming system and correlates well with the data presented in Chapter 6.

The precipitated $BaCl_2$ seen in Runs 12 and 13 is not an unusual find. The exclusion of salt from the hydrate structure will result in a more concentrated salt solution, therefore it is unsurprising that some of the salt may precipitate out. It is likely that salt has precipitated out of the solution during previous hydrate formation runs described in Chapter 6, but this salt dropped to the bottom of the cell due to its high density. In these porous media runs, precipitated salt was trapped at its site of precipitation due to the tight sand pack.

7.5 Conclusions

CMT was used to form gas hydrates in the presence of porous media. As Rees et al.[128] found for CH_4 hydrates, CO_2 hydrate morphology can be different for each hydrate formation run. This was clearly seen when CO_2 hydrates were formed in glass beads: once the cell was warmed above 25°C and hydrates were reformed, they grew in smaller shapes in new locations. The salt solution was the wetting phase of the porous media in experiments, though when the sand pack was not fully saturated due to hydrate formation, this wetting layer was very thin. Precipitated $BaCl_2$ was found in areas of the cell depleted of hydrate forming solution, indicating that hydrates did form in large quantities as salt is excluded from the hydrate structure.

CO_2 hydrates formed in glass beads and CO_2 and CH_4-CO_2 hydrates in Ottawa sand were found to grow according to the pore filling hydrate growth model. The presence of liquid CO_2 and possible CO_2 hydrates in Ottawa sand initially resulted in a pore filling morphology but became grain displacing over time. This change in morphology is most likely due to Ostwald ripening, and it could have implications on the stability of the ocean floor for hydrates formed below the seafloor. If liquid CO_2 and hydrates form in a sand pack on the ocean floor during CO_2 sequestration, a change in morphology from pore filling to grain displacing will affect the sediment matrix.

Chapter 8

8.0 Conclusions

8.1 Macro-Scale Baseline Experiments: Jerguson Cell

CO_2 and 62% CH_4-38% CO_2 gas mixtures were utilized to form gas hydrates in a 300 ppm SDS solution without porous media.

1) Both CO_2 and mixed CH_4-CO_2 hydrates successfully formed in this excess water system.
2) Gas hydrates accumulated in the aqueous phase at the bottom of the cell and not at the gas-liquid interface. The gas-liquid interface remained intact during hydrate formation, indicating that hydrates may have nucleated in the bulk solution or at the gas-liquid interface and then accumulated in the aqueous phase due to density differences.
3) The hydrate formation time was found to vary from 17 h to seven days. The conversion of about 32% of CO_2 gas into hydrates was measured when SDS, a known hydrate former, was present.
4) The overall CO_2 hydrate yield could be increased with multiple gas charges though subsequent hydrate yield was low. This is explained by a decreased SDS concentration in the solution as SDS tends to precipitate out after single use.
5) A finding that CH_4-CO_2 gas mixtures that are CH_4-rich yield a higher concentration of CH_4 hydrates is contradictory to many previous findings, though these studies did not have gas mixtures made of predominantly CH_4.
6) It was also found that while initially the gas phase of the cell was predominantly CO_2, as time went on, the concentration of CH_4 in the gas phase increased, indicating that CH_4 and CO_2 exchanged in the hydrate form, which is in agreement with previous studies.

8.2 Macro-Scale CH_4-CO_2 Exchange Experiments

Experiments were performed to study the CH_4-CO_2 exchange phenomenon with and without porous media in artificial seawater. Experiments were performed to form CH_4 hydrates, followed by a CO_2 injection to investigate gas exchange in hydrates, as well as experiments to form CO_2 hydrates, followed by a CH_4 gas injection to monitor CO_2 hydrate stability.

1) CH_4 and CO_2 hydrates were found to form during all experiments performed.
2) CO_2 hydrate induction times were generally shorter than CH_4, by as much as a factor of four, with or without sediments.
3) Hydrate formation data showed that when a secondary gas was injected into a system containing already formed hydrates, the newly injected gas entered the hydrate phase instantly (within minutes).
4) CO_2 hydrates formed in a system that already contained CH_4 hydrates were found to be more stable, whereas CH_4 hydrates formed in a system consisting of CO_2 hydrates as hosts were initially stable, but CH_4 gas in hydrates quickly exchanged with free CO_2 gas to form more stable CO_2 hydrates.
5) Gas hydrates were found to form even when the partial pressures of CH_4 and CO_2 were not within the hydrate stability region.
6) In all five experiments, even though the system was depressurized, left for over a week at room temperature, and flushed with nitrogen gas in between runs, the system still exhibited the hydrate memory effect. These results contradict those previously reported in literature.
7) Overall, the observed fast CO_2 hydrate formation from free CO_2 gas in the presence of preformed CH_4 hydrates indicates the feasibility of developing a CO_2 sequestration scheme using natural CH_4 hydrate reservoirs.

8.3 Baseline Runs to Prepare for CMT Imaging

A series of experiments were performed in the Jerguson cell to form hydrates from a 50% CH_4 – 50% CO_2 gas mixture, form CH_4 hydrates followed by a CO_2 gas injections, and form CO_2 hydrates followed by a CH_4 injection using $BaCl_2$ solutions similar to those to be imaged using CMT. In addition, numerous experiments were performed to form pure CH_4 and pure CO_2

hydrates in ¼", ½", and 1" OD reactors to test hydrate formation on a small scale prior to CMT experiments.

1) CH_4 and CO_2 hydrates did form on a macroscale in the Jerguson cell in 5 wt% $BaCl_2$ solutions.
2) Gas hydrates formed in the Jerguson cell were witnessed to mostly accumulate at the gas-liquid interface, which is why CMT experiments performed without a sand pack were imaged at the gas-liquid interface.
3) In the small volume cells, both CH_4 and CO_2 hydrates were found to form.
4) While the pressure drop and conversion of gas into hydrates varied from run to run, factors that were found to best encourage hydrates to form were: a) using higher gas pressures, b) using lower liquid volumes, and c) agitating the cell using stainless steel balls and shaking.
5) While larger percentages of hydrates were generally found to form in the ½" and 1" OD cells, the diameters of those reactors are too large for CMT imaging, so a ¼" OD CMT cell was utilized for CMT imaging experiments.
6) Though the 300 ppm SDS solution was better for hydrate formation, since a contrasting agent is needed to increase the x-ray attenuation coefficient of the hydrate forming solution, solutions containing varying proportions of $BaCl_2$ were used for CMT imaging.

8.4 CMT Experiments – CH_4, CO_2, and CH_4-CO_2 Hydrate Formation without Porous Media

CMT was used to image CH_4, CO_2, and mixed CH_4-CO_2 hydrates formed in salt solutions without porous media.

1) Pure CH_4, pure CO_2, and mixed CH_4-CO_2 hydrates formed without porous media accumulated in large volumes near the gas-solution interface.
2) Hydrate morphology was unique for different gases, gas compositions, and hydrate formation driving forces as CH_4 formed more spherically shaped, gas bubble-coating hydrates, CO_2 formed dendritic branched hydrates, 50%-50% CH_4-CO_2 mixtures formed a combination of amorphous shaped and branched

hydrates, and unequal proportions of CH_4-CO_2 gas resulted in needle-like hydrates.

3) Kinetic driving forces (diffusion and gas solubility) affected hydrate induction times more than thermodynamic driving forces (pressure-temperature conditions).
4) X-ray radiation may play a role in reducing hydrate induction times.
5) In several experiments, a hydrate network with a scaffold-like appearance was seen to form in the gas phase of the cell above the gas-liquid interface. No such network has been reported in previous literature.
6) A pressure drop during cell cooling, followed by a pressure increase during hydrate formation in mixed CH_4-CO_2 systems was witnessed during CMT experiments, as well as during experiments performed without x-ray imaging. This is likely to be the result of a salinity increase in the system due to hydrate formation and CH_4-CO_2 interactions in hydrates in small volume systems.
7) The fact that gas hydrates grew differently under similar temperatures but different pressures and gas compositions could have implications on the extraction of CH_4 hydrates and sequestration of CO_2 on the ocean floor.

8.5 CMT Experiments –CO_2 and CH_4-CO_2 Hydrate Formation within Porous Media

CMT was used to form CO_2 and CH_4-CO_2 hydrates in salt solutions in the presence of porous media.

1) CO_2 hydrate morphology can vary for each hydrate formation experiment performed using the same gas and hydrate forming solution. When the cell was warmed above 25°C and hydrates were reformed, hydrates grew in smaller shapes in new locations.
2) The salt solution was the wetting phase of the porous media, and less saturated sand packs still appear to have a thin solution layer between gas hydrates and porous media.
3) Precipitated $BaCl_2$ was found in areas of the cell depleted of hydrate forming solution, indicating that hydrates did form in appreciable quantities as salt is excluded from the hydrate structure.

4) CO_2 hydrates formed in glass beads and CO_2 and CH_4-CO_2 hydrates in Ottawa sand were found to grow according to the pore filling hydrate growth model.
5) The presence of liquid CO_2 and possible CO_2 hydrates in Ottawa sand initially resulted in a pore-filling morphology but became grain-displacing over time due to Ostwald ripening.
6) Morphology changes in a sand matrix in the presence of liquid CO_2 and CO_2 hydrates could affect the stability of the seafloor during CO_2 sequestration.

8.6 Future Work

As the Copenhagen Accord's 2°C temperature rise for the planet is within sight, it is imperative to gain a better understanding of the effects of CO_2 sequestration in ocean CH_4 hydrate reservoirs. Further studies of gas hydrate formation in the gas phase of a system using imaging techniques with better spatial resolution could provide information on possible hydrate networks. CMT imaging technologies should be utilized to understand the stability of gas hydrates grown with an overburden confining pressure, similar to the pressures felt on the ocean floor. Greater knowledge of gas exchange in hydrates is necessary to advancing CH_4 extraction and CO_2 sequestration, thereby CMT experiments could be performed by forming CH_4 hydrates, followed by a CO_2 gas injection.

In addition, further investigation of the effects of the presence of liquid CO_2 on the ocean floor during CO_2 sequestration should be performed. Any changes to hydrate morphology or to the sand matrix could be monitored to gain a better understanding of natural ocean CH_4 extraction and CO_2 sequestration events. Overall, further field tests need to be performed, especially in marine sediments where a majority of CH_4 hydrates can be found, to form CO_2 hydrates while extracting CH_4.

Chapter 9

9.0 References

1 Bennaceur, K. *et al.* CO_2 Capture and Storage - A Solution Within. *Oil Field Review*, 44-61 (2004).

2 Goel, N. In situ methane hydrate dissociation with carbon dioxide sequestration: Current knowledge and issues. *J Petrol Sci Eng* **51**, 169-184, doi:10.1016/j.petrol.2006.01.005 (2006).

3 Administration, N. O. A. A. *Trends in Atmospheric Carbon Dioxide*, <http://www.esrl.noaa.gov/gmd/ccgg/trends/>

4 Laboratory, N. E. T. 2010 Carbon Sequestration Atlas of the United States and Canada. **Third Edition** (2010).

5 Agency, I. E. World Energy Outlook 2010. (2010).

6 Geophysical Fluid Dynamics Laboratory, N. O. a. A. A. *Climate Impact of Quadrupling CO2*, <http://gfdl.noaa.gov/index/knutson-climate-impact-of-quadrupling-co2> (1999).

7 Shukla, R., Ranjith, P., Haque, A. & Choi, X. A review of studies on CO(2) sequestration and caprock integrity. *Fuel* **89**, 2651-2664, doi:DOI 10.1016/j.fuel.2010.05.012 (2010).

8 Rouchon, V., Orberger, B., Hofmann, A. & Pinti, D. L. Diagenetic Fe-carbonates in Paleoarchean felsic sedimentary rocks (Hooggenoeg Formation, Barberton greenstone belt, South Africa): Implications for CO(2) sequestration and the chemical budget of seawater. *Precambrian Res* **172**, 255-278, doi:10.1016/j.precamres.2009.04.010 (2009).

9 Wang, Z. *et al.* Adsorption and desorption on coals for CO_2 sequestration. *Mining Science and Technology (China)* **19**, 8-13 (2009).

10 Ravagnani, A. T. F. S. G., Ligero, E. L. & Suslick, S. B. CO(2) sequestration through enhanced oil recovery in a mature oil field. *J Petrol Sci Eng* **65**, 129-138, doi:10.1016/j.petrol.2008.12.015 (2009).

11 Rosenbauer, R. J., Koksalan, T. & Palandri, J. L. Experimental investigation of CO2-brine-rock interactions at elevated temperature and pressure: Implications for CO2 sequestration in deep-saline aquifers. *Fuel Process Technol* **86**, 1581-1597, doi:10.1016/j.fuproc.2005.01.011 (2005).

12 Wright, J. F., Cote, M. M., Dallimore, S. R. Overview of Regional Opportunities for Geological Sequestration of CO2 as Gas Hydrate in Canada in *Proceedings of the 6th International Conference on Gas Hydrates* (2008)

13 Laboratory, N. E. T. Energy Resource Potential of Methane Hydrate. (2011).

14 Administration, U. S. E. I. Annual Energy Outlook 2014 (2014).

15 Mahajan, D., Taylor, C. E. & Mansoori, G. A. An introduction to natural gas hydrate/clathrate: The major organic carbon reserve of the Earth. *J Petrol Sci Eng* **56**, 1-8, doi:10.1016/j.petrol.2006.09.006 (2007).
16 Ohgaki, K., Takano, K. & Moritoki, M. Exploitation of Ch4 Hydrates under the Nankai Trough in Combination with Co2 Storage. *Kagaku Kogaku Ronbun* **20**, 121-123 (1994).
17 Sloan, E. D. & Koh, C. A. *Clathrate hydrates of natural gases*. 3rd edn, (CRC Press, 2008).
18 Tohidi, B., Yang, J. H., Salehabadi, M., Anderson, R. & Chapoy, A. CO(2) Hydrates Could Provide Secondary Safety Factor in Subsurface Sequestration of CO(2). *Environ Sci Technol* **44**, 1509-1514, doi:10.1021/es902450j (2010).
19 Makogon, Y. F., Holditch, S. A. & Makogon, T. Y. Natural gas-hydrates - A potential energy source for the 21st Century. *J Petrol Sci Eng* **56**, 14-31, doi:DOI 10.1016/j.petrol.2005.10.009 (2007).
20 Gornitz, V. & Fung, I. Potential distribution of methane hydrates in the world's oceans. *Global Biogeochemical Cycles* **8**, 335-347, doi:10.1029/94gb00766 (1994).
21 Survey, U. S. G. *U.S. Geological Survey Gas Hydrates Project*, <www.woodshole.er.usgs.gov/project-pages/hydrates/index.html>
22 Sun, R. & Duan, Z. Prediction of CH_4 and CO_2 hydrate phase equilibrium and cage occupancy from ab initio intermolecular potentials. *Geochim Cosmochim Ac* **69**, 4411-4424 (2005).
23 Chatti, I., Delahaye, A., Fournaison, L. & Petitet, J. P. Benefits and drawbacks of clathrate hydrates: a review of their areas of interest. *Energ Convers Manage* **46**, 1333-1343, doi:DOI 10.1016/j.enconman.2004.06.032 (2005).
24 Folger, P. Carbon Capture and Sequestration (CCS). (2009).
25 Ota, M. *et al.* Replacement of CH4 in the hydrate by use of liquid CO2. *Energ Convers Manage* **46**, 1680-1691, doi:10.1016/j.enconman.2004.10.002 (2005).
26 Mines, C. S. o. *Software*, <http://hydrates.mines.edu/CHR/Software.html> (2009).
27 Lee, H., Seo, Y., Seo, Y. T., Moudrakovski, I. L. & Ripmeester, J. A. Recovering methane from solid methane hydrate with carbon dioxide. *Angew Chem Int Edit* **42**, 5048-5051, doi:10.1002/anie.200351489 (2003).
28 Kvamme, B., Qasim, M., Baig, K., Kivelä, P.-H. & Bauman, J. Hydrate phase transition kinetics from Phase Field Theory with implicit hydrodynamics and heat transport. *International Journal of Greenhouse Gas Control* **29**, 263-278, doi:http://dx.doi.org/10.1016/j.ijggc.2014.08.003 (2014).
29 Mao, W. L., Koh, C. A. & Sloan, E. D. Clathrate, hydrates under pressure. *Phys Today* **60**, 42-47 (2007).
30 Wallmann, K. B., J.; Utecht, C. *The SUGAR Project*, <http://cpatw.iccip.net/downloads/sugar_project.pdf>
31 Garrison, T. & Ellis, R. Oceanography: An Invitation to Marine Science. (Cengage Learning, Boston, MA, 2015).
32 Liquide, A. *Gas Encyclopedia*, <http://encyclopedia.airliquide.com/encyclopedia.asp?LanguageID=11>
33 Guo, H., Chen, Y., Lu, W., Li, L. & Wang, M. In situ Raman spectroscopic study of diffusion coefficients of methane in liquid water under high pressure and wide temperatures. *Fluid Phase Equilibr* **360**, 274-278, doi:http://dx.doi.org/10.1016/j.fluid.2013.09.051 (2013).

34 Lu, W., Guo, H., Chou, I. M., Burruss, R. C. & Li, L. Determination of diffusion coefficients of carbon dioxide in water between 268 and 473 K in a high-pressure capillary optical cell with in situ Raman spectroscopic measurements. *Geochim Cosmochim Ac* **115**, 183-204, doi:http://dx.doi.org/10.1016/j.gca.2013.04.010 (2013).
35 Committee, M. H. A. Report of the Methane Hydrate Advisory Committee on Methane Hydrate Issues and Opportunities. (2002).
36 Youngjune Park, D.-Y. K., Jong-Won Lee, Dao-Gee Huh, Keun-Pil Park, Jaehyoung Lee, and Huen Lee. Sequestering carbon dioxide into comples structures of naturally occuring gas hydrates. *PNAS* **103**, 12690-12694 (2006).
37 Maslin, M. *et al. Gas hydrates: past and future geohazard?* , Vol. 368 (2010).
38 Centre for Gas Hydrate Research, H. W. I. o. P. E. *Why are Gas Hydrates Important?*, <www.pet.hw.ac.uk/research/hydrate/hydrates_why.cfm>
39 Kashchiev, D. & Firoozabadi, A. Driving force for crystallization of gas hydrates. *J Cryst Growth* **241**, 220-230, doi:http://dx.doi.org/10.1016/S0022-0248(02)01134-X (2002).
40 Makogon, I. U. r. F., Makogon, J. F., Ingénieur, R. & Engineer, R. *Hydrates of natural gas*. (PennWell Books Tulsa, Oklahoma, 1981).
41 Tegze, G. *et al.* Multiscale approach to CO2 hydrate formation in aqueous solution: Phase field theory and molecular dynamics. Nucleation and growth. *J Chem Phys* **124**, doi:Artn 234710 Doi 10.1063/1.2207138 (2006).
42 Freer, E. M., Selim, M. S. & Sloan, E. D. Methane hydrate film growth kinetics. *Fluid Phase Equilibr* **185**, 65-75, doi:Doi 10.1016/S0378-3812(01)00457-5 (2001).
43 Uchida, T., Ebinuma, T., Kawabata, J. & Narita, H. Microscopic observations of formation processes of clathrate-hydrate films at an interface between water and carbon dioxide. *J Cryst Growth* **204**, 348-356, doi:Doi 10.1016/S0022-0248(99)00178-5 (1999).
44 Ohmura, R. *et al.* Clathrate hydrate crystal growth in liquid water saturated with a hydrate-forming substance: variations in crystal morphology. *Philos Mag* **84**, 1-16, doi:Doi 10.1080/14786430310001623542 (2004).
45 Moon, C., Taylor, P. C. & Rodger, P. M. Molecular Dynamics Study of Gas Hydrate Formation. *J Am Chem Soc* **125**, 4706-4707, doi:10.1021/ja028537v (2003).
46 Zhang, J. F. *et al.* Molecular dynamics study of methane hydrate formation at a water/methane interface. *J Phys Chem B* **112**, 10608-10618, doi:Doi 10.1021/Jp076904p (2008).
47 Radhakrishnan, R. & Trout, B. L. A new approach for studying nucleation phenomena using molecular simulations: Application to CO2 hydrate clathrates. *J Chem Phys* **117**, 1786-1796, doi:Doi 10.1063/1.1485962 (2002).
48 Servio, P. & Englezos, P. Morphology of methane and carbon dioxide hydrates formed from water droplets. *Aiche J* **49**, 269-276, doi:DOI 10.1002/aic.690490125 (2003).
49 Englezos, P., Kalogerakis, N., Dholabhai, P. D. & Bishnoi, P. R. Kinetics of Gas Hydrate Formation from Mixtures of Methane and Ethane. *Chem Eng Sci* **42**, 2659-2666, doi:Doi 10.1016/0009-2509(87)87016-1 (1987).
50 Englezos, P., Kalogerakis, N., Dholabhai, P. D. & Bishnoi, P. R. Kinetics of Formation of Methane and Ethane Gas Hydrates. *Chem Eng Sci* **42**, 2647-2658, doi:Doi 10.1016/0009-2509(87)87015-X (1987).
51 Malegaonkar, M. B., Dholabhai, P. D. & Bishnoi, P. R. Kinetics of carbon dioxide and methane hydrate formation. *The Canadian Journal of Chemical Engineering* **75**, 1090-1099, doi:10.1002/cjce.5450750612 (1997).

52 Skovborg, P. & Rasmussen, P. A Mass-Transport Limited Model for the Growth of Methane and Ethane Gas Hydrates. *Chem Eng Sci* **49**, 1131-1143, doi:Doi 10.1016/0009-2509(94)85085-2 (1994).
53 Mochizuki, T. & Mori, Y. H. Clathrate-hydrate film growth along water/hydrate-former phase boundaries - numerical heat-transfer study. *J Cryst Growth* **290**, 642-652, doi:DOI 10.1016/j.jcrysgro.2006.01.036 (2006).
54 Wu, Q. & Zhang, B. Memory effect on the pressure-temperature condition and induction time of gas hydrate nucleation. *Journal of Natural Gas Chemistry* **19**, 446-451, doi:10.1016/s1003-9953(09)60086-4 (2010).
55 Dvorkin, J. & Nur, A. Elasticity of high-porosity sandstones: Theory for two North Sea data sets. *Geophysics* **61**, 1363-1370 (1996).
56 Dai, J., Xu, H., Snyder, F. & Dutta, N. Detection and Estimation of Gas Hydrates Using Rock Physics and Seismic Inversion: Examples from the Northern Deepwater Gulf of Mexico. *The Leading Edge*, 60-66 (2004).
57 Durham, W. B., Kirby, S. H., Stern, L. A. & Zhang, W. The strength and rheology of methane clathrate hydrate. *J Geophys Res-Sol Ea* **108**, doi:Artn 2182 Doi 10.1029/2002jb001872 (2003).
58 Dai, S., Santamarina, J. C., Waite, W. F. & Kneafsey, T. J. Hydrate morphology: Physical properties of sands with patchy hydrate saturation. *J Geophys Res-Sol Ea* **117**, doi:Artn B11205 Doi 10.1029/2012jb009667 (2012).
59 Juanes, R. & Bryant, S. L. Mechanisms Leading to Co-existence of Gas and Hydrate in Ocean Sediments. (U.S. Department of Energy, 2006).
60 Gupta, A. *Methane Hydrate Dissociation Measurements and Modeling: The Role of Heat Transfer and Reaction Kinetics*, Colorado School if Mines, (2007).
61 Stern, L. A., Circone, S., Kirby, S. H. & Durham, W. B. Temperature, pressure, and compositional effects on anomalous or "self" preservation of gas hydrates. *Canadian Journal of Physics* **81**, 271-283, doi:10.1139/p03-018 (2003).
62 Circone, S., Stern, L. A. & Kirby, S. H. The effect of elevated methane pressure on methane hydrate dissociation. *Am Mineral* **89**, 1192-1201 (2004).
63 Falenty, A. & Kuhs, W. F. "Self-Preservation" of CO2 Gas Hydrates—Surface Microstructure and Ice Perfection. *The Journal of Physical Chemistry B* **113**, 15975-15988, doi:10.1021/jp906859a (2009).
64 Collett, T. S. *GAS HYDRATE RESOURCES OF THE UNITED STATES*. (1995).
65 Milkov, A. V. & Sassen, R. Preliminary assessment of resources and economic potential of individual gas hydrate accumulations in the Gulf of Mexico continental slope. *Mar Petrol Geol* **20**, 111-128, doi:Doi 10.1016/S0264-8172(03)00024-2 (2003).
66 Francisca, F., Yun, T. S., Ruppel, C. & Santamarina, J. C. Geophysical and geotechnical properties of near-seafloor sediments in the northern Gulf of Mexico gas hydrate province. *Earth Planet Sc Lett* **237**, 924-939, doi:DOI 10.1016/j.epsl.2005.06.050 (2005).
67 Scientists, E. Integrated Ocean Drilling Program Expedition 311 Preliminary Report: Cascadia Margin Gas Hydrates. (2005).
68 Paull, C. K. M., R. 1. Leg 164 Overview. *Proceedings of the Ocean Drilling Program, Scientific Results* **164** (2000).
69 Collett, T. S. L., J. Detection of Gas Hydrate with Downhole Log and Assessment of Gas Hydrate Concentrations (Saturations) and Gas Volumes on the Blake Ridge with

Electrical Resistivity Log Data. *Proceedings of the Ocean Drilling Program, Scientific Results* **164** (2000).
70 Max, M. D. & Lowrie, A. OCEANIC METHANE HYDRATES: A "FRONTIER" GAS RESOURCE. *Journal of Petroleum Geology* **19**, 41-56, doi:10.1111/j.1747-5457.1996.tb00512.x (1996).
71 Clennell, M. B., Hovland, M., Booth, J. S., Henry, P. & Winters, W. J. Formation of natural gas hydrates in marine sediments: 1. Conceptual model of gas hydrate growth conditioned by host sediment properties. *Journal of Geophysical Research: Solid Earth* **104**, 22985-23003, doi:10.1029/1999jb900175 (1999).
72 Hovland, M., Gallagher, J. W., Clennell, M. B. & Lekvam, K. Gas hydrate and free gas volumes in marine sediments: Example from the Niger Delta front. *Mar Petrol Geol* **14**, 245-255, doi:http://dx.doi.org/10.1016/S0264-8172(97)00012-3 (1997).
73 Holland, M., Schultheiss, P., Roberts, J. & Druce, M. in *6th International Conference on Gas Hydrates.*
74 Whiticar, M. J., Hovland, M., Kastner, M. & Sample, J. C. Organic Geochemistry of Gases, Fluids, and Hydrates at the Cascadia Accretionary Margin. *Proceedings of the Ocean Drilling Program, Scientific Results* **146**, 385-397 (1995).
75 Matsumoto, R. & Borowski, W. S. Gas Hydrate Estimates from Newly Determined Oxygen Isotopic Fractionation (αGH–IW) and δ18O Anomalies of the Interstitial Waters: Leg 164, Blake Ridge. *Proceedings of the Ocean Drilling Program, Scientific Results* **164**, 59-66 (2000).
76 Sassen, R. *et al.* Massive vein-filling gas hydrate: relation to ongoing gas migration from the deep subsurface in the Gulf of Mexico. *Mar Petrol Geol* **18**, 551-560, doi:http://dx.doi.org/10.1016/S0264-8172(01)00014-9 (2001).
77 Abegg, F. B., G.; Kuhs, W. 21. Data Report: Shapes and Structures of Gas Hydrates Imaged by Computed Tomographic Analyses, ODP LEG 204, Hydrate Ridge. *Proceedings of the Ocean Drilling Program, Scientific Results* **204**, 1-11 (2006).
78 Demirbas, A. Methane hydrates as potential energy resource: Part 2-Methane production processes from gas hydrates. *Energ Convers Manage* **51**, 1562-1571, doi:DOI 10.1016/j.enconman.2010.02.014 (2010).
79 Sloan, E. D. Fundamental principles and applications of natural gas hydrates. *Nature* **426**, 353-363 (2003).
80 Pierce, B. & Collett, T. in *5 th Conference and Exposition on Petroleum Geophysics, Hyderabad, India.* 899-903.
81 in *Fire in the Ice Methane Hydrate Newsletter* Vol. 13 1-2 (National Energy Technology Laboratory, 2013).
82 Collett, T. *et al.* Methane Hydrates in Nature—Current Knowledge and Challenges. *Journal of Chemical & Engineering Data*, doi:10.1021/je500604h (2014).
83 Baig, K., Kvamme, B., Kuznetsova, T. & Bauman, J. Impact of water film thickness on kinetic rate of mixed hydrate formation during injection of CO2 into CH4 hydrate. *AIChE Journal*, n/a-n/a, doi:10.1002/aic.14913 (2015).
84 Jung, J. W., Espinoza, D. N. & Santamarina, J. C. Properties and phenomena relevant to CH4-CO2 replacement in hydrate-bearing sediments. *J Geophys Res-Sol Ea* **115**, doi:Artn B10102 Doi 10.1029/2009jb000812 (2010).
85 Deusner, C., Bigalke, N., Kossel, E. & Haeckel, M. Methane Production from Gas Hydrate Deposits through Injection of Supercritical CO2. *Energies* **5**, 2112-2140 (2012).

86 Komatsu, H., Ota, M., Smith Jr, R. L. & Inomata, H. Review of CO2–CH4 clathrate hydrate replacement reaction laboratory studies – Properties and kinetics. *Journal of the Taiwan Institute of Chemical Engineers* **44**, 517-537, doi:http://dx.doi.org/10.1016/j.jtice.2013.03.010 (2013).
87 Jadhawar, P., Mohammadi, A. H., Yang, J. & Tohidi, B. Subsurface Carbon Dioxide Storage through Clathrate Hydrate Formation. *Advances in the Geological Storage of Carbon Dioxide*, 111-126 (2006).
88 Graue, A. *et al.* MRI Visualization of Spontaneous Methane Production from Hydrates in Sandstone Core Plugs When Exposed to CO_2. *SPE Journal*, 146-152 (2008).
89 Baldwin, B. A. *et al.* Using magnetic resonance imaging to monitor CH4 hydrate formation and spontaneous conversion of CH4 hydrate to CO2 hydrate in porous media. *Magnetic Resonance Imaging* **27**, 720-726 (2009).
90 White, R. K., T. Methane Hydrate Production Technique Set for January Testing. *Platts Gas Daily* **28** (2011).
91 Schoderbek, D. *et al.* ConocoPhillips Gas Hydrate Production Test Final Technical Report. (ConocoPhilips Company, 2013).
92 Tsouris, C. *et al.* Scaled-up ocean injection of CO2-Hydrate composite particles. *Energ Fuel* **21**, 3300-3309, doi:Doi 10.1021/El070197h (2007).
93 Brewer, P. G. *et al.* Deep Sea Field Test of the CH4 Hydrate to CO2 Hydrate Spontaneous Conversion Hypothesis. *Energ Fuel*, doi:10.1021/ef501430h (2014).
94 Walsh, M. R. *et al.* Preliminary report on the commercial viability of gas production from natural gas hydrates. *Energy Economics* **31**, 815-823, doi:http://dx.doi.org/10.1016/j.eneco.2009.03.006 (2009).
95 Milkov, A. v. S., Roger. Economic geology of offshore gas hydrate accumulations and provinces. *Marine and Petroleum Geology* **19**, 1-11 (2002).
96 Facility, E. S. R. *What is a synchrotron?*, <http://www.esrf.eu/about/synchrotron-science/synchrotron>
97 Dunsmuir, J. H. (ed ExxonMobil Research and Engineering Co.) (Annandale, N.J.).
98 *Beamline X2B*, <http://beamlines.ps.bnl.gov/beamline.aspx?blid=X2B>
99 Limaye, A. Drishti – Volume Exploration and Presentation Tool in *Poster Presentation, Vis 2006,*.
100 Kester, D. R., Duedall, I. W., Connors, D. N. & Pytkowic.Rm. Preparation of Artificial Seawater. *Limnol Oceanogr* **12**, 176-& (1967).
101 Ussler, W. & Paull, C. K. Effects of Ion-Exclusion and Isotopic Fractionation on Pore-Water Geochemistry during Gas Hydrate Formation and Decomposition. *Geo-Mar Lett* **15**, 37-44, doi:Doi 10.1007/Bf01204496 (1995).
102 Company, U. S. S. *Material Safety Data Sheet Silica Sand and Ground Silica*, 2012).
103 Biospec Products, I. *Materials Safety Data Sheet From OSHA Form 20*, <http://www.biospec.com/msds_information/>
104 Horvat, K., Kerkar, P., Jones, K. & Mahajan, D. Kinetics of the Formation and Dissociation of Gas Hydrates from CO2-CH4 Mixtures. *Energies* **5**, 2248-2262 (2012).
105 Ricaurte, M., Torré, J.-P., Asbai, A., Broseta, D. & Dicharry, C. Experimental Data, Modeling, and Correlation of Carbon Dioxide Solubility in Aqueous Solutions Containing Low Concentrations of Clathrate Hydrate Promoters: Application to CO2–CH4 Gas Mixtures. *Ind Eng Chem Res* **51**, 3157-3169, doi:10.1021/ie2023993 (2012).

106 Sugaya, M. & Mori, Y. H. Behavior of clathrate hydrate formation at the boundary of liquid water and a fluorocarbon in liquid or vapor state. *Chem Eng Sci* **51**, 3505-3517 (1996).
107 Ripmeester, J. A. & Alavi, S. Molecular Simulations of Methane Hydrate Nucleation. *Chemphyschem* **11**, 978-980, doi:10.1002/cphc.201000024 (2010).
108 Lee, J. W., Zhang, J. S. & Lee, S. Does SDS micellize under methane hydrate-forming conditions below the normal Krafft point? *J Colloid Interf Sci* **315**, 313-318, doi:10.1016/j.jcis.2007.06.049 (2007).
109 Seo, Y. T., Lee, H. & Yoon, J. H. Hydrate phase equilibria of the carbon dioxide, methane, and water system. *J Chem Eng Data* **46**, 381-384 (2001).
110 Uchida, T. *et al.* Kinetics and stability of CH4-CO2 mixed gas hydrates during formation and long-term storage. *Chemphyschem* **6**, 646-654, doi:10.1002/cphc.200400364 (2005).
111 Horvat, K. & Mahajan, D. Carbon Dioxide-Induced Liberation of Methane from Laboratory-formed Methane Hydrates. *Canadian Journal of Chemistry*, doi:10.1139/cjc-2014-0562 (2015).
112 Bishnoi, P. R. & Natarajan, V. Formation and Decomposition of Gas Hydrates. *Fluid Phase Equilibr* **117**, 168-177 (1996).
113 Sinaiski, E. G. & Lapiga, E. J. *Separation of Multiphase, Multicomponent Systems*. (Wiley, 2007).
114 Handa, Y. P. & Stupin, D. Y. Thermodynamic properties and dissociation characteristics of methane and propane hydrates in 70-.ANG.-radius silica gel pores. *The Journal of Physical Chemistry* **96**, 8599-8603, doi:10.1021/j100200a071 (1992).
115 Jensen, L., Thomsen, K. & von Solms, N. Propane hydrate nucleation: Experimental investigation and correlation. *Chem Eng Sci* **63**, 3069-3080, doi:http://dx.doi.org/10.1016/j.ces.2008.03.006 (2008).
116 He, Y., Rudolph, E. S. J., Zitha, P. L. J. & Golombok, M. Kinetics of CO2 and methane hydrate formation: An experimental analysis in the bulk phase. *Fuel* **90**, 272-279, doi:http://dx.doi.org/10.1016/j.fuel.2010.09.032 (2011).
117 Golombok, M., Ineke, E., Luzardo, J. C. R., He, Y. Y. & Zitha, P. Resolving CO2 and methane hydrate formation kinetics. *Environ Chem Lett* **7**, 325-330, doi:DOI 10.1007/s10311-008-0173-y (2009).
118 Zhang, B. Y., Wu, Q., Gao, X., Liu, C. L. & Ye, Y. G. Memory effect on hydrate formation and influential factors of its sustainability in new hydrate-based coal mine methane separation method. *Int J Environ Pollut* **53**, 201-212, doi:Doi 10.1504/Ijep.2013.059913 (2013).
119 Mazloum, S., Yang, J., Chapoy, A. & Tohidi, B. A New Method for Hydrate Early Warning System Based on Hydrate Memory in *7th International Conference on Gas Hydrates (ICGH 2011)*.
120 Qasim, M., Kvamme, B. & Baig, K. Phase field theory modeling of CH4/CO2 gas hydrates in gravity fields. *International Journal of Geology* **5**, 48-52 (2011).
121 Diamond, L. W. & Akinfiev, N. N. Solubility of CO2 in water from -1.5 to 100 degrees C and from 0.1 to 100 MPa: evaluation of literature data and thermodynamic modelling. *Fluid Phase Equilibr* **208**, 265-290, doi:Doi 10.1016/S0378-3812(03)00041-4 (2003).
122 Fujino, K., Lewis, E. L. & Perkin, R. G. The freezing point of seawater at pressures up to 100 bars. *Journal of Geophysical Research* **79**, 1792-1797, doi:10.1029/JC079i012p01792 (1974).

123 Ritman, E. L. Micro-computed tomography-current status and developments. *Annu Rev Biomed Eng* **6**, 185-208, doi:DOI 10.1146/annurev.bioeng.6.040803.140130 (2004).
124 Freifeld, B. & Kneafsey, T. (eds Charles Taylor & Jonathan Kwan) 227-238 (Springer US, 2004).
125 Kneafsey, T. J. *et al.* Methane hydrate formation and dissociation in a partially saturated core-scale sand sample. *J Petrol Sci Eng* **56**, 108-126, doi:10.1016/j.petrol.2006.02.002 (2007).
126 Priest, J., Kingston, E., Clayton, C., Schultheiss, P. & Druce, M. The Structure of Hydrate Bearing Fine Grained Marine Sediments in *Proceedings of the 6th International Conference on Gas Hydrates (ICGH 2008).*
127 Choi, J. H., Seol, Y., Boswell, R. & Juanes, R. X-ray computed-tomography imaging of gas migration in water-saturated sediments: From capillary invasion to conduit opening. *Geophys Res Lett* **38**, doi:Artn L17310 Doi 10.1029/2011gl048513 (2011).
128 Rees, E. V. L., Kneafsey, T. J. & Seol, Y. Methane Hydrate Distribution from Prolonged and Repeated Formation in Natural and Compacted Sand Samples: X-Ray CT Observations. *Journal of Geological Research*, 1-15 (2011).
129 Kerkar, P. *et al.* Direct observations of three dimensional growth of hydrates hosted in porous media. *Appl Phys Lett* **95**, doi:10.1063/1.3120544 (2009).
130 Kerkar, P. B., Horvat, K., Jones, K. W. & Mahajan, D. Imaging methane hydrates growth dynamics in porous media using synchrotron X-ray computed microtomography. *Geochemistry, Geophysics, Geosystems* **15**, 4759-4768, doi:10.1002/2014gc005373 (2014).
131 Technology, N. I. o. S. a. *XCOM*, <http://physics.nist.gov/PhysRefData/Xcom/html/xcom1.html> (
132 Li, S.-L. *et al.* New Observations and Insights into the Morphology and Growth Kinetics of Hydrate Films. *Sci. Rep.* **4**, doi:10.1038/srep04129 http://www.nature.com/srep/2014/140219/srep04129/abs/srep04129.html#supplementary-information (2014).
133 Glicksman, M. E. Mechanism of Dendritic Branching. *Metall Mater Trans A* **43A**, 391-404, doi:DOI 10.1007/s11661-011-0984-5 (2012).
134 Watanabe, S., Saito, K. & Ohmura, R. Crystal Growth of Clathrate Hydrate in Liquid Water Saturated with a Simulated Natural Gas. *Cryst Growth Des* **11**, 3235-3242, doi:Doi 10.1021/Cg2005024 (2011).
135 Buanes, T., Kvamme, B. & Svandal, A. Two approaches for modelling hydrate growth. *J Math Chem* **46**, 811-819, doi:DOI 10.1007/s10910-009-9551-3 (2009).
136 Libbrecht, K. G. The physics of snow crystals. *Rep Prog Phys* **68**, 855-895, doi:Doi 10.1088/0034-4885/68/4/R03 (2005).
137 Husebo, J., Ersland, G., Graue, A. & Kvamme, B. Effects of salinity on hydrate stability and implications for storage of CO(2) in natural gas hydrate reservoirs. *Enrgy Proced* **1**, 3731-3738, doi:DOI 10.1016/j.egypro.2009.02.172 (2009).
138 Takenouchi, S. & Kennedy, G. C. The solubility of carbon dioxide in NaCl solutions at high temperatures and pressures. *American journal of science* **263**, 445-454 (1965).
139 Circone, S. *et al.* CO2 Hydrate: Synthesis, Composition, Structure, Dissociation Behavior, and a Comparison to Structure I CH4 Hydrate. *J Phys Chem B* **107**, 5529-5539 (2003).

140 Mazloum, S., Chapoy, A., Yang, J. & Tohidi, B. A Simple Correlation for Calculating the Hydrate Suppression Temperature Based on Water Activity in *7th International Conference on Gas Hydrates (ICGH 2011).*
141 Herslund, P. J. *et al.* Thermodynamic promotion of carbon dioxide–clathrate hydrate formation by tetrahydrofuran, cyclopentane and their mixtures. *International Journal of Greenhouse Gas Control* **17**, 397-410, doi:http://dx.doi.org/10.1016/j.ijggc.2013.05.022 (2013).
142 Handa, Y. P. Effect of Hydrostatic-Pressure and Salinity on the Stability of Gas Hydrates. *J Phys Chem-Us* **94**, 2652-2657, doi:Doi 10.1021/J100369a077 (1990).
143 Østergaard, K. K., Anderson, R., Llamedo, M. & Tohidi, B. Hydrate phase equilibria in porous media: effect of pore size and salinity. *Terra Nova* **14**, 307-312, doi:10.1046/j.1365-3121.2002.00433.x (2002).
144 Liu, X. & Flemings, P. B. Capillary effects on hydrate stability in marine sediments. *Journal of Geophysical Research: Solid Earth* **116**, B07102, doi:10.1029/2010jb008143 (2011).
145 Yao, J. H., Elder, K. R., Guo, H. & Grant, M. Theory and Simulation of Ostwald Ripening. *Physical Review B* **47**, 14110-14125, doi:DOI 10.1103/PhysRevB.47.14110 (1993).
146 Katsuki, D., Ohmura, R., Ebinuma, T. & Narita, H. Formation, growth and ageing of clathrate hydrate crystals in a porous medium. *Philos Mag* **86**, 1753-1761, doi:Doi 10.1080/14786430500509062 (2006).
147 Gabitto, J. F. & Tsouris, C. Physical Properties of Gas Hydrates: A Review. *Journal of Thermodynamics* **2010**, doi:10.1155/2010/271291 (2010).
148 Kingston, E., Clayton, C. & Priest, J. Gas hydrate growth morphologies and their effect on the stiffness and damping of a hydrate bearing sand in *Proceedings of the 6th International Conference on Gas Hydrates (ICGH 2008).*